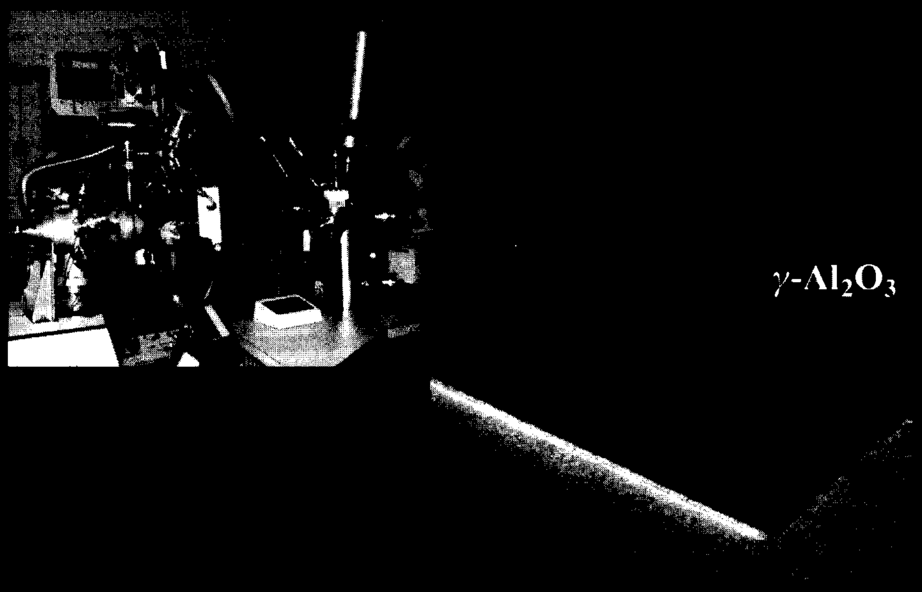
γ-Al_2O_3

TK 3725 S

Stellingen behorende bij het proefschrift

On the Initial Oxidation of Aluminium in Oxygen Gas

door L.P.H. Jeurgens

1. Tot een zekere kritische filmdikte, kan een amorfe oxidefilm op zijn metaalsubstraat thermodynamisch stabieler zijn dan de corresponderende kristallijne oxidefilm op hetzelfde substraat (zie hoofdstuk II van dit proefschrift).

2. Voor een correcte, kwantitatieve analyse van elektronen-emissie spectra van 'vrije-elektronen' materialen, dient naast de geïntegreerde intensiteit van de intrinsieke hoofdpiek(en) ook de geïntegreerde intensiteit van de bijbehorende intrinsieke plasmonenstruktuur beschouwd te worden (zie hoofdstuk III van dit proefschrift).

3. Een verschuiving van de bindingsenergie ('chemical shift') van een foto-elektron geëmitteerd van een element in een film op een substraat hoeft niet a-priori te zijn veroorzaakt door een verandering van de bindingstoestand van het desbetreffende element in de film (zie hoofdstuk V van dit proefschrift).

4. De aanname dat transport van kationen door een uniforme aluminiumoxide film de enige snelheidsbepalende stap is voor de oxidelaaggroei op aluminium (zie bijv. Ref. [1]), geldt alleen voor de groei van een amorfe aluminiumoxide film bij relatief lage temperaturen.

   [1] A. Jimenéz and D. Schmeisser, Surface Science 250 (1991), 59.

5. Bij de ontwikkeling van de huidige hoge-temperatuur metallurgische coatings wordt hoofdzakelijk de relatie tussen de eigenschappen en de chemische samenstelling beschouwd (zie bijv. Ref. [2]). De invloed van de (micro-)structuur van de coating op de eigenschappen is hierbij echter van minstens even groot belang.

   [2] G.W. Goward, Surface and Coatings Technology 108-109 (1998), 73.

6. Het onderscheid tussen amorf en nano-kristallijn op basis van een transmissie-elektronen beeld is subjectief.

7. In een staalfabriek zit meer techniek dan in een internetprovider.

8. De vaak toegepaste tactiek van het 'laten zwemmen' van een student(e) tijdens hem of haar afstudeeronderzoek staat haaks op de basis van goed wetenschappelijk onderwijs, het enthousiast maken én houden van studenten.

9. De enige structurele oplossing voor het fileprobleem en de chaos bij de Nederlandse spoorwegen is het verplaatsen van de werkplek naar thuis, of omgekeerd.

10. Verdere automatisering van het bedrijfsleven zal leiden tot een nog hoger papiergebruik: nog meer softwarehandleidingen en proefprintjes.

TR 3725

3724
760863

On the Initial Oxidation of Aluminium in Oxygen Gas

Proefschrift

BIBLIOTHEEK TECHNISCHE UNIVERSITEIT
Prometheusplein 1
DELFT

ter verkrijging van de graad van doctor
aan de Technische Universiteit Delft,
op gezag van de Rector Magnificus prof. ir. K.F. Wakker,
voorzitter van het College voor Promoties,
in het openbaar te verdedigen op maandag 10 september 2001 om 10:30 uur

door

Lars Petrus Henricus JEURGENS

doctorandus in de geologie
geboren te Aarle-Rixtel

Dit proefschrift is goedgekeurd door de promotor:
Prof. dr. ir. E.J. Mittemeijer

Samenstelling promotiecommissie

Rector Magnificus, voorzitter
Prof. dr. ir. E.J. Mittemeijer, Technische Universiteit Delft, promotor
Prof. dr. ir. S. van der Zwaag, Technische Universiteit Delft
Prof. dr. R. Boom, Technische Universiteit Delft
Prof. dr. J.Th.M. De Hosson, Rijksuniversiteit Groningen
Prof. dr. J. Schoonman, Technische Universiteit Delft
Dr. ir. W.G. Sloof, Technische Universiteit Delft
Dr. ir. A.E.T. Kuiper, Philips Research Lab

Dr. ir. W.G. Sloof en dr. ir. F.D. Tichelaar hebben als begeleider in belangrijke mate aan de totstandkoming van dit proefschrift bijgedragen.

The work described in this thesis was made possible by financial support from the Foundation for Fundamental Research of Matter (FOM).

ISBN 90-9015009-9
Copyright © 2001 by L.P.H. Jeurgens

Contents

1. GENERAL INTRODUCTION 1

I. BACKGROUND 2

II. THERMODYNAMIC STABILITY OF THIN OXIDE FILMS ON THEIR METAL SUBSTRATES: THE ROLE OF INTERFACES 3

III. THERMAL OXIDATION OF BARE METAL SUBSTRATES 4

IV. METHODS OF CHARACTERISATION 6

V. OUTLINE 8

REFERENCES 9

2. THERMODYNAMIC STABILITY OF AMORPHOUS OXIDE FILMS ON METALS: *APPLICATION TO ALUMINIUM-OXIDE FILMS ON ALUMINIUM SUBSTRATES* **11**

I. INTRODUCTION 12

II. BASIS OF THE THERMODYNAMICAL MODEL 13

III. THE ENERGY OF METAL-SUBSTRATE / OXIDE-FILM INTERFACES 15

A. Energy of the crystalline – amorphous <M>-{MO_x} interface 16

1. *Interaction contribution to the <M>-{MO_x} interfacial energy* 16
2. *Entropy contribution to the <M>-{MO_x} interfacial energy* 17
3. *Enthalpy contribution to the <M>-{MO_x} interfacial energy* 19
4. *Expression for the <M>-{MO_x} interfacial energy* 20

B. Energy of the crystalline–crystalline <M>-<MOx> interface 20

1. *Interaction contribution to the <M>-<MO_x> interfacial energy* 20
2. *Mismatch contribution to <M>-<MO_x> interfacial energy* 20
3. *Expression for the <M>-<MO_x> interfacial energy* 22

IV. THERMODYNAMICS OF AMORPHOUS AND CRYSTALLINE ALUMINIUM-OXIDE FILMS ON ALUMINIUM SUBSTRATES 22

A. Difference in bulk energy of {Al_2O_3} and <γ-Al_2O_3> 23

B. Difference in surface energy of $\{Al_2O_3\}$ and $<\gamma\text{-}Al_2O_3>$ 25
C. Difference in energy of $<Al>$-$\{Al_2O_3\}$ and $<Al>$-$<\gamma\text{-}Al_2O_3>$ interfaces 26
V. STABILITY OF AMORPHOUS ALUMINIUM-OXIDE FILMS ON CRYSTALLINE ALUMINIUM SUBSTRATES 32
VI. CONCLUSIONS 35
APPENDIX 36
REFERENCES 37

3. DETERMINATION OF TOTAL PRIMARY ZERO LOSS INTENSITIES IN MEASURED ELECTRON EMISSION SPECTRA OF BARE AND OXIDISED METALS: APPLICATION TO ALUMINIUM OXIDE FILMS ON ALUMINIUM SUBSTRATES **41**

I. INTRODUCTION 42
II. EXPERIMENTAL 45
III. DATA EVALUATION 46
IV. RESULTS AND DISCUSSION 51
V. CONCLUSIONS 56
REFERENCES 57

4. DETERMINATION OF THICKNESS AND COMPOSITION OF ALUMINIUM-OXIDE FILMS ON ALUMINIUM SUBSTRATES **59**

I. INTRODUCTION 60
II. XPS SPECTRA EVALUATION 61
III. DETERMINATION OF THICKNESS AND COMPOSITION; RESULTS AND DISCUSSION 63
REFERENCES 66

5. GROWTH KINETICS, MICROSTRUCTURE AND COMPOSITION OF ALUMINIUM-OXIDE FILMS FORMED BY THERMAL OXIDATION OF ALUMINIUM **69**

I. INTRODUCTION 70
II. EXPERIMENTAL 71
A. Sample preparation 71

B. Thermal oxidation and XPS analysis 72

C. Preparation of HREM cross-sections and analysis 74

III. XPS DATA EVALUATION 75

IV. STRUCTURE OF THE OXIDE FILM 80

A. Crystallinity of the oxide film 80

B. Morphology of the oxide film 86

C. Oxide surface 90

V. OXIDE-FILM GROWTH KINETICS 93

VI. OXIDE-FILM CONSTITUTION DURING GROWTH 97

A. Composition of the oxide film 97

1. *Low temperature oxide films* 99

2. *High temperature oxide films* 102

B. Composition at the oxide surface 103

C. Chemical state of Al and O 105

1. *The Al 2p oxide-film and surface-oxide components* 105

2. *The Al $KL_{23}L_{23}$ oxide-film and surface-oxide components* 108

3. *The O 1s oxide-film and surface-oxide components* 109

4. *Chemical and binding state plots* 110

5. *Origin of binding (and kinetic) energy shifts of oxide-film components* 112

VII. GENERAL DISCUSSION 115

A. Formation of a 'closed' oxide film 115

B. Growth of a 3D oxide film 118

1. *Low temperature oxidation* 118

a. Application of Mott-Cabrera model to low temperature oxidation of Al 120

2. *High temperature oxidation* 123

VIII. CONCLUSIONS 125

A. Oxide-film morphology 125

B. Oxide-film constitution and structure 126

C. Oxide-film growth kinetics and mechanisms 127

APPENDIX A: CALCULATION OF OXIDE-FILM COMPOSITION AND THICKNESS 128

1. Metallic, oxidic and oxygen PZL photoelectron intensities 128

2. Calculation of oxide-film composition 130

3. Calculation of oxide-film thickness 131

APPENDIX B: DERIVATION OF PZL PHOTOELECTRON INTENSITY EQUATIONS 132

APPENDIX C: GAUSS-LORENZ FUNCTION 133
APPENDIX D: ESTIMATION OF MOLAR DENSITIES OF O AND AL 134
REFERENCES 136

SUMMARY **141**

SAMENVATTING **147**

CURRICULUM VITAE **153**

Chapter 1

General Introduction

The desire to control the physical and chemical properties of very thin metal-oxide films (< 10 nm) by tailoring the oxide-film growth, morphology, chemical composition and microstructure has increased the interest for the process of dry, thermal oxidation of bare metal surfaces in various application areas such as microelectronics, catalysis and surface coatings (cf. Refs. [1-11]). However, the processes that occur and the changes that take place at the metal surface, in the developing oxide film, and at the metal/oxide and oxide/gas interfaces during the initial and subsequent stages of oxide-film growth are still poorly understood [2-5, 8]. Even for a classical metal/oxide system such as Al/Al_2O_3, as considered in this study, comprehensive and fundamental knowledge of the relationships between the mechanism(s) that govern the oxide-film growth and the resulting chemical composition, morphology and (micro)structure of the developing oxide film lacks [2-5, 8].

This study addresses in particular the thermodynamic stability of amorphous versus crystalline aluminium-oxide films on single-crystalline Al substrates, as well as the processes that control the growth kinetics, chemical composition, morphology and microstructure of these very thin oxide films grown by the dry, thermal oxidation on bare, single-crystalline Al substrates at different oxidation conditions (e.g. various oxidation times and temperatures, partial oxygen pressures, and crystallographic orientations of the parent metal substrate).

In this work, it has been shown on a thermodynamic basis that an amorphous structure for an oxide film on its metal substrate can be more stable than the crystalline structure. The thermodynamic stability of a thin amorphous metal-oxide film on top of its single-crystal metal substrate has been modelled as a function of growth temperature, oxide-film thickness and crystallographic orientation of the metal substrate. To this end expressions have been derived for the estimation of the energies of the metal-substrate / amorphous-oxide film interface and the metal-substrate / crystalline-oxide film interface as a function of growth temperature, and crystallographic orientation of the substrate (including the effect of strain due to the lattice mismatch).

To establish the relations between the oxide-film growth kinetics, the chemical composition, the morphology and the microstructure as a function of the oxidation conditions, bare single-crystalline Al substrates were exposed to oxygen at a partial oxygen pressure of 1.33×10^{-4} Pa in the temperature range from 373 to 773 K. An UHV specimen processing chamber was specially developed and built for these type of experiments. This UHV chamber, which is directly coupled to the instrument for X-ray photoelectron spectroscopy (XPS) analysis, is equipped with: (*i*) an ion-gun to clean the metal surface prior to oxidation, (*ii*) a unit for the controlled admission of oxygen, (*iii*) a quadrupole mass spectrometer to monitor the partial oxygen pressure, and (*iv*) a specimen heating device.

The oxide-film thickness, chemical composition and morphology, as well as the changes in chemical and binding state of the concerned ions in the grown oxide films, were investigated using in-situ X-ray photoelectron spectroscopy (XPS). XPS is very suitable for studying such very thin metal-oxide films on their metal substrates, because the inelastic mean free path (IMFP) of the emitted photoelectrons is of the same order of magnitude as the thickness of the grown oxide films (several nanometers). The development of the microstructure and morphology of the aluminium-oxide film as a function of the oxidation temperature, as well as the crystallographic orientation relation between the observed oxide phases and the parent metal substrate, were studied on an atomic scale using high-resolution transmission electron microscopy (HREM).

I. Background

For a geologist, it is well know that aluminium is the third most abundant element on earth after silicon and oxygen, but does not exists in Nature as a free element. It is found in most rocks, clay, soil and vegetation only in combination with oxygen or other elements. The most common ore of Al is Bauxite, a mineral containing some 55-65% Al-oxide with mostly Fe- and Ti-oxides.

Due to the unique combination of properties such as low density, good thermal and electrical conductivity, high reflectivity, and the formation of a protective oxide film, aluminium has found many applications and its properties has initiated many new technologies. For example, Al plays a dominant role in air, space, packing and storage industries and is the only suitable metal to use for overhead transmission cables. Today, it's has also found application in e.g. CD-ROMs and microelectronics.

Although aluminium is a relative base metal (i.e. it has a much higher affinity for oxygen than e.g. iron), a stable, 2 - 3 nm thick, insulating aluminium-oxide film, that resists further oxidation of the underlying metal, is formed on its bare surface within a few seconds upon exposure in air. The chemical composition, morphology and microstructure of such thin aluminium-oxide films grown on aluminium substrates have a direct bearing to a variety of important properties such as: corrosion resistance, friction, adhesion and dielectric capacity etc. For example, for the case of an amorphous oxide film formed on the bare Al substrate surface, the absence of grain boundaries in the oxide film reduces the ionic migration through the oxide, thereby improving its electronic properties (e.g. high dielectric strength and low leakage current) and increasing its corrosion resistance.

Nowadays, thin aluminium-oxide films are used in various types of microelectronic devices as dielectric, diffusion and/or tunnel barrier (cf. Refs. [6, 12-15]), because of its specific physical and chemical properties (i.e. large dielectric constant (~ 10), large barrier height for electron tunnelling (~ 2 eV), high corrosion resistance, good thermal and mechanical stability, good adhesion). For such applications, the thickness, morphology, chemical composition and (micro)structure of the grown oxide film are of great importance [2, 4, 6, 11, 13, 14].

II. Thermodynamic stability of thin oxide films on their metal substrates: the role of interfaces

To date, the kinetics of oxide-film growth on metal substrates has been used as the principal tool for studying the oxidation behaviour of metals. The thermodynamics of oxide-film growth on metal substrates, which states the conditions of temperature, pressure, and chemical composition under which a given oxide phase can form on a metal, have received only little attention.

As a general rule it can be stated that the *bulk* Gibbs free energy of a crystalline metal-oxide will be lower than that of the corresponding amorphous metal-oxide. Hence, provided that the formation of the crystalline oxide is not kinetically hindered, for relatively thick oxide films grown on their metal substrates by e.g. dry, thermal oxidation, the oxide formed on its metal substrate is, in all cases, expected to be crystalline. However, as will be demonstrated in Chapter 2 of this thesis, a crystalline structure does not need to occur for very thin oxide films on their metal substrates, where the surface and interface energies are the dominating energy contributions for the *total* Gibbs free energy of the oxide film on its metal substrate.

In many cases, the energy of the interface between an amorphous phase and a crystalline phase is lower than that of the corresponding crystalline-crystalline interface [1, 16, 17]. Moreover, the surface energy of an amorphous oxide is often lower than that of the corresponding crystalline oxide (cf. Ref. [1, 18]). Hence it follows that, up to a certain critical oxide-film thickness, a thin amorphous metal-oxide film on its metal substrate can be the stable modification with respect to the corresponding crystalline metal-oxide film on the same substrate due to the relatively low sum of the surface and interfacial energies of the metal-substrate / amorphous-oxide film system (see Fig. 1).

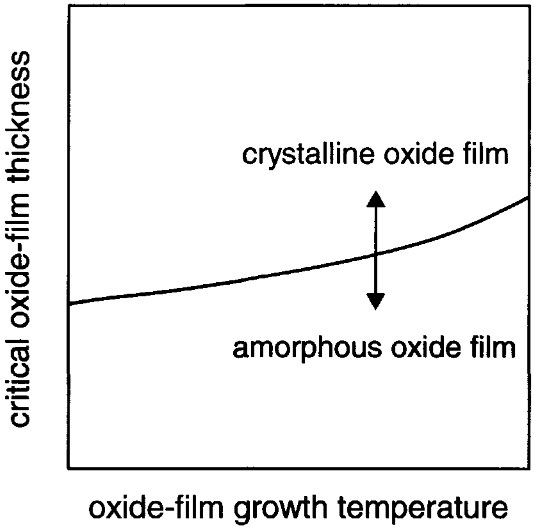

Figure 1. The critical oxide-film thickness up to which an amorphous oxide film in stead of the corresponding crystalline oxide film is preferred on the metal substrate as a function of the oxide-film growth temperature for a given metal-oxide system MO_x.

III. Thermal oxidation of bare metal substrates

Dry, thermal oxidation of a metal, in a general sense, is the reaction of a metal with oxygen gas to produce an oxide film on the metal surface. Since, the oxide product is a solid, it separates the two reactants. Oxide-film growth after formation of a 'closed' oxide film on the metal substrate therefore requires that metal and/or oxygen species dissolve in and move through the developing oxide film towards the oxide-gas and/or metal-oxide interface, respectively. The migrating species is generally assumed to be ionic (e.g. for Al, Fe, Cu and Ta substrates; cf. Refs. [8, 19-26]). For the realization of migration of an ionic species, electrons must also move through the oxide to maintain overall charge neutrality.

A complete description of the initial and subsequent stages of dry, thermal oxidation of a bare metal surface actually comprises a series of steps, such as arrival of oxygen molecules from the gas phase and subsequent dissociative chemisorption onto the metal surface, nucleation and growth of an oxide-film covering the metal surface, and transport of ionic, as well as electronic, species through the developing oxide film towards the oxide-gas and/or metal-oxide interface, respectively (see Fig. 2). One of these steps, being much slower than the rest, may be said to limit the oxide-film growth rate. During the oxidation process, a balance between the flux of ionic and electronic species is established in such a way that the rate-limiting step proceeds at the maximum possible rate (cf. Refs. [7-9, 19, 20, 22-24, 27-29]). If transport of one of the concerned charged species through the oxide film occurs intrinsically at a relative faster rate, then an electric field will be set up within the oxide film. The direction of the field will be such that the transport of the less mobile, rate-limiting species is enhanced. When modeling the oxide-film growth, it is generally assumed that no net electric charge is transported through the oxide and no space charge builds up in the oxide film (e.g. the Coupled-Currents approach of Fromhold and Cook; cf. Refs. [20, 28, 29]). In this case, the magnitude of the established electric field will be such that the net charge currents of ionic and electronic species are equalized (cf. Refs. [8, 20, 24, 28, 29]).

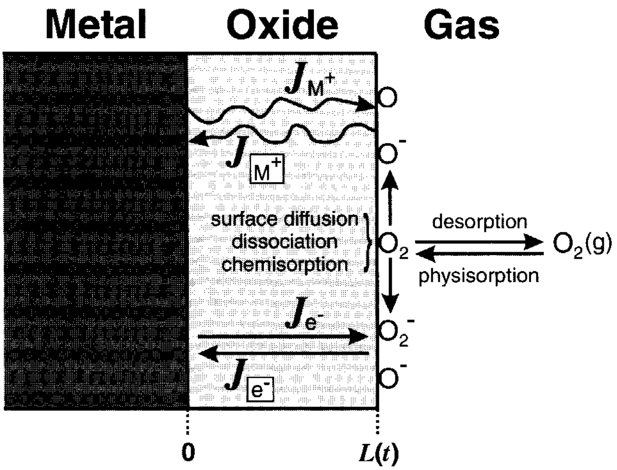

Figure 2. Schematic illustration of some processes involved during the initial and subsequent stages of dry, thermal oxidation of a bare metal substrate. In the case depicted here, continuing growth of the oxide-film is realised by the coupled currents of cationic and electronic species (transport of anionic species is not considered). The flux of cation interstitials and vacancies, and the flux of electrons and electron holes, are denoted with J_{M^+} and $J_{\boxed{\mathrm{M}^+}}$, and J_{e^-} and $J_{\boxed{e^-}}$, respectively. See text for details.

Energy barriers for both ion and electron movement into and through the oxide exist. At relative *high temperatures* ($T > 573$ K), the thermal energy is sufficient to allow existing ions or electrons to surmount this energy barrier. Consequently, at high temperatures, (*i*) the diffusion of ionic species into and through the developing oxide film under influence of the concentration gradient (chemical potential) is relatively fast, and (*ii*) electrons may be transported through the developing oxide film by both tunnelling and thermionic (and Schottky [30]) emission of electrons from the Fermi level of the metal into the conduction band of the oxide. Hence, at relative high temperatures, the concentration gradient (i.e. chemical potential) across the oxide-film is the dominating driving force for continuing oxide-film growth, and oxide-film growth results in the formation of relative thick (i.e. > 10 nm), usually crystalline oxide films. A parabolic oxide-film growth rate law is generally followed.

This contrasts with the oxidation at low temperatures ($T < 573$ K), where the thermal energy is insufficient to allow existing ions or electrons to surmount the energy barrier. Consequently, at low temperatures, (*i*) the chemical diffusion into and through the oxide film is usually negligibly small, and (*ii*) the contribution to electron transport by thermionic emission is virtually zero (thus tunneling of electrons through the developing oxide film is the dominating electron transport mechanism). Hence, an alternative driving force such as an electric field (see above) is postulated to account for the initially very fast, oxidation rates observed at low temperatures. Logarithmic-type oxide-film growth kinetics are usually followed in this case: i.e. the initial fast oxide-film growth regime, is followed by a transition to a slower growth regime, ending up with, often amorphous, oxide-films of *limiting* thicknesses in the range of 0.5 to about 10 nm. The actual temperature of transition from low to high temperature oxidation depends on the metal involved, its microstructure and its purity.

IV. Methods of characterisation

An ultrahigh vacuum (UHV) specimen processing chamber in combination with in-situ surface sensitive analytical techniques such as X-ray photoelectron spectroscopy (XPS) are prerequisites to study the initial stages of oxidation of bare metal substrates. XPS is based on the photon-induced emission of electrons from the characteristic energy levels of the concerned elements within the solid. From the electron emission spectrum (i.e. electron intensity versus binding energy; cf. Fig. 3) recorded from an oxidised metal substrate, in principle, the oxide-film thickness, chemical composition, and chemical state of the concerned ions in the grown oxide films, can be obtained for oxide-film thicknesses of the order of the inelastic mean free path (IMFP) of the emitted photoelectrons (i.e. up to about 6 nm). Additional features in the measured XPS spectra of the clean and oxidised metal, such as the bulk and surface plasmon peaks associated with the metal substrate (see Fig. 3), can give additional information on e.g. the morphology of the grown oxide film (see Chapters 3 and 5 of this thesis).

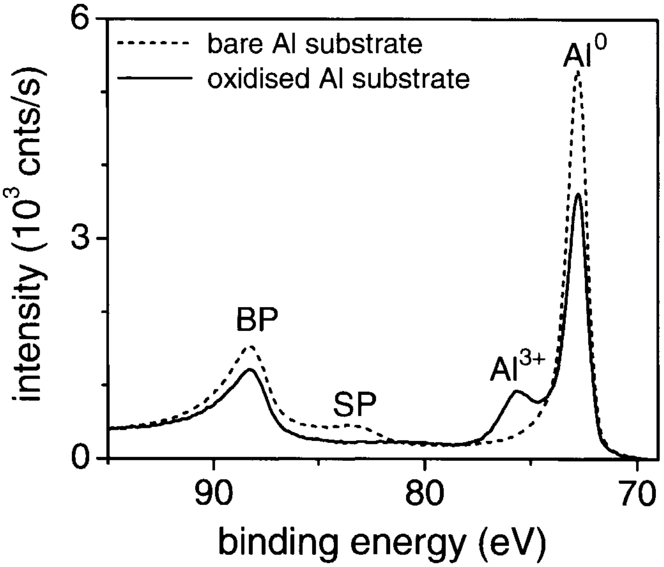

Figure 3. Measured XPS spectra in the Al 2*p* binding energy range, as recorded from a bare Al substrate (*dashed lines*) and the Al substrate after dry, thermal oxidation for 100 s at 373 K and $p_{O_2} = 1.33\times10^{-4}$ Pa (*solid lines*). The first bulk plasmon (BP) and surface plasmon (SP) peak, associated with the Al 2*p* metallic main peak (Al^0), as well as the corresponding oxidic main peak (Al^{3+}) have been indicated.

For the *quantitative* analysis of measured XPS spectra recorded from thin oxide-films on metal substrates, it is necessary to determine the *total* primary zero loss (PZL) intensity of each core-electron level separately. The total PZL intensity of a given core-level in a measured spectrum of the solid, comprises all recorded electrons that have been emitted from the concerned core-electron level and left unaffected until recorded (i.e. all recorded unscattered or elastically scattered photoelectrons). In this thesis, a novel method is presented to determine the *total* metallic and oxidic PZL intensity for each core-electron level in measured XPS spectra of bare and oxidised free-electron like metals (Chapter 3). From these total PZL intensities correct values can be obtained for the thicknesses and compositions of the thin aluminium-oxide films grown on aluminium metal substrates by dry, thermal oxidation (Chapter 4).

It is generally stated that a change in binding energy (BE) of the detected photoelectrons emitted from thin oxide films on metal substrates is directly related to a change in chemical state of the concerned ions in the oxide due to structural changes of the oxide film (e.g. as a result of the transformation from amorphous to crystalline oxide). However, as shown in Chapter 5, these BE shifts may simply be related to shifts in the Fermi level of the oxide, induced by defect states at the oxide surface or the metal/oxide interface.

The evolution of the microstructure and morphology of the developing aluminium-oxide films on aluminium substrates is studied by high-resolution transmission electron microscopic (HREM) analysis of several metal-oxide cross sections. In this way, detailed information is obtained on the crystallographic structure of the involved oxide phases, the morphology and constitution of the oxide-film, as well as the structure of the corresponding interface with its parent metal substrate.

V. Outline

In Chapter 2, the thermodynamic stability of a thin amorphous metal-oxide film on top of its single-crystal metal substrate is modelled as a function of growth temperature, oxide-film thickness and crystallographic orientation of the metal substrate. Chapters 3 and 4 are devoted to quantitative analysis in electron spectroscopy (determination of PZL intensities, Chapter 3, and determination of oxide-film thickness and composition, Chapter 4). Finally, in Chapter 5, the growth kinetics, chemical composition, morphology and (micro)structure of the developing oxide film are investigated as a function of oxidation temperature for the dry, thermal oxidation of a bare Al(431) substrate at a partial oxygen pressure of 1.33×10^{-4} Pa in the temperature range of 373 - 773 K. To explain the various relations as determined in this study, models were adopted for the mechanisms that govern the oxide-film growth during the different stages of oxidation at different temperatures (Chapter 5).

References

[1] L.P.H. Jeurgens, W.G. Sloof, F.D. Tichelaar and E.J. Mittemeijer, Phys. Rev. B **62** (2000), 4707.

[2] I. Popova, Z. Zhukov and J.T. Yates, J. Appl. Phys. **87** (2000), 8143.

[3] Z. Zhukov, I. Popova, and J.T. Yates, J. Vac. Sci. Technol. A **17** (1999), 1727.

[4] D.R. Jennison, C. Verdozzi, P.A. Schultz and M.P. Sears, Phys. Rev. B **59** (1999), R15605.

[5] A. Bogicevic and D.R. Jennison, Phys. Rev. Lett. **82** (1999), 4050.

[6] J.M. De Teresa , A. Barthélemy, A. Fert, J.P. Contour, F. Montaigne and P. Seneor, Science **286** (1999), 507.

[7] Á. Szökefalvi-Nagy and E. Fromm, Phil. Mag. Lett. **79** (1999), 289.

[8] E. Fromm, Kinetics of Met-Gas Interactions at Low Temperatures: Hydriding, Oxidation, Poisoning (Springer, Berlin, 1998), Chap. 5

[9] P.C.J. Graat, M.A.J. Somers, A.M. Vredenberg and E.J. Mittemeijer, J. Appl. Phys. **82** (1997), 1416.

[10] J. Trost, H. Brune, J. Wintterlin, R.J. Behm and G. Ertl, J. Chem. Phys. **108** (1998), 1740.

[11] S.W. Gaarenstroom, J. Vac. Sci. Techn.A **15** (1997), 470.

[12] M. Sharma, S.X. Wang and J.H. Nickel, Phys. Rev. Lett. **82** (1999), 616.

[13] T.W. Hickmott, J. Appl. Phys. **88** (2000), 2805.

[14] E.S. Snow, P.M. Campbell, R.W. Rendell, F.A. Buaot, D. Park, C.R.K. Marrian and R. Magno, Semicond. Sci. Technol. **13** (1998), A75.

[15] A.T.M. van Gogh, S.J. van der Molen, J.W.J. Kerssemakers, N.J. Koeman and R. Griessen, Appl. Phys. Lett. **77** (2000), 815.

[16] R. Benedictus, A. Böttger and E. J. Mittemeijer, Phys. Rev. B **54** (1996), 9109.

[17] E.J. Mittemeijer, M.H. Biglari, A.J. Böttger, N.M. van der Pers, W.G. Sloof and F.D. Tichelaar, Scripta Materialia **41** (1999), 625.

[18] S. Blonski and S.H. Garofalini, Surf. Sci. **295** (1993), 263.

[19] F.P. Fehler, Low-temperature oxidation: the role of vitreous oxides (Wiley-Interscience, New York, 1981).

[20] A.T. Fromhold and R.G. Fromhold, in *Comprehensive chemical kinetics*, Vol. 21: Reactions of solids with gases, edited by C.H. Bamford, C.F.H. Tipper and R.G. Compton (Elsevier, Amsterdam, 1984), Chap. 1.

[21] V. Zhukov, I. Popova and J.T. Yates, Surf. Sci. **441** (1999), 251.

[22] N. Cabrera and N.F. Mott, Rep. Progr. Phys. **12** (1949), 163.

[23] F.P. Fehlner and N.F. Mott, Ox. Metals **2** (1970), 59.

[24] V. Grajewski and E. Fromm, in *Science of Ceramic Interfaces*, edited by J. Nowotny (Elsevier, Amsterdam, 1991), p. 487-506.

[25] T.N. Rhodin, J. Am. Chem. Soc. **72** (1950), 5102.

[26] T.N. Rhodin, J. Am. Chem. Soc. **73** (1951), 3143.

[27] N.F. Mott, Trans. Faraday Soc. **43** (1947), 429.

[28] A.T. Fromhold and E.L. Cook, Phys. Rev. **158** (1967), 600.

[29] A.T. Fromhold and E.L. Cook, Phys. Rev. **163** (1967), 650.

[30] P.R. Emtage and W. Tantraporn, Phys. Rev. Lett. **8** (1962), 267.

Chapter 2

Thermodynamic Stability of Amorphous Oxide Films on Metals

Application to Aluminium-Oxide Films on Aluminium Substrates

L.P.H. Jeurgens,[1] W.G. Sloof,[1] F.D. Tichelaar,[1] and E.J. Mittemeijer[1,2]

[1] *Delft University of Technology, Laboratory of Materials Science, Rotterdamseweg 137, 2628 AL Delft, The Netherlands*

[2] *Max Planck Institute for Metals Research, Seestrasse 92, 70174 Stuttgart, Germany*

Abstract

It has been shown on a thermodynamic basis that an amorphous structure for an oxide film on its metal substrate can be more stable than the crystalline structure. The thermodynamic stability of a thin amorphous metal-oxide film on top of its single-crystal metal substrate has been modelled as a function of growth temperature, oxide-film thickness and crystallographic orientation of the metal substrate. To this end expressions have been derived for the estimation of the energies of the metal-substrate / amorphous-oxide film interface and the metal-substrate / crystalline-oxide film interface as a function of growth temperature, and crystallographic orientation of the substrate (including the effect of strain due to the lattice mismatch). It follows that, up to a certain critical thickness of the amorphous oxide film, the higher bulk Gibbs free energy of the amorphous oxide film, as compared to the corresponding crystalline oxide film, can be compensated for by its lower sum of the surface and interfacial energies. The predicted occurrence of an amorphous aluminium-oxide film on various crystallographic faces of aluminium agrees well with previous transmission electron microscopy observations.

I. Introduction

Upon exposure of a clean metal or semiconductor substrate to oxygen at relatively low temperatures (say < 500 K), often a thin (thickness < 10 nm) passivating amorphous oxide film is formed (this holds for e.g. Si, Ta, Nb, Al, Ge, Cr and Te), whereas at higher temperatures thicker films develop and the (resulting) structure of the corresponding oxide film is in most cases crystalline (cf. Refs. [1-5]). However, for metals such as Cu, Co, Fe, Ni, Mo, and Zn low temperature oxidation is known to proceed by the direct formation and (epitaxial) growth of a crystalline oxide (cf. Refs. [3, 4, 6-9]), and upon oxidation of Si, an amorphous SiO_2 film forms even at temperatures as high as 1300 K (cf. Refs. [3, 5]).

For all these oxides, the bulk Gibbs free energy of formation of the amorphous oxide is larger than that of the corresponding crystalline oxide. Hence, for relatively thick oxide films where the contribution of the surface and interfacial energies is small, the oxide formed on its metal (or semiconductor)[1] substrate is expected to be crystalline at all temperatures. As will be demonstrated in this paper, a crystalline structure need not occur for thin oxide films on their metal substrates, where the surface and interface energies can be the dominating contributions for the total Gibbs free energy of the oxide film on its metal substrate. As shown in recent work on the thermodynamics of solid-state amorphization [10], the energy of the interface between an amorphous phase and a crystalline phase is in many cases lower than that of the corresponding crystalline-crystalline interface. This also holds for the oxide film formed on a clean metal substrate, as will be shown here. Moreover, the surface energy of the amorphous metal oxide is often lower than that of the corresponding crystalline metal oxide (cf. Ref. [11]). Consequently, up to a certain critical oxide-film thickness, a thin amorphous metal-oxide film on its metal substrate can be the stable modification with respect to the corresponding crystalline metal-oxide film on the same substrate due to the relatively low surface and interfacial energies of the metal-substrate / amorphous-oxide film system.

In this paper, first a general thermodynamic basis is presented for assessment of bulk, surface and interfacial energies. At present, experimental values are usually not available for the interfacial energies of the metal- (semiconductor-) substrate / amorphous-oxide film and the corresponding metal- (semiconductor-) substrate / crystalline-oxide film interfaces as a function of growth temperature and crystallographic orientation of the substrate. Therefore, expressions for these quantities are derived here on the basis of the 'macroscopic atom' approach (cf. Refs. [10, 12-15]).

---

[1] The thermodynamical model presented here for the case of thin metal-oxide films formed on their metal substrates is equally valid for thin oxide films formed on their semiconductor substrates (e.g. Si or Ge). Therefore, in this paper no distinction will be made between the two.

The thermodynamic model is applied to the case of an aluminium-oxide film on the {111}, {110} and {100} crystallographic faces of an aluminium substrate. In this case, the crystalline oxide γ-Al_2O_3 competes with the amorphous Al_2O_3 oxide (cf. Refs. [1, 16-19]). The predictions, as obtained by application of the model to the Al-Al_2O_3 system, are compared with experimental data obtained by transmission electron microscopy.

II. Basis of the thermodynamical model

Consider two situations for a homogeneous metal-oxide film MO_x of uniform thickness h on its single-crystalline metal substrate M. In Fig. 1a an *amorphous* oxide film, denoted by $\{MO_x\}$, with uniform thickness $h_{\{MO_x\}}$ is on top of its single crystal metal substrate, denoted by <M>. In Fig. 1b, on the other hand, a *crystalline* oxide film, denoted by $<MO_x>$, with uniform thickness h_{MO_x} is on top of the single crystal metal substrate <M>. The composition of the amorphous and crystalline oxides is the same, and both films have been formed from the same molar quantity of oxygen on identical metal substrates <M>. The thermodynamics of the <M>-$\{MO_x\}$ and the <M>-$<MO_x>$ configuration will be described for cells of volume $h_{\{MO_x\}} \times l^2_{\{MO_x\}}$ and $h_{MO_x} \times l^2_{MO_x}$, respectively, as indicated in Figs. 1a and 1b. Both cells contain the same molar quantity of oxide.

If an elastic strain exists within the amorphous $\{MO_x\}$ cell (cf. Fig. 1a) then the volume $V^{str}_{\{MO_x\}}$ occupied by one mole $\{MO_x\}$ in the cell is related to the molar volume of strain free $\{MO_x\}$, $V_{\{MO_x\}}$, by the fraction $\Omega_{\{MO_x\}}$: $V^{str}_{\{MO_x\}} = \Omega_{\{MO_x\}} V_{\{MO_x\}}$. Analogously, if an elastic strain resides within the crystalline $<MO_x>$ cell (cf. Fig. 1b), then Ω_{MO_x} is defined by $V^{str}_{MO_x} = \Omega_{MO_x} V_{MO_x}$, where definitions for the quantities concerned are analogous to those given above.

Then, for the case of an amorphous oxide film $\{MO_x\}$ of uniform thickness $h_{\{MO_x\}}$ on the substrate <M>, the total Gibbs free energy G_{am} of the cell considered (see Fig. 1a) is given by

$$G_{am} = l^2_{\{MO_x\}} \left(h_{\{MO_x\}} \frac{G_{\{MO_x\}}}{\Omega_{\{MO_x\}} V_{\{MO_x\}}} + \gamma_{\{MO_x\}\text{-ambient}} + \gamma_{M-\{MO_x\}} \right) \qquad (1)$$

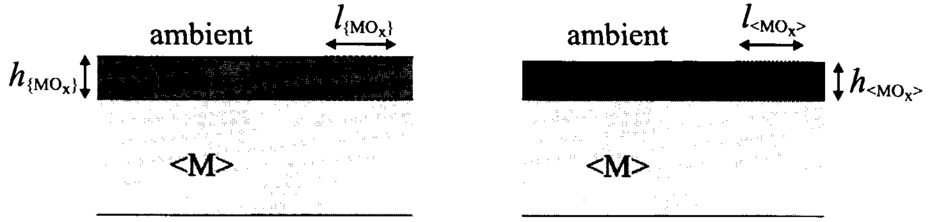

(a) amorphous $\{MO_x\}$ (b) crystalline $<MO_x>$

Figure 1. Schematic drawing of a homogeneous MO_x oxide overlayer with uniform thickness on top of its single crystalline metal substrate <M>. (**a**) displays an amorphous oxide film $\{MO_x\}$ with uniform thickness $h_{\{MO_x\}}$ on the <M> substrate, whereas (**b**) shows a crystalline oxide film $<MO_x>$ of uniform thickness $h_{\langle MO_x\rangle}$ on the <M> substrate (the braces { } refer to the amorphous phase and the brackets < > to the crystalline phase). The composition of $\{MO_x\}$ and $<MO_x>$ is the same, and both films have been formed from the same molar quantity of oxygen on an identical metal substrate of <M>. The two cells of volume $h_{\{MO_x\}}\times l^2_{\{MO_x\}}$ and $h_{\langle MO_x\rangle}\times l^2_{\langle MO_x\rangle}$, as indicated in (a) and (b), respectively, contain the same molar quantity of oxide. The ambient phase may be vacuum, a gas atmosphere or an adsorbed layer.

where $G_{\{MO_x\}}$ is the bulk Gibbs free energy of one mole of the amorphous oxide; $\gamma_{\{MO_x\}\text{-ambient}}$ represents the surface energy of the amorphous oxide; $\gamma_{\langle M\rangle-\{MO_x\}}$ is the energy of the interface between the metal substrate and the amorphous oxide; and $l_{\{MO_x\}}$ denotes the width and length of the cell, both parallel to the interface.

Analogously, for a crystalline layer $<MO_x>$ of uniform thickness $h_{\langle MO_x\rangle}$ on the metal substrate <M>, the total Gibbs free energy G_c of the cell considered (see Fig. 1b) is expressed by

$$G_c = l^2_{\langle MO_x\rangle}\left(h_{\langle MO_x\rangle}\frac{G_{\langle MO_x\rangle}}{\Omega_{\langle MO_x\rangle}V_{\langle MO_x\rangle}} + \gamma_{\langle MO_x\rangle\text{-ambient}} + \gamma_{\langle M\rangle-\langle MO_x\rangle}\right) \tag{2}$$

where $G_{<MO_x>}$ is the molar bulk Gibbs free energy of the crystalline oxide; $\gamma_{\langle MO_x\rangle\text{-ambient}}$ represents the surface energy of the crystalline oxide; $\gamma_{\langle M\rangle-\langle MO_x\rangle}$ is the energy of the interface between the metal substrate and the crystalline oxide; and finally $l_{\langle MO_x\rangle}$ denotes the width and length of the cell, both parallel to the interface.

The amorphous oxide film $\{MO_x\}$ is stable with respect to the corresponding crystalline oxide film $<MO_x>$, as long as the total Gibbs free energy G_{am} of the $\{MO_x\}$ cell in the crystalline-amorphous configuration, $<M>-\{MO_x\}$, is lower than the total Gibbs free energy G_c of the corresponding $<MO_x>$ cell in the crystalline-crystalline configuration, <M>-

<MO_x>: $\Delta G \equiv G_{am} - G_c < 0$. To arrive at an explicit expression for ΔG, first the bulk energy terms in Eqs. (1) and (2) are considered; the interfacial energy terms are dealt with separately in Sec. III.

The Gibbs free energy of formation $\Delta G^f_{\{MO_x\}}$ of one mole $\{MO_x\}$ out of its elements in their stable configuration, for a given temperature and pressure, is defined as

$$\Delta G^f_{\{MO_x\}} \equiv G_{\{MO_x\}} - G_{M} - \frac{x}{2} \cdot G_{O_2(g)} \qquad \textbf{(3a)}$$

Likewise, the Gibbs free energy of formation $\Delta G^f_{<MO_x>}$ of one mole <MO_x> is given by

$$\Delta G^f_{MO_x} \equiv G_{MO_x} - G_{M} - \frac{x}{2} \cdot G_{O_2(g)} \qquad \textbf{(3b)}$$

Because both cells are of the same composition and contain the same molar quantity of oxygen it holds that

$$\frac{l^2_{\{MO_x\}} h_{\{MO_x\}}}{\Omega_{\{MO_x\}} V_{\{MO_x\}}} = \frac{l^2_{MO_x} h_{MO_x}}{\Omega_{MO_x} V_{MO_x}} \qquad \textbf{(4a)}$$

Now, defining χ as the ratio of the surface areas of the <MO_x> and $\{MO_x\}$ cells, i.e.

$$\chi = \frac{l^2_{MO_x}}{l^2_{\{MO_x\}}}, \qquad \textbf{(4b)}$$

it follows from Eqs. (1)-(4b) that $\Delta G \equiv G_{am} - G_c$ per *unit area* of the <M>-$\{MO_x\}$ interface of the amorphous $\{MO_x\}$ cell can be expressed as

$$\Delta G = h_{\{MO_x\}} \left(\frac{\Delta G^f_{\{MO_x\}} - \Delta G^f_{MO_x}}{\Omega_{\{MO_x\}} V_{\{MO_x\}}} \right) + \gamma_{\{MO_x\}\text{-ambient}} + \gamma_{M\text{-}\{MO_x\}} - \chi \left(\gamma_{MO_x\text{-ambient}} + \gamma_{M\text{-}MO_x} \right) \qquad \textbf{(5)}$$

III. The energy of metal-substrate / oxide-film interfaces

In most cases, experimental values are not available for the energies between the metal substrate and the oxide film. In the following, expressions will be derived for these interfacial energies on the basis of the 'macroscopic atom' approach (cf. Refs. [10, 12-15]).

III.A. Energy of the crystalline – amorphous <M>-{MO$_x$} interface

To assess the energy of the interface between the crystalline metal substrate <M> and the amorphous oxide film {MO$_x$}, the interface between a crystalline solid (i.e. <M>) and a configurationally frozen liquid (as a model for {MO$_x$}) is considered. Then, three contributions to the interfacial energy $\gamma_{\langle M\rangle-\{MO_x\}}$ can be recognized [10, 12-15]:

$$\gamma_{\langle M\rangle-\{MO_x\}} = \gamma^{\text{interaction}}_{\langle M\rangle-\{MO_x\}} + \gamma^{\text{entropy}}_{\langle M\rangle-\{MO_x\}} + \gamma^{\text{enthalpy}}_{\langle M\rangle-\{MO_x\}} \tag{6}$$

It is assumed that, at the oxide-film growth temperature, mismatch strain does not occur in the amorphous oxide film (and the metal substrate) due to the relative large free volume [20, 21], and the bond flexibility of the amorphous structure [2, 22], which make viscous flow in the oxide film easy [2, 20-25]. Therefore, at the growth temperature, $\Omega_{\{MO_x\}}$ = 1 [cf. Eq. (5) in Sec. II]. It is noted that, even in the absence of viscous flow and with a large mismatch between the amorphous oxide film and its metal substrate, the strain in the amorphous oxide film (at the growth temperature) may be small [23].

III.A.1. Interaction contribution to the <M>-{MO$_x$} interfacial energy

The interaction between the metal substrate <M> and the amorphous oxide film {MO$_x$} across the <M>-{MO$_x$} interface can be subdivided into chemical and London-van der Waals interactions between (*i*) the M atoms of the metal substrate <M> and the O atoms of the oxide ($\gamma^{\text{interaction}}_{\langle M\rangle-O}$), and (*ii*) the M atoms of the metal substrate <M> and the M atoms of the oxide ($\gamma^{\text{interaction}}_{\langle M\rangle-M}$) [12, 26, 27], i.e.

$$\gamma^{\text{interaction}}_{\langle M\rangle-\{MO_x\}} = \gamma^{\text{interaction}}_{\langle M\rangle-O} + \gamma^{\text{interaction}}_{\langle M\rangle-M} \tag{7a}$$

The metal-oxygen interaction energy $\gamma^{\text{interaction}}_{\langle M\rangle-O}$ across the <M>-{MO$_x$} interface can be estimated from the enthalpy of mixing at infinite dilution of one mole O(*g*) atoms in <M>, $\Delta H^{\infty}_{\text{O in M}}$ [12, 13, 27]. If the O atoms would be fully surrounded by M atoms, then $\Delta H^{\infty}_{\text{O in M}}$ is the enthalpy increase per mole O(g) atoms in an infinitely diluted system. At the <M>-{MO$_x$} interface, only a fraction *p* of the total surface area of the O atomic cell is in contact with M atoms of the <M> substrate. Thus the metal-oxygen interaction energy $\gamma^{\text{interaction}}_{\langle M\rangle-O}$ *per mole* O atoms at the interface equals $p\Delta H^{\infty}_{\text{O in M}}$. Then, if the molar interface area $A_{\{O\}}$ is defined as the area of the <M>-{MO$_x$} interface containing one mole O atoms, the interaction energy $\gamma^{\text{interaction}}_{\langle M\rangle-O}$ *per unit area* of the <M>-{MO$_x$} interface becomes

$$\gamma^{\text{interaction}}_{\text{M-O}} = \frac{p\Delta H^{\infty}_{\text{O in M}}}{A_{\{\text{O}\}}} \tag{7b}$$

The fraction p depends on the shape of the Wigner-Seitz cell of oxygen in $\{MO_x\}$ and can be taken, on average, as $p = \frac{1}{3}$, assuming a shape of the oxygen atomic cell between a cube ($p = \frac{1}{6}$) and a sphere ($p = \frac{1}{2}$) [10, 12]. For those metal-oxide systems for which the enthalpy of mixing at infinite dilution of one mole O(g) atoms in <M>, i.e. $\Delta H^{\infty}_{\text{O in M}}$, is unknown, a value can be estimated from the following empirical relation between $\Delta H^{\infty}_{\text{O in M}}$ and the enthalpy of formation $\Delta H^{f}_{MO_x}$ per mole O, as obtained from the data in Refs. [28-31]:

$$\Delta H^{\infty}_{\text{O in M}} \cong 1.2\Delta H^{f}_{MO_x} + 1\times10^{5} \qquad (\text{Jmol}^{-1}\ \text{O}) \tag{7c}$$

Since, for most metal-oxide systems the metal-oxygen bond formation is strongly exothermic, the relatively large *negative* metal-oxygen interaction energy $\gamma^{\text{interaction}}_{\langle M\rangle-O}$ is the dominant contribution to the interfacial energy $\gamma_{M-\{MO_x\}}$. Thus the lowest interfacial energy $\gamma_{M-\{MO_x\}}$ is achieved by maximizing the number of metal-oxygen bonds across the <M>-{MO$_x$} interface per unit area of the interface, resulting in a dense packing of the amorphous oxide at the interface. The value of $A_{\{O\}}$ for an amorphous oxide film {MO$_x$} on the different crystallographic faces of its metal substrate <M> in Eq. (7b) may therefore be approximated by taking it to be equal to the molar interface area A_O at the most densely packed plane of the corresponding (unstrained) crystalline phase <MO$_x$>.

The metal-metal interaction energy $\gamma^{\text{interaction}}_{\langle M\rangle-M}$ across the <M>-{MO$_x$} interface between an M atom of the <M> substrate and an M atom of the amorphous oxide {MO$_x$} [cf. Eq. (7a)] can be estimated analogously from the enthalpy of mixing at infinite dilution of one mole M atoms in an infinitely large reservoir of <M>, $\Delta H^{\infty}_{\text{M in M}}$. Since the enthalpy of solution of one mole M atoms in an infinitely large reservoir of <M>, $\Delta H^{\infty}_{\text{M in M}} \equiv 0$, the metal-metal interaction energy across the <M>-{MO$_x$} interface, $\gamma^{\text{interaction}}_{\text{M-M}} = 0$. However, for metal-oxide interfaces <M^{I}>-{M^{II}O$_x$}, where $M^{I} \neq M^{II}$, the M^{I}-M^{II} interaction energy $\gamma^{\text{interaction}}_{M^{II}-M^{I}}$ across the interface should, of course, not be neglected as, in general, the enthalpy of solution of M^{II} in an infinitely large reservoir of metal M^{I}, $\Delta H^{\infty}_{M^{II}\text{ in }M^{I}} \neq 0$.

III.A.2. Entropy contribution to the <M>-{MO$_x$} interfacial energy

The entropy contribution to the <M>-{MO$_x$} interfacial energy, $\gamma^{\text{entropy}}_{\langle M\rangle-\{MO_x\}}$, is ascribed to the *decrease* in configurational entropy of the amorphous {MO$_x$} phase near the interface relative to that of bulk {MO$_x$} [32-34]. Due to the strong interaction between the crystalline metal substrate and the amorphous oxide film across the <M>-{MO$_x$} interface (cf.

Sec. III.A.1), ordering of the amorphous phase occurs near the <M>-$\{MO_x\}$ interface. Because the structure of the crystalline metal substrate remains unaltered up to the interface, the (positive) entropy contribution to the <M>-$\{MO_x\}$ interfacial energy is solely due to the decrease in entropy of the amorphous $\{MO_x\}$ phase near the interface.

The decrease of configurational entropy per mole $\{MO_x\}$, $\Delta S^{\text{deficient}}_{\{MO_x\}}$, i.e. the difference in entropy of $\{MO_x\}$ at the <M>-$\{MO_x\}$ interface relative to that of bulk $\{MO_x\}$, is associated with the following contribution to the interfacial energy $\gamma_{\langle M\rangle-\{MO_x\}}$ per *unit area* interface,

$$\gamma^{\text{entropy}}_{\langle M\rangle-\{MO_x\}} = \frac{-T\Delta S^{\text{deficient}}_{\{MO_x\}}}{xA_{\{O\}}} \qquad \textbf{(8a)}$$

where the area occupied by one mole $\{MO_x\}$ at the interface follows from the molar interface area of O at the interface, $A_{\{O\}}$ (cf. Sec. III.A.1), multiplied by x.

An (over)estimate for the entropy of the ordered $\{MO_x\}$ phase *at* the <M>-$\{MO_x\}$ interface, $S^{\text{interface}}_{\{MO_x\}}$, is obtained by taking it to be equal to the entropy of the corresponding crystalline oxide of identical composition, $S_{\langle MO_x\rangle}$. Then the decrease in entropy of $\{MO_x\}$ at the interface relative to the entropy $S_{\{MO_x\}}$ of bulk $\{MO_x\}$ is given by $\Delta S^{\text{deficient}}_{\{MO_x\}} \cong S_{\langle MO_x\rangle} - S_{\{MO_x\}} < 0$.

Another estimate for $\Delta S^{\text{deficient}}_{\{MO_x\}}$ can be obtained on the basis of the structural model for the solid-liquid <A>-{A} interface, considered as an interface between a dense random packing of hard spheres (i.e. the liquid) and a close-packed crystal plane (i.e. the solid) [32, 33]. As demonstrated in Ref. [10] for the case of an amorphous binary alloy {AB} in contact with a crystalline metal <A>, the decrease in configurational entropy of {AB} at the interface relative to that of bulk {AB} is given by $0.904R$ JK^{-1} (R is the gas constant) per mole {AB} at the <A>-{AB} interface. Accordingly, for the <M>-$\{MO_x\}$ interface considered here, it then follows that

$$\gamma^{\text{entropy}}_{M-\{MO_x\}} = \frac{0.904RT}{xA_{\{O\}}} \qquad \textbf{(8b)}$$

In the estimation of the entropy term $0.904R$ in Eq. (8b), the atoms of $\{MO_x\}$ are considered as equally sized hard spheres [10, 15, 32, 33], and therefore Eq. (8b) can only be considered as a crude estimate. In this paper, Eq. (8a) (with $\Delta S^{\text{deficient}}_{\{MO_x\}} \cong S_{\langle MO_x\rangle} - S_{\{MO_x\}}$; see above) will be used to estimate the entropy contribution.

III.A.3. Enthalpy contribution to the <M>-{MO$_x$} interfacial energy

The enthalpy contribution to the <M>-{MO$_x$} interfacial energy, $\gamma^{\text{enthalpy}}_{\text{M -\{MO}_x\}}$, is ascribed to the *increase* in enthalpy of the M atoms of the <M> substrate *at* the interface relative to that of the M atoms in the bulk <M> substrate [10, 12, 15, 34]. Because the interface between the crystalline substrate <M> and the amorphous oxide film {MO$_x$} is considered as a crystalline-liquid rather than a crystalline-crystalline type of interface (cf. Sec. III.A), the M atoms of the crystalline substrate <M> at the interface will be increased in enthalpy relative to that of bulk <M> due to the liquid type of bonding with the atoms of {MO$_x$} at the <M>-{MO$_x$} interface [10, 12, 15, 34]). If the enthalpy increase of the M atoms of <M> at the <M>-{MO$_x$} interface is taken to be the same as the enthalpy increase of the M atoms of the <M> substrate in contact with its amorphous phase {M}, then the enthalpy increase of the M atoms of the crystalline substrate <M> *at* the <M>-{MO$_x$} interface relative to that of bulk <M> will be proportional to the enthalpy of fusion of <M>, $H^{\text{fuse}}_{\langle \text{M}\rangle}$ [10, 12, 15, 34].

Since, at the interface, only a fraction p of the total surface area of the atomic <M> cell is in contact with the amorphous {MO$_x$} phase, the enthalpy increase of one mole <M> atoms in the first atomic layer of the <M> substrate at the <M>-{MO$_x$} interface is estimated by $pH^{\text{fuse}}_{\langle \text{M}\rangle}$ [10, 12, 15, 34]). Now the enthalpy contribution $\gamma^{\text{enthalpy}}_{\langle \text{M}\rangle\text{-\{MO}_x\}}$ to the total <M>-{MO$_x$} interfacial energy per *unit area* interface is obtained by dividing $pH^{\text{fuse}}_{\langle \text{M}\rangle}$ by the area A_{M} occupied by one mole M atoms of the <M> substrate at the interface, i.e.

$$\gamma^{\text{enthalpy}}_{\langle \text{M}\rangle\text{-\{MO}_x\}} = \frac{pH^{\text{fuse}}_{\langle \text{M}\rangle}}{A_{\langle \text{M}\rangle}} \tag{9}$$

For a given crystallographic orientation of the <M> substrate, the molar interface area A_{M} can be calculated if the lattice parameter and the crystal structure of <M> are known.[2] The fraction p can be taken, on average, as $p = \frac{1}{3}$ (see Sec. III.A.1).

---

[2] In this paper the actual molar interface area will be used instead of the commonly used approximation for the average molar interface area of a crystalline phase <M>, i.e. $\overline{A}_{\langle \text{M}\rangle} = pC_0V^{2/3}_{\langle \text{M}\rangle}$, where C_0 is a constant depending on the shape of the Wigner-Seitz cell of M and $V_{\langle \text{M}\rangle}$ denotes the molar volume of <M> (cf. Refs. [10, 12-15]).

III.A.4. Expression for the <M>-{MO$_x$} interfacial energy

Substitution of Eqs. (7b), (8a) and (9) into Eq. (6) finally leads to the following expression for the interfacial energy $\gamma_{\langle M\rangle-\{MO_x\}}$:

$$\gamma_{M-\{MO_x\}} = \frac{p\Delta H^{\infty}_{O\,in\,M}}{A_{\{O\}}} + \frac{-T\Delta S^{deficient}_{\{MO_x\}}}{xA_{\{O\}}} + \frac{pH^{fuse}_{M}}{A_M} \tag{10}$$

III.B. Energy of the crystalline–crystalline <M>-<MO$_x$> interface

The energy $\gamma_{\langle M\rangle-\langle MO_x\rangle}$ of the interface between the crystalline metal substrate <M> and the crystalline oxide <MO$_x$> is the resultant of a chemical and a structural term [10, 12, 13, 15, 35]. As for the crystalline-amorphous <M>-{MO$_x$} interface, the chemical term is related to the interaction between the atoms of <M> and <MO$_x$> across the interface, whereas the structural term is related to the strain induced by the mismatch at the interface between the two adjacent crystalline phases <M> and <MO$_x$>, i.e.

$$\gamma_{\langle M\rangle-\langle MO_x\rangle} = \gamma^{interaction}_{\langle M\rangle-\langle MO_x\rangle} + \gamma^{mismatch}_{\langle M\rangle-\langle MO_x\rangle} \tag{11}$$

III.B.1. Interaction contribution to the <M>-<MO$_x$> interfacial energy

Following the treatment given in Sec. III.A.1 for the interaction energy across the crystalline-amorphous <M>-{MO$_x$} interface, the interaction energy $\gamma^{interaction}_{\langle M\rangle-\langle MO_x\rangle}$ across the corresponding crystalline-crystalline <M>-<MO$_x$> interface is expressed by

$$\gamma^{interaction}_{M-MO_x} = \frac{p\Delta H^{\infty}_{O\,in\,M}}{A_O} \tag{12}$$

Note that for a strained oxide film <MO$_x$> on its metal substrate <M>, the correct molar interface area of oxygen A_O, i.e. the area occupied by one mole O atoms of <MO$_x$> at the <M>-<MO$_x$> interface, is calculated from the strained lattice spacing of <MO$_x$> *at* the interface (see Sec. IV.C).

III.B.2. Mismatch contribution to <M>-<MO$_x$> interfacial energy

Besides the relatively large negative contribution of the metal-oxide interaction energy $\gamma^{interaction}_{\langle M\rangle-\langle MO_x\rangle}$, the <M>-<MO$_x$> interfacial energy $\gamma_{\langle M\rangle-\langle MO_x\rangle}$ also contains an additive positive energy contribution $\gamma^{mismatch}_{\langle M\rangle-\langle MO_x\rangle}$ corresponding to the strain induced by the mismatch at the interface between the two adjacent crystalline phases <M> and <MO$_x$>. In the case considered here, i.e. the formation of a thin crystalline <MO$_x$> film on its metal substrate <M>, a coherent <M>-<MO$_x$> interface may occur as a result of epitaxial growth (cf. Refs. [1, 3, 4, 6-9, 16-19, 36]). In such a case the mismatch between the adjacent lattices of the two crystalline phases is accommodated by elastic deformation. Generally, the mismatch in the boundary is characterized by the mismatch values in two directions within the boundary. One such mismatch f can be defined by (cf. Refs. [37, 38])

$$f = \frac{d^{hkl}_{<\mathrm{M}>} - d^{HKL}_{<\mathrm{MO}_x>}}{d^{HKL}_{<\mathrm{MO}_x>}} \quad \textbf{(13a)}$$

where $d^{HKL}_{<\mathrm{MO}_x>}$ and $d^{hkl}_{<\mathrm{M}>}$ represent the unstrained lattice spacings in the direction concerned of the (*hkl*) and (*HKL*) lattice planes perpendicular to the boundary of the <M> lattice and <MO$_x$> lattice, respectively. The unstrained lattice spacings of both lattices depend on temperature T according to

$$d^{hkl}_{<\mathrm{M}>} = d^{hkl,\mathrm{o}}_{<\mathrm{M}>}\,(1+\alpha^{hkl}_{<\mathrm{M}>}\Delta T) \quad \textbf{(13b)}$$

and

$$d^{HKL}_{<\mathrm{MO}_x>} = d^{HKL,\mathrm{o}}_{<\mathrm{MO}_x>}\,(1+\alpha^{HKL}_{<\mathrm{MO}_x>}\Delta T) \quad \textbf{(13c)}$$

where $d^{hkl,\mathrm{o}}_{<\mathrm{M}>}$ and $d^{HKL,\mathrm{o}}_{<\mathrm{MO}_x>}$ are the unstrained lattice spacings at the reference temperature T_o, $\alpha^{hkl}_{<\mathrm{M}>}$ and $\alpha^{HKL}_{<\mathrm{MO}_x>}$ denote the coefficients of linear thermal expansion of <M> and <MO$_x$>, respectively, and $\Delta T = (T - T_\mathrm{o})$.

Because the epitaxial oxide film is very thin as compared with the metal substrate, all mismatch between the oxide film and the substrate will be accommodated fully elastically by the oxide film and thus the strain in the oxide film in the direction pertaining to Eq. (13a) in a plane parallel to the interface, $\varepsilon_{\|}$, satisfies $\varepsilon_{\|} = f$ [cf. Eq. (13a)]. It should be noted that here the mismatch energy in the system is assigned to the <M>-<MO$_x$> interfacial energy instead of the bulk Gibbs free energy of the oxide film; this choice has no effect on the outcome of the model calculations.

Thus the contribution of the mismatch strain to the interfacial energy [see Eq. (11)] is obtained as the elastic strain energy stored in the oxide film per unit area of the interface between the <MO$_x$> film and the metal substrate <M> (cf. Ref. [38]). Then, for those cases where the mismatch f and thus the strain $\varepsilon_{\|}$ is independent of the direction within the plane parallel to the <M>-<MO$_x$> interface (e.g. the <Al>-<γ-Al$_2$O$_3$> interfaces considered in Sec.

IV.C.), the contribution of the mismatch energy to the interfacial energy $\gamma_{\langle M\rangle-\langle MO_x\rangle}$ equals (cf. Ref. [38])

$$\gamma^{\mathrm{mismatch}}_{\mathrm{M-MO_x}} = h_{\mathrm{MO_x}} \left(\frac{E}{1-\nu}\right) \varepsilon_{\|}^2 \tag{13d}$$

where $h_{\mathrm{MO_x}}$ is the thickness of the <MO$_x$> film and ν and E denote the Poisson's ratio and the Young's modulus of <MO$_x$>, respectively.

In principle part of the mismatch f may be compensated by plastic deformation. For plastic deformation to occur the mismatch and the oxide-film thickness must exceed critical values that increase with increasing bonding strength across the interface (cf. Refs. [37, 38]). For an epitaxial $Ge_{0.25}Si_{0.75}$ film on a Si substrate, where the lattice mismatch f = 0.01, a critical thickness of 16.3 nm was calculated [39]. Most <M>-<MO$_x$> systems have lattice mismatches f = 0.02-0.07 (cf. Refs. [1, 6-8]), and then up to an oxide-film thickness of, say, 5-10 nm, plastic deformation is considered not to play a role here (Frank-van der Merwe theory; cf. Refs. [37, 38 and 40]).

III.B.3. Expression for the <M>-<MO$_x$> interfacial energy

Substitution of Eqs. (12) and (13d) in Eq. (11) finally leads to the following expression for the interfacial energy $\gamma_{\langle M\rangle-\langle MO_x\rangle}$

$$\gamma_{\mathrm{M-MO_x}} = \frac{p\Delta H^{\infty}_{\mathrm{O\,in\,M}}}{A_{<O>}} + h_{\mathrm{MO_x}} \left(\frac{E}{1-\nu}\right) \varepsilon_{\|}^2 \tag{14}$$

IV. Thermodynamics of amorphous and crystalline aluminium-oxide films on aluminium substrates

The thermodynamic model developed in Secs. II and III will be applied to the case of aluminium oxide films on the {111}, {110} and {100} crystallographic faces of an aluminium substrate. Such an oxide film can be produced by e.g. dry, thermal oxidation of a clean Al substrate. The crystalline oxide competing with the amorphous oxide {Al_2O_3} of the same composition is γ-Al_2O_3 (cf. Refs. [1, 16-19]). First the difference in bulk, surface, and interfacial energies of the amorphous {Al_2O_3} cell on the <Al> substrate and the corresponding crystalline <γ-Al_2O_3> cell on the same substrate will be discussed. Then the stability of the oxide films is discussed as a function of growth temperature, oxide-film thickness, and crystallographic orientation of the <Al> substrate.

Table I. Some physical data of the Al-Al_2O_3 system at standard state pressure $p_o = 1\times10^5$ Pa ($T_o = 298.15$ K and N is Avogradro's number).

Name	Value	Unit	Ref.
Coefficients of linear thermal expansion	$\alpha(T) = a + b\Delta T + c\Delta T^2$ $(T_0 \leq T \leq 900\ \text{K})$	K^{-1}	
	<Al> : $a = 2.3889 \times 10^{-5}$	K^{-1}	[41]
	$b = -1.1162 \times 10^{-9}$	K^{-2}	
	$c = 2.1757 \times 10^{-11}$	K^{-3}	
	<γ-Al_2O_3> : $a = 2.6068 \times 10^{-6}$	K^{-1}	[42]
	$b = 1.1499 \times 10^{-8}$	K^{-2}	
	$c = 0$	K^{-3}	
Unstrained lattice parameters of unit cells at T_0	$a^0_{Al} = 4.0494 \times 10^{-10}$	m	[43]
	$a^0_{\gamma-Al_2O_3} = 7.924 \times 10^{-10}$	m	[44]
Molar volumes at T_o	$V^0_{Al} = 1.00 \times 10^{-5}$	m^3mole^{-1}	
	$V^0_{\gamma-Al_2O_3} = 2.81 \times 10^{-5}$	m^3mole^{-1}	
	$V^0_{\{Al_2O_3\}} = 3.19 \times 10^{-5}$	m^3mole^{-1}	[45]
Molar interface areas of <Al>	$\{111\} : A_{Al} = \frac{1}{4}\ 3a^2_{Al}\ N$	m^2mole^{-1}	
	$\{110\} : A_{Al} = \frac{1}{2}\ 2a^2_{Al}\ N$	m^2mole^{-1}	
	$\{100\} : A_{Al} = \frac{1}{2}a^2_{Al}\ N$	m^2mole^{-1}	
O molar interface area of {Al_2O_3}	$A_{\{O\}} = \frac{1}{4}\sqrt{3}(\frac{1}{2}a_{\gamma-Al_2O_3})^2 N$	m^2mole^{-1}	
Poisson's ratio of <γ-Al_2O_3>	$\nu = 0.24\ (\pm 0.02)$		[46]
Young's modulus of <γ-Al_2O_3>	$E = 2.53 \times 10^{11}\ (\pm 0.22 \times 10^{11})$	Nm^{-2}	[46]

IV.A. Difference in bulk energy of {Al_2O_3} and <γ-Al_2O_3>

The values for the Gibbs free energy of formation,[3] the enthalpy of formation and the entropy of γ-Al_2O_3 and the configurationally frozen Al_2O_3 liquid (as model for amorphous

---

[3] For the calculation of the Gibbs free energy of formation of amorphous {Al_2O_3} in this work, the heat capacity C^0_p of amorphous {Al_2O_3} below the liquid-glass transition temperature at 1350 K was taken to be the same as that of γ-Al_2O_3 (see Ref. [28]).

$\{Al_2O_3\}$; see Sec. III.A) are taken from Ref. [28]. The molar volumes of the cubic phases <Al> and $<\gamma\text{-}Al_2O_3>$ from T_o = 298.15 K up to the melting point of <Al> at 933.45 K are calculated from $V(T) = V^{o}(1+\alpha\Delta T)^3$, where α and V^{o} denote the coefficient of linear thermal expansion at $T > T_o$ and the molar volume at T_o, respectively (see Table I). The coefficient of linear thermal expansion of $\{Al_2O_3\}$ is taken the same as that of $<\gamma\text{-}Al_2O_3>$. All values used for the calculation were taken at a standard state pressure of $p_o = 1\times10^5$ Pa; it is noted that the effect of pressure on the *difference* in bulk, surface and interfacial energies of $\{Al_2O_3\}$ and $<\gamma\text{-}Al_2O_3>$ can be neglected (see Sec. V).

The calculated difference in the bulk Gibbs free energy of the $\{Al_2O_3\}$ cell and the corresponding $<\gamma\text{-}Al_2O_3>$ cell per unit area of the <Al>-$\{Al_2O_3\}$ interface [cf. Eq. (5) in Sec. II] is plotted in Fig. 2 as a function of $h_{\{Al_2O_3\}}$ (i.e. thickness of the amorphous oxide film) for both T_o and T = 900 K. The crystalline $<\gamma\text{-}Al_2O_3>$ cell is of course thermodynamically more stable than the amorphous $\{Al_2O_3\}$ cell when only considering the difference in bulk energy of the two phases. Since at the melting temperature of $\gamma\text{-}Al_2O_3$ it holds that $\Delta G^{f}_{\gamma\text{-}Al_2O_3} \equiv \Delta G^{f}_{\{Al_2O_3\}}$, the $\{Al_2O_3\}$ cell becomes relatively more stable at higher T (see Fig. 2).

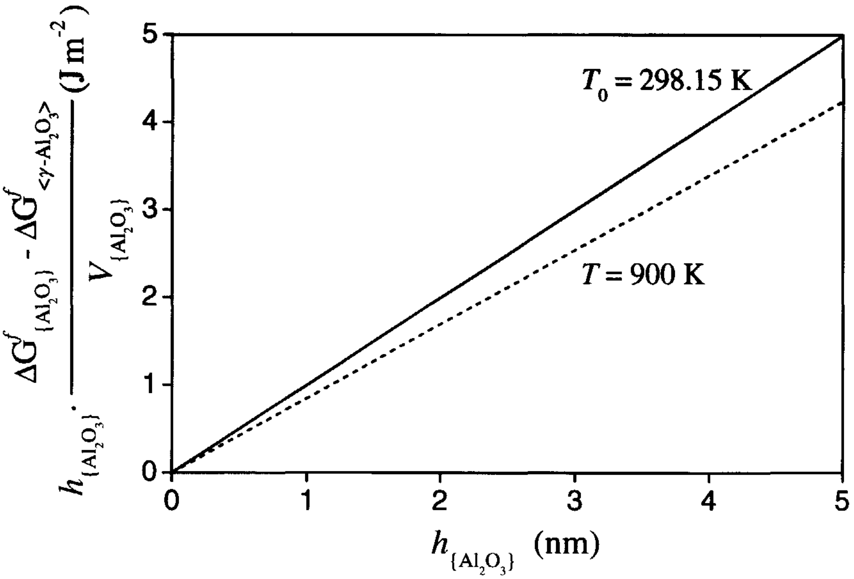

Figure 2. Difference in bulk Gibbs free energy of the amorphous $\{Al_2O_3\}$ cell and the corresponding crystalline $<\gamma\text{-}Al_2O_3>$ cell per unit area of the <Al>-$\{Al_2O_3\}$ interface [cf. Eq. (5) in Sec. II] as a function of $h_{\{Al_2O_3\}}$ (i.e. thickness of the amorphous oxide film) at both T_o = 298.15 K and T = 900 K. Note that $\Omega_{\{Al_2O_3\}} = 1$ in Eq. (5) of Sec. II (cf. Sec. III.A below Eq. (6) and Ref. [25]).

IV.B. Difference in surface energy of $\{Al_2O_3\}$ *and* $<\gamma\text{-}Al_2O_3>$

The only values reported in the literature for the surface energies of the {111}, {110} and {100} crystallographic faces of γ-Al_2O_3, are theoretical ones obtained from molecular dynamics simulations pertaining to 300 K of the corresponding relaxed and unrelaxed surfaces of γ-Al_2O_3 in contact with vacuum (i.e. $\gamma_{\gamma\text{-Al}_2\text{O}_3\text{-vac}}$) [11]. For Al_2O_3 films grown on Al substrates in an oxygen ambient e.g. by dry thermal oxidation, the surface energies of the oxygen-terminated surfaces of γ-Al_2O_3 are adopted. Many crystalline metal-oxides lower their surface energy by surface relaxation (cf. Refs. [11, 47]), and then the relaxed surface energies need to be considered.

According to Ref. [11], $\gamma_{\{110\}\gamma\text{-Al}_2\text{O}_3\text{-vac}} = 2.54$ Jm^{-2} and $\gamma_{\{100\}\gamma\text{-Al}_2\text{O}_3\text{-vac}} = 1.94$ Jm^{-2} for the relaxed oxygen-terminated {110} and {100} crystallographic faces of γ-Al_2O_3 at $T = 300$ K, respectively. These theoretical values can be compared with the experimental value of $\gamma_{\gamma\text{-Al}_2\text{O}_3\text{-vac}} = 1.67$ Jm^{-2} determined for nanocrystalline γ-Al_2O_3 at T_o [48]. For the linear temperature dependencies of the surface energies of the {110} and {100} crystallographic faces of γ-Al_2O_3, an average linear temperature coefficient of -0.50×10^{-3} Jm^{-2}K^{-1} is taken as estimated from the experimental and theoretical values of $\gamma_{\gamma\text{-Al}_2\text{O}_3\text{-vac}}$ at various temperatures reported in Refs. [48, 49], i.e. $\gamma_{\gamma\text{-Al}_2\text{O}_3\text{-vac}}(T) = \gamma_{\gamma\text{-Al}_2\text{O}_3\text{-vac}}(T_o) - 0.50\times10^{-3}(T - T_o)$.

Data for the oxygen-terminated {111} crystallographic face of γ-Al_2O_3 are not available. Only the two possible aluminium-terminated {111} γ-Al_2O_3 surfaces were simulated, which both became amorphous upon relaxation as a result of surface reconstruction [11]. Therefore, the resulting value for the surface energy of the two relaxed aluminium-terminated {111} crystallographic faces of γ-Al_2O_3 at 300 K of 0.88 Jm^{-2} [11], in fact represents the value for the surface energy of $\{Al_2O_3\}$ at 300 K, i.e. $\gamma_{\{\text{Al}_2\text{O}_3\}\text{-vac}} (= \gamma_{\langle\{111\}\gamma\text{-Al}_2\text{O}_3\rangle\text{-vac}}) = 0.88$ Jm^{-2}. Taking for the linear temperature coefficient of $\gamma_{\{\text{Al}_2\text{O}_3\}\text{-vac}}$ (see above) the value experimentally determined for liquid Al_2O_3, i.e. -0.187×10^{-3} [50], then the calculated theoretical value of $\gamma_{\{\text{Al}_2\text{O}_3\}\text{-vac}}$ at the melting point $T_m = 2325$ K becomes 0.50 Jm^{-2}, which agrees well with the corresponding experimental value of 0.57 Jm^{-2} for the surface energy of liquid Al_2O_3 at T_m [50].

It may be assumed that, as for the relaxed Al-terminated {111} γ-Al_2O_3 surfaces, the relaxed O-terminated {111} surface is also amorphous due to surface reconstruction and therefore also has a surface energy at T_o of 0.88 Jm^{-2} (see above). Then it can be concluded from the above data that the surface energy of the relaxed O-terminated surfaces of γ-Al_2O_3 increases with decreasing atomic density at the (unrelaxed) γ-Al_2O_3 surface: $\gamma_{\langle\{111\}\gamma\text{-Al}_2\text{O}_3\rangle\text{-vac}} < \gamma_{\langle\{100\}\gamma\text{-Al}_2\text{O}_3\rangle\text{-vac}} < \gamma_{\langle\{110\}\gamma\text{-Al}_2\text{O}_3\rangle\text{-vac}}$.

The calculated difference in surface energy between $\{Al_2O_3\}$ and $<\gamma\text{-}Al_2O_3>$ per unit area of the $\{Al_2O_3\}$ surface [cf. Eq. (5) in Sec. II] is plotted in Fig. 3 as a function of T for the three different crystallographic faces of γ-Al_2O_3 considered. The ratio χ relating the surface areas of the (unstrained) $\{Al_2O_3\}$ cell (cf. Sec. III.A below Eq. (6) and Ref. [25]) and the (strained) $<\gamma\text{-}Al_2O_3>$ cell [see Eq. (4b) in Sec. II] was calculated using Eq. (A2) in the Appendix. As follows from Fig. 3, the surface energy of amorphous $\{Al_2O_3\}$ is smaller than those of the {110} and {100} surfaces of $<\gamma\text{-}Al_2O_3>$ (at T_0: 1.57 and 0.99 Jm^{-2} smaller, respectively), whereas it is slightly larger than that of the {111} surface of $<\gamma\text{-}Al_2O_3>$ (this difference would be zero if χ equals 1; cf. the Appendix). The temperature dependencies of the differences in surface energies are negligible.

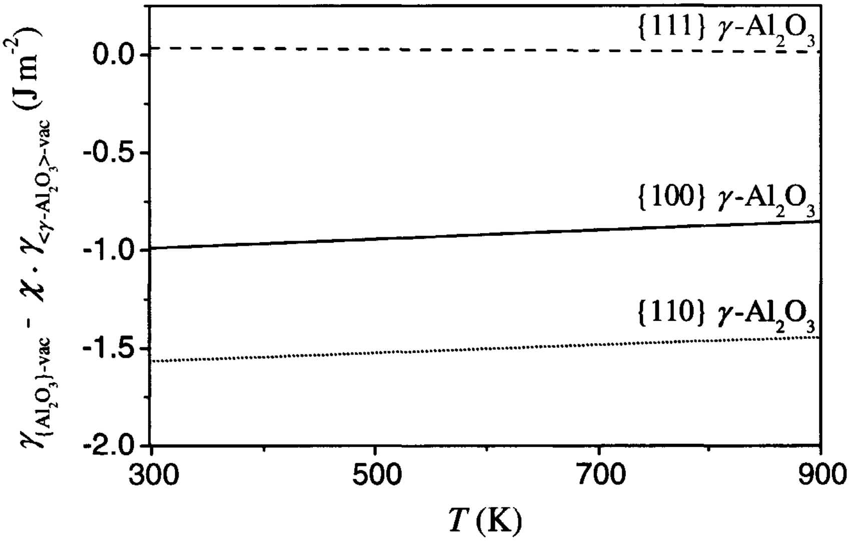

Figure 3. Difference in surface energy of the amorphous $\{Al_2O_3\}$ cell and the corresponding crystalline $<\gamma\text{-}Al_2O_3>$ cell per unit area of the $\{Al_2O_3\}$ surface [cf. Eq. (5) in Sec. II], as a function of T for the {111}, {110} and {100} crystallographic faces of γ-Al_2O_3. The ratio χ relates the surface areas of the $\{Al_2O_3\}$ cell and the strained $<\gamma\text{-}Al_2O_3>$ cell, and has been calculated using Eq. (A2) in the Appendix.

IV.C. Difference in energy of $<Al>\text{-}\{Al_2O_3\}$ and $<Al>\text{-}<\gamma\text{-}Al_2O_3>$ interfaces

The value of the interfacial energy of the crystalline-amorphous $<Al>\text{-}\{Al_2O_3\}$ interface (i.e. $\gamma_{Al\text{-}\{Al_2O_3\}}$) is the sum of the interaction, entropy and enthalpy contributions (see Sec. III.A). Values for these separate energy contributions for the $<Al>\text{-}\{Al_2O_3\}$ interface (calculated as indicated in Sec. III.A) and the resulting value of the interfacial energy $\gamma_{Al\text{-}\{Al_2O_3\}}$ are reported in Table II for the three crystallographic faces of <Al> considered.

Table II. Interfacial energy of the crystalline–amorphous <Al>-{Al_2O_3} interface, as calculated using Eq. (10) given in Sec. III.A.4, for an {Al_2O_3} oxide film on the {111}, {110} and {100} crystallographic faces of an <Al> substrate at different growth temperatures *T*. The interaction, entropy and enthalpy contributions to the interfacial energy $\gamma_{Al-\{Al_2O_3\}}$ were obtained using Eqs. (7b), (8a) and (9) given in Sec. III.A, respectively. Data used were taken from Ref. [28] and Table I.

T(K)	$\gamma^{interaction}_{Al-\{Al_2O_3\}}$ (Jm^{-2})	$\gamma^{entropy}_{Al-\{Al_2O_3\}}$ (Jm^{-2})	$\gamma^{enthalpy}_{Al-\{Al_2O_3\}}$ (Jm^{-2})			$\gamma_{Al-\{Al_2O_3\}}$ (Jm^{-2})		
			{111}	{110}	{100}	{111}	{110}	{100}
298	-4.583	+0.036	+0.083	+0.051	+0.072	-4.463	-4.495	-4.474
600	-4.560	+0.057	+0.082	+0.050	+0.071	-4.420	-4.452	-4.431
900	-4.511	+0.069	+0.080	+0.049	+0.070	-4.361	-4.393	-4.372

The value of the interfacial energy $\gamma_{Al-\{Al_2O_3\}}$ is dominated by the negative contribution of the Al-O interaction energy (cf. discussion below Eq. (7c) in Sec. III.A.1). Therefore, $\gamma_{Al-\{Al_2O_3\}} < 0$ and its value only slightly increases (i.e. becomes less negative) with increasing growth temperature *T* due to the small increases of both the interaction energy contribution and the entropy energy contribution with increasing *T*. As an approximation for the molar interface area of oxygen of the amorphous oxide at the three <Al>-{Al_2O_3} interfaces considered, the molar interface area of oxygen in the most densely packed plane of <γ-Al_2O_3>, i.e. the {111} γ-Al_2O_3 plane, has been taken (see Table I), as discussed below Eq. (7c) in Sec. III.A.1. Consequently, only the relatively small positive enthalpy contribution to the interfacial energy depends on the crystallographic orientation of the <Al> substrate [cf. Table II and Eq. (9)]. It can be concluded that the interfacial energy $\gamma_{Al-\{Al_2O_3\}} < 0$ and that its value is approximately independent of both the growth temperature and the crystallographic orientation of the <Al> substrate (see Table II).

The value of the interfacial energy of the crystalline-crystalline <Al>-<γ-Al_2O_3> interface (i.e. $\gamma_{Al-\gamma\text{-}Al_2O_3}$) is the sum of the interaction and the mismatch contributions (see Sec. III.B). For all three crystallographic faces of <Al> considered,[4] the orientation relationship between <Al> and <γ-Al_2O_3> is given by [1, 17-20]: $(111)_{Al}\|(111)_{\gamma\text{-}Al_2O_3}$ and $[110]_{Al}\|[110]_{\gamma\text{-}Al_2O_3}$. From the crystallographic structure of <Al> and <γ-Al_2O_3> (cf. Refs.

---

[4] In Refs. [18, 19] an additional orientation relationship between γ-Al_2O_3 and the Al substrate was found for the {100} crystallographic face of Al.

[43] and [44], respectively) it then follows that,[5] at the oxide-film growth temperature, the 'growth' mismatch f (see Sec. III.B.2) in all directions parallel to the <Al>-<γ-Al_2O_3> interface is the same for the three crystallographic faces of <Al> considered and equals

$$f = \frac{2a_{<\mathrm{Al}>}}{a_{\gamma\text{-}\mathrm{Al_2O_3}}} - 1 \tag{15}$$

where a_{Al} and $a_{\gamma\text{-}\mathrm{Al_2O_3}}$ are the unstrained lattice parameters of the Al and γ-Al_2O_3 unit cells (see footnote 5) at the growth temperature T, as calculated according to Eqs. (13b) and (13c) (using the values reported in Table I), respectively. Since $f > 0$ and all growth mismatch is accommodated fully elastically by the thin (epitaxial) <γ-Al_2O_3> film (see Sec. III.B.2), a tensile strain $\varepsilon_{\|}$ of value f resides within the oxide film parallel to the <Al>-<γ-Al_2O_3> interface. The contribution of the mismatch energy to the interfacial energy $\gamma_{\mathrm{Al}-\gamma\text{-}\mathrm{Al_2O_3}}$ can be calculated using Eq. (13d) in Sec. III.B.2.

The contribution of the Al-O interaction energy to the interfacial energy $\gamma_{\mathrm{Al}-\gamma\text{-}\mathrm{Al_2O_3}}$ can be calculated applying Eq. (12) in Sec. III.B.1. To this end, the molar interface area A_{O} must be calculated from the *strained* lattice parameter of <γ-Al_2O_3> at the interface (see Sec. III.B.1). All mismatch strain is accommodated fully elastically by the thin <γ-Al_2O_3> film (see above), and thus [cf. Eq. (15)] the *strained* lattice parameter of <γ-Al_2O_3> is equal to twice the *unstrained* lattice parameter of <Al> (see also footnote 5). From the crystallographic structure and composition of the <Al> and <γ-Al_2O_3> unit cells (see footnote 5), it then follows that, for the three <Al>-<γ-Al_2O_3> interfaces concerned, the atomic density of oxygen of <γ-Al_2O_3> at the interface is equal to the atomic density of Al atoms of the <Al> substrate at the interface, and consequently $A_{\mathrm{O}} = A_{\mathrm{Al}}$. Expressions for the calculation of the molar interface area A_{Al} (and thus of A_{O}) are given in Table I.

Values for both the interaction and mismatch contribution to the energy of the crystalline-crystalline <Al>-<γ-Al_2O_3> interface and the resulting value of the interfacial energy $\gamma_{\mathrm{Al}\,-\,\gamma\text{-}\mathrm{Al_2O_3}}$ are presented in Table III for the three crystallographic faces of <Al> considered. Note that the calculated values of the mismatch energy and thus the interfacial energy $\gamma_{\mathrm{Al}\,-\,\gamma\text{-}\mathrm{Al_2O_3}}$ in Table III apply to the temperature at which the oxide film has been grown. For an oxide-film thickness $h_{\gamma\text{-}\mathrm{Al_2O_3}} < 5$ nm, the value of $\gamma_{\mathrm{Al}\,-\,\gamma\text{-}\mathrm{Al_2O_3}}$ is dominated by the large negative contribution of the interaction energy, implying $\gamma_{\mathrm{Al}\,-\,\gamma\text{-}\mathrm{Al_2O_3}} < 0$. It is noted that for oxide-film thicknesses $h_{\gamma\text{-}\mathrm{Al_2O_3}} > 5$ nm the positive contribution of the mismatch energy becomes dominant and $\gamma_{\mathrm{Al}\,-\,\gamma\text{-}\mathrm{Al_2O_3}}$ can become positive.

---

[5] Aluminium metal has a fcc structure (spacegroup: F$m3m$) with a unit cell with an (unstrained) lattice parameter at T_o = 298.15 K of $a^{\mathrm{o}}_{\mathrm{Al}}$ = 4.0494 Å [43]. γ-Al_2O_3 has a defect cubic spinel structure (spacegroup: F$d\bar{3}m$) with a unit cell with an unstrained lattice parameter $a^{\mathrm{o}}_{\gamma\text{-}\mathrm{Al_2O_3}}$ = 7.924 Å [44]. The unit cell contains 32 oxygen anions in a 2 × 2 × 2 array of fcc cells of the anion sublattice and $21\frac{1}{3}$ aluminium cations divided over the octrahedral and tetrahedral interstices. Hence, using the given orientation relationship between the <Al> substrate and the thin epitaxial <γ-Al_2O_3> film [see above Eq. (15) in Sec. IV.C], it follows, for the three <Al>-<γ-Al_2O_3> interfaces considered, that: $a^{\mathrm{o,strained}}_{\langle\gamma\text{-}\mathrm{Al_2O_3}\rangle} = 2 \times a^{\mathrm{o}}_{\mathrm{Al}}$.

Table III. Interfacial energy of the crystalline–crystalline <Al>-<γ-Al_2O_3> interface as calculated using Eq. (14) in Sec. III.B.3 for an (epitaxial) <γ-Al_2O_3> oxide film on the {111}, {110} and {100} crystallographic faces of an <Al> substrate at different growth temperatures T and for various film thicknesses $h_{\langle\gamma\text{-}\mathrm{Al_2O_3}\rangle}$. The interaction and mismatch contributions to the interfacial energy $\gamma_{\mathrm{Al}\,-\,\gamma\text{-}\mathrm{Al_2O_3}}$ were obtained using Eqs. (12) and (13d), respectively. Data used were taken from Ref. [28] and Table I.

T(K)	$h_{\gamma\text{-}\mathrm{Al_2O_3}}$ (nm)	$\gamma^{\mathrm{interaction}}_{\mathrm{Al}\,-\,\gamma\text{-}\mathrm{Al_2O_3}}$ (Jm^{-2})			$\gamma^{\mathrm{mismatch}}_{\mathrm{Al}\,-\,\gamma\text{-}\mathrm{Al_2O_3}}$ (Jm^{-2})	$\gamma_{\mathrm{Al}\,-\,\gamma\text{-}\mathrm{Al_2O_3}}$ (Jm^{-2})		
		{111}	{110}	{100}		{111}	{110}	{100}
298	1	-4.387	-2.686	-3.799	+0.162	-4.225	-2.524	-3.637
	3				+0.486	-3.901	-2.200	-3.313
	5				+0.810	-3.577	-1.876	-2.989
600	1	-4.315	-2.642	-3.736	+0.262	-4.053	-2.380	-3.475
	3				+0.786	-3.529	-1.856	-2.951
	5				+1.310	-3.005	-1.332	-2.427
900	1	-4.209	-2.578	-3.645	+0.414	-3.795	-2.164	-3.231
	3				+1.241	-2.968	-1.336	-2.404
	5				+2.068	-2.141	-0.509	-1.577

The coefficient of linear thermal expansion of <Al> is approximately ten times larger than that of <γ-Al_2O_3> (see Table I), and therefore the growth mismatch f [cf. Eq. (15)] increases, virtually linearly, with increasing *growth* temperature T from 0.022 at $T_0 = 298.15$ K to 0.035 at $T = 900$ K. Consequently, the (positive) mismatch contribution and thus the interfacial energy $\gamma_{\mathrm{Al}\,-\,\gamma\text{-}\mathrm{Al_2O_3}}$ increases with increasing growth temperature. For most metal-substrate / oxide-film systems, the coefficient of linear thermal expansion of the metal substrate is larger than that of the oxide film. Hence it can be concluded that for the general case of an <MO_x> film as formed by epitaxial growth on its substrate <M>, the crystalline-crystalline <M>-<MO_x> interface will be less stable for increasing growth temperature if the growth mismatch $f > 0$. Note that this temperature dependence will be reversed (i.e. the <M>-<MO_x> interfacial energy decreases for increasing growth temperature) for metal-oxide systems with a growth mismatch $f < 0$.

In contrast with the mismatch energy, the Al-O interaction energy depends on the orientation of the <Al> substrate: the *smaller* the molar interface area A_O of oxygen at the <Al>-<γ-Al_2O_3> interface, the larger the Al-O interaction energy per unit area of the interface [cf. Eq. (12)] and thus the *lower* the resulting value of $\gamma_{Al-\gamma\text{-}Al_2O_3}$ (see Table III). Since the value of A_O is equal to the molar interface area A_{Al} of Al atoms of the <Al> substrate at the interface (see above), it follows that the lowest interfacial energy $\gamma_{Al-\gamma\text{-}Al_2O_3}$ occurs for the most densely packed plane of <Al> at the interface, i.e. the {111} plane (see Table III).

It can be concluded that, in contrast with the crystalline-amorphous interfacial energy $\gamma_{Al-\{Al_2O_3\}}$, the crystalline-crystalline interfacial energy $\gamma_{Al-\gamma\text{-}Al_2O_3}$ does depend on oxide-film thickness, the growth temperature and the crystallographic orientation of the <Al> substrate (cf. Tables II and III).

In Ref. [51], the epitaxial interface between the {111} crystallographic plane of Nb and the {0001} crystallographic plane of α-Al_2O_3 was modelled using an atomistic, static lattice simulation technique. Neglecting the mismatch of $f = 0.019$ between the lattices of the two phases at the <Nb>-<α-Al_2O_3> interface, an interfacial energy of $\gamma_{\langle Nb\rangle-\langle\alpha\text{-}Al_2O_3\rangle} = -3.61$ Jm^{-2} was obtained [51]. This value is of the same magnitude as the values of the interfacial energies, calculated using Eq. (12) in Sec. III.B.1, for the three <Al>-<γ-Al_2O_3> interfaces with $\gamma^{\text{mismatch}}_{\langle Al\rangle-\langle\gamma\text{-}Al_2O_3\rangle} = 0$ at T_o: i.e. -4.387, -2.690 and –3.799 Jm^{-2} for a <γ-Al_2O_3> film on the {111}, {110} and {100} crystallographic faces of <Al>, respectively. Hence it may be concluded that the values obtained in this work for the interfacial energies $\gamma_{Al-\{Al_2O_3\}}$ and $\gamma_{Al-\gamma\text{-}Al_2O_3}$ are realistic (cf. Tables II and III).

The calculated difference between the interfacial energies $\gamma_{Al-\{Al_2O_3\}}$ and $\gamma_{Al-\gamma\text{-}Al_2O_3}$ per unit area of the <Al>-{Al_2O_3} interface [cf. Eq. (5) in Sec. II], i.e. $\gamma_{Al-\{Al_2O_3\}} - \chi \cdot \gamma_{Al-\gamma\text{-}Al_2O_3}$, at T_o, is plotted in Fig. 4 as a function of oxide-film thickness for the three crystallographic faces of <Al> considered. The dependence of the interfacial energy difference on the oxide-film growth temperature is shown in Fig. 5 for oxide films of variable thickness on a {100} Al substrate (similar results have been obtained for {110} and {111} <Al> substrates). Note that for a given thickness $h_{\{Al_2O_3\}}$ of the amorphous {Al_2O_3} film, the thickness $h_{\gamma\text{-}Al_2O_3}$ of the *corresponding* epitaxial <γ-Al_2O_3> film (cf. Sec. II) differs somewhat from $h_{\{Al_2O_3\}}$ due to both the difference in molar volumes of {Al_2O_3} and <γ-Al_2O_3> and the occurrence of mismatch strain (see the Appendix).

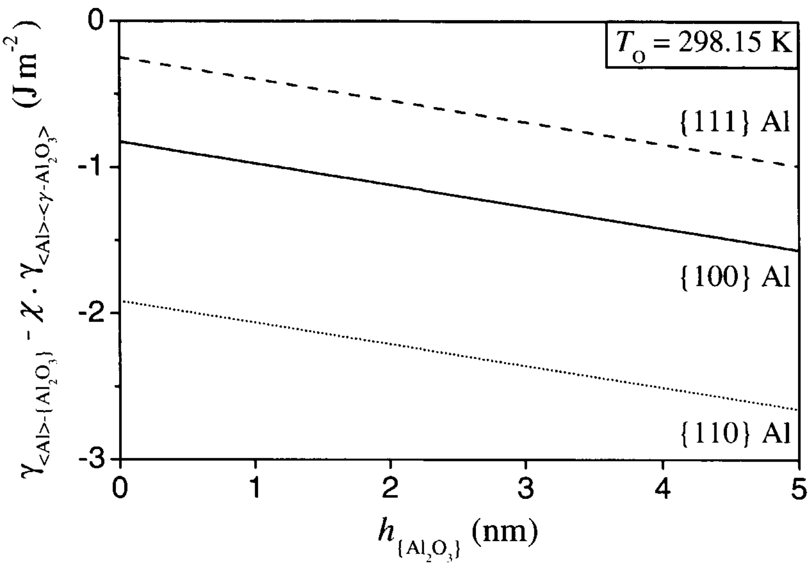

Figure 4. Difference in interfacial energy of the metal-substrate / oxide-film interface of the amorphous $\{Al_2O_3\}$ cell and the corresponding crystalline <γ-Al_2O_3> cell per unit area of the <Al>-$\{Al_2O_3\}$ interface [cf. Eq. (5) in Sec. II] at T_0 = 298.15 K as a function of the thickness $h_{\{Al_2O_3\}}$ of the $\{Al_2O_3\}$ film (cf. Fig. 1 in Sec. II). Results are shown for Al_2O_3 films on {111}, {110} and {100} Al substrates.

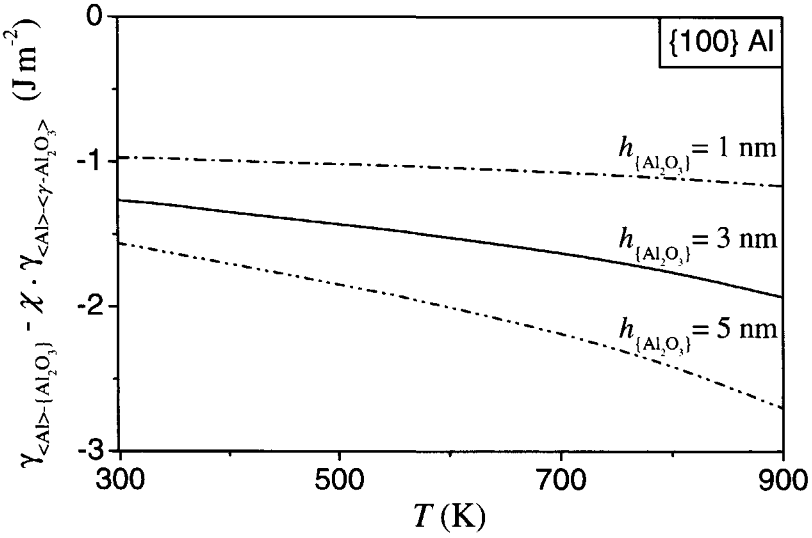

Figure 5. Difference in the interfacial energy of the metal-substrate / oxide-film interface of the amorphous $\{Al_2O_3\}$ cell and the corresponding crystalline <γ-Al_2O_3> cell per unit area of the <Al>-$\{Al_2O_3\}$ interface [cf. Eq. (5) in Sec. II] as a function of the growth temperature T for an $\{Al_2O_3\}$ film of variable thickness $h_{\{Al_2O_3\}}$ on a {100} Al substrate.

It follows that the <Al>-{Al_2O_3} interface is more stable than the corresponding <Al>-<γ-Al_2O_3> interface for all three crystallographic orientations of the <Al> substrate, even if $h_{\{Al_2O_3\}} \to 0$ (i.e. when the mismatch energy contribution is zero). Since the growth mismatch $f > 0$, the <Al>-{Al_2O_3} interface becomes more stable with respect to the corresponding <Al>-<γ-Al_2O_3> interface at higher growth temperature, in accordance with the above discussion.

V. Stability of amorphous aluminium-oxide films on crystalline aluminium substrates

An amorphous {Al_2O_3} film of thickness $h_{\{Al_2O_3\}}$ on an <Al> substrate will be more stable than a crystalline <γ-Al_2O_3> film of corresponding thickness $h_{\gamma\text{-}Al_2O_3}$ on the same substrate if $\Delta G = G_{am} - G_{cryst} < 0$ (see Sec. II). For sufficiently thick oxide films, the bulk energy contribution dominates for the total energy of the metal / oxide system. Thus, a critical thickness $h_{\{Al_2O_3\}}^{critical}$ can be defined as the oxide-film thickness of the {Al_2O_3} cell for which $\Delta G = G_{am} - G_{cryst} = 0$; for $h_{\{Al_2O_3\}}$ < $h_{\{Al_2O_3\}}^{critical}$ the stable oxide film is the amorphous one. It follows from Eq. (5) using Eqs. (11), (13d) and (A4) that

$$h_{\{Al_2O_3\}}^{critical} = \frac{\left[\chi\left(\gamma_{\langle\gamma\text{-}Al_2O_3\rangle\text{-vac}} + \gamma^{interaction}_{\langle Al\rangle\text{-}\langle\gamma\text{-}Al_2O_3\rangle}\right) - \gamma_{\{Al_2O_3\}\text{-vac}} - \gamma_{\langle Al\rangle\text{-}\{Al_2O_3\}}\right]}{\left[\dfrac{\Delta G^f_{\{Al_2O_3\}} - \Delta G^f_{\langle\gamma\text{-}Al_2O_3\rangle}}{V_{\{Al_2O_3\}}} - \chi\xi\left(\dfrac{E}{1-\nu}\right)f^2\right]} \qquad \textbf{(16)}$$

where the ratio χ between the surface areas and the ratio ξ between the oxide film thicknesses of the {Al_2O_3} and the <γ-Al_2O_3> cell (as formed by epitaxial growth) are obtained from Eqs. (A2) and (A4) in the Appendix, respectively. Note that $\Omega_{\{Al_2O_3\}} = 1$ (Eq. (5) of Sec. II; see Sec. III.A and Ref. [25]).

The value of $h_{\{Al_2O_3\}}^{critical}$, calculated by application of Eq. (16) using the results for the bulk, surface and interfacial energies presented in Sec. IV, has been plotted in Fig. 6 as a function of the growth temperature T for an oxide film on the {111}, {110} and {100} crystallographic faces of <Al>: the amorphous oxide film is stable up to a thickness of 0.25, 4.08 and 2.13 nm at T_0 = 298.15 K, and up to a thickness of 0.44, 7.11 and 3.52 nm at T = 900 K, respectively (see Fig. 6).

The increased stability of the amorphous {Al_2O_3} film for increasing growth temperature is the result of both (*i*) the *decrease* of the bulk Gibbs free-energy difference between the $\{Al_2O_3\}$ and the $<\gamma\text{-}Al_2O_3>$ film with increasing growth temperature (cf. Fig. 2), and (*ii*) the *increase* of the crystalline-crystalline $<Al>$-$<\gamma\text{-}Al_2O_3>$ interfacial energy with increasing growth temperature (being more pronounced for thicker oxide films; cf. Fig. 5). Note that this temperature dependence may be much weaker or even of reversed nature for metal-oxide systems $<MO_x>$ with a growth mismatch $f < 0$, because then the interfacial energy γ_{M-MO_x} decreases with increasing growth temperature (see Sec. IV.C).

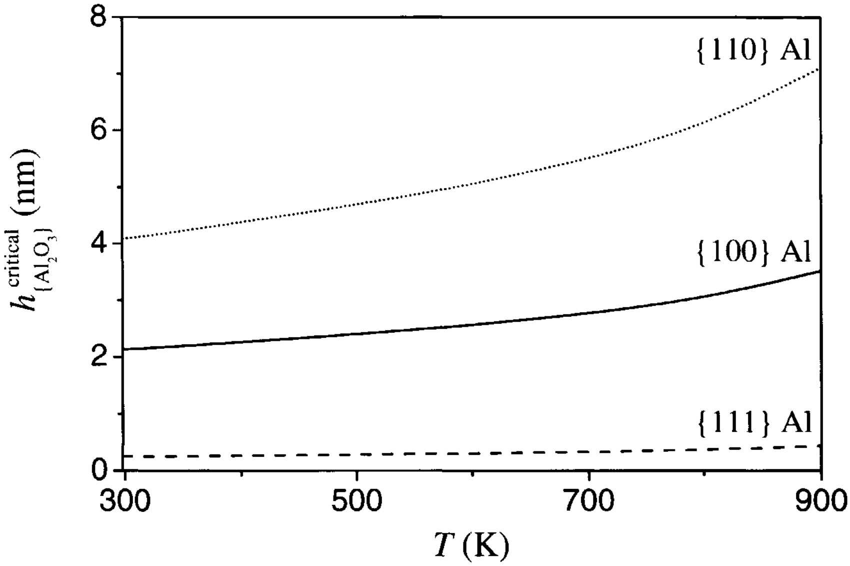

Figure 6. The critical thickness $h^{\text{critical}}_{\{Al_2O_3\}}$, up to which an amorphous $\{Al_2O_3\}$ film in stead of a crystalline $<\gamma\text{-}Al_2O_3>$ film is preferred on the $<Al>$ metal substrate, as a function of the growth temperature T. Results are shown for Al_2O_3 films on {111}, {110} and {100} Al substrates.

Clearly, for the most densely packed crystallographic face of Al, i.e. the {111} face, the critical thickness is about 1-2 'oxide monolayers' (1 ML $\cong \frac{1}{4}a^{o}_{\gamma\text{-}Al_2O_3} \cong 0.2$ nm; cf. footnote 5 in Sec. IV.C), approximately independent of the growth temperature. Thus, after the very first stage of oxygen chemisorption and oxide formation, oxide-film growth on a {111} Al substrate is predicted to proceed by the direct formation and epitaxial growth of $\gamma\text{-}Al_2O_3$. For growth of an oxide film on the more 'open' {110} and the {100} crystallographic faces of Al, preferred initial formation of an amorphous $\{Al_2O_3\}$ film is predicted, up to a critical oxide-film thickness $h^{\text{critical}}_{\{Al_2O_3\}}$ of 4.08 and 2.13 nm at $T_0 = 298.15$ K, respectively. This difference in the stability of an $\{Al_2O_3\}$ film, on the three different crystallographic faces of $<Al>$, is directly related to the differences in both surface and interfacial energy of the corresponding $<\gamma\text{-}Al_2O_3>$ film on the three different $<Al>$ substrates (cf. Figs. 3 and 4 with Fig. 6).

As follows from Figs. 2, 3 and 4, for thin {Al_2O_3} films (i.e. $h_{\{Al_2O_3\}} < 3$ nm) on {100} and {110} <Al> substrates at a growth temperature T_o = 298.15 K, the difference in bulk Gibbs free energy between {Al_2O_3} and <γ-Al_2O_3> is compensated for by about equally large corresponding differences in surface energy and interfacial energy, whereas at higher growth temperatures and for thicker oxide films the difference in interfacial energy becomes dominant. Further, the surface energy of (anhydrous) γ-Al_2O_3 is lowered upon chemisorption of H_2O [48]. Hence the chance of initial formation of a crystalline <γ-Al_2O_3> film on an <Al> substrate is enhanced by the presence of small amounts of water vapour.

Since the effect of pressure (within the range of, say, UHV up to 1 MPa) on the bulk and surface energies of {Al_2O_3} and <γ-Al_2O_3> is approximately the same, the effect of pressure on the *difference* in bulk and surface energies [cf. Eq. (5) in Sec. II] can be neglected. Moreover, the effect of pressure on the enthalpy and entropy (per molar volume) of the solid phases is small, because the coefficient of volume expansion β of solid phases is small ($\beta = 10^{-5}$-10^{-4} K^{-1}) (see footnote 6) and approximately the same for both {Al_2O_3} and <γ-Al_2O_3>. The energy of the <Al>-<γ-Al_2O_3> interface (cf. Eq. (14) in Sec. III.B.3) depends on the growth mismatch f and the Poisson ratio and Young's modulus of <γ-Al_2O_3>, which are nearly independent of pressure due to the high compressibility of the solid phases (i.e. ~10^{11} Pa). Thus it can be concluded that the stability of an {Al_2O_3} film on an <Al> substrate (i.e. the value of $h^{\text{critical}}_{\{Al_2O_3\}}$) is virtually independent of pressure.

The predictions obtained in this work on the thermodynamic stability of an amorphous {Al_2O_3} film on the different crystallographic faces of <Al> may be compared with available transmission electron microscopy (TEM) observations of the developing microstructure of Al_2O_3 films on Al substrates. Unfortunately, for most of the TEM analyses reported (e.g. Refs. [1, 18, 52]), a 2 to 3 nm thick native oxide film was already present on the Al surface before heating and subsequent oxidation. Oxidation of the *bare* {100} and {110} crystallographic faces of Al up to temperatures of 823 K and an oxygen pressure p_{O_2}= 1.33×10^{-3} Pa, was shown to lead to the formation of an amorphous {Al_2O_3} film [17], as predicted by the results shown in Fig. 6; after a long period of annealing (> 60 h) at 823 K and p_{O_2}= 1.33×10^{-3} Pa, nucleation and growth of γ-Al_2O_3 was observed [17]. The oxidation of a *bare* {111} Al substrate at 773 K and p_{O_2}= 2.67×10^{-5} Pa, was observed to occur by the direct formation and *outward* growth of γ-Al_2O_3 islands and the development of an amorphous

---

[6] The effect of pressure on enthalpy and entropy per molar volume can be estimated from (cf. Ref. [28]): $V^{-1}(\partial H / \partial p)_T = (1 - \beta T)$ and $V^{-1}(\partial S / \partial p)_T = -\beta$, where β is the coefficient of volume expansion.

oxide was not observed [16]. Indeed, the corresponding critical thickness $h^{\text{critical}}_{\{Al_2O_3\}}$ is predicted to be very small (see Fig. 6).

Knowledge on the thermodynamic stability of amorphous oxide films on their metal (or semiconductor; see footnote 1) substrates is a prerequisite for technological applications where the formation of a stable thin amorphous oxide film with uniform thickness on the substrate is desired: for example, to realize passivation of metals and semiconductors and to establish diffusion barriers in solid state devices (e.g. tunnel junctions). The absence of grain boundaries and other lattice defects in the amorphous oxide reduce ionic migration through the oxide [2, 3, 22], improve electronic properties (e.g. high dielectric strength and low leakage current) and increase corrosion resistance [2, 3, 5, 22]. Moreover, due to the relatively large free volume [20, 21] and the bond flexibility [2, 22] of the amorphous oxides, a mismatch with their substrates can be accommodated by viscous flow [2, 20-25], thereby promoting strong adhesion across the substrate/film interface [2, 3, 5, 22].

VI. Conclusions

- The energy of the interface between a crystalline metal <M> and its oxide MO_x is generally smaller for the amorphous oxide $\{MO_x\}$ than for the crystalline oxide $<MO_x>$.
- For sufficiently thin oxide films on a metal substrate <M>, the amorphous state can be preferred over the crystalline state, because the higher bulk energy of the amorphous oxide film $\{MO_x\}$, as compared to the corresponding crystalline oxide film $<MO_x>$, can be overcompensated by the relatively low sum of the $\{MO_x\}$ surface energy and <M>-$\{MO_x\}$ interfacial energy.
- Adopting a 'macroscopic atom' approach (cf. Refs. [10, 12-15]), thermodynamic parameters for a description of interfacial energies of metal / metal-oxide systems can be well assessed.
- By calculating the total energy of the metal-substrate / metal-oxide-film system, i.e. including Gibbs energies of formation, mismatch energy, interfacial and surface energies, a critical thickness of the oxide film can be calculated up to which the amorphous oxide is thermodynamically more stable than the corresponding crystalline oxide.
- The difference in thermodynamic stability of an amorphous $\{MO_x\}$ film on its metal substrate <M> (with respect to the corresponding epitaxial $<MO_x>$ film on the same

substrate) as a function of *growth temperature* is governed by (*i*) the decrease of the bulk Gibbs free energy difference between the {MO_x} and the <MO_x> film with increasing growth temperature, and (*ii*) the change of the growth mismatch between the lattices of <MO_x> and <M> at the interface with increasing growth temperature. In most cases, where a tensile growth stress occurs in the crystalline oxide film parallel to the interface and the thermal expansion coefficient of the metal substrate is larger than that of the oxide, the amorphous {MO_x} film on the <M> substrate will be more stable with respect to the corresponding epitaxial <MO_x> film at higher growth temperatures; the reverse can be true in the case of a compressive growth stress.

- The differences in the relative stability of an amorphous {MO_x} film on *different crystallographic faces* of the <M> substrate are caused by the differences in the crystalline-crystalline <M>-<MO_x> interfacial energy. Formation of a crystalline oxide is more likely for a more densely packed crystallographic face of the <M> substrate.
- The predicted stabilities for an amorphous {Al_2O_3} film on a <Al> substrate agree well with previous transmission electron microscopy observations: amorphous Al_2O_3 develops on {100} Al and {110} Al and crystalline γ-Al_2O_3 develops on {111} Al.

Acknowledgments

Financial support by the Foundation for Fundamental Research of Matter (FOM) is gratefully acknowledged. The authors are grateful to Dr. A.J. Böttger for helpful discussions on the estimation of interfacial energies.

Appendix

For a thin crystalline <γ-Al_2O_3> film formed by epitaxial growth on the {111}, {110} or {100} crystallographic faces of an <Al> substrate, the tensile strain $\varepsilon_{\|}$ at the growth temperature is (*i*) independent of the direction within the plane parallel to the <Al>-<γ-Al_2O_3> interface, (*ii*) the same for the three interfaces considered, and (*iii*) equal to the growth mismatch f [see discussion above Eq. (15) in Sec. IV.C].

Then the width and length $l_{\gamma\text{-}Al_2O_3}$ of the accordingly strained <γ-Al_2O_3> cell on the <Al> substrate [cf. Fig. 1(b) in Sec. II], are related to the width and length of the unstrained <γ-Al_2O_3> cell, $l^{\text{unstr}}_{\gamma\text{-}Al_2O_3}$, by (cf. Secs. II and III.B.2)

$$l_{\gamma\text{-Al}_2\text{O}_3} = l^{\text{unstr}}_{\gamma\text{-Al}_2\text{O}_3}(1+f) \tag{A1}$$

The corresponding amorphous $\{\text{Al}_2\text{O}_3\}$ cell (cf. Fig. 1 in Sec. II) is unstrained, as discussed below Eq. (6) in Sec. III.A (see also Ref. [25]). It then follows that the ratio χ in Eq. (4b) in Sec. II between the surface areas of the $\{\text{Al}_2\text{O}_3\}$ and $<\gamma\text{-Al}_2\text{O}_3>$ cells is related to the molar volumes $V_{\{\text{Al}_2\text{O}_3\}}$ and $V_{\gamma\text{-Al}_2\text{O}_3}$ of $\{\text{Al}_2\text{O}_3\}$ and unstrained $<\gamma\text{-Al}_2\text{O}_3>$ according to

$$\chi = \left(\frac{l_{\gamma\text{-Al}_2\text{O}_3}}{l_{\{\text{Al}_2\text{O}_3\}}}\right)^2 = \left(\frac{l^{\text{unstr}}_{\gamma\text{-Al}_2\text{O}_3}(1+f)}{l_{\{\text{Al}_2\text{O}_3\}}}\right)^2 = \left(\frac{V_{\gamma\text{-Al}_2\text{O}_3}}{V_{\{\text{Al}_2\text{O}_3\}}}\right)^{2/3}(1+f)^2 \tag{A2}$$

The thickness $h_{\gamma\text{-Al}_2\text{O}_3}$ of the strained $<\gamma\text{-Al}_2\text{O}_3>$ film is related to the thickness $h^{\text{unstr}}_{\gamma\text{-Al}_2\text{O}_3}$ of the corresponding unstrained $<\gamma\text{-Al}_2\text{O}_3>$ cell by (cf. Eq. A1)

$$h_{\gamma\text{-Al}_2\text{O}_3} = h^{\text{unstr}}_{\gamma\text{-Al}_2\text{O}_3}(1-2\nu f) \tag{A3}$$

where ν denotes the Poisson ratio of $<\gamma\text{-Al}_2\text{O}_3>$. Thus the ratio ξ of the heights of the strained $<\gamma\text{-Al}_2\text{O}_3>$ cell and the corresponding unstrained $\{\text{Al}_2\text{O}_3\}$ cell is related to the molar volumes $V_{\{\text{Al}_2\text{O}_3\}}$ and $V_{\gamma\text{-Al}_2\text{O}_3}$ of the unstrained phases by [cf. Eq. (A2)]

$$\xi = \frac{h_{\gamma\text{-Al}_2\text{O}_3}}{h_{\{\text{Al}_2\text{O}_3\}}} = \left(\frac{h^{\text{unstr}}_{\gamma\text{-Al}_2\text{O}_3}(1-2\nu f)}{h_{\{\text{Al}_2\text{O}_3\}}}\right) = \left(\frac{V_{\gamma\text{-Al}_2\text{O}_3}}{V_{\{\text{Al}_2\text{O}_3\}}}\right)^{1/3}(1-2\nu f) \tag{A4}$$

Using the data in Table I and the values of f as obtained from Eq. (15) in Sec. IV.C, it follows that χ increases from 0.960 at T_0 (= 298.15 K) to a value of 0.985 at 900 K, whereas ξ decreases from 0.949 at T_0 to 0.943 at 900 K.

References

[1] P. E. Doherty and R. S. Davis, J. Appl. Phys. **34**, 619 (1963).

[2] A. G. Reversz and F. P. Fehlner, Ox. Met. **15**, 297 (1981).

[3] F. P. Fehlner, Low-temperature oxidation: the role of vitreous oxides (Wiley-Interscience, New York, 1981).

[4] K. R. Lawless, Rep. Prog. Phys. **37**, 231 (1973).

[5] A. G. Revesz, Phys. Status Solidi **24**, 115 (1967); **19**, 193 (1967).

[6] H. M. Kennet and A. E. Lee, Surf. Sci. **48**, 633 (1975).

[7] J. V. Cathcart and G. F. Petersen, J. Electrochem. Soc. **115**, 595 (1968).

[8] T. M. Christensen, C. Raoul and J. M. Blakely, Appl. Surf. Sci. **26**, 408 (1986).

[9] G. Rovida and M. Maglietta, in *Proceedings of the 7th International Vacuum Congress and 3rd International Conference on Solid Surfaces, Vienna, 1977*, edited by R. Dobrozemsky, F. Rüdenauer, F. P. Viehböck and A. Breth (Berger & Söhne, Horn, 1977), p. 963.

[10] R. Benedictus, A. Böttger and E. J. Mittemeijer, Phys. Rev. B **54**, 9109 (1996).

[11] S. Blonski and S.H.Garofalini, Surf. Sci. **295**, 263 (1993).

[12] F. R. de Boer, R. Boom, W. C. M. Mattens, A. R. Miedema and A. K. Niessen, *Cohesion in Metals: Transition Metals Alloys* (North-Holland, Amsterdam, 1989), Chaps. 2 and 4.

[13] A. R. Miedema and P. F. De Châtel, in *Theory of Alloy Phase Formation*, edited by L. H. Bennet (AIME, New Orleans, 1980), p. 344.

[14] A. R. Miedema, J. Less-Common Met. **32**, 117 (1973).

[15] A. R. Miedema and F. J. A. den Broeder, Z. Metallkd. **70**, 14 (1979).

[16] J. I. Eldridge, R. J. Hussey, D. F. Mitchell and M. J. Graham, Oxid. Met. **30**, 301 (1988).

[17] K. Shinohara, T. Seo and H. Kyogoku, Z. Metallkd. **73**, 774 (1982).

[18] K. Thomas and M. W. Roberts, J. Appl. Phys. **32**, 70 (1961).

[19] R. K. Hart and J. K. Maurin, Surf. Sci. **20**, 285 (1970).

[20] F. Spaepen, Acta Metall. **25**, 407 (1977).

[21] S. Sundaram and R. J. Clifton, Mech. Mater. **29**, 233 (1998).

[22] A. G. Revesz and J. Kruger, in *Passivity of Metals*, edited by R. P. Frankenthal and J. Kruger (Electrochemical Society, Princeton, 1978), p.137.

[23] N. F. Mott, Philos. Mag. B **55**, 117 (1987).

[24] E. A. Irene, E. Tierney and J. Angilello, J. Electrochem. Soc. **129**, 2594 (1982).

[25] J. S. Leach and P. Neufeld, Corros. Sci. **9**, 255 (1969).

[26] J. E. McDonald and J. G. Eberhart, Trans. Metall. Soc. AIME **233**, 512 (1965).

[27] D. Chatain, I. Rivollet and N. Eustathopoulos, J. Chim. Phys. Phys.-Chim. -Biol. **83**, 561 (1986); **84**, 201 (1987).

[28] M. W. Chase, *NIST-JANAF Thermochemical Tables 4th Ed., Part I, Al*-Co (American Institute of Metals, New York, 1998), p. 156-159.

[29] T. Tokuda and H. Harada, in *Proceedings of the 2nd International Conference on the properties of liquid metals, Tokyo, 1972*, edited by S. Takeuchi (Taylor & Francis, London, 1973), p.583.

[30] O. Kubaschewski and C.B. Alcock, *Metallurgical thermochemistry* (Pergamon, Oxford, 1979), p. 477.

[31] E. Fromm, O. Mayer and W. Nickerson, Surf. Sci. **57**, 775 (1976).

[32] F. Spaepen, Acta Metall. **23**, 729 (1975).

[33] F. Spaepen and R. B. Meyer, Scr. Metall. **10**, 257 (1976).

[34] R. H. Ewing, Philos. Mag. **25**, 779 (1972).

[35] D. Turnbull, in *Impurities and Imperfections*, edited by O. T. Marzke (American Society of Metals, Cleveland, 1955), p. 121.

[36] J. N. Chirigos, in *Physical Metallurgy of stress corrosion fracture*, edited by T. H. Rhodin (Interscience, New York, 1959), p. 70.

[37] Y. Ikuhara and P. Pirouz, Micr. Res. Tech. **40**, 206 (1998).

[38] D. L. Smith, *Thin-Film Deposition: Principles and Practice* (McGraw-Hill, New York, 1995), Chap. 6.

[39] J. R. Willis, S. C. Jain and R. Bullough, Philos. Mag. A **62**, 115 (1990).

[40] J.H. van der Merwe, Surf. Sci. **31**, 198 (1972).

[41] E. A. Brandes and G. B. Brook, *Smithells Metals Reference Book 7th Ed.* (Butterworth-Heinemann, Oxford, 1992), p. 14-3.

[42] H. Yanagida and G. Yamaguchi, Bull. Chem. Soc. Jpn **37**, 1229 (1964).

[43] Powder Diffraction file, 04-0787 from International Center for Diffraction Data (ICDD).

[44] Powder Diffraction file, 29-0063 from International Center for Diffraction Data (ICDD).

[45] W. J. Bernard and J. W. Cook, J. Electrochem. Soc. **106**, 643 (1959).

[46] M. R. Gallas and G. J. Piermarini, J. Am. Ceram. Soc. **77**, 2917 (1994).

[47] X. G. Wang, W. Weiss, Sh. K. Shaikhutdinov, M. Ritter, M. Petersen, F. Wagner, R. Schlögl and M. Scheffler, Phys. Rev. Lett. **81**, 1038 (1998).

[48] J. M. McHale, A. Aroux, A .J. Perrotta and A. Navrotsky, Science **277**, 788 (1997).

[49] F. Réti, I. Bertóti and G. Mink, Solid State Ionics **44**, 33 (1990).

[50] Y. S. Anisimov, E. F. Grits and B. S. Mitin, Izv. Akad. Nauk SSSR, Neorg. Mater. **13**, 1444 (1977) [Inorg Mater. (Transl. of Neorg. Mater.) **13**, 1168 (1977)].

[51] D. M. Duffy, J. H. Harding and A. M. Stoneham, Acta Mater. **44**, 3293 (1996).

[52] K. Shimizu, A. Gotoh, K. Kobayashi, G. E. Thompson and G. C. Wood, in *Microscopy of Oxidation*, edited by M. J. Bennet and G. W. Lorimer (Institute of Metals, London, 1991), p. 144.

Chapter 3

Determination of Total Primary Zero Loss Intensities in Measured Electron Emission Spectra of Bare and Oxidised Metals

Application to Aluminium-Oxide Films on Aluminium Substrates

L.P.H. Jeurgens,[1] W.G. Sloof,[1] C.G. Borsboom,[2] F.D. Tichelaar,[1]
and E.J. Mittemeijer[1,2]

[1] *Delft University of Technology, Laboratory of Materials Science, Rotterdamseweg 137, 2628 AL Delft, The Netherlands*

[2] *Max Planck Institute for Metals Research, Seestrasse 92, 70174 Stuttgart, Germany*

Abstract

A method is presented to determine the *total* metallic primary zero loss (PZL) intensity and the total oxidic PZL intensity, for each core-electron level in measured electron emission spectra of bare and oxidised free electron like metals (and semiconductors like Si and Ge), from the resolved PZL intensity of *only* the corresponding metallic main peak and the corresponding oxidic main peak, respectively. The contribution of the intrinsic plasmon structure, associated with a core level metallic main peak, to the corresponding total *metallic* PZL intensity is taken into account using the intrinsic bulk (BP) and surface (SP) plasmon excitation probabilities for the concerned core level electron emission process in the metal. The total *oxidic* PZL intensity, as given fully by the intensity of the oxidic main peak, is obtained from the measured spectrum of the oxidised metal after subtraction of a reconstructed metallic main peak. Additionally, as demonstrated for the Al 2*p* photoemission process in the Al metal, values for the intrinsic BP and SP excitation probabilities concerned can be determined separately from the intensities of the metallic and oxidic main peaks as obtained from a series of measured photoelectron spectra recorded from the bare metal substrate and the metal substrate covered with a thin oxide overlayer of which the thickness is varied.

I. Introduction

In X-ray Photoelectron (XPS), Ultraviolet Photoelectron (UPS) and Auger Electron (AES) Spectroscopy the *primary* (or *intrinsic*) electron emission spectrum corresponding to each core-electron level represents the photo- and Auger-electrons immediately after their generation due to the absorption of incoming photons or electrons. However, part of the generated electrons will experience inelastic scattering events during their passage through the solid and escape through the surface. Consequently, these *extrinsically* scattered electrons will be detected at lower kinetic energies and therefore contribute to the background in the spectrum recorded. The total background of inelastically scattered electrons is usually designated as the *secondary* electron spectrum. All recorded electrons that have been emitted from the k^{th} core-electron level and left unaffected until recorded (i.e. all recorded unscattered or elastically scattered photoelectrons) constitute the total primary *zero loss* spectrum of the k^{th} core-electron level.

For the quantitative analysis of measured electron spectra as obtained by XPS, AES and UPS, it is necessary to determine the *total* primary zero loss (PZL) intensity of each core-electron level separately. Although it is known that in some cases up to 50% of the total intensity of the plasmon structure at the higher binding energy (BE) side of the core level main peak in a electron emission spectrum of a free-electron like metal (see Fig. 1) can be *intrinsic* in origin (i.e. part of the total primary zero loss electron spectrum; for extrinsic origin of the plasmon structure, see below; cf. Refs. [1,2]), it is often neglected in practice. Also, usually only a small part of the characteristic *intrinsic* tail of the asymmetrically shaped metallic main peak, which extends some 20 eV towards the higher BE side (i.e. lower kinetic energy side) of the main peak (see Figs. 1 and 2), is taken into account, leading to an even larger underestimation of the total metallic PZL intensity. Obviously, this leads to large errors when, for example, calculating thicknesses of thin oxide films on metal substrates from the PZL intensity ratios of only the oxidic and metallic main peaks in the measured core electron spectra of the oxidised metal involved [3].

Intrinsic bulk plasmon (BP) and surface plasmon (SP) excitations are a direct result of the coupling of the localised core hole created in the photo- (or Auger-) electron emission process with the 'gas' of free electrons in the solid (i.e. conduction electrons in metals) [1, 2, 4-9]. The energy of the N electron system, immediately before photoelectron emission, is equal to the energy of the $(N - 1)$ electron system plus the kinetic energy of the emitted photoelectron after its ejection from the k^{th} core level. If because of the mentioned coupling one or more plasmons are created simultaneously with the emission of a core-electron, the

(N - 1) electron system left behind is not at its 'relaxed' ground state, and it follows that an intrinsic plasmon fine-structure occurs at the higher BE side of the metallic (ground state) main peak [1, 2, 4-9]. The sudden creation of a localised core-hole in the photoemission process may also trigger a chaotic rearrangement of electrons in the conduction band of the metal, resulting in the generation of many low energy conduction electron-hole pairs (i.e. charge density fluctuations) [10, 11]. This process gives rise to the tailing off of the metallic (ground state) main peak (as well as of the associated intrinsic plasmon peaks) towards higher BE values in measured core electron emission spectra of metals (cf. Figs. 1 and 2 and Refs. [10, 11]). For the core-level photoemission process in free-electron like metals (e.g. Al and Mg), as well as in semiconductors like Si and Ge, plasmon and conduction electron-hole pair excitations are by far the dominant intrinsic energy loss processes [1, 2, 4-9].

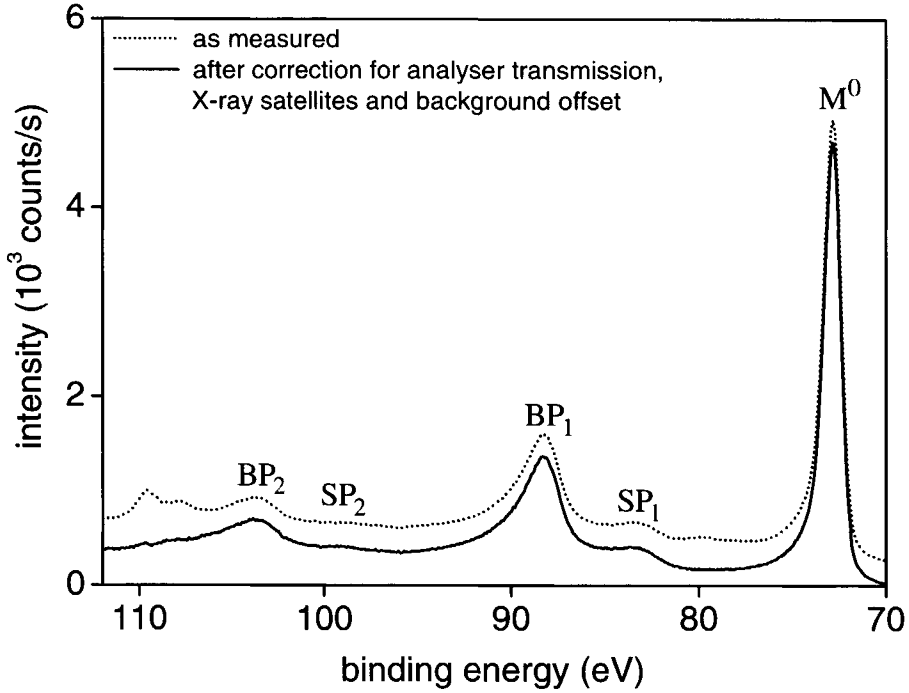

Figure 1. As measured Al 2p XPS spectrum as recorded from a bare Al substrate (*dotted line*). The corresponding spectrum after correction for the analyser transmission function, X-ray satellites and constant background offset (see Sec. III) is also shown (*solid line*). The positions of the first and second surface (SP_1 and SP_2) and bulk plasmon (BP_1 and BP_2) peaks associated with the Al 2p metallic main peak (M_0) have been indicated.

Extrinsic energy loss processes are the result of inelastic scattering events of the generated photoelectrons during their passage through the solid and escape through the surface. For free-electron like metals and semiconductors like Si and Ge, the dominating extrinsic energy loss processes are extrinsic BP and SP excitations, which arise as a result of the coupling of the electric field of a moving photoelectron with that of the free electrons in the solid [4-9].

For the core level photoemission process in free-electron like metals, the intrinsic (i.e. core-hole induced) and extrinsic (i.e. photoelectron induced) plasmon excitations (either BP or SP) each produce a series of photoelectron peaks centred at energies $E_0 - \hbar\omega_p$, $E_0 - 2\hbar\omega_p$, $E_0 - 3\hbar\omega_p$, etc., at the higher BE side of the asymmetric core level (ground state) metallic main peak with maximum at E_0 (cf. Fig. 1). Here $\hbar\omega_p$ denotes the plasmon energy, which value is about the same for the intrinsic and extrinsic plasmon excitations (e.g. for Al metal, both the intrinsic and extrinsic BP and SP energies are equal to $\hbar\omega_p$ = 15.7 ± 0.1 eV and $\hbar\omega_p$ = 11.0 ± 0.2 eV, respectively [12]). Then, since the intrinsic part of the resulting plasmon structure constitutes a part of the total (i.e. intrinsic plus extrinsic) plasmon intensity, it is very difficult to resolve the contribution of the intrinsic plasmon structure to the total metallic PZL intensity in a measured core level XPS spectrum of the metal.

In this contribution a novel approach is presented to retrieve the correct *total* metallic and oxidic PZL intensities from measured core-level electron emission spectra of bare and oxidised free-electron like metals from the resolved PZL intensities of *only* the metallic and oxidic main peaks. The total *oxidic* PZL intensity, as given fully by the intensity of the oxidic main peak, is obtained from the measured spectrum of the oxidised metal after subtraction of a reconstructed metallic main peak. The total metallic PZL intensity (i.e. the intensity of the metallic main peak *plus* the associated intrinsic plasmon structure) is determined from the intensity of *only* the metallic main peak using the corresponding probabilities for intrinsic bulk (BP) and surface (SP) plasmon excitations upon core-level photoemission in the metal. As shown for the Al 2*p* photoemission process in the Al metal, values for these probabilities can be determined straightforwardly from the intensities of the metallic and oxidic main peaks as obtained for a series of measured XPS spectra recorded from the clean metal substrate (i.e. before oxidation) and from the metal substrate after several, different oxidations (implying measurements of XPS spectra from the metal substrate covered with a thin oxide overlayer of which the thickness is varied). Comparison is made with previously obtained values for the intrinsic plasmon excitation probabilities pertaining to the Al 2*p* photoemission process in the Al metal.

II. Experimental

Disc shaped specimens (diameter 10 mm and thickness 1 mm) of recrystallised (at 773 K) aluminium (> 99.999 wt%) containing several large grains of 1 to 3 mm diameter were used. Prior to introducing the specimen into an UHV processing chamber, the surface was prepared by successively grinding, lapping and polishing. The polishing was performed on soft cloths, first with paste of 6 μm diamond grains and then with 1 μm diamond grains. Thereafter, polishing was carried out using a chemical resistant cloth with a suspension of 0.05 μm γ-Al_2O_3 grains. After each step in the above treatment of the specimen surface, the specimen was thoroughly cleaned ultrasonically in isopropanol and dried by blowing with pure compressed nitrogen gas. Finally the surface of the specimen was chemically polished for 1.5 minutes in a solution composed of 70 ml H_3PO_4, 25 ml H_2SO_4 and 5 ml HNO_3 heated to 85°C. This procedure resulted in very smooth surfaces as observed using light optical microscopy applying interference contrast.

In the UHV processing chamber (base pressure < 2.5×10^{-8} Pa) coupled to the instrument for XPS analysis (base pressure < 1×10^{-8} Pa), first the 2-3 nm thick native oxide film was removed by sputtering with a focussed 4 keV Ar^+ beam (200 nA; angle of incidence of 40° with respect to the sample surface normal) scanning the specimen surface area. Next, the sample and sample holder were outgassed by a three days treatment of 3 cycles of annealing at 773 K during about 4 hours and subsequent cleaning by sputtering with a focussed 1 keV Ar^+ beam (20 nA) scanning the specimen surface area at room temperature. Finally, prior to the oxidation treatment and XPS measurements (see below), the specimen was annealed at 773 K during 20 min. After this treatment the sample was fully cleaned and its crystal order restored.

As indicated by LEED analysis of single-crystalline Al substrates after cyclic treatments of Ar^+ sputtering and subsequent annealing at 700 K to 800 K, the crystallinity of the Al surfaces is fully restored after each cycle [13, 14], as confirmed in the present work by High Resolution Transmission Electron Microscopy (HREM) analysis of the metal substrate / oxide film cross sections (see Chapter 5 of this thesis). For the sputtered clean, annealed Al surfaces, no surface contamination of C, O and Ar was detected by XPS measurement at the energy ranges of the C 1*s*, O 1*s* and Ar 2*p* photoelectron lines, employing a detection angle of 30° with the sample surface. The XPS measurements were performed such that a detection limit of about 0.01 monolayer coverage was reached (for instrumental details see below).

Oxide layers were grown in the UHV processing chamber as function of total oxygen exposure time by heating the clean Al substrate to 305, 573, 673, or 773 K and subsequent exposure to pure oxygen gas (99.998 vol. %) at a partial oxygen pressure p_{O_2} of 1.33×10^{-4} or 1.33×10^{-5} Pa (for further details on the oxidation it is referred to Chapter 5 of this thesis). Total exposure times varied from 100 to 1000 s for the oxidation experiments performed at $p_{O_2} = 1.33\times10^{-4}$ Pa and from 500 to 10000 s for $p_{O_2} = 1.33\times10^{-5}$ Pa. Before each oxidation experiment, the oxidised Al surface was cleaned and its crystallinity restored by a similar treatment of sputtering and subsequent annealing described above (i.e. removal of previous grown oxide film by sputtering with 4 keV Ar^+ beam, annealing at 773 K during 30 min, sputtering with 1 keV Ar^+ beam and annealing at 773 K during 20 min).

For each oxidation series (executed as a function of oxidation time at a given temperature and oxygen pressure), the XPS analysis of the metal substrate before and after oxidation was performed on the same single-crystal grain (with the elliptic XPS analysis area of 1.1 x 1.6 mm falling entirely within the area of the grain). The crystal grain was selected with a light optical microscope (magnification 5-20X) attached to the instrument for XPS analysis and aligned with respect to both the optical axes of the electron analyser input lens and the beam of the ion-gun.

XPS spectra of the Al 2*s*, Al 2*p*, O 1*s* and C 1*s* photoelectron lines were recorded before and after oxidation with a PHI 5400 ESCA instrument set at constant analyser pass energy of 35.75 eV and with a step size of 0.1 eV, using unmonochromatised incident Mg X-ray radiation (Mg $K\alpha_{1,2}$ = 1253.6 eV). The electrons emitted from the specimen were detected at an angle of 45° with respect to the specimen surface.

III. Data evaluation

The Al 2*p* PZL intensities of the asymmetrically shaped metallic main peak (i.e. including the tail towards higher BE values, but excluding the intrinsic plasmon intensity) and the symmetrically shaped oxidic main peak were determined from the measured Al 2*p* XPS spectra of both the clean and the oxidised Al substrate as follows.

First, the spectral intensities were corrected for the electron kinetic energy dependent transmission of the spherical capacitor analyser of the spectrometer by multiplying each spectral intensity with its corresponding kinetic energy [16]. Next, X-ray satellites present in the measured spectra as a consequence of the nonmonochromatic nature of the incident X-ray source (see Sec. II) were removed using the relative heights and displacements with respect to the height and position of the $K\alpha_{1,2}$ line, characteristic for a Mg X-ray anode [17] (cf. Fig. 1).[1]

For the case of the clean metal (i.e. the specimen before oxidation), the background of inelastically scattered photoelectrons associated with the metallic main peak must be subtracted from the measured Al 2*p* photoelectron spectrum. This background can be calculated using Tougaard's formalism [18] if the differential cross section for inelastic electron scattering is known for the system under investigation. However, detailed knowledge of this cross section usually does not exist because it is especially difficult to incorporate the effect of the extrinsic surface plasmon (SP) loss processes (cf. Sec. I and Ref. [18]). Subtraction of the inelastic background can therefore only be performed satisfactorily from the lower BE side of the metallic main peak up to the first SP peak, which is located at approximately 10.3 eV towards the higher BE side of the metallic Al 2*p* main peak positioned at a BE of 72.8 eV (see Fig. 1). Therefore, in the evaluation of the PZL intensity of the metallic and oxidic Al 2*p* main peaks, only the part of the measured Al 2*p* spectrum from the lower BE side of the metallic main peak (i.e. 70 eV) up to the first plasmon feature (i.e. up to 80 eV) was considered (see Figs. 1 and 2).

Then, for the case of the *clean Al metal*, the intensity of the Al 2*p* PZL *metallic* main peak (i.e. including the tail towards higher BE values, but excluding the intrinsic plasmon PZL intensity) was determined from the measured Al 2*p* XPS spectrum of the clean metal in the BE range from 70 to 80 eV (after correcting for the analyser transmission function and X-ray satellites; see above) by (see Fig. 2):

(*i*) Setting the lower BE side of the metallic main peak to zero (background) intensity by subtraction of a constant background, as taken equal to the minimum intensity at the lower BE side of the metallic main peak (i.e. the measured intensity at 70 eV).

(*ii*) Subtraction of an inelastic background from the thus obtained spectrum over the BE range from 70 eV to 80 eV. This background was calculated using Tougaard's formalism [18] for the case of a homogeneous, infinitely thick (as compared to the inelastic mean free path (IMFP) of the concerned photoelectrons) bare metal substrate, while adopting the universal cross section for inelastic-electron scattering (i.e. 'universal' Tougaard background; cf. Ref. [19]).

---

[1] Note that in order to remove all X-ray satellites in the BE range of the Al 2*p* main peak between 70 and 80eV (see Figs. 1 and 2) the total BE range up to about 125 eV (thus including the Al 2*s* metallic main peak positioned at a BE of 118 eV) had to be considered.

(*iii*) Integration of the resulting (background corrected) intensity over this BE range (i.e. 70 – 80 eV), and adding to this integrated PZL intensity, the integrated PZL intensity of the excluded tail of the metallic main peak in the region of the plasmon structure from 80 eV towards higher BE values (see Fig. 2). This tail is estimated by linear least squares (LLS) fitting of the obtained PZL metallic main peak in the BE range from 70 to 80 eV (see Fig. 2) with the Doniach-Sunjic line-shape function [10] according to the procedure described in Ref. [11],[2] and subsequently extrapolating the fitted function over the BE range from 80 eV to 100 eV.

Next, for the case of the *oxidised Al metal*, the shape and position of the Al 2*p* *metallic* main peak over the BE range from 70 to 80 eV, as obtained from the spectrum recorded from the clean metal (see above), were used to separate the Al 2*p* metallic main peak, due to the Al metal substrate, from the measured Al 2*p* spectrum of the oxidised Al metal, as follows (see Fig. 3). An Al 2*p* PZL metallic main peak plus its associated 'universal' Tougaard background (see above) was constructed in the BE region from 70 to 80 eV, for the case of the metal substrate covered with a thin (as compared to the IMFP of the concerned photoelectrons), homogeneous oxide film of uniform thickness (cf. Refs. [18, 19]). This calculation was performed repeatedly for variable oxide-film thickness, while LLS fitting the lower BE side of this synthetic PZL metallic main peak (i.e. in the BE range from 70 to 72.9 eV) plus its associated background to the lower BE side of the Al 2*p* metallic main peak in the spectrum of the oxidised metal (corrected for the analyser transmission function, X-ray satellites and background offset; see above and Fig. 3). To account for possible small energy shifts of the metallic main peak in the measured spectrum of the oxidised metal with respect to the BE position of the metallic main peak as observed from the clean metal (e.g. as a result of charging of the thin oxide film during XPS analysis), the BE range of the spectrum of the oxidised metal was allowed to shift up to 0.05 eV towards lower BE values during the fitting.

Then, the intensity of the Al 2*p* *metallic* main peak in the spectrum of the *oxidised Al metal* was obtained by (see Fig. 3):

---

[2] Due to the spin-orbit splitting of the Al 2*p* core level, the (background corrected) Al 2*p* metallic main peak is fitted with two identically shaped Doniach-Sunjic lineshapes (for the Al $2p_{3/2}$ and Al $2p_{1/2}$ core electron levels) with a constrained peak intensity ratio of 2:1, but with the position of each peak of the doublet as fit parameter [11].

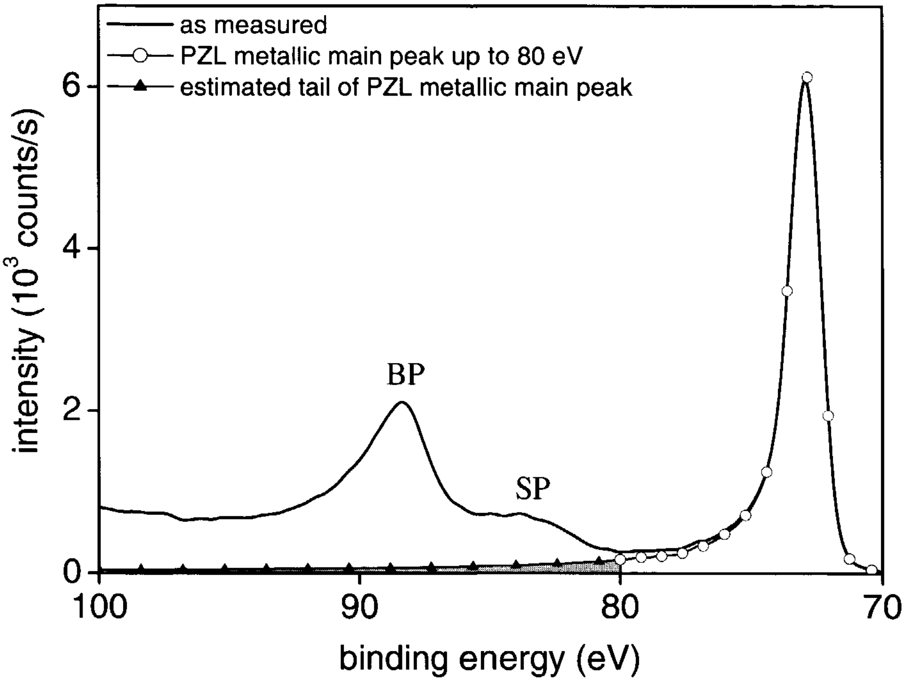

Figure 2. Reconstruction of the primary zero loss (PZL) Al 2*p* metallic main peak from a measured Al 2*p* XPS spectrum of the clean aluminium metal. The 'as measured' spectrum as shown had already been corrected for the analyser transmission function, X-ray satellites and background offset. The first surface (SP) and bulk plasmon (BP) peaks, associated with the Al 2*p* metallic main peak, have been indicated. The metallic main peak in the binding energy range from 70 to 80 eV has been obtained by subtraction of the calculated 'universal' Tougaard background of inelastically scattered (i.e. extrinsic) photoelectrons over this BE region. The part of the tail of the metallic main peak in the BE range of the first SP and BP peaks from 80 eV up to 100 eV, as estimated by extrapolating the fitted Doniach-Sunjic lineshape function in the BE region from 70 to 80 eV towards higher BE values, is indicated by the grey area.

(*i*) Integration of the, background corrected, intensity of the optimised metallic main peak over the BE range from 70 to 80 eV.

(*ii*) Adding to this metallic PZL intensity, the intensity of the excluded tail towards higher BE values as described above for the metallic main peak in the spectrum of the clean metal (cf. Fig. 2).[3]

---

[3] Because the shape of the, background corrected, Al 2*p* metallic main peak in the spectrum of the oxidised metal is identical to that of the, background corrected, Al 2*p* metallic main peak in the spectrum of the clean metal, it follows that the relative contribution of the excluded part of the tail (from 80 eV towards higher BE values) to the PZL intensity of the Al 2*p* metallic main peak is the same in both XPS spectra.

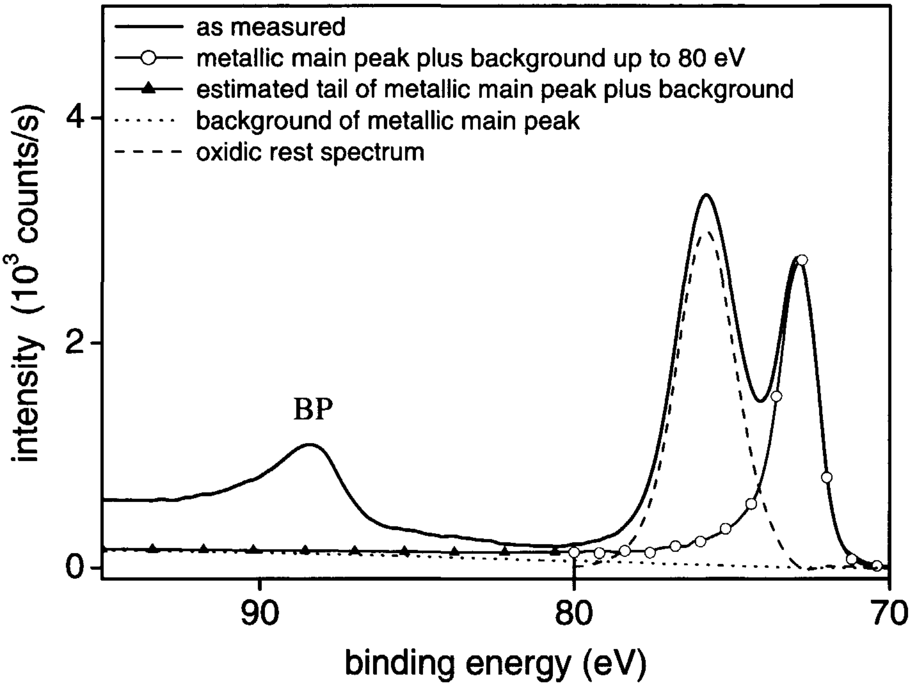

Figure 3. Reconstruction of the primary zero loss (PZL) Al 2*p* metallic main peak plus its associated inelastic background and the oxidic rest spectrum in the BE region from 70 to 80 eV from a measured Al 2*p* XPS spectrum of the aluminium substrate pertaining to Fig. 2 after oxidation for 400 s at a temperature of 673 K and an oxygen pressure of 1.33×10^{-4} Pa. The 'as measured' spectrum as shown had already been corrected for the analyser transmission function, X-ray satellites and background offset (see Sec. III). The optimised metallic main peak plus its associated inelastic background (excluding extrinsic bulk plasmon (BP) losses; see Secs. I, III and IV), as well as the oxidic rest spectrum, have been plotted separately. The estimated part of the tail of the metallic main peak in the BE range of the first SP and BP peaks from 80 eV towards high BE values is also shown.

The intensity of the Al 2*p* *oxidic* main peak in the spectrum of the *oxidised Al metal* was obtained by (see Fig. 3):

(*i*) Subtraction of the fitted metallic main peak plus its associated background from the spectrum of the oxidised metal.

(*ii*) Subtraction of an 'universal' Tougaard background (calculated for the case of a homogeneous oxide film of a thickness as obtained in the above described fitting of the metallic main peak) from the thus remaining oxidic rest spectrum.

(*iii*) Integration of the resulting, background corrected, oxidic intensity over the BE range from 70 to 80 eV.

In all cases studied, the symmetrically shaped (there is no tail towards higher BE values; cf. Sec. I) PZL oxidic main peak resided entirely within the binding energy range from 70 to 80 eV. Note that: (*a*) the contribution of any intrinsic fine-structure associated with the oxidic main peak to the total oxidic PZL intensity can be neglected (see Sec. IV), and (*b*) besides the tail of the metallic main peak, all other intrinsic loss features associated with the Al 2*p* metallic main peak (i.e. the intrinsic BP and SP peaks) lie outside the binding energy from 70 eV to 80 eV within which the oxidic and metallic main peaks were resolved (cf. Sec. I and Figs. 2 and 3).

IV. Results and discussion

Consider the k^{th} core level photoemission process in a homogeneous metal with plasmon and conduction electron-hole pair excitations as the dominant intrinsic (i.e. core-hole induced) energy loss processes (see Sec. I). In the resulting photoelectron spectrum as observed from the bare metal substrate, the intrinsic BP excitation probability α, pertaining to the k^{th} core level photoemission process in the metal, is defined as the (PZL) intensity of the intrinsic BP structure relative to the (PZL) intensity J_{m}^{∞} of the corresponding k^{th} core level metallic *main* peak (including the PZL intensity of the tail towards higher BE values; cf. Sec. I and Fig. 2). Analogously, the intrinsic SP excitation probability β is defined as the (PZL) intensity of the intrinsic SP structure relative to J_{m}^{∞}. Thus, in the observed photoelectron spectrum as recorded from the *bare* metal substrate (i.e. before oxidation), the *total* metallic PZL intensity I_{m}^{∞} pertaining to the k^{th} core-level photoemission process in the metal is given by

$$I_{\text{m}}^{\infty} = J_{m}^{\infty}(1 + \alpha + \beta) \qquad \textbf{(1)}$$

For the *oxidised* metal substrate, the 'free' electrons in the conduction band of the metal atoms in the substrate adjacent to the metal/oxide interface will become localised as a result of the chemical bonding to oxygen from the oxide (cf. Refs. [20, 21]). The resulting decrease in 'free' (i.e. delocalised) electron density in the metal substrate adjacent to the metal / oxide interface leads to a strong decrease in the probability for intrinsic (as well as extrinsic) SP excitations [9, 22, 23]. For example, in measured Al 2*p* or Al 2*s* XPS and UPS spectra of the clean Al metal, the sharp SP structure associated with the metallic main peak has virtually disappeared after one monolayer oxygen coverage [23, 24], and then any contribution of the intrinsic SP structure to the total metallic PZL intensity can be neglected (i.e. $\beta \approx 0$). Since the value of the intrinsic BP excitation probability α is unaffected by the presence of the oxide overlayer (cf. Ref. [23]), it follows that for this case of oxidised metal the *total* metallic PZL intensity I_m pertaining to the k^{th} core-level photoemission process in the metal substrate, as observed in a measured photoelectron spectrum of the *oxidised* metal, is described by

$$I_m = J_m(1+\alpha) \qquad (2)$$

with J_m as the PZL photoelectron intensity of the corresponding k^{th} core level metallic main peak.

For the oxidised metal any plasmon loss structure associated with the k^{th} core level *oxidic* main peak can only be the result of the coupling of the core hole (i.e. intrinsic) or photoelectron (i.e. extrinsic) created in the k^{th} core level photoemission process of a metal ion in the oxide film, with *delocalised* (i.e. 'free') electrons in the valence band of the oxide (cf. Ref. [22]). In semiconductors or insulators with a wide bandgap, like Al_2O_3 and SiO_2 with a bandgap of respectively 7.5 and 9.0 eV (cf. Ref. [9]), most valence electrons in the oxide will be localised on the oxygen ions due to the relative high electronegativity of oxygen (cf. Refs. [9, 20, 21]).[4] Thus, the 'free' electron density in the valence band of the oxide is very small, as compared to the pure metal. Consequently, for these oxides the core level oxidic main peak is associated with an only very weak plasmon loss structure [9, 22]. Moreover, in measured photoelectron spectra of Al_2O_3 and SiO_2 no other intrinsic loss features associated with the oxidic core level main peak (e.g. as a result of band-to-band transitions) occur (cf. Refs. [9, 22]). It then follows that in measured XPS spectra of the oxidised aluminium metal, the *total* oxidic PZL intensity I_o, pertaining to the k^{th} core-level photoemission process of a Al ion in the oxide film, as observed in a measured photoelectron spectrum of the oxidised Al metal, is described fully by *only* the PZL intensity J_o of the k^{th} oxidic main peak: i.e. $I_o = J_o$.

Now, in order to determine the intrinsic BP and SP excitation probabilities α and β, pertaining to the Al 2*p* core level photoemission process in the Al metal, the (PZL) intensity ratio of the Al 2*p* oxidic and metallic main peaks, as resolved from the measured XPS spectra of the oxidised Al metal (see Sec. III), and the (PZL) intensity ratio of the metallic main peaks from the clean metal and from the oxidised metal are utilised as follows.

In a measured core level XPS spectrum of a metal substrate covered with a thin uniform oxide film of thickness *d* (of the order of the inelastic mean free path (IMFP) of the photoelectrons analysed), the ratio of the total oxidic (o) to metallic (m) PZL intensities is given by (cf. Ref. [16])

---

[4] For example, the (fully occupied) valence band in the Al_2O_3 is primarily composed of the O 2*s* and O 2*p* states, whereas the (empty) conduction band is mainly Al-like (cf. Refs. [20, 21]).

$$\frac{I_o}{I_m} = \frac{C_o \lambda_o}{C_m \lambda_m}\left[\exp\left(\frac{d}{\lambda_o \sin\theta}\right) - 1\right] \tag{3}$$

where I_m and I_o are the total metallic and oxidic PZL photoelectron intensities of the spectral components, respectively; C_m and C_o represent the volume densities of the metal atoms in the metal and in the oxide; λ_m and λ_o denote the IMFPs of the emitted photoelectrons with kinetic energy E propagating through the metal and the oxide, respectively; and θ is the detection angle with respect to the sample surface (here: $\theta = 45°$; see Sec. II). In the derivation of Eq. (3) the photo-ionisation cross section $\sigma_{m,k}$ for ejecting a photoelectron from the k^{th} core level of the metal atom in the substrate and the metal ion in the oxide have been taken equal, as is justified by measured and calculated data [25, 26].

Provided the measured XPS spectra of the clean and the oxidised metal substrate have been recorded under identical conditions, the ratio of the total PZL intensity recorded from the clean metal (I_m^{∞}) and that recorded from the oxidised metal (I_m), is given by (cf. Ref. [16])

$$\frac{I_m^{\infty}}{I_m} = \exp\left(\frac{d}{\lambda_o \sin\theta}\right) \tag{4}$$

where I_m and I_m^{∞} are defined by Eqs. (1) and (2), respectively.

The effect of elastic scattering of the photoelectrons propagating through the solid (cf. Ref. [16]) has been neglected in the derivation of Eqs. (3) and (4), but the depth dependence of the IMFP of the photoelectrons due to changes in composition (as experienced proceeding from the pure metal to the oxide) has been accounted for [27]. From Eqs. (1-4) it follows:

$$\frac{J_m^{\infty}}{J_m} = \frac{1}{(1+\alpha+\beta)} \cdot \left[1+\alpha+\frac{J_o}{J_m}\left\{\frac{C_m \lambda_m}{C_o \lambda_o}\right\}\right] \tag{5}$$

Hence, a linear relation is predicted between the main peak intensity ratios J_m^{∞} / J_m and J_o / J_m . Indeed, using all the PZL intensities of the Al 2*p* oxidic and metallic main peaks as resolved from the measured XPS spectra of the clean and the oxidised Al metal (Sec. III) in this study (Sec. II), such a linear relation is observed: see Fig. 4.

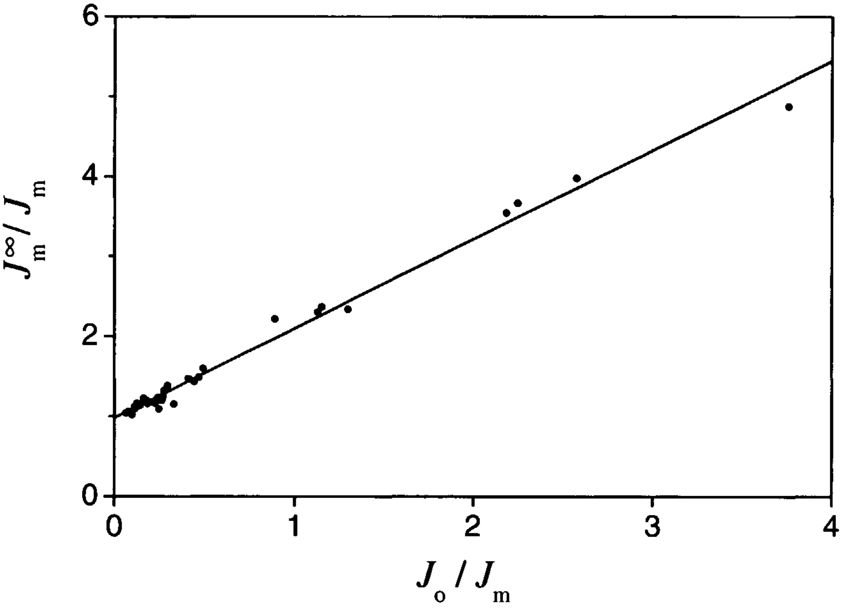

Figure 4. Al 2*p* main peak (PZL) intensity ratio, J_o/J_m, versus Al 2*p* main peak (PZL) intensity ratio J^∞_m / J_m as resolved from the measured XPS spectra of the clean and oxidised Al substrate. Oxidation experiments were executed on differently oriented single-crystal Al substrates, oxidised for various times at different constant temperatures and partial pressures of oxygen (see Sec. II).

If the tangent of the straight line fitted through all data points in Fig. 4 is designated with *m*, and its intercept with the ordinate with *a*, then it follows from Eq. (5), that the intrinsic BP excitation probability, α, and the intrinsic SP excitation probability, β, are obtained according to

$$\alpha = \frac{a}{m}\cdot\left\{\frac{C_m\lambda_m}{C_o\lambda_o}\right\}-1 \quad \text{and} \quad \beta = \frac{(1-a)}{m}\cdot\left\{\frac{C_m\lambda_m}{C_o\lambda_o}\right\} \tag{6}$$

Values used for the IMFPs λ_m and λ_o were calculated from the so-called TPP-2M algorithm given in Ref. [28]: λ_m = 2.23 nm and λ_o = 2.40 nm. The HREM investigation, performed in this work, of several of the thin (< 4 nm) aluminium-oxide films showed the presence of an amorphous oxide film of uniform thickness (containing some local nuclei of crystalline γ-Al_2O_3 only for the oxide films grown at 773 K) [15]. The theoretical density C_o of Al in γ-Al_2O_3 is 71.85 mole/dm^3 [29]. This value of the volume density is taken as the best approximation for the volume density of Al in the amorphous aluminium oxide as well. The volume density of Al in the metal, C_m, corresponds with 100.14 mole/dm^3 [30].

Then, using the above data and Eq. (6), it follows from the straight line fitted through the data shown in Fig. 4 for the intrinsic Al 2*p* BP and SP plasmon excitation probabilities, pertaining to the Al 2*p* photoemission process in the Al substrate using incident Mg $K\alpha_{1,2}$ radiation[5]: $\alpha = 0.14 \pm 0.01$ and $\beta = 0.022 \pm 0.001$, respectively.[6]

To our knowledge, values for the SP excitation probability β in metals have not been presented before. Values for the so called 'intrinsic bulk plasmon creation rate', *b*, upon Al 2*p* and Al 2*s* core level photoemission in the Al metal were determined in Refs. [1, 31] from measured Al 2*p* and Al 2*s* XPS spectra of the bare Al metal. Neglecting intrinsic SP excitations as done in Refs. [1, 31], then this 'intrinsic BP creation rate' is related to the BP excitation probability α as follows. With reference to Eq. (1) the relative contribution of the n^{th} intrinsic bulk plasmon peak to the total metallic PZL intensity can be written as J_n / J_m^∞. Thus:

$$\alpha = \sum_{n=1}^{\infty} J_n / J_m^\infty \tag{7a}$$

According to Refs. [1, 31]: $J_n / J_m^\infty = b^n / n!$, where *b* is the so-called 'intrinsic plasmon creation rate'. Thus

$$\alpha = \sum_{n=1}^{\infty} b^n / n! \tag{7b}$$

Using Al $K\alpha_{1,2}$ radiation, values of $b = 0.10 \pm 0.01$ and $b = 0.11 \pm 0.01$ were reported in respectively Refs. [1] and [31] for the 'intrinsic bulk plasmon creation rate' upon Al 2*p* and Al 2*s* photoemission in the Al metal. From Eq. (7b) it follows that these values correspond to intrinsic BP excitation probabilities (for Al $K\alpha_{1,2}$ radiation) of $\alpha = 0.11 \pm 0.01$ and $\alpha = 0.12 \pm 0.01$, respectively. These values of α for Al $K\alpha_{1,2}$ radiation are somewhat lower than the experimental finding presented above for Mg $K\alpha_{1,2}$ radiation ($\alpha = 0.14 \pm 0.01$), whereas the reverse was expected (see footnote 5). This may be caused by uncertainties introduced by different data evaluation methods (e.g. background subtraction and fitting). On the basis of knowledge of the intrinsic plasmon excitation probabilities, correct values can be obtained for thicknesses and compositions of, for example, oxide films on metal substrates [3].

---

[5] Note that the probabilities for intrinsic plasmon and conduction electron-hole pair excitations upon core-level photoemission depend on the energy of the incident photon source, i.e. they increase with increasing photon energy (i.e. with increasing kinetic energy of the emitted photoelectron) (cf. Ref. [4]).

[6] The values of ± 0.01 and ± 0.001 denote only the statistical errors in the determination of α and β, respectively, pertaining to the data plotted in Fig. 3. Here, it is noted that reliable values of α and β can only be obtained if an oxidation series with a sufficiently wide range of oxide-film thicknesses of, say, from 0 up to about 4 nm is used (cf. Fig. 4 and Eqs. (3) and (4)).

V. Conclusions

- For the correct quantitative analysis of the core level electron emission spectra of metals (or semiconductors) with bulk and surface plasmons as the dominating intrinsic energy loss features, as in the evaluation of e.g. thicknesses of thin oxide films on metal substrates, the *total* metallic primary zero loss (PZL) intensity (i.e. the intensity of the metallic main peak *plus* its associated intrinsic plasmon structure) has to be used.
- For the determination of this total metallic PZL intensity, it suffices to determine the intensity of *only* the core level metallic main peak concerned, provided that the corresponding intrinsic bulk and surface plasmon excitation probabilities are known.
- For semiconductors and insulators with a wide bandgap (e.g. Al_2O_3 and SiO_2) these probabilities can be determined separately from the intensities of the metallic and oxidic main peaks as resolved from a series of measured core level electron emission spectra of the bare metal substrate and the metal substrate covered with a thin oxide overlayer of which the thickness is varied.
- For the first time the intrinsic bulk and surface plasmon excitation probabilities have been separately determined experimentally for the Al *2p* photoelectron emission in the aluminium metal (applying Mg $K\alpha_{1,2}$ X-ray radiation): $\alpha = 0.14 \pm 0.01$ and $\beta = 0.022 \pm 0.001$, respectively.

Acknowledgements

Financial support by the Foundation for Fundamental Research of Matter (FOM) is gratefully acknowledged. The authors are indebted to dr. P.C. Graat for providing computer programs on the calculation of the 'universal' Tougaard backgrounds.

References

[1] P. Steiner, H. Höchst and S. Hüfner, Z. Phys. B **30** (1978), 12; Phys. Lett. **61A** (1977), 410.

[2] D.R. Penn, Phys. Rev. Lett. **38** (1977), 1429.

[3] L.P.H. Jeurgens, W.G. Sloof, F.D. Tichelaar, C.G. Borsboom and E.J. Mittemeijer, Appl. Surf. Sci. **144-145** (1999), 11.

[4] J.W. Gadzuk, J. Electr. Spectr. Rel. Phenom. **11** (1977), 355.

[5] J.W. Gadzuk and M. Sunjic, Phys. Rev. B **12** (1975), 524.

[6] J.J. Chang and D.C. Langreth, Phys. Rev. B **8** (1973), 4638; **5** (1972), 3512.

[7] D.C. Langreth, Phys. Rev. Lett. **26** (1971), 1229.

[8] D. Šokcevic and M. Šunjic, Phys. Rev. B **30** (1984), 6965.

[9] T.L. Barr, Modern ESCA: The Principles and Practice of X-ray Photoelectron spectroscopy, (CRC Press, Boca Raton, 1990), chap. 6.

[10] S. Doniach and M. Sunjic, J. Phys. C **3** (1970), 285.

[11] P.H. Citrin, G.K. Wertheim, Y. Baer, Phys. Rev. B **16** (1977), 4256.

[12] R.J. Baird, C.S. Fadley, S.M. Goldberg, P.J. Feibelman and M. Šunjic, Surf. Sci. **72** (1978), 495.

[13] H. Brune, J. Wintterlin, J. Trost and G. Ertl, J. Wiechers, R.J. Behm, J. Chem. Phys. **99** (1993), 2128.

[14] F. Jona, J. Phys. Chem. Solids **28** (1967), 2155.

[15] L.P.H. Jeurgens, W.G. Sloof, F.D. Tichelaar, and E.J. Mittemeijer, to be published.

[16] S. Hofmann, in: Practical Surface Analysis, Vol. 1, 2nd edn., Eds. D. Briggs and M.P. Seah (Wiley, Chichester, 1990), p. 143; M.P. Seah, p. 201.

[17] J.F. Moulder, W.F. Stickle, P.E. Sobol and K.D. Bomben, Handbook of X-ray photoelectron spectroscopy, Ed. J. Chastian (Perkin-Elmer, Physical Electronics Division, Eden Pairie, USA, 1992), p. 18.

[18] S. Tougaard, Surf. Interf. Anal. **11** (1988), 453.

[19] S. Tougaard, Solid State Commun. **61** (1987), 547.

[20] S. Ciraci, I.P. Batra, Phys Rev. B **28** (1983), 982.

[21] S. Ciraci, I.P. Batra, Phys. Rev. Let. **38** (1977), 774.

[22] T.L. Barr, B. Kramer, S.I. Shah, M. Ray, J.E. Greene, Mat. Res. Soc. Symp. Proc. **47** (1985), 205.

[23] A.M. Bradshaw, W.Domcke, L.S. Cederbaum, Phys. Rev. B **16** (1977), 1480.

[24] S.A. Flodstrom, R.Z. Bachrach, R.S. Bauer and S.B.M. Hagström, Phys. Rev. Lett. **37**, 1282 (1976).

[25] C.D. Wagner, L.E. Davis, M.V. Zeller, J.A. Taylor, R.H. Raymond and L.H. Gale, Surf. Interf. Anal. **3** (1981), 211.

[26] J.H. Scofield, J. Electr. Spectr. Rel. Phenom. **8** (1976), 129.

[27] P.C.J. Graat, M.A.J. Somers and A. Böttger, Surf. Interf. Anal. **23** (1995), 44.

[28] S. Tanuma, C.J. Powell & D.R. Penn, Surf. Int. Anal. **17** (1991), 911 and 927.

[29] Powder Diffraction file, 29-63 from International Center for Diffraction Data (ICDD).

[30] *Handbook of Chem. & Physics*, 56th edition (1975-76), edited by R.C. Weast (CRC Press, 1974), p. B-67.

[31] T. Greber, J. Osterwalder, S. Hüfner and L.Schlapbach, Phys. Rev. B **44** (1991), 8958.

Chapter 4

Determination of Thickness and Composition of Aluminium-Oxide Films on Aluminium Substrates

L.P.H. Jeurgens,[1] W.G. Sloof,[1] F.D. Tichelaar,[1] C.G. Borsboom[1]
and E.J. Mittemeijer[1,2]

[1] *Delft University of Technology, Laboratory of Materials Science, Rotterdamseweg 137, 2628 AL Delft, The Netherlands*

[2] *Max Planck Institute for Metals Research, Seestrasse 92, 70174 Stuttgart, Germany*

Abstract

A novel method is presented to determine the thickness and the composition of oxide films on metal substrates using the measured XPS spectra of the clean and the oxidised metal. The method is applied to aluminium-oxide films on aluminium substrates. The oxide-film thickness is derived from the primary zero-loss intensities of only the metallic and oxidic Al 2*p* *main* peaks, utilising the known value of the intrinsic bulk plasmon excitation probability for the Al 2*p* core-level photoelectron emission process. It is shown that this new method for layer-thickness determination gives results that can differ 20% from results obtained by the less correct methods used in common practice. The actual composition, expressed as the O/Al atomic ratio, of the oxide film is determined from the *total* primary zero-loss intensities of the O 1*s* peak and the Al 2*p* peak of Al 2*p* oxidic rest spectrum. This spectrum of the oxide is obtained after subtraction of a reconstructed metallic Al 2*p* peak from the measured XPS spectrum.

I. Introduction

For the quantitative determination of thickness and composition of thin oxide overlayers on metal substrates using X-ray Photoelectron Spectroscopy (XPS), as for example in studies of the initial stages of oxide-film growth on metal substrates, it is necessary to determine the *total* primary zero-loss photoelectron intensity of each core-electron level separately. The total primary zero-loss spectrum of the k^{th} core-level comprises all photon-excited electrons emitted from the k^{th} core-level that have been left unaffected until recorded (i.e. all unscattered or elastically scattered photoelectrons).

In practice, for quantitative XPS analysis of thin (< 5 nm) overlayers on free-electron like metal substrates, the total metallic primary zero-loss spectrum in a measured core-level XPS spectrum is usually assumed to consist of *only* the, asymmetrically shaped, metallic main peak. Thereby, the existence of an associated intrinsic plasmon fine structure at the lower kinetic energy side of the metallic main peak is ignored (see Fig. 1 and e.g. Refs. [1-4]), which can lead to significant errors: for core-level XPS spectra of the Al metal, the intrinsic plasmon fine-structure associated with the metallic main peak amounts to approximately 15% of the total metallic primary zero-loss intensity [1, 4]. Ignorance of this contribution in determinations of e.g. oxide-film thicknesses from the intensity ratios of the oxidic and metallic main peaks in the measured XPS spectra of the oxidised Al metal, results in an overestimation of the thickness values of about 8%.[1] Moreover, in practice the characteristic tail of the asymmetrically shaped metallic main peak, which extends some 30 eV towards the lower kinetic energy side of the metallic main peak (see Fig. 1), is usually cut off at some arbitrary position before the first surface plasmon in the measured XPS spectrum, by which approximately 10% of the total metallic primary zero-loss intensity is ignored. Hence, in total the aluminium oxide-film thickness is easily overestimated with about 14%.[1]

In this contribution a novel, accurate method is presented for the determination of oxide-film thickness and composition from measured XPS spectra of the oxidised metal. To this end, the primary zero-loss intensities of the oxidic and metallic main peaks were resolved and the contribution of the intrinsic plasmon fine-structure to the total metallic primary zero-loss intensity was accounted for utilising the probability of intrinsic bulk plasmon excitation upon core-level photoelectron emission in the Al metal, as determined previously by the present authors [4].

---

[1] Estimated for film thicknesses of the order of the inelastic mean free path, see below Eq.(1).

II. XPS spectra evaluation

Oxidation experiments were executed on a pure Al substrate having its (431) crystallographic plane parallel to the specimen surface (deviation ± 2°) (for details see Ref. [4]). XPS spectra of the Al 2*p* and O 1*s* photoelectron lines were recorded before and after oxidation with a PHI 5400 ESCA set at constant analyser pass energy of 35.75 eV with a step size of 0.1 eV, using unmonochromatised incident Mg X-ray radiation. The angle of photoelectron detection with respect to the specimen-surface normal was 45°.

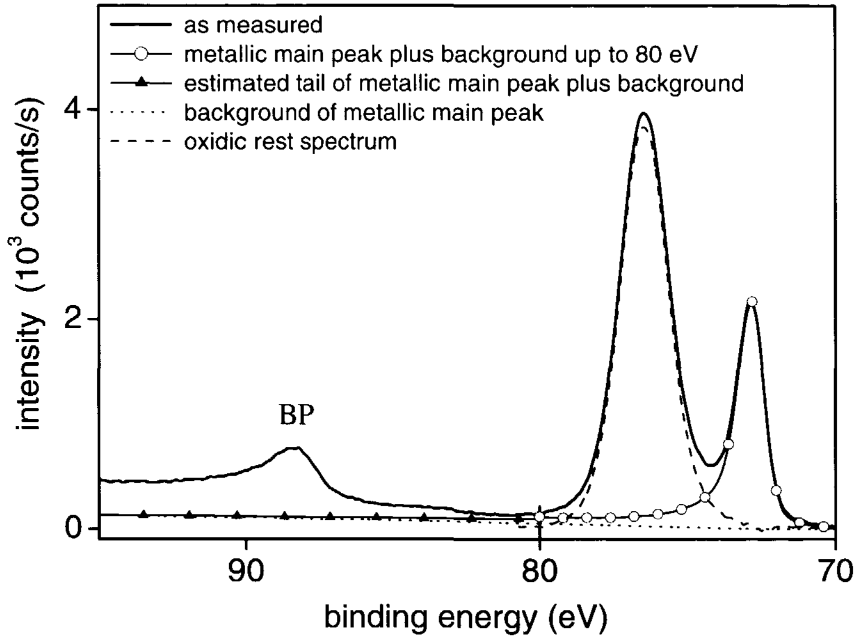

Figure 1. Reconstruction of the primary zero loss (PZL) Al 2*p* metallic main peak plus its associated inelastic background and the oxidic rest spectrum from a measured Al 2*p* XPS spectrum of an (110) aluminium substrate after oxidation for 1×10^4 s at a temperature of 673 K and an oxygen pressure of 1.33×10^{-5} Pa. The 'as measured' spectrum as shown had already been corrected for the analyser transmission function, X-ray satellites and background offset (see Sec. II). The optimised metallic main peak plus its associated inelastic background (excluding extrinsic bulk plasmon (BP) losses; see Sec. II and Ref. [4]), as well as the oxidic rest spectrum, have been plotted separately. The estimated part of the tail of the metallic main peak in the BE range of the first SP and BP peaks from 80 eV towards high BE values is also shown.

The main steps involved in determining the primary zero-loss intensities of the Al 2*p* metallic and oxidic main peaks in the measured XPS spectra of the clean and oxidised Al metal are as follows (see Ref. [4] for details).

For the case of the *clean metal*, the intensity of the Al 2*p* metallic main peak was determined from the measured Al 2*p* XPS spectrum of the sputtered clean Al substrate (after correction for the electron kinetic energy dependent transmission of the analyser and the presence of X-ray satellites [4]) by: (*i*) subtraction of an inelastic background from the measured XPS spectrum over the binding energy range from 70 eV to 80 eV, using Tougaard's formalism and adopting the universal cross section for inelastic-electron scattering [5] (i.e. 'universal' Tougaard background), (*ii*) integration of the resulting, background corrected, intensity over this binding energy range, and (*iii*) adding to this intensity, the integrated intensity of the excluded tail of the metallic main peak by fitting the background corrected part of the metallic main peak with a Doniach-Sunjic line-shape function [6].

Next, for the case of the *oxidised specimens*, the shape and the position of the previously obtained clean metal main peak over the binding energy range from 70 to 80 eV were used to remove the metallic main peak, due to the substrate, from the measured Al 2*p* spectrum of the oxidised specimen, as follows. A metallic main peak plus its associated 'universal' Tougaard background was constructed for the case of a homogeneous metal substrate covered with a homogeneous oxide-film of uniform thickness *d*. This calculation was performed repeatedly for variable *d*, while least-squares fitting the lower binding energy side of this synthetic metallic main peak plus its associated background to the lower binding energy side of the peak envelop in the measured spectrum of the oxidised metal (see Fig. 1).

The thus obtained metallic main peak plus its associated background, was subtracted from the spectrum of the oxidised metal. From the remaining oxidic rest spectrum (see Fig. 1), the integrated intensity of the oxidic main peak was obtained after subtracting its associated 'universal' Tougaard background calculated adopting an oxide film of thickness *d*, as determined in the above mentioned fitting of the metallic main peak in the spectrum of the oxidised metal. The integrated intensity of the O 1*s* main peak was determined analogously from the measured spectrum of the oxidised metal.

In all cases studied, the oxidic Al 2*p* main peak resided entirely within the binding energy range from 70 to 80 eV. Note that all plasmon peaks associated with the metallic main peak lie outside this binding energy range (see Fig. 1).

III. Determination of thickness and composition; results and discussion

The *thickness* of a uniform oxide-film on an oxidised metal substrate can be calculated from the relative photoelectron intensity of the oxidic or the metallic component with respect to that of the corresponding oxide or clean metal, respectively. Then, two XPS spectra are required which have to be recorded separately employing identical conditions. The composition and the structure of the oxide or metal reference must be identical to that of the oxide film or the metal substrate, of the specimen to be investigated, respectively.

The above prerequisites can be circumvented by determining the oxide-film thickness from the ratio of the total primary zero-loss photoelectron intensities of the oxidic (o) and metallic (m) components, I_o and I_m respectively, evaluated from a single XPS measurement of the oxidised metal. For oxide-film thicknesses of the order of the inelastic mean free path (IMFP) of the photoelectrons analysed, the oxide-film thickness, d, is related to the ratio of the oxidic to metallic total primary zero-loss intensities, by (cf. Ref. [7] and footnote 2)

$$d = \lambda_o \sin\theta \ln\left[\frac{C_m \lambda_m}{C_o \lambda_o} \cdot \frac{I_o}{I_m} + 1\right] \tag{1}$$

where C_m and C_o represent the volume densities of metal atoms in the metal and oxide; λ_m and λ_o denote the IMFP's of the analysed photoelectrons propagating through the metal and oxide, respectively. For the aluminium-oxide film on an aluminium substrate considered here, C_m and C_o are taken as 100.14 and 71.85 mole/dm^3 [4], and λ_m and λ_o are taken as 2.23 and 2.40 nm [8]. These values for the IMFP's pertain to the Al $2p$ photoelectrons emitted using Mg $K\alpha_{1,2}$ radiation (see also Sec. III of Chapter 5 of this thesis).

The total metallic primary zero-loss intensity, i.e. the intensity of the metallic main peak plus its associated intrinsic plasmon structure, is given by $I_m = J_m(1+\alpha+\beta)$ with J_m as the primary zero-loss intensity of the core-level metallic main peak, as resolved from the measured XPS spectrum of the oxidised metal (see Sec. II), and, α and β as the intrinsic bulk

---

[2] In the derivation of Eq. (1) the photoionization cross section for ejecting a core electron from the Al $2p$ energy level of the Al atom in the pure metal and the Al ion in the oxide are taken the same and the effect of elastic scattering of electrons propagating through the solid (cf. Ref. [7]) has been neglected. For a derivation of Eq. (1) it is referred to Appendices A and B of Chapter 5 of this thesis.

(BP) and surface (SP) plasmon excitation probabilities, respectively, relative to the primary zero-loss intensity of the associated metallic main peak [4].

For the oxidised aluminium substrate, the electrons in the conduction band of the Al atoms in the substrate adjacent to the metal/oxide interface will become localised as a result of chemical bonding to oxygen and therefore their contribution to the intrinsic plasmon excitation process becomes very small. Thus, in measured XPS spectra of the oxidised Al metal, the intrinsic SP intensity associated with the metallic Al main peak can be neglected (i.e. $\beta \approx 0$).

The intrinsic BP excitation probability for a free-electron metal (as Al) can be determined straightforwardly from a series of measured XPS spectra of the clean and the oxidised metal, as described in Ref. [4]. The thus obtained value of the intrinsic BP excitation probability, α, for the Al 2*p* photoelectron emission process in the aluminium metal using a Mg $K\alpha_{1,2}$ radiation is 0.14 ± 0.01 [4].

Because there are practically no free electrons in the aluminium-oxide layer (insulator), any intrinsic BP and SP intensity associated with the oxidic main peak can be neglected (cf. Ref. [4]). Then, the total primary zero-loss intensity of the oxidic component, I_o, is given fully by the primary zero-loss intensity of the oxidic main peak, J_o.

Hence, it can be concluded that the oxide-film *thickness* can be calculated from the primary zero-loss intensities of only the metallic and oxidic (Al 2*p*) *main* peaks, provided these main peaks can be resolved from measured XPS spectra of the oxidised metal, and the corresponding intrinsic BP excitation probability of the metal is known.

The *composition*, expressed as the oxygen to aluminium atomic ratio (O/Al-ratio), of the oxide films can be determined from the total primary zero-loss intensity ratio of the O 1*s* and the oxidic Al 2*p* components (as given fully by the main peaks; see above), as obtained from a single XPS measurement of the oxidised aluminium. As a reference to determine the composition of the oxide-film from this intensity ratio, the corresponding intensity ratio of sapphire (α-Al_2O_3) was used with an O/Al-ratio of $\frac{3}{2}$ (see also Eq. (A4a) in Appendix A of Chapter 5 of this thesis).

An example of the above discussed determination from XPS spectra of both the changes in thickness and composition of an oxide film[3] on aluminium are shown in Fig. 2 (*solid lines*) as a function of oxidation time. Further, the analogous results as obtained by application of a commonly used procedure, i.e. Shirley-background subtraction of the Al 2*p* and O 1*s* XPS spectra of the oxidised metal and standard curve-fitting of the Al 2*p* region between the binding energy range from 70 to 80 eV (in order to resolve the oxidic and metallic component), are given for comparison (see *dashed lines* in Fig. 2).[4]

---

[3] According to TEM analysis performed in this study, the oxide-layers were amorphous and of uniform thickness.

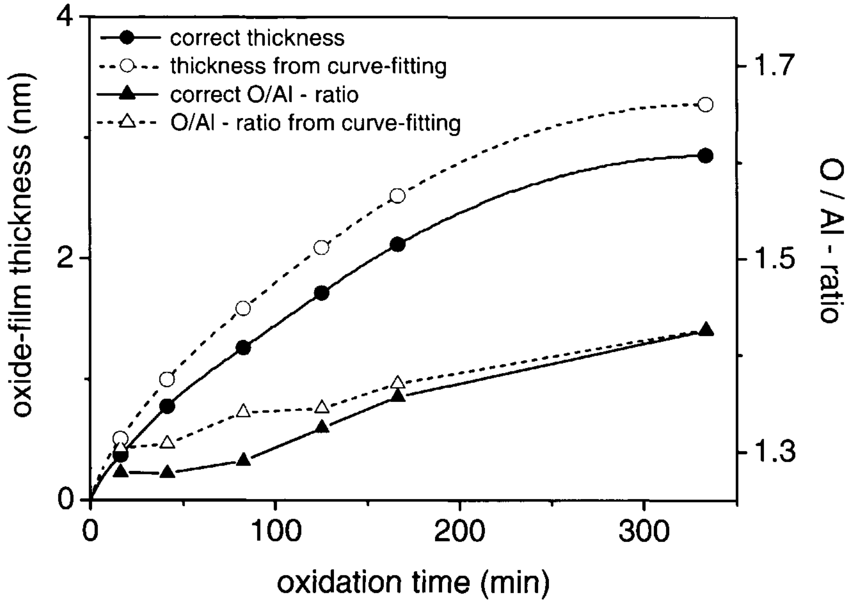

Figure 2. Changes in thickness and composition as a function of oxidation time, for the case of an Al(431) substrate oxidised at 673 K and $p_{O_2}=1.33\times10^{-5}$ Pa. The results as obtained from standard curve-fitting of the Al 2*p* XPS spectra of the oxidised metal after a Shirley-background subtraction are given for comparison. See text for details.

Clearly, applying only Shirley-background subtraction and standard curve fitting of the Al 2*p* spectra, results in an overestimation of the oxide-film thickness of about 20%. Hence, in addition to the errors introduced by the ignorance of the tail and the intrinsic BP structure associated with the metallic main peak (i.e. 14%, cf. Section 1), an error of 6% arises due to an erroneous determination of the metallic main peak intensity by Shirley-background subtraction and standard curve-fitting. This additional error of 6% is due to overestimation of the contribution of photoelectrons originating from the substrate to the inelastic background caused by Shirley-background subtraction, leading to underestimation of the metallic main peak intensity.

---

[4] Here, the measured XPS spectra of the oxidised metal were also first corrected for the analyser transmission function and the presence of X-ray satellites.

The O/Al-ratio of the grown oxide film as determined from the oxidic Al 2*p* and O 1*s* main peaks by standard curve-fitting and Shirley-background subtraction is somewhat higher (especially for short oxidation times) than the corresponding values inherent to the in principle more correct method of XPS spectra evaluation presented in this paper. Since both main peaks (i.e. the oxidic Al 2*p* and O 1*s* main peak) are constituted only of photoelectrons originating from the thin oxide overlayer (i.e. from relative shallow depths below the surface), their contribution to the inelastic background is small, and thus the determination of the corresponding integrated intensities is insensitive to the method of background subtraction employed. The lower O/Al-ratio of the grown oxide film as determined by standard curve-fitting and Shirley-background subtraction is therefore mainly the result of the above discussed overestimation of the oxide-film thickness, as required for the calculation of the oxide-film composition (see also Eq. (A4a) in Appendix A of Chapter 5 of this thesis).

Acknowledgements

Financial support by the Foundation for Fundamental Research of Matter (FOM) is gratefully acknowledged. The authors are indebted to dr. P.C. Graat for providing computer programs on the calculation of the 'universal' Tougaard backgrounds.

References

[1] P. Steiner, H. Höchst and S. Hüfner, Z. Phys. B **30** (1978), 129.

[2] J.W. Gadzuk, J. Electr. Spectr. Rel. Phenom. **11** (1977), 355.

[3] D.C. Langreth, Phys. Rev. Lett. **26** (1971), 1229; J.J. Chang and D.C. Langreth, Phys. Rev. B **8** (1973), 4638.

[4] L.P.H. Jeurgens, W.G. Sloof, F.D. Tichelaar, C.G. Borsboom and E.J. Mittemeijer, Appl. Surf. Sci. **161** (2000), 139.

[5] S. Tougaard, Surf. Interf. Anal. **11** (1988), 453; Solid State Commun. **61** (1987), 547.

[6] S. Doniach and M. Sunjic, J. Phys. C **3** (1970), 285.

[7] S. Hofman, in: *Practical Surface Analysis*, Vol. 1, 2nd edn., Eds. D. Briggs and M.P. Seah (Wiley, Chichester, 1990), p. 143; M.P. Seah, p. 201.

[8] S. Tanuma, C.J. Powell and D.R. Penn, Surf. Int. Anal. **17** (1991), 911 & 927.

Chapter 5

Growth Kinetics, Microstructure and Composition of Aluminium-Oxide Films Formed by Thermal Oxidation of Aluminium

L.P.H. Jeurgens,[1] W.G. Sloof,[1] F.D. Tichelaar,[1] and E.J. Mittemeijer[1,2]

[1] *Delft University of Technology, Laboratory of Materials Science, Rotterdamseweg 137, 2628 AL Delft, The Netherlands*

[2] *Max Planck Institute for Metals Research, Seestrasse 92, 70174 Stuttgart, Germany*

Abstract

The growth kinetics, morphology, chemical composition and microstructure of thin aluminium-oxide films grown by the dry, thermal oxidation of a bare Al(431) substrate at a partial oxygen pressure of 1.33×10^{-4} Pa in the temperature range of 373 - 773 K were studied using X-ray photoelectron spectroscopy (XPS) and high resolution electron microscopy (HREM). The initial oxidation of the bare Al substrate proceeds by an *island-by-layer* growth mechanism, involving the lateral diffusion over the bare Al substrate surface of mobile oxygen species. At low temperatures ($T \leq 573$ K) an amorphous oxide film develops that attains a limiting thickness. It was shown that the oxygen content of these films is constant, whereas the Al content increases with temperature and time. XPS analysis established the occurrence of a relatively Al-enriched oxide at the very surface. At high temperatures ($T > 573$ K) growth is *not* impeded at a limiting thickness. At these temperatures the oxide film gradually attains the stoichiometric composition of Al_2O_3 and becomes crystalline γ-Al_2O_3. Kinetic analysis established the occurrences of two different oxide-film growth regimes: an initial regime of very *fast* oxide-film growth and a second, much *slower* oxidation stage that is observed only at $T > 573$ K. These results could be discussed in terms of electric-field controlled, interstitial, outward transport of Al cations through a close packing of O anions in the amorphous films, and inward diffusion of O along grain boundaries in the crystalline films, respectively. During the second, slow oxidation stage at high temperatures, the oxide film attains the stoichiometric composition of Al_2O_3 and becomes crystalline γ-Al_2O_3.

I. Introduction

The growth of an oxide film on a bare metal surface by oxidation is a complex process usually obstructing description in terms of a single rate-determining mechanism. The initial and subsequent stages of oxide-film growth subsequently involve the absorption and dissociation of oxygen on the bare metal surface, and nucleation and growth of an (eventually 'closed') oxide film covering the metal surface, in association with transport of cations and/or anions, as well as electrons, through the developing oxide film (cf. Refs. [1-4]). Further, the nature of the atomic arrangement in the developing oxide film can be variable. For metals such as Fe, Co, Ni, Cu, Zn, Mo and W oxidation proceeds by the direct formation and growth of a crystalline oxide (cf. Refs. [1, 4]), whereas on e.g. Al, Si, Cr, Ge, Nb and Ta initially an amorphous oxide film is formed and, which depending on oxidation temperature, time and thickness, subsequently transforms into a crystalline oxide (cf. Refs. [1, 4-8]).

The processes that occur and the changes that take place at the metal surface, in the developing oxide film, and at the metal/oxide and oxide/gas interfaces during the initial and subsequent stages of oxide-film growth are still poorly understood (cf. Refs. [9-12]). Even for a classical metal/oxide system such as Al/Al_2O_3, as considered in this study, comprehensive and fundamental knowledge of the relationships between the mechanism(s) that govern the oxide-film growth and the resulting chemical composition, morphology and (micro)structure of the developing oxide film lacks (cf. Refs. [9-12]). For example, until very recently it was not known that up to a certain critical oxide-film thickness and even for high oxidation temperatures, an amorphous aluminium-oxide film can be *thermodynamically rather than kinetically*, more stable than the corresponding crystalline γ-Al_2O_3 film [5].

Thin aluminium-oxide films have a great importance for applications in microelectronics and catalysis, and for protection against wear and corrosion. For example, thin aluminium-oxide films are used in various types of microelectronic devices as a dielectric, diffusion and/or tunnelling barrier (cf. Refs. [13-17]), because of their specific physical and chemical properties (i.e. large dielectric constant (~ 10), large barrier height for electron tunnelling (~ 2 eV), high corrosion resistance, good thermal and mechanical stability, good adhesion). For such applications, the thickness, morphology, chemical composition, and the (micro)structure of the oxide film are of great importance (cf. Refs. [10, 11, 13, 15, 16, 18]).

The present study focuses on the relations between the oxide-film growth kinetics and the evolution of the chemical composition, the morphology and the (micro)structure of the developing oxide-film as a function of the oxidation temperature, for the dry, thermal oxidation of a bare, single-crystalline Al substrate. To explain the various relations as determined in this study, models were adopted for the mechanisms that govern the oxide-film growth during the different stages of oxidation at different temperatures.

Bare Al(431) substrates were exposed to oxygen at a partial oxygen pressure of 1.33×10^{-4} Pa in the temperature range from 373 to 773 K. In-situ X-ray photoelectron spectroscopy (XPS) was applied to determine the oxide-film thickness, chemical composition and morphology, as well as the changes in chemical and binding state of the concerned ions in the grown oxide films. The development of the microstructure and morphology of the oxide film as a function of oxidation temperature, as well as the crystallographic orientation relation between the observed crystalline oxide phases and the parent Al metal substrate, were determined using high resolution transmission electron microscopy (HREM).

II. Experimental

II.A. Sample preparation

Disc shaped specimens (diameter 10 mm and thickness 1 mm) of recrystallised (at 773 K) aluminium (> 99.999 wt%) containing several large grains of 1 to 3 mm diameter were used. Prior to introducing the specimen into an UHV processing chamber, the surface was prepared by successively grinding, lapping and polishing. The polishing was performed on soft cloths, first with paste of 6 μm diamond grains and then with 1 μm diamond grains. Thereafter, polishing was carried out using a chemical resistant cloth with a suspension of 0.05 μm γ-Al_2O_3 grains. After each step in the above treatment of the specimen surface, the specimen was thoroughly cleaned ultrasonically in isopropanol and dried by blowing with pure compressed nitrogen gas. Next, the surface of the specimen was chemically polished for 1.5 minutes in a solution composed of 70 ml H_3PO_4, 25 ml H_2SO_4 and 5 ml HNO_3 heated to 85°C, after which the sample was annealed at atmospheric pressure for one hour at 773 K in a flow of pure Ar gas in a quartz tube furnace. Finally, the surface of the specimen was again chemically polished as described above. This procedure resulted in very smooth surfaces as observed using light optical microscopy applying interference contrast.

In the UHV processing chamber (base pressure $< 2.5\times10^{-8}$ Pa) coupled to the instrument for XPS analysis (base pressure $< 1\times10^{-8}$ Pa), first the 2-3 nm thick native oxide film was removed by sputtering with a focused 4 keV Ar^+ beam (200 nA; angle of incidence of 40° with respect to the sample surface normal) scanning the specimen surface area. Next, the sample and sample holder were outgassed by a three days treatment of 3 cycles of annealing at 773 K during about 4 hours and subsequent cleaning by sputtering with a focused 1 keV Ar^+ beam (20 nA) scanning the specimen surface area at room temperature. Finally, prior to the oxidation treatment and XPS measurements (see below), the specimen was annealed at 773 K during 20 min (as indicated in Fig. 1a). After this treatment the sample was fully cleaned and its crystal order restored.

As indicated by LEED analysis of single-crystalline Al substrates after cyclic treatments of Ar^+ sputtering and subsequent annealing at 700 K to 800 K, the crystallinity of the Al surfaces is fully restored after each cycle [9, 19, 20], as confirmed in the present work by High Resolution Transmission Electron Microscopy (HREM) analysis of the metal-substrate / oxide-film cross-sections (see Sec. IV.A). For the sputtered clean, annealed Al surfaces, no surface contamination of C, O and Ar was detected by XPS measurement at the energy ranges of the C 1*s*, O 1*s* and Ar 2*p* photoelectron lines, employing a detection angle of 30° with the sample surface. The XPS measurements were performed such that a detection limit of about 0.01 monolayer coverage was reached (for instrumental details see Sec. II.B).

II.B. Thermal oxidation and XPS analysis

Oxide layers were grown in the UHV processing chamber as function of total oxygen exposure time (t) by heating the clean Al substrate to temperatures (T) of 373, 473, 573, 673, or 773 K and subsequent exposure to pure oxygen gas (99.998 vol. %) at a partial oxygen pressure (p_{O_2}) of 1.33×10^{-4} Pa. Total exposure times varied from 100 to 15000 s. Before each oxidation experiment, the oxidised Al surface was cleaned and its crystallinity restored by the treatment of sputtering and subsequent annealing as described in Sec. II.A.

The partial oxygen pressure was kept constant during oxidation (i.e. independent of changes of the total system pressure e.g. due to outgassing) by a feed back of the measured oxygen signal, as monitored by a Balzers QMS 112 quadrupole mass spectrometer (QMS), to the setpoint of the oxygen valve control unit (Balzers, RVG 050B). The value of the setpoint for $p_{O_2} = 1.33\times10^{-4}$ Pa was obtained from the determined linear relationship between the measured QMS oxygen signal (in Volts) and the total oxygen pressure as measured with a Bayerd-Alpert nude pressure gauge (operation range: 1.33×10^{-1} to 2.67×10^{-9} Pa). Heating of the specimen was performed by focussing the light emitted by a halogen light bulb on the backside of the specimen using an elliptical mirror. The temperature of the sample was measured with a type K (NiAl / NiCr) thermocouple, which was spot welded to the backside of the sample. The behaviour of the system pressure during annealing and subsequent oxidation, as well as the heating and cooling for a typical oxidation run, are shown in Fig. 1. For each oxidation experiment, the total oxygen exposure time was determined from the integrated area below the curve of the partial oxygen pressure versus the oxidation time (see Fig. 1c).

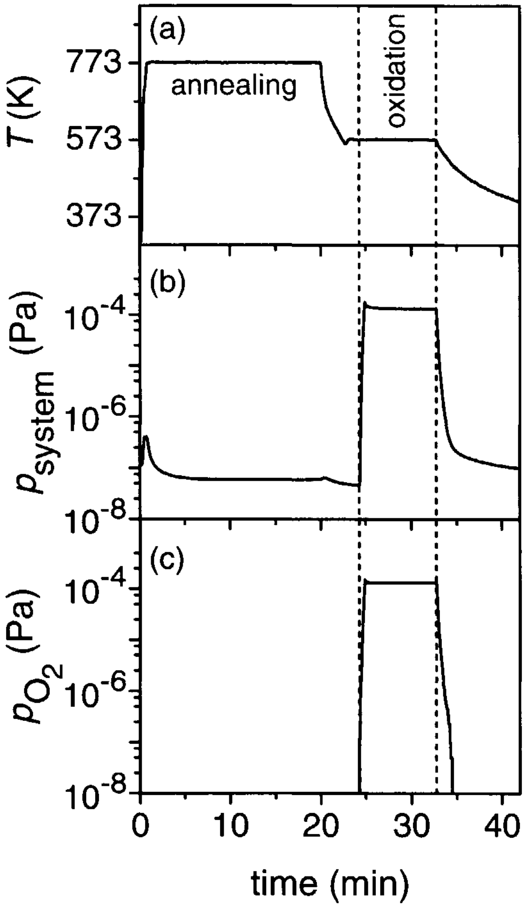

Figure 1. Recorded (**a**) metal-substrate temperature T, (**b**) total system pressure p_{system} , and (**c**) partial oxygen pressure p_{O_2} for an oxidation experiment involving 20 min of annealing at 773 K and subsequent oxidation for 500 s at a temperature of 573 K and $p_{O_2} = 1.33\times10^{-4}$ Pa.

Except for the preparation of the HREM metal-substrate / oxide-film cross-sections (see Sec. II.C), all oxidation experiments executed to study the oxide-film growth kinetics and the evolution of the oxide-film composition using XPS (see Sec. II.B) were executed on the same specimen. Moreover, for each oxidation series (executed as a function of oxidation time at a given temperature and oxygen pressure), the XPS analysis of the metal substrate before and after oxidation was performed on the same crystal grain (with the elliptic XPS analysis area of 1.1 x 1.6 mm falling entirely within the area of the grain). The crystal grain was selected with a light optical microscope (magnification 5-20X) attached to the instrument for XPS analysis and aligned with respect to both the optical axes of the electron analyser input lens and the beam of the ion-gun. The selected crystal grain has its (431) crystallographic plane parallel to the specimen surface (deviation ± 2°) as determined using X-ray diffraction employing the back reflection Laue method [21].

XPS spectra of the Al 2*s*, Al 2*p*, O 1*s* and C 1*s* photoelectron lines and the Al $KL_{23}L_{23}$ Auger line[1] were recorded before and after oxidation with a PHI 5400 ESCA instrument set at constant analyser pass energy of 35.75 eV and with a step size of 0.1 eV, using unmonochromatised incident Mg X-ray radiation (Mg $K\alpha_{1,2}$ = 1253.6 eV). The energy scale of the Spherical Capacitor Analyser (SCA) spectrometer was calibrated according to the procedure described in Ref. [23]. The electrons emitted from the specimen were detected at an angle of 45° with respect to the specimen surface.

II.C. Preparation of HREM cross-sections and analysis

The metal-substrate / oxide-film cross-sections to study the microstructure of the grown oxide films using HREM were prepared in the following way. First a specimen containing a large Al(431) crystal grain was selected and its surface prepared according to the procedure described in Sec. II.A. Next, the specimen was introduced into UHV, outgassed and its surface cleaned and annealed according to the procedure described in Sec. II.A. Then, the bare metal substrate was oxidised for 20×10^3 s at a temperature of 573, 673 or 773 K and a partial oxygen pressure of $p_{O_2} = 1.33\times10^{-4}$ Pa. After XPS analysis of the selected oxidised crystal grain (see Sec. II.B), an approximately 100 nm thick Cu layer was deposited on top of the grown oxide film by evaporation using an evaporator (OMICRON EFM3) equipped with a Mo-crucible containing high purity Cu (99.999 wt%). The evaporation was performed in a side UHV chamber (base pressure < 3×10^{-5} Pa) coupled directly to the UHV processing chamber (see Sec. II.A).

Next, the specimen was removed from UHV. Then, first a 1 mm thick glass plate was glued on the Cu side of the specimen, after which a 0.5-1 mm thick slide, traversing the crystal grain analysed with XPS, was cut from the specimen perpendicular to the sample surface with a diamond saw. Next, both sides of the cross section were mechanically ground and polished until the slide had attained a thickness of about 15 μm. Subsequently, the slide was put on a Cu slot grid. Finally, both sides of the cross-section were ion milled using ion milling apparatus (GATAN Precision Ion Polishing System (PIPS), type 691) applying a 4 kV Ar^+ beam at an angle of 3-5° with respect to the surface until a hole was formed. Then, at the edge of the hole, electron transparent areas were present for HREM analysis of the metal-substrate / oxide-film microstructure.

---

[1] The Al $KL_{23}L_{23}$ Auger electrons with a kinetic energy of about 1394 eV can only be generated with the help of the 'Bremsstrahlung' produced by the X-ray source operating at 15 kV and 400 Watt using the Mg anode, and is therefore recorded at an apparent negative binding energy [22].

The HREM analysis was performed with a Philips CM30UT-FEG electron microscope equipped with a field emission gun, operated at an accelerating voltage of 300 kV. During HREM analysis of the metal-oxide cross-sections, energy dispersive x-ray (EDX) element analysis was performed to confirm the location of the oxide film and check for the presence of any impurities. HREM images were digitised and Fourier transforms ('diffraction patterns') of selected regions in the micrographs were calculated. If possible, the aluminium lattice fringes in each HREM micrograph (preferably the Al(111) lattice fringes) were used for internal calibration of the magnification.

III. XPS data evaluation

The oxide-film *thickness* was calculated from the *total* metallic Al 2*p* and oxidic Al 2*p* primary zero-loss (PZL) photoelectron intensities in a single XPS spectrum of the oxidised aluminium according to the procedure described in Ref. [24] (see also Eq. (A5) in Sec. A.3 of Appendix A). The total *metallic* Al 2*p* PZL intensity - i.e. the PZL intensity of the metallic main peak plus its associated intrinsic plasmon structure - was obtained from the resolved PZL intensity of *only* the metallic main peak (which includes the intensity of the tail of the asymmetrically shaped metallic main peak towards lower kinetic energies) by utilising the value of $\alpha = 0.14$ for the intrinsic bulk plasmon (BP) excitation probability of the Al 2*p* core-level photoelectron emission process [25]. The total *oxidic* Al 2*p* PZL intensity is given fully by the intensity of the oxidic main peak(s) of the oxidic Al 2*p* rest spectrum [24, 25] (cf. Fig. 2). The Al 2*p* oxidic rest spectra (as well as the oxidic Al $KL_{23}L_{23}$ rest spectra; see below and Fig. 3) were obtained after subtraction of a reconstructed metallic main peak plus its associated inelastic Tougaard background from the measured spectrum of the oxidised aluminium substrate (see Refs. [24, 25] for details).

The *composition* of the oxide film, expressed as its O/Al atomic ratio, was determined from the total PZL photoelectron intensity ratio of the O 1*s* main peak(s) and the oxidic Al 2*p* main peak(s) (of a single XPS spectrum measured from the oxidised aluminium), using as a reference the corresponding intensity ratio of α-Al_2O_3 (polished, sputtered clean α-Al_2O_3 single crystal (99.9%) supplied by Goodfellow Cambridge Ltd.) with an O/Al-ratio of $\frac{3}{2}$ (see Ref. [24] and Eq. (A4c) in Sec. A.2 of Appendix A).[2] Since the measured O 1*s* spectra have only a relatively small contribution of inelastically scattered electrons [24], the O 1*s* PZL intensities were insensitive to the method of background subtraction. Therefore, the O 1*s* spectra (corrected for the analyser transmission function and X-ray satellites; see Ref. [25]) were subjected to subtraction of a simple Shirley type background (cf. Ref. [26]) in the BE range from 525 to 540 eV.

The values for the concerned Inelastic Mean Free Paths (IMFPs; symbol λ) required in the calculations of the oxide-film thickness and composition were obtained from the so-called TPP-2M algorithm in Ref. [27]: using the average binding energy (BE) of the 'oxide-film' O 1*s* main peak (533.0 eV), the metallic Al 2*p* main peak (72.80 eV) and the 'oxide-film' Al 2*p* main peak (76.2 eV), as determined in the present work (see Sec. VI.C; see also Figs. 2 and 4), it follows that $\lambda_{O^{2-},ox}$ = 1.65 nm, $\lambda_{Al^0,met}$ = 2.40 nm and $\lambda_{Al^{3+},ox}$ = 2.40 nm (i.e. $\lambda_{Al^0,ox} \cong \lambda_{Al^{3+},ox}$), respectively (cf. Appendix A). For the calculation of the oxide-film thickness, the theoretical molar density (symbol *C*) of Al atoms in the Al metal of $C_{Al^0,met}$ = 100.03 mole/dm^3 was used (cf. Ref. [5]). The molar density of O and Al ions in the Al-oxide film were taken equal to the corresponding theoretical molar densities in γ-Al_2O_3: i.e. $C_{Al^{\delta+},ox} = 71.20$ mole/dm^3 and $C_{O^{\delta-},ox} = 106.80$ mole/dm^3, respectively (cf. Ref. [5]).[3]

The symmetrical oxidic Al 2*p* (and Al $KL_{23}L_{23}$) and O 1*s* main peak(s) (cf. Refs. [25, 26]) constituting the corresponding PZL spectra (see above) were resolved by linear-least-squares (LLS) fitting of each spectrum with up to two (symmetrical) mixed Gauss-Lorenz functions: one Gauss-Lorenz function per component (see Appendix C). When comparing the spectral intensities of the fitted components in the oxidic rest spectra of different XPS measurements (cf. Fig. 14 in Sec. IV.C), the concerned intensities were first *normalised* in order to correct for possible variations of the XPS instrument, e.g. the flux of photons from the X-ray source and/or count rate of the electron analyser. In this case each oxidic (or oxygen) PZL intensity was divided by the corresponding *metallic* (i.e. substrate) PZL intensity after its correction for the presence of its Al-oxide overlayer of appropriate uniform thickness d (see Eq. (B4c) in Appendix B).

---

[2] The composition of the oxide film refers to a weighted averaged value due to the attenuation of the emitted photoelectrons (cf. Appendix A.2).

[3] The structure of the amorphous Al-oxide is well described by a distorted fcc packing of oxygen atoms with the Al ions distributed over the octahedral and tetrahedral interstices (Al is predominantly tetrahedrally coordinated) [28, 29]. This structure closely resembles that of γ-Al_2O_3 (cf. Refs. [5, 28-30]), and indeed crystalline γ-Al_2O_3 instead of α-Al_2O_3 is formed in the case of thicker oxide films grown at elevated temperatures in the present study (see Sec. IV.A). Therefore, the molar densities of Al and O ions in γ-Al_2O_3 are considered to be better approximates for the corresponding molar densities in the amorphous Al-oxide films grown by dry thermal oxidation in this work than the corresponding molar densities in α-Al_2O_3.

Typical Al $2p$ and Al $KL_{23}L_{23}$ oxidic and O $1s$ PZL rest spectra together with their fitted peak components are shown in Figs. 2, 3 and 4, respectively. For oxidation temperatures $T \leq 573$ K all rest spectra could be accurately fitted with only two peak components: (*i*) one pronounced (mixed Gauss-Lorenz) component associated with the ions in the Al-oxide film, further designated as '*oxide-film*' component, and (*ii*) one relative much weaker, pure Gauss[4] component. As discussed in Sec. IV.C, this weak component is associated with a surface species, and will therefore be designated as '*surface-oxide*' component.

For the oxidic rest spectra pertaining to $T = 673$ K, the intensity of the surface-oxide component is much smaller than for oxidic rest spectra pertaining to lower temperatures (i.e. $T \leq 573$ K), and consequently its associated peak is hardly discernable from the noise of the background intensity.[5] In this case, the surface-oxide component in the oxidic rest spectra pertaining to $T = 673$ K was either included or excluded from the fit depending on (*i*) the intensity of the surface-oxide component as compared to the noise of the background intensity, and (*ii*) the degree of overlap of the oxide-film and surface-oxide components (as mainly determined by their energy separation and the Full Width at Half Maximum (FWHM) and peak height of the predominant oxide-film component). The surface-oxide component was resolved in the oxidic Al $2p$, oxidic Al $KL_{23}L_{23}$ and O $1s$ rest spectra of $T = 673$ K for oxidation times up to 2500 s, 250 s and 100 s, respectively. For $T = 773$ K the surface-oxide component could not be distinguished for all oxidation times (cf. Fig. 3b), and in this case all oxidic rest spectra could be accurately fitted with *only one* (mixed Gauss-Lorenz) component, the shape of which (i.e. FWHM and fraction Gauss; see Appendix C) resembles that of the oxide-film component in the oxidic rest spectra pertaining to lower temperatures.

---

[4] Since the quality of the fit was insensitive to the fraction Gauss incorporated in the surface-oxide component, its value was fixed at one (i.e. $g = 1$ for a pure Gauss component; see Appendix C).

[5] It is noted that the Al $KL_{23}L_{23}$ Auger spectra were acquired with a lower signal to noise ratio than the corresponding Al $2p$ and O $1s$ spectra.

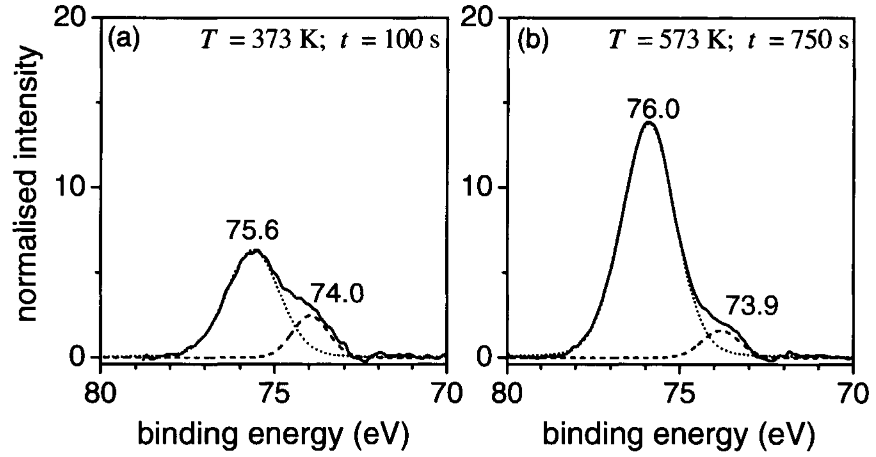

Figure 2. The Al 2*p* PZL oxidic rest spectrum (*solid lines*) as resolved from the measured XPS spectrum of the bare (431) Al substrate after dry, thermal oxidation (**a**) for 100 s at 373 K, and (**b**) for 750 s at 573 K (and p_{O_2} = 1.33×10^{-4} Pa). The fitted oxide-film and surface-oxide component are designated by the *dotted* and *dashed* lines, respectively. The binding energy (in eV) of each fitted peak component at its peak maximum has been indicated.

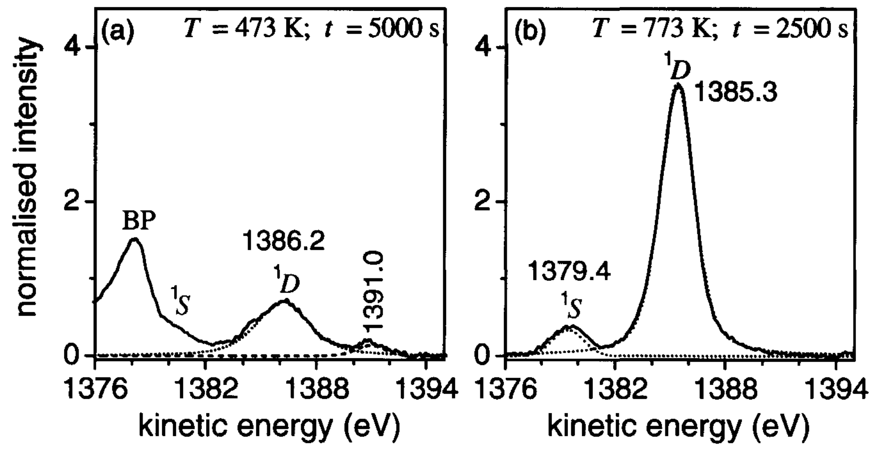

Figure 3. The Al $KL_{23}L_{23}$ PZL oxidic rest spectrum (*solid* lines) as resolved from the measured XPS spectrum of the bare (431) Al substrate after dry, thermal oxidation (**a**) for 5000 s at 473 K, and (**b**) for 2500 s at 773 K (and p_{O_2} = 1.33×10^{-4} Pa). The fitted oxide-film component, which includes the oxidic Al $KL_{23}L_{23}$ (^1D) peak and the associated oxidic Al $KL_{23}L_{23}$ (^1S) Auger peak, as well as the surface-oxide component (only identified in (**a**)) have been designated by the *dotted* and *dashed* lines, respectively. The bulk plasmon (BP) associated with the metallic Al $KL_{23}L_{23}$ (^1D) main peak remains after subtraction of the reconstructed metallic Al $KL_{23}L_{23}$ (^1D) and associated (relative weak) Al $KL_{23}L_{23}$ (^1S) main peak (cf. Refs. [24, 25]). The kinetic energy (in eV) of each fitted peak component at its peak maximum has been indicated.

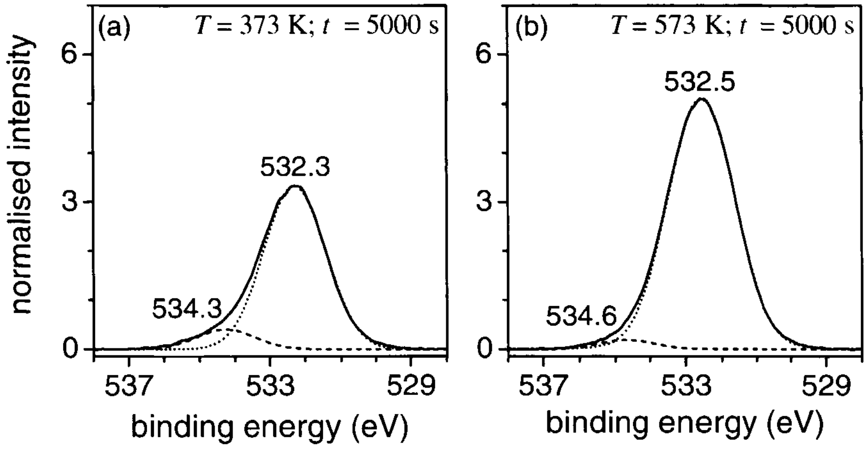

Figure 4. The O 1*s* PZL oxidic rest spectrum (*solid lines*) as resolved from the measured XPS spectrum of the bare (431) Al substrate after dry, thermal oxidation (**a**) for 5000 s at 373 K, and (**b**) for 5000 s at 573 K (and p_{O_2} = 1.33×10^{-4} Pa). The fitted oxide-film and surface-oxide component are designated by the *dotted* and *dashed* lines, respectively. The binding energy (in eV) of each fitted peak component at its peak maximum has been indicated.

For assigning a value to the BE or KE of the detected electrons emitted from the thin (< 6 nm; cf. Fig. 15 in Sec. V) oxide films grown in this study (cf. Sec. VI.C) it has been assumed that (*i*) the Fermi-level of the oxide is coupled to that of the parent Al substrate (and thus to the spectrometer), and (*ii*) no charging of the oxide film occurs during XPS measurement. Ad (*i*): several literature studies on the *electric* tunnelling behaviour of thin Al | Al-oxide | metal devices (cf. Refs. [31-34]) have shown that this assumption is valid for the case of an Al substrate covered by a thin Al-oxide film as grown by thermal oxidation. Ad (*ii*): as extensively investigated in Ref. [35], this assumption is valid for oxide-film thicknesses up to at least 4 nm, provided that a non-monochromatic X-ray source is used. Then, any built up of positive charge in the thin oxide film during XPS measurement will be neutralised not only by the electrons from the parent metal substrate, but also by the stray of secondary electrons emitted from the Al window of the X-ray source onto the oxide surface [35].

IV. Structure of the oxide film

IV.A. Crystallinity of the oxide film

Bare Al(431) substrates, oxidised for 20×10^3 s (at p_{O_2} = 1.33×10^{-4} Pa) at three different temperatures of 573, 673 and 773 K, were analysed by HREM. A HREM micrograph of a cross-section of the Al(431) substrate oxidised for 20×10^3 s at 573 K is shown in Fig. 5. The oxide film is entirely amorphous and is of approximately uniform thickness over 10 to 30 nm parallel to the substrate-film interface until locally a change of the oxide-film thickness ('necking') occurs (see arrow in Fig. 5).

The local 'necking' of the oxide film also occurs for the oxide film grown at 673 K, as shown in the bright field electron micrograph of the cross-section of the Al(431) substrate oxidised for 20×10^3 s at 673 K in Fig. 6. HREM micrographs of the oxide film grown at 673 K are shown in Figs. 7, 8 and 9. Although some parts of the oxide film grown at 673 K are still amorphous (see Fig. 7), the initial, (presumably fully) amorphous (see also Sec. VI.C.1) oxide film has largely transformed into crystalline Al_2O_3 (see Figs. 8 and 9).

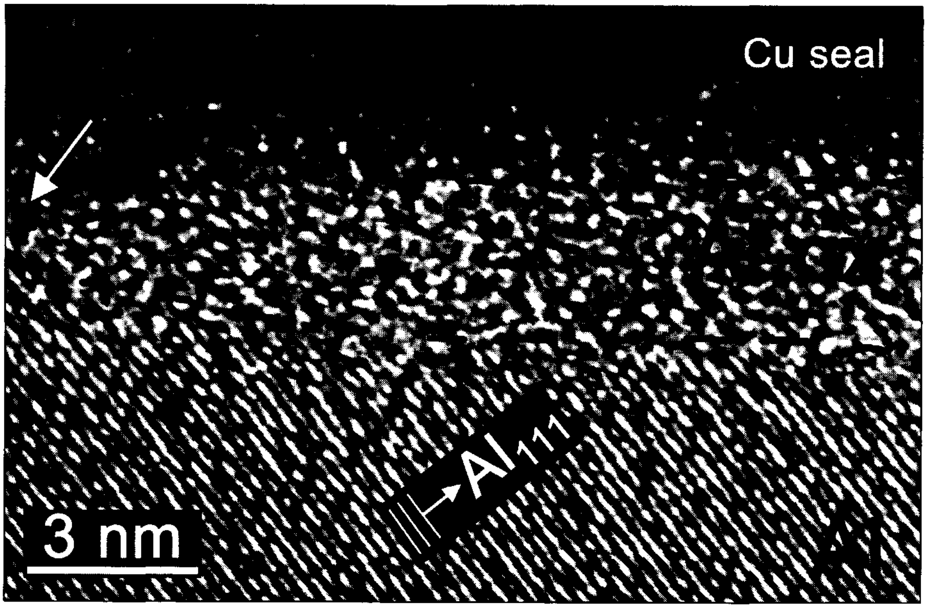

Figure 5. High resolution electron micrograph of the amorphous Al_2O_3 film grown on an initially bare Al(431) substrate by dry, thermal oxidation for 20×10^3 s at 573 K (and p_{O_2} = 1.33×10^{-4} Pa). The oxide film is entirely amorphous and of approximately uniform thickness over some 10 - 30 nm parallel to the substrate-film interface until locally 'necks' in the oxide film occur (see arrow) as shown here.

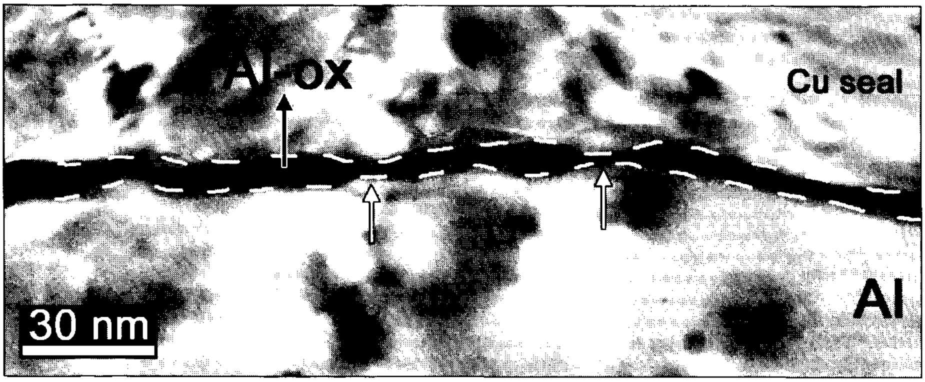

Figure 6. Bright field electron micrograph of a cross-section of an initially bare Al(431) substrate oxidised for 20×10^3 s at 673 K (and p_{O_2} = 1.33×10^{-4} Pa). As for the oxide film grown at 573 K (see Fig. 5), the oxide film formed is of rather uniform thickness over tenths of nanometers parallel to the substrate-film interface until locally 'necks' in the oxide film occur as indicated by the white arrows.

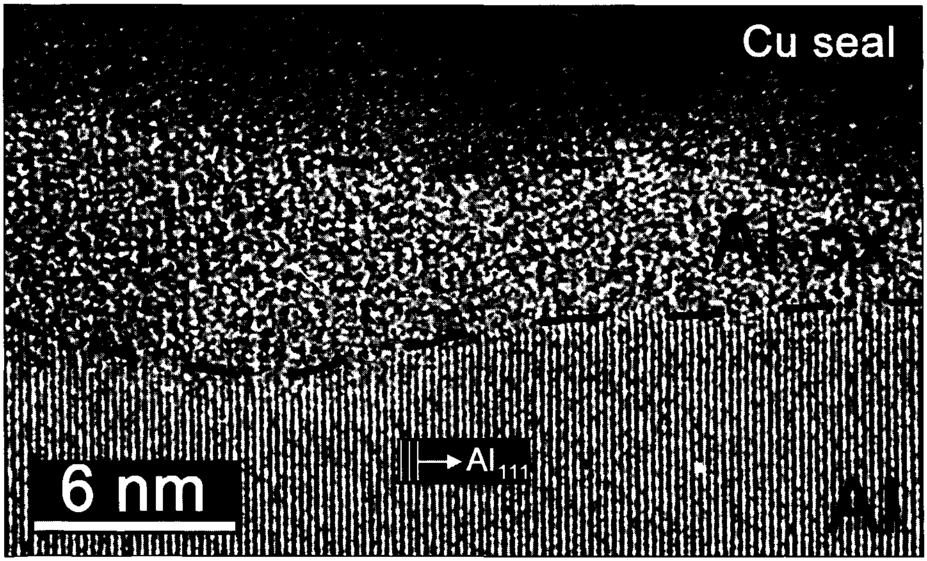

Figure 7. High resolution electron micrograph of an amorphous part of the Al_2O_3 film grown on an initially bare Al(431) substrate by dry, thermal oxidation for 20×10^3 s at 673 K (and p_{O_2} = 1.33×10^{-4} Pa). Locally the film is still amorphous, as shown here. However, in most cases the initial (presumably fully) amorphous oxide film has largely transformed into crystalline Al_2O_3 (see Figs. 8 and 9).

In some cases the crystalline oxide could be identified from the 'diffraction patterns' (i.e. 2D Fourier transforms of selected areas of the HREM micrographs) as γ-Al_2O_3 (footnote 6) and the following orientation relationship was established between the γ-Al_2O_3 film and the parent Al(431) substrate: $(111)_{\text{Al}}\|(111)_{\gamma\text{-Al}_2\text{O}_3}$ and $[110]_{\text{Al}}\|[110]_{\gamma\text{-Al}_2\text{O}_3}$ (see Fig. 8b). This orientation relationship is generally found for thin γ-Al_2O_3 films formed on the {111}, {110} and {100} crystallographic faces of an Al substrate by thermal oxidation (cf. Refs. [6, 7, 36-38]). At the oxidation temperature of 673 K, the growth mismatch between the lattices of the Al substrate and the epitaxial γ-Al_2O_3 film at the interface equals 2.4% and a corresponding tensile strain resides within the oxide film parallel to the interface [5].[7]

In other cases, the crystalline oxide could *not* be identified as either γ-Al_2O_3 or the fcc, amorphous-to-γ-Al_2O_3, transition oxide γ'-Al_2O_3, as reported in Ref. [39] (see for example Fig. 9). The nucleation of such unidentified crystalline Al-oxide phase was observed to occur preferentially at the substrate / oxide-film interface, where {111} lattice planes of the parent Al substrate are parallel to a lattice plane in the oxide (see Fig. 9). Although, in some 10 cases studied, the lattice spacings of the unidentified Al-oxide could be matched to those in γ-Al_2O_3 within about 2 to 4% (and not to those in γ'-Al_2O_3), the angles between the different lattice planes deviated some 2 to 4° from those for γ-Al_2O_3 (the estimated experimental errors of the determined lattice spacings and angles are 2% and 1°, respectively). In contrast with an ideal spinel structure, the *defect* spinel structure of γ-Al_2O_3 (cf. footnote 6) contains (intrinsic) cation vacancies. Therefore small changes in the cation distribution may occur (the specific distribution depending on e.g. the temperature history of the material [40]) with small effects on the anion sublattice. This may lead to tetragonality [41]. Therefore, the above observations suggest that the Al-oxide phase with unidentified crystal structure is a transition oxide between amorphous and γ-Al_2O_3.

---

[6] Unstrained γ-Al_2O_3 has a defect cubic spinel structure (spacegroup: $Fd\bar{3}m$) with a unit cell with a lattice parameter at 298.15 K of $a^{0}_{\gamma\text{-Al}_2\text{O}_3}$ = 7.924 Å (cf. Ref. [30]). The unit cell contains 32 oxygen anions in a 2 × 2 × 2 array of fcc cells of the anion sublattice and $21\frac{1}{3}$ aluminum cations divided over the octrahedral and tetrahedral interstices.

[7] Because the coefficient of linear thermal expansion of Al is about 10 times larger than that of γ-Al_2O_3 [5], upon cooling of the oxidised metal substrate from the oxidation temperature of 673 K to room temperature, a decrease of the tensile strain of about 0.9% occurs.

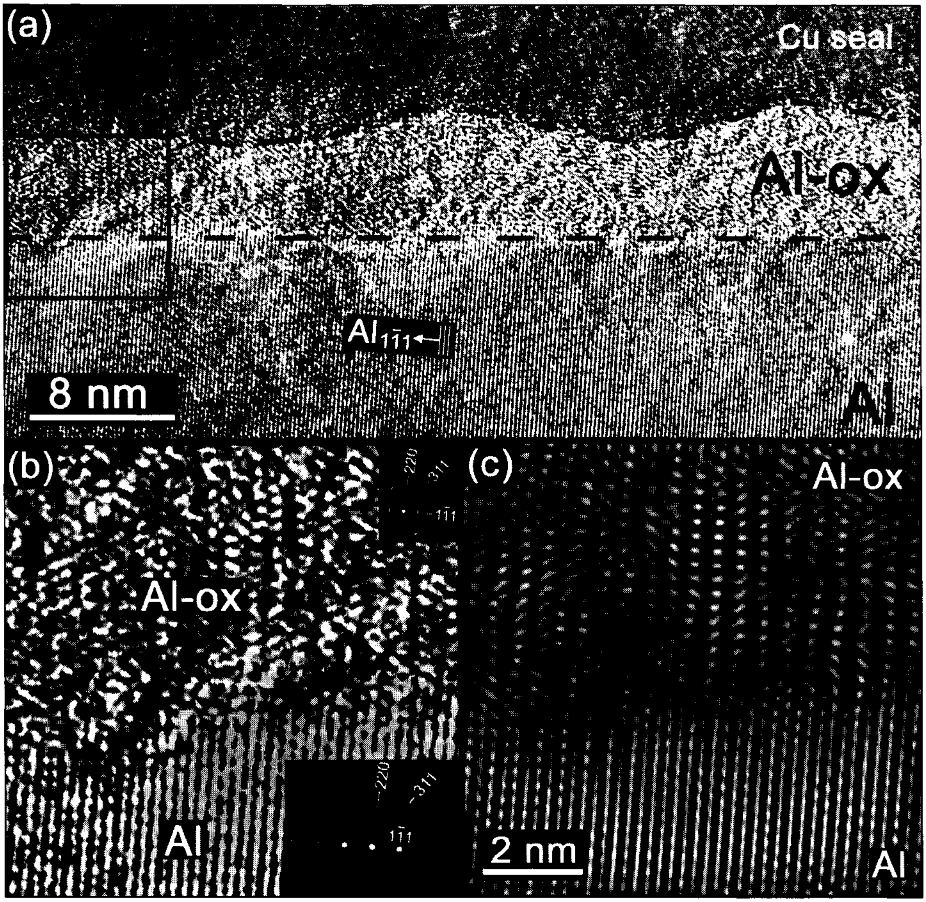

Figure 8. (**a**) High resolution electron micrograph of the Al_2O_3 film formed on an initially bare Al(431) substrate by dry, thermal oxidation for 20×10^3 s at 673 K (and p_{O_2} = 1.33×10^{-4} Pa). The oxide film is predominantly crystalline and appears to have been formed by an island-by-layer-growth mechanism (see also Fig. 12 plus associated discussion). (**b**) Enlargement of part of the epitaxial interface between the parent Al substrate and the crystalline Al_2O_3 film, as indicated by the square box in (a). The 'diffraction patterns' shown in the inlets are 2D Fourier transforms of the regions below and above the interface with a mask for removing noise in the 'diffraction pattern' (i.e. Fourier filtering has been applied; the noise mainly originates from amorphous regions in the oxide and the presence of a native (amorphous) oxide formed during preparation on top of the Al-substrate part of the HREM cross-section). From the 'diffraction patterns' it follows that the electron beam was (approximately) directed along $[\bar{1}12]_{Al} \parallel [\bar{1}12]_{\gamma\text{-}Al_2O_3}$, and the orientation relationship between the crystalline oxide, identified as γ-Al_2O_3, and the Al substrate is: $(111)_{Al} \| (111)_{\gamma\text{-}Al_2O_3}$ and $[110]_{Al} \| [110]_{\gamma\text{-}Al_2O_3}$. (**c**) The inverse Fourier transform of the masked (i.e. Fourier filtered) 'diffraction pattern' of the entire field of (b).

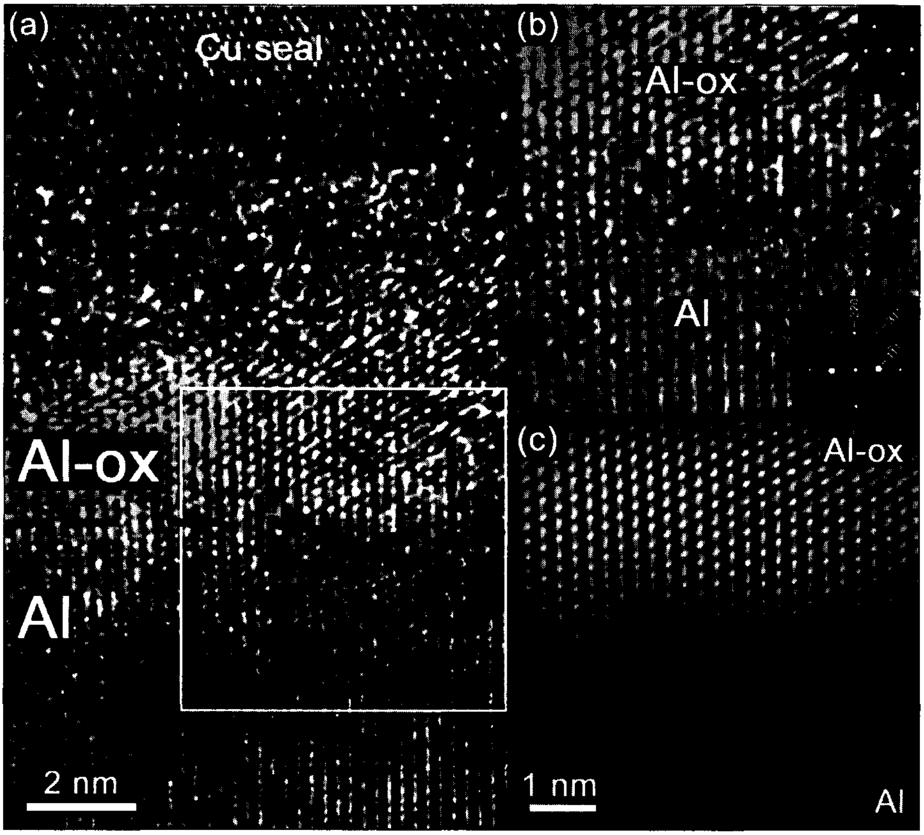

Figure 9. (**a**) High resolution electron micrograph of the oxide film formed on an initially bare Al(431) substrate by dry, thermal oxidation for 20×10^3 s at 673 K (and p_{O_2} = 1.33×10^{-4} Pa). Note that the bottom of the oxide film is crystalline, whereas the top of the film is predominantly amorphous. (**b**) Enlargement of the epitaxial interface between the Al substrate and the crystalline Al_2O_3 film, as indicated by the square box in (a). The inlets show the 'diffraction patterns' (i.e. masked 2D Fourier transforms; see Fig. 8) of the regions above and below the interface. Note that the reflections of the crystalline oxide could not be identified in this case. The electron beam was (approximately) directed along $[\bar{1}12]_{Al}$. (**c**) The inverse Fourier transform of the masked (i.e. Fourier filtered) 'diffraction pattern' of the entire field of (b). See Fig. 8 for details.

Bright field electron micrographs of a cross-section of the Al(431) substrate oxidised for 20×10^3 s at 773 K are shown in Fig. 10. The oxide film consists of large γ-Al_2O_3 crystallites (see Fig. 11) with locally on top of it some remnants of the presumably initial, amorphous oxide film. The largest γ-Al_2O_3 crystallites (about 40 by 60 nm) have partly grown into the parent metal substrate. The observation of local remnants of the presumably initial, amorphous oxide film on top of the γ-Al_2O_3 crystallites complies with the above given interpretation of the HREM images of the specimen oxidised at 673 K: nucleation of γ-Al_2O_3 takes place preferentially at the interface between the initial, amorphous oxide film and the parent Al metal substrate. The inward growth (i.e. into the parent metal substrate) revealed by some large γ-Al_2O_3 crystallites (cf. Fig. 10) indicates that inward diffusion of oxygen (preferentially along existing grain boundaries) has played an important role during growth of these γ-Al_2O_3 crystallites.

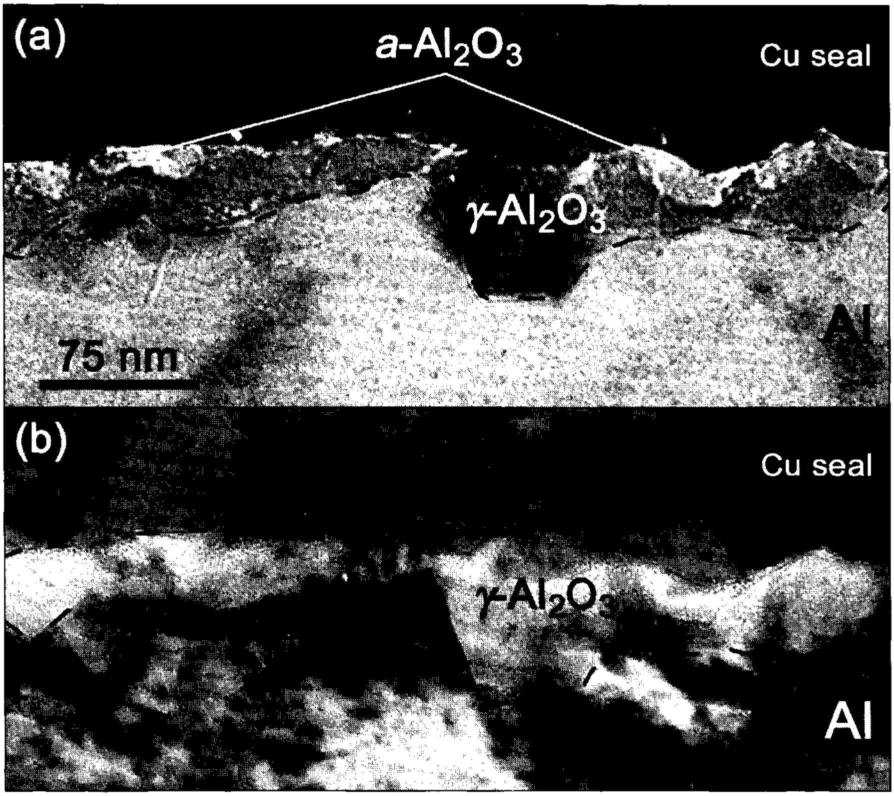

Figure 10. Bright field electron micrographs of a cross-section of an initially bare Al(431) substrate oxidised for 20×10^3 s at 773 K (and p_{O_2} = 1.33×10^{-4} Pa). In (**a**) the specimen was oriented with respect to the incident electron beam such that the diffraction of the γ-Al_2O_3 crystallites was maximized, whereas in (**b**) the specimen was tilted and rotated in order to maximize the diffraction in both the Al substrate and the Cu seal. Although the film is predominantly crystalline, some remnants of the presumably initial, amorphous oxide film are also present. Since the grown oxide film is non-uniform of thickness in 3 dimensions, the dashed lines can only be considered as rough indications of the positions of both the substrate-film interface and the film-seal interface.

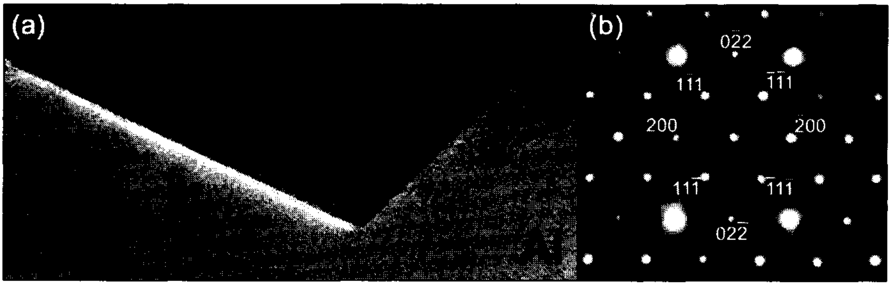

Figure 11. (**a**) High resolution electron micrograph of the interface between a γ-Al_2O_3 crystallite and the Al metal substrate as observed in a cross-section of an initially bare Al(431) substrate oxidised for 20×10^3 s at 773 K (and $p_{O_2} = 1.33\times10^{-4}$ Pa). (**b**) Convergent electron beam diffraction pattern of the γ-Al_2O_3 crystallite shown in (a), using a small condenser aperture. The electron beam was directed along $[011]_{\gamma\text{-}Al_2O_3}$.

As shown in Ref. [5], up to a certain 'critical' oxide-film thickness, an amorphous Al_2O_3 film on its Al substrate can be thermodynamically preferred over the corresponding crystalline γ-Al_2O_3 film on the same substrate, because the higher value for the bulk Gibbs free energy of amorphous Al_2O_3 as compared to that of γ-Al_2O_3, can be overcompensated for by the lower sum of the surface and interfacial energies of the metal-substrate / amorphous-oxide system (as compared to the metal-substrate / γ-Al_2O_3 system). Indeed, the HREM investigation shows that after 20×10^3 s of oxidation at 573 K, the ~ 2 nm thick (see Table I in Sec. IV.B) oxide film is (still) entirely amorphous, whereas after 20×10^3 s of oxidation at 673 K the resulting 4 - 6 nm thick (see Table I in Sec. IV.B), presumably initially (fully) amorphous (see also Sec. VI.C.1), oxide film has already largely transformed into crystalline γ-Al_2O_3 (or γ-like Al_2O_3). This suggests that the 'critical' thickness up to which an amorphous oxide film is preferred on the parent Al(431) substrate (instead of a crystalline of γ-Al_2O_3 film) at a growth temperature of 673 K is about 4 nm. This value for the critical oxide-film thickness of an amorphous Al_2O_3 film on the Al(431) substrate, lies in between the critical thickness values calculated for an Al_2O_3 film formed on an {100} and {110} Al substrate at a growth temperature of 673 K in Ref. [5]: 2.7 and 5.3 nm respectively.

IV.B. Morphology of the oxide film

Quantitative analysis of the Al 2*p* spectra recorded in UHV directly after oxidation and subsequent cooling of the samples to room temperature (i.e. before preparation of the HREM cross-sections), yielded values for the average thickness and composition (as expressed by its O/Al atomic ratio) of the grown oxide films (see Secs. II.C and III). According to the XPS analysis of the oxidised Al substrates, all oxide films considered for the HREM analysis exhibit the composition of Al_2O_3 (i.e. O/Al-ratio of $\frac{3}{2}$). The oxide-film thicknesses as obtained with XPS, as well as the values for the local oxide-film thicknesses observed in the HREM micrographs of the metal-oxide cross-sections, have been gathered in Table 1. It should be noted that the thickness and composition obtained with XPS pertain to averages for the entire area of the oxidised metal surface analysed with XPS, whereas information on the variation (i.e. non-uniformity) of the (local) thickness is obtained from the corresponding HREM micrographs.

Table I. Average values for the thickness of the oxide films grown on an initially bare Al(431) substrate at temperature T (and $p_{O_2} = 1.33\times10^{-4}$ Pa), as determined from the Al $2p$ XPS spectra of the oxidised metal (see Sec. III), and values for the thickness (and their variation) as obtained from the high resolution electron micrographs of the corresponding metal-substrate oxide-film cross-sections (see Sec. II.C).

T (K)	thickness (nm)		
	XPS	HREM	
573	1.3	*range* :	0.5 - 4
		average :	2 (± 1)
673	4.5	*range* :	1 - 8
		average :	4 (± 2)
773	> 6.5*	*range* :	10 - 80#
		average :	30 (± 10)

* *Thicknesses of Al-oxide films larger than about 6.5 nm cannot be determined reliably by XPS (cf. Sec. III).*

Average thickness of the remnants of the initial, amorphous Al-oxide film (cf. Fig. 10) is about 6 to 8 nm.

The oxide films grown at T = 573 and 673 K, show a relatively large variation of the oxide-film thickness as observed in the HREM micrographs (see Table I) due to the necking of the oxide film (cf. arrows in Figs. 5 and 6 in Sec. IV.A). The oxide film grown at T = 773 K, possesses a large spread in oxide-film thickness due to the presence of large crystallites of γ-Al_2O_3 grown into the parent Al substrate (cf. Fig. 10 in Sec. IV.A). In general it can be stated that the grown oxide-film is of less uniform thickness for higher oxidation temperature. The average thickness values of the oxide films grown at 573 and 673 K as determined with

XPS agree well with those estimated from the corresponding HREM micrographs (see Table I).[8]

To study the uniformity of the thickness of the oxide film formed on the bare Al substrate during the initial stages of oxide-film growth, the surface plasmon (SP) structure associated with the Al 2*p* metallic main peak (in the measured XPS spectrum of the oxidised Al substrate) was traced with increasing oxidation time for the different temperatures considered (see Fig. 12). As soon as the *entire* Al substrate area analysed with XPS is covered with an Al_2O_3 monolayer (= ML; 1 Al_2O_3 ML ~ 0.2 nm [5]), the SP structure associated with the Al 2*p* metallic main peak must have disappeared in the measured XPS spectrum of the oxidised metal [25]. For the oxide films grown at 373 K and 473 K, of eventual, 'limiting' thickness of 0.5 - 0.6 nm (i.e. ~ 2 - 3 oxide MLs) (see Sec. V), the SP peak associated with the metallic Al 2*p* main peak has already disappeared after 100 s of oxidation (at $p_{O_2} = 1.33\times10^{-4}$ Pa), as shown in Figs. 12a and c. It is therefore concluded that oxide-film growth on the bare Al substrate at temperatures $T \leq 473$ K results in the formation of uniform 2 - 3 MLs thick oxide films. On the other hand, after 100 s of oxidation at temperatures $T \geq 573$ K, a distinct SP peak is still visible in the measured Al 2*p* XPS spectra of the oxidised metal, the intensity of which increases with increasing oxidation temperature (see Figs. 12b and d). The SP peak in the Al 2*p* XPS spectra of the oxidised metal has disappeared after 200, 500 and 750 s at 573, 673 K and 773, respectively. This indicates that, for the oxidation at $T \geq 573$ K, bare metal and oxidised metal surfaces coexist up to oxidation times of 200, 500 and 750 s at 573, 673 K and 773 K, respectively (with the fraction of the metal-substrate surface covered with oxide after 100 s of oxidation decreasing with increasing temperature).

It is concluded that at higher oxidation temperatures the initial oxidation involves the formation and growth of oxide islands on the bare Al substrate. The higher the temperature, the lower the density of oxide islands on the bare metal substrate, and thus the longer the oxidation time before the entire metal surface is covered with oxide. It may then be expected that, the (eventually closed) oxide film formed on the Al(431) substrate after longer oxidation times is of less uniform thickness for the higher oxidation temperatures, as indeed evidenced by the observed HREM thickness ranges in Table I. The local 'necks' in the oxide film, as observed in the studied HREM cross-sections (cf. Figs. 5 and 6), may be considered as remnants of the island-by-layer oxide-film growth mechanism. 'Regular' variations of the thickness of amorphous oxide films grown on single-crystalline Al substrates by thermal oxidation have also been observed for the oxidation of {110} and {111} Al substrates, whereas oxidation of {100} Al substrates resulted in the formation of oxide films of highly uniform thickness [6]. It follows that the uniformity of the initial, amorphous Al-oxide film as grown by thermal oxidation depends on the crystallographic orientation of the Al substrate, as well as on the oxidation temperature.

---

[8] For T = 773K, the thickness of the grown oxide-film could no longer be determined using XPS, because the metallic main peak in the corresponding Al 2*p* XPS spectrum of the oxidised metal is undetectable.

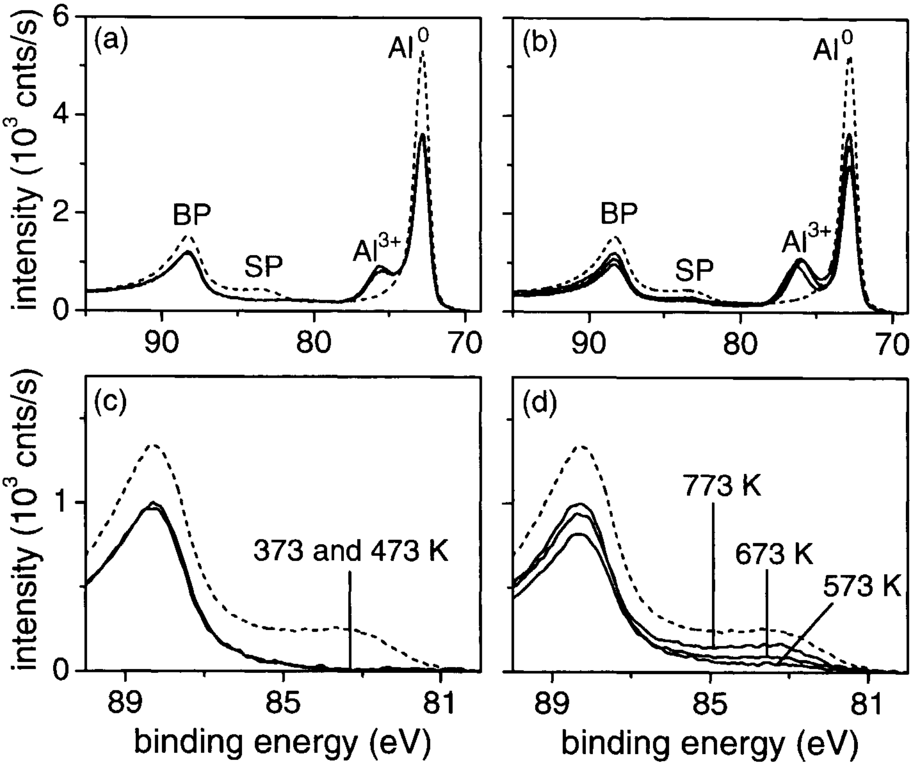

Figure 12. Measured Al $2p$ XPS spectra including the first bulk and surface plasmon region as recorded from the bare (431) Al substrate (*dashed lines*) and the metal substrate after dry, thermal oxidation for 100 s (*solid lines*) at (**a**) 373 and 473 K, and (**b**) 573, 673 and 773 K (and p_{O_2} = 1.33×10^{-4} Pa). The 'as measured' spectra shown have been corrected for the analyser transmission function, X-ray satellites and background offset at a BE value of 70 eV [25]. The first bulk plasmon (BP) and surface plasmon (SP) peak, associated with the Al $2p$ metallic main peak (Al^0), as well as the corresponding oxidic main peak (Al^{3+}) have been indicated. Panels (**c**) and (**d**) show enlargements of the SP and BP region of respectively panel (**a**) and panel (**b**) after background offset at a binding energy of 80 eV. Note that, after 100 s of oxidation, the SP is already absent for T = 373 and 473 K, whereas at higher oxidation temperatures a distinct SP plasmon peak is still visible, the intensity of which increases with increasing oxidation temperature.

These interpretations are supported by recent results obtained with Scanning Tunnelling Microscopy (STM) [19, 42] and High-Resolution Electron Energy-Loss Spectroscopy (HREELS) [9, 10] on the dissociative adsorption of O_2(g) and subsequent oxide formation on a bare Al(111) substrate in the temperature range from room temperature to 773 K. It was found that above 300-350 K the chemisorbed oxygen species on the Al (and Al-oxide) surface becomes mobile, and islands of chemisorbed oxygen develop which subsequently transform into oxide (see also discussion in Sec. VII.A).

IV.C. Oxide surface

As revealed by the presence of two spectral components in the oxidic Al 2*p*, oxidic Al $KL_{23}L_{23}$ and O 1*s* PZL spectra for oxidation temperatures $T \leq 673$ K (i.e. the oxide-film and surface-oxide component; see Sec. III), the oxide films grown at these temperatures are not homogeneous. Evidence that the weak component is associated with a surface species located at the top of the oxide film in contact with the ambient, is obtained from a series of Al 2*p* XPS spectra of the oxidised metal, recorded as a function of photoelectron detection angle θ with respect to the sample surface. For a surface species (which is very thin as compared to the IMFP) the associated intensity is approximately independent of the detection angle θ (for a constant XPS analysis area), whereas for a very thin substrate/layer-interface species the intensity decreases with decreasing detection angle θ (for a constant XPS analysis area) due to the photoelectron escape probability becoming lower (cf. Eq. A3 in Sec. A.1 of Appendix A). The intensity of both the weak, 'surface-oxide' and the predominant, 'oxide-film' component as resolved from a series of oxidic Al 2*p* and O 1*s* PZL spectra recorded from the oxidised Al(431) substrate (cf. Figs. 2 and 4 in Sec. III, respectively) have been plotted as a function of the detection angle θ in Figs. 13a and b, respectively.[9] Indeed, the intensity of the surface-oxide component is approximately independent of detection angle θ, whereas the intensity of the oxide-film component decreases with decreasing θ. Hence, the weak component in the oxidic Al 2*p*, oxidic Al $KL_{23}L_{23}$ and O 1*s* PZL spectra is associated with a surface species located at the top of the oxide film in contact with the ambient.

---

[9] The total volume of oxide-film analysed with XPS equals $d\pi r^2 / \sin\theta$, where d denotes the oxide-film thickness, r is the radius of the aperture of the electron-analyser-input lens, and θ represents the detection angle between the specimen surface and the optical axes of the analyser-input lens. Thus, to correct the resolved PZL intensities of both the oxide-film and surface-oxide component for the increase in oxide-film volume as sampled with decreasing θ, the intensities were multiplied with $\sin\theta$.

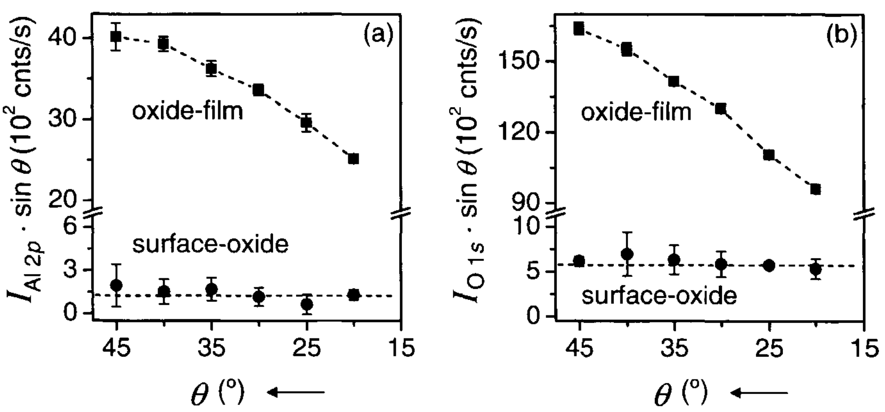

Figure 13. PZL photoelectron intensity of the weak 'surface-oxide' and the predominant 'oxide-film' component in the (**a**) oxidic Al 2*p* PZL and (**b**) oxygen O 1*s* PZL spectra (see Figs. 2 and 4 in Sec. III, respectively) versus the photoelectron detection angle θ (with respect to the sample surface). The spectra were resolved from a series of XPS spectra recorded from the bare Al(431) substrate covered with a 0.9 nm thick oxide film as grown by dry, thermal oxidation for 10×10^3 s at 573 K (and $p_{O_2} = 1.33\times10^{-4}$ Pa). Note that the intensities were multiplied with sin θ to correct for the increase in oxide-film volume as sampled with XPS for decreasing detection angle θ (see footnote 9).

Further evidence that the weak component is associated with a surface species is obtained by plotting the normalised intensity of the 'surface-oxide' component (see Sec. III) versus the oxide-film thickness (see Sec. V) for the different oxidation temperatures considered, as shown in Fig. 14. If the weak component would correspond with an interface species, its intensity is expected to *decrease* exponentially with increasing oxide-film thickness at constant oxidation temperature (cf. Eq. (B4c) in Appendix B). If the weak component would correspond with a surface species, its intensity is expected to be approximately *independent* of thickness at constant temperature (assuming a steady state or equilibrium at the oxide/oxygen gas interface during growth).[10] As shown in Fig. 14, the 'surface-oxide' intensity at constant oxidation temperature is indeed approximately independent of the oxide-film thickness.[11] The spread in the Al 2*p* surface-oxide intensities for $T = 373$ and 473 K at constant oxide-film thickness (see Fig. 14) is due to a slight decrease of the concerned intensity with increasing oxidation time (towards a constant value) after oxide-film growth has stopped (i.e. at the 'limiting' oxide-film thickness; see Sec. V). This decrease of the Al 2*p* surface-oxide intensity is accompanied by a small increase of the corresponding oxide-film Al 2*p* intensity (with the *total* Al 2*p* oxidic PZL intensity remaining practically constant), indicating that the surface oxide is to some extent transformed into the same oxide as the 'bulk oxide film' (i.e. some surface reconstruction occurs) at the 'limiting' oxide-film thickness for $T = 373$ and 473 K.

---

[10] For an oxide species that is distributed in the oxide film, the corresponding photoelectron intensity is predicted to increase with increasing oxide-film thickness (as long as the oxide film is not 'infinitely' thick as compared to the IMFP of the concerned photoelectrons).

[11] Corresponding plots of the normalised intensity of the Al $KL_{23}L_{23}$ and O 1*s* surface-oxide component versus the oxide-film thickness give the same result, i.e. an approximate constant intensity at constant oxidation temperature, independent of the thickness.

As discussed in Sec. VI.C.3, based on the position of the peak maximum of the O 1*s* surface-oxide component, it can be ruled out that the surface component is associated with a simple *chemisorbed* species (due to the bonding of Al ions of the oxide or Al atoms of the substrate with chemisorbed oxygen at the surface), as has been reported in Refs. [9, 10, 43]. Instead, the surface component found in the present work is attributed to a *surface-oxide* species (rather than a *chemisorption* species) (see Secs. IV.C and VI.C.3).

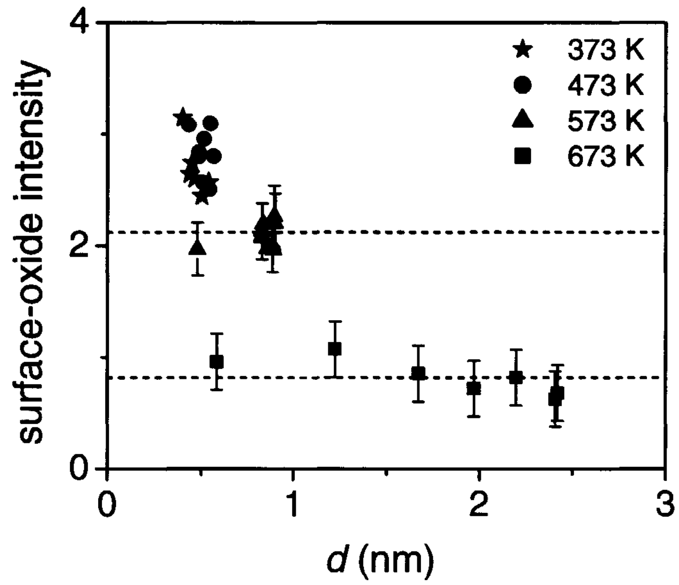

Figure 14. Normalised Al 2*p* PZL intensity of the weak surface-oxide component, as resolved from the Al 2*p* PZL oxidic rest spectra (see Sec. III), versus the oxide-film thickness *d* (see Sec. V) for the different oxidation temperatures considered. Note that the surface-oxide component has not been observed for $T = 773$ K and has disappeared at $T = 673$ K for oxidation times $t > 2500$ s (see Sec. III). The horizontal dashed lines indicate the average value of the Al 2*p* surface-oxide intensity for $T = 573$ and 673 K.

The average Al 2*p*, Al $KL_{23}L_{23}$ and O 1*s* surface-oxide intensities have been plotted versus the oxidation temperature in Figs. 15a to c. As indicated by the strong decrease in intensity of both the oxidic and oxygen surface-oxide component for $T \geq 573$ K, the quantity of surface oxide present on the oxidised Al substrate becomes strongly reduced for oxidation temperatures $T \geq 573$ K (*note*: at 673 K for $t > 2500$ s and at 773 K the surface oxide is no longer observed).[12] As evidenced by the HREM analysis of the oxide films grown at 573, 673 and 773 K (see Sec. IV.A), the strong decrease in intensity of the surface-oxide component for $T \geq 573$ K (and its eventual disappearance at $T = 773$ K as well as for the thicker films grown at 673 K) runs parallel with the (gradual) transition from amorphous Al_2O_3 to crystalline γ-Al_2O_3.

V. Oxide-film growth kinetics

The oxide-film thickness as a function of the oxidation time (t), for the oxidation of the (431) crystallographic face of the Al substrate at temperatures (T) between 373 and 773 K (at $p_{O_2} = 1.33 \times 10^{-4}$ Pa),[13] has been plotted in Figs. 16 and 17. Evidently, for temperatures $T \leq$ 673 K, the oxide-film growth rate increases with increasing temperature. For $T = 773$ K up to 750 s, oxide-film growth is slower than the initial growth rate at 573 and 673 K (see Fig. 17). Such an effect (i.e. an initial growth rate that decreases with increasing temperature) is generally attributed to a reduction of the sticking coefficient of oxygen on the metal surface with increasing temperature [45]. Indeed, in Refs. [9, 45] the O_2 sticking probability on a bare Al(111) surface was found to decrease with increasing temperature for $T > 623$ K, whereas in the temperature range from 243 - 600 K an increase in the O_2 sticking probability was observed.

---

[12] Although the XPS measurement were performed *directly* after pumping away the oxygen gas and cooling down to room temperature (see Sec. II.B), it cannot be excluded that the surface oxide is to some extent transformed into the same oxide as the 'bulk oxide film' (i.e. some surface reconstruction occurs) during cooling and XPS analysis (especially for the high temperature oxide films).

[13] Note that all results presented in this work pertain to the dry, thermal oxidation of an Al{431} crystallographic surface at $p_{O_2} = 1.33 \times 10^{-4}$ Pa, and all XPS measurements were performed on the same selected Al(431) crystal grain (see Sec. II.B).

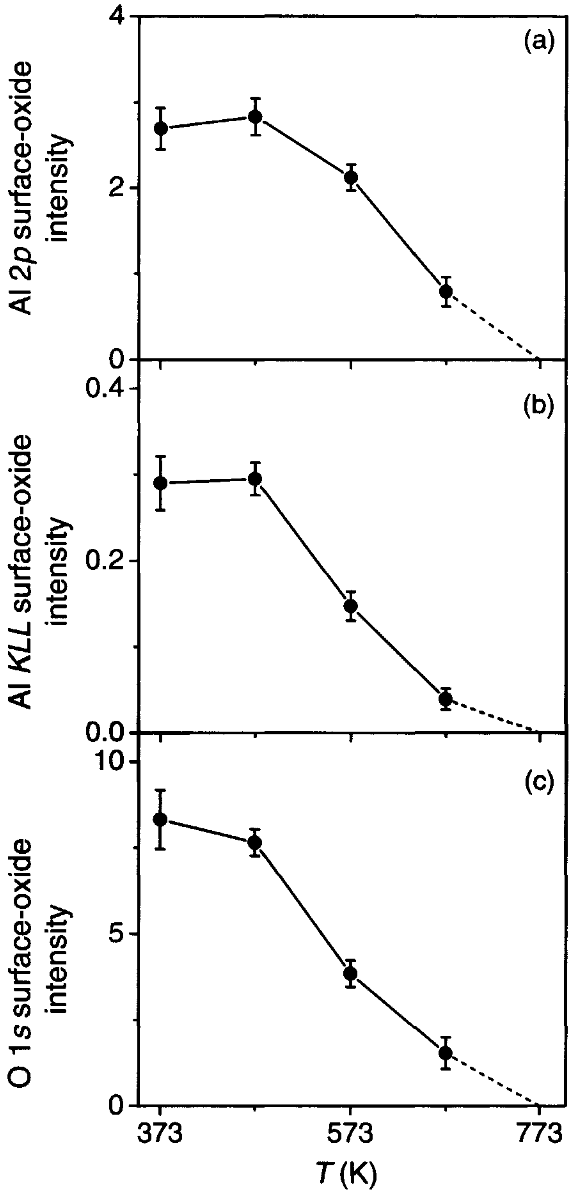

Figure 15. Average, normalised intensity of the surface-oxide component as resolved from the (**a**) oxidic Al 2*p*, (**b**) oxidic Al $KL_{23}L_{23}$ and (**c**) oxygen O 1*s* PZL spectra (see Sec. III) versus the oxidation temperature *T*. The error bars correspond to the standard deviations of the concerned intensities for the different oxidation times at the temperature considered (cf. Fig. 14). Note that the surface-oxide component has not been observed for $T = 773$ K and has disappeared at $T = 673$ K for oxidation times $t >$ 2500 s (see Sec. III).

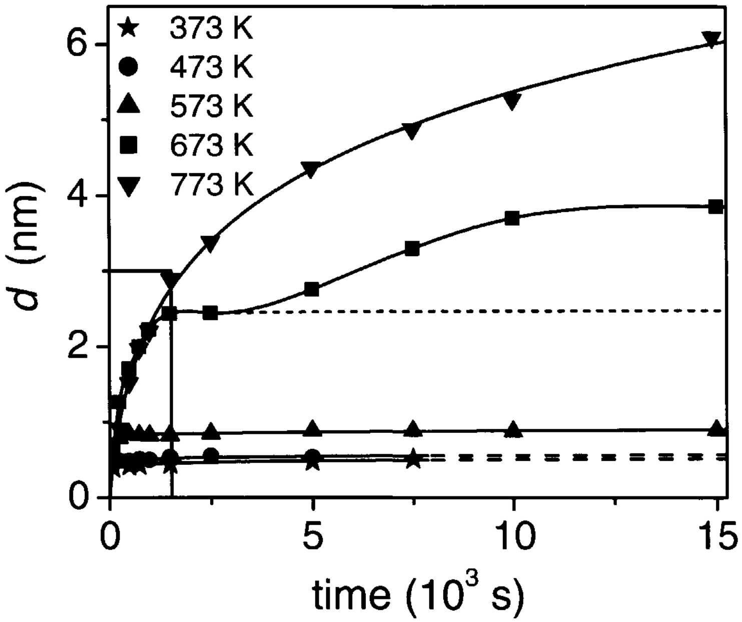

Figure 16. Oxide-film thickness (d) as a function of oxidation time, for the oxidation of the bare (431) Al substrate at various temperatures (and p_{O_2} = 1.33×10^{-4} Pa). An enlargement of the initial fast oxide-film growth stage, as comprised by the rectangular box, is shown in Fig. 17.

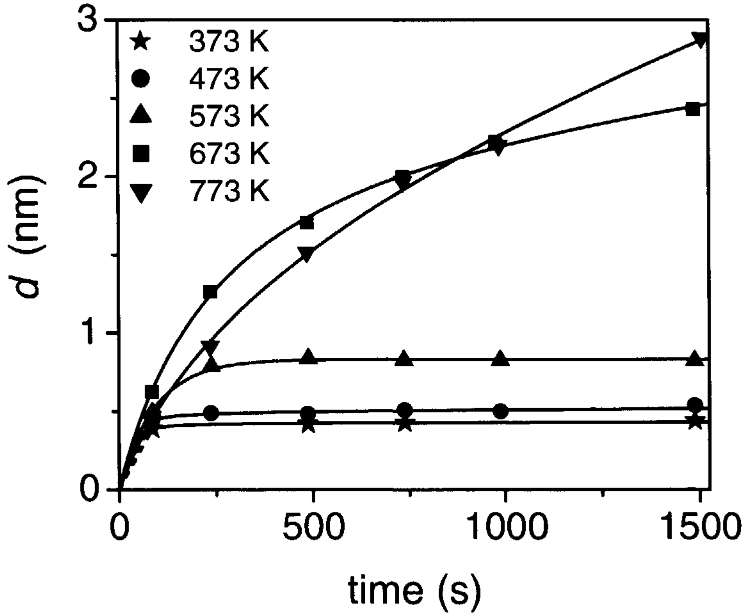

Figure 17. Initial oxide-film growth kinetics for the oxidation of the bare (431) Al substrate at various temperatures (and p_{O_2} = 1.33×10^{-4} Pa). Enlargement of part of Fig. 16.

For $T \leq 673$ K, after an initial regime of fast oxide-film growth, the oxide-film growth rate becomes virtually zero, reaching a 'limiting' oxide-film thickness which increases with increasing temperature; at 373, 473, 573 and 673 K a 'limiting' oxide-film thickness of 0.5, 0.6, 0.9 and 2.4 nm is reached within about 100, 250, 500 and 1500 s, respectively. For $T = 673$ K, after a short 'incubation' time of about 500 s, the regime of fast initial oxide-film growth is followed by a second stage of much slower but *continuing* (i.e. no limiting thickness is observed) oxide-film growth reaching an oxide-film thickness of 3.9 nm after 15000 s. For the highest temperature of 773 K, no plateau (i.e. 'limiting' oxide-film thickness) in the growth curve is observed (see Fig. 16); i.e. oxide-film growth continues, reaching an oxide-film thickness of 6.1 nm after 15000 s. However, as indicated by the plots of the corresponding growth rate and change in growth rate as a function of the oxidation time in Figs. 18b and 18c, respectively, a transition from an initial rapid oxide-film growth regime to a much slower oxidation regime can also be distinguished for the oxidation at 773 K (as for $T = 673$ K); initially, the oxide-film growth rate rapidly decreases with increasing oxidation time, reaching a much slower, but continuing oxidation stage after about 1500 s. As indicated by the linear fits through the solid data points in the inverse logarithmic, direct logarithmic and parabolic plots of Figs. 19a, b and c, respectively, a determination on the basis of such plots of the type of growth rate kinetics prevailing during the second stage is rather arbitrary.

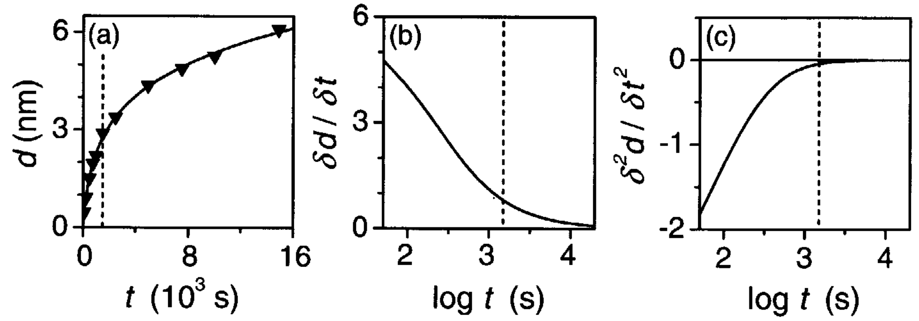

Figure 18. (**a**) Oxide-film thickness d versus oxidation time t, and (**b**) growth rate $\partial d/\partial t$ and (**c**) change in growth rate $\partial^2 d/\partial t^2$ versus log t for the oxidation of the bare (431) Al substrate at 773 K and $p_{O_2} = 1.33\times10^{-4}$ Pa (see Figs. 16 and 17). The growth rate and change in growth rate are simply the first and second derivative of the curve fitted through the growth curve of (a). The transition from an initial, fast oxide-film growth regime to a second, much slower oxidation stage around $t = 1500$ s is indicated by the vertical dashed lines.

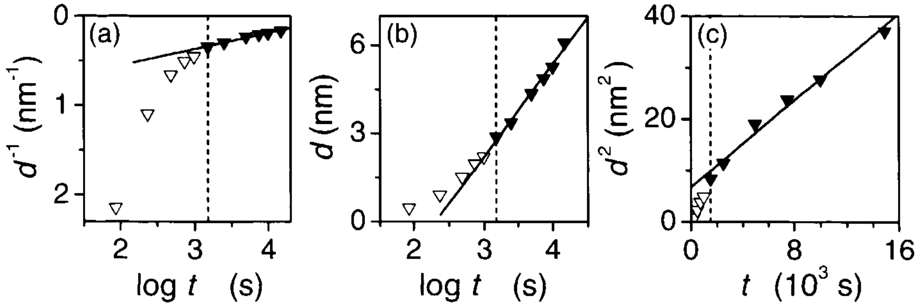

Figure 19. (**a**) Inverse logarithmic, (**b**) direct logarithmic and (**c**) parabolic plots of the oxide-film thickness d vs. the oxidation time t for the oxidation of the bare (431) Al substrate at 773 K and p_{O_2} = 1.33×10^{-4} Pa (see Figs. 16 and 17). The transition from an initial, fast oxide-film growth regime to a second, much slower oxidation stage around t = 1500 s is indicated by the vertical dashed lines (see Fig. 18). The solid lines represent linear fits through the solid data points for $t \geq 1500$.

Thus it can be concluded that for $T \leq 573$ K (at p_{O_2} = 1.33×10^{-4} Pa), the oxide-film growth process on a (431) Al substrate is *self-limiting* within less than about 250 s, reaching a 'limiting' oxide-film thickness which increases with increasing oxidation temperature, whereas for higher temperatures the fast initial oxidation regime is succeeded by a second stage of much slower but *continuing* oxide-film growth.

VI. Oxide-film constitution during growth

VI.A. Composition of the oxide film

To determine the composition (i.e. the O/Al-ratio) of the developing oxide film, the PZL intensities of *only* the oxide-film component in the oxidic Al 2p and O 1s spectra must be considered (i.e. excluding the corresponding PZL intensities of the surface-oxide component: see Secs. III and IV.C). The thus obtained O/Al-ratio of the developing oxide film (see Sec. III and Eq. (A4c) in Sec. A.2 of Appendix A) has been plotted as a function of oxidation time for the different temperatures considered in Fig. 20. Since the XPS measurements were performed directly after cooling down the sample to room temperature (see Sec. II.B), the determined O/Al-ratios are considered to represent the composition of the developing oxide film during growth. To our knowledge this is the first and detailed investigation of the changes in composition of the thin Al-oxide films as grown by dry, thermal oxidation at different oxidation times and temperatures.

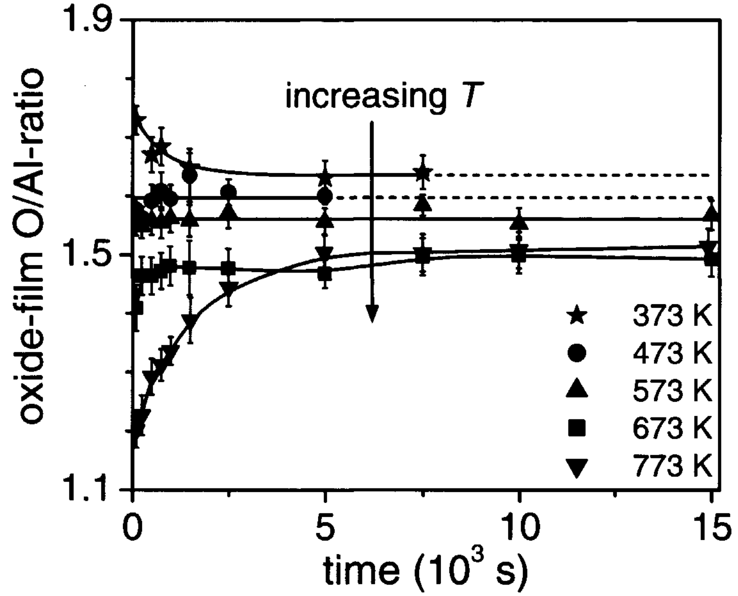

Figure 20. O/Al-ratio of the oxide-film as a function of oxidation time, for the oxidation of the bare (431) Al substrate at various temperatures (and $p_{O_2} = 1.33\times10^{-4}$ Pa). The O/Al-ratio was derived from the PZL intensities of only the oxide-film component in the resolved oxidic Al 2*p* and O 1*s* PZL spectra (see Sec. III). Note that for stoichiometric Al_2O_3 the O/Al-ratio equals $\frac{3}{2}$.

At all temperatures considered, initially a *non*-stoichiometric oxide film is formed. At $T \leq 573$ K, the initial oxide film has an O/Al-ratio > 1.5, whereas at higher oxidation temperatures the initial O/Al-ratio < 1.5. At $T = 473$ and 573 K, the composition of the developing oxide film is approximately independent of the oxidation time at the limiting thickness, whereas at 373 K the O/Al-ratio of the oxide film, after the limiting thickness has been attained (i.e. after 100 s of oxidation; cf. Fig. 17 in Sec. V), still slightly decreases with increases oxidation time towards a constant value of 1.6 after about 3000 s. This contrasts with the oxide films formed at higher temperatures (especially for $T = 773$ K); at these temperatures the O/Al-ratio of the oxide film increases with increasing oxidation time during the initial, fast oxidation stage (see Sec. V) reaching a constant stoichiometric O/Al-ratio of $\frac{3}{2}$ after about 5000 s (i.e. during the second, slow oxidation stage).

To determine whether the non-stoichiometric oxide films pertaining to Fig. 20 are relatively enriched with or deficient of Al and/or O as compared to stoichiometric Al_2O_3, the oxygen anion ($C_{O^{\xi-},ox}$) and aluminium cation ($C_{Al^{\delta+},ox}$) molar densities (in [mole/dm^3]) in the grown oxide films were estimated from the metallic Al 2*p*, oxide-film Al 2*p* and oxide-film O 1*s* PZL photoelectron intensities according to the iterative procedure described in Appendix

D. In this calculation it is assumed that the amorphous oxide films grown in this study (cf. Sec. IV.A) can be described by a homogeneous close packing of oxygen anion spheres with aluminium cation spheres in the interstices (see footnote 3 in Sec. III). Also, any volume difference with crystalline γ-Al_2O_3, due to excess free volume changes (differences) in the amorphous oxide is neglected. The thus obtained molar densities of oxygen anions and aluminium cations in the developing oxide film have been plotted as a function of oxidation time for the different temperatures considered in Figs. 21a and b, respectively. The results for the molar density of Al cations at the limiting oxide-film thickness, as well as the corresponding values of the limiting thickness (see Sec. V) have been plotted as a function of the oxidation temperature in Figs. 22a and b, respectively. It follows that, for all temperatures, the change in oxide-film composition (i.e. O/Al-ratio) with increasing oxidation time at constant temperature is mainly due to a change in the Al cation concentration (see Fig. 21). The initial Al cation concentration increases with increasing temperature. The observation that the calculated molar density of O anions is approximately constant, independent of both the oxidation temperature and the oxidation time, supports our previous assumption (see footnote 3 in Sec. III) that the amorphous Al-oxide films are well described by a close packing of oxygen anions with the (relative smaller) Al cations distributed over the octahedral and tetrahedral interstices.[14]

VI.A.1. Low temperature oxide films

The low temperature (i.e. $T \leq 573$ K) non-stoichiometric oxide films exhibit a deficiency of Al cations (as compared to γ-Al_2O_3) even at the limiting thickness. At $T = 473$ and 573 K the concentration of Al cations (and O anions) in the developing oxide film is practically independent of the oxidation time at the limiting thickness, whereas at 373 K the initially relative low Al cation concentration still slightly increases with increases oxidation time at the limiting thickness (reaching a constant value after about 3000 s). The Al cation concentration at the limiting thickness increases with increasing temperature (see Fig. 22).

---

[14] Indeed, direct calculation of the Al molar densities using Eqs. (A4c) and (A6b) (in Appendix A.2 and A.3, respectively), assuming a constant molar density of O anions in the oxide film, taken equal to the corresponding O molar density in γ-Al_2O_3, gives practically the same results as those obtained from the iterations according to the procedure described in Appendix D (see Fig. 21b).

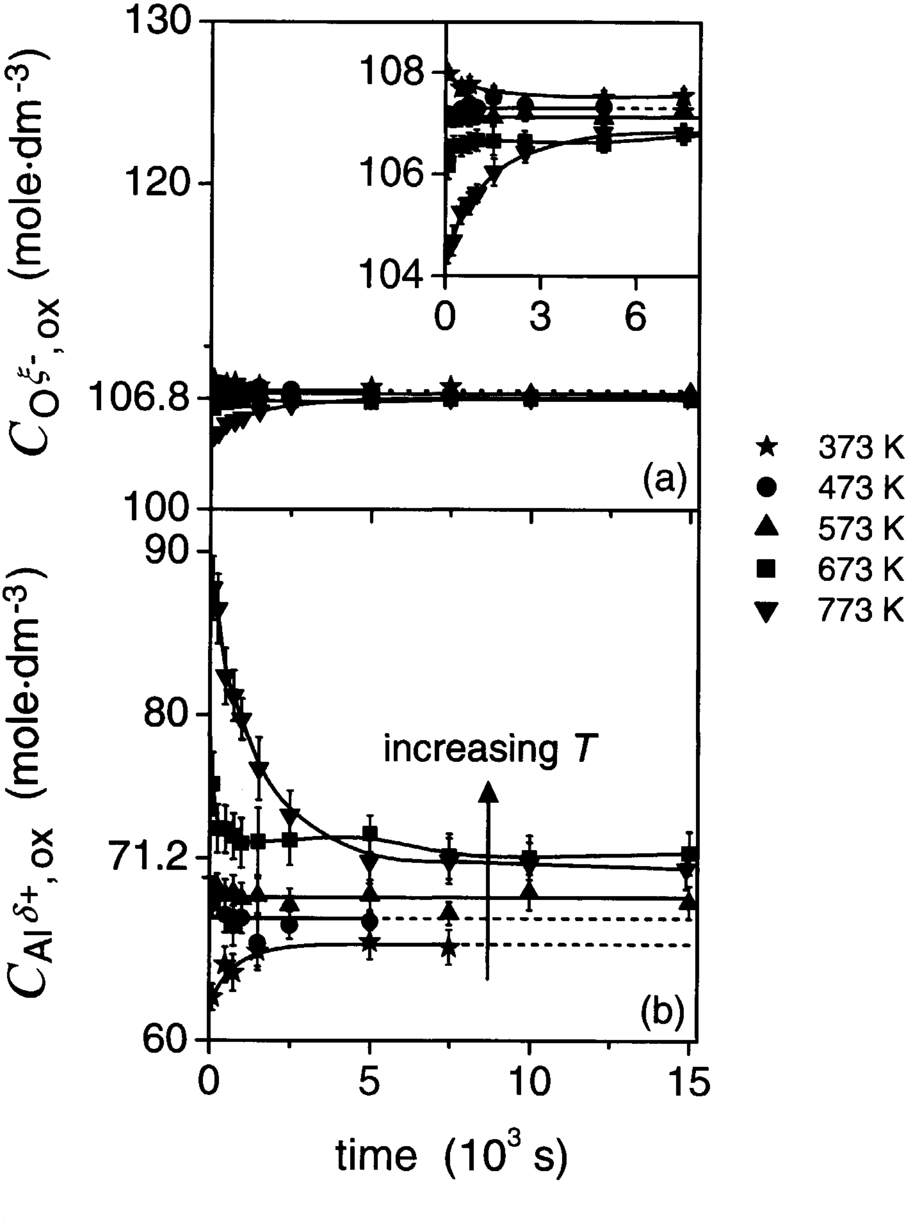

Figure 21. Molar density of (**a**) oxygen anions, $C_{O^{\xi-},ox}$, and (**b**) aluminium cations, $C_{Al^{\delta+},ox}$, in the oxide film as a function of oxidation time, for the oxidation of the bare (431) Al substrate at various temperatures (and p_{O_2} = 1.33×10^{-4} Pa). The molar densities were estimated from the metallic Al 2*p*, oxidic Al 2*p* and O 1*s* PZL photoelectron intensities of *only* the oxide-film component (cf. Sec. III) according to the procedure described in Appendix D. The Al and O molar densities of γ-Al_2O_3 are equal to 71.2 and 106.8 mole/dm^3, respectively (see Sec. III).

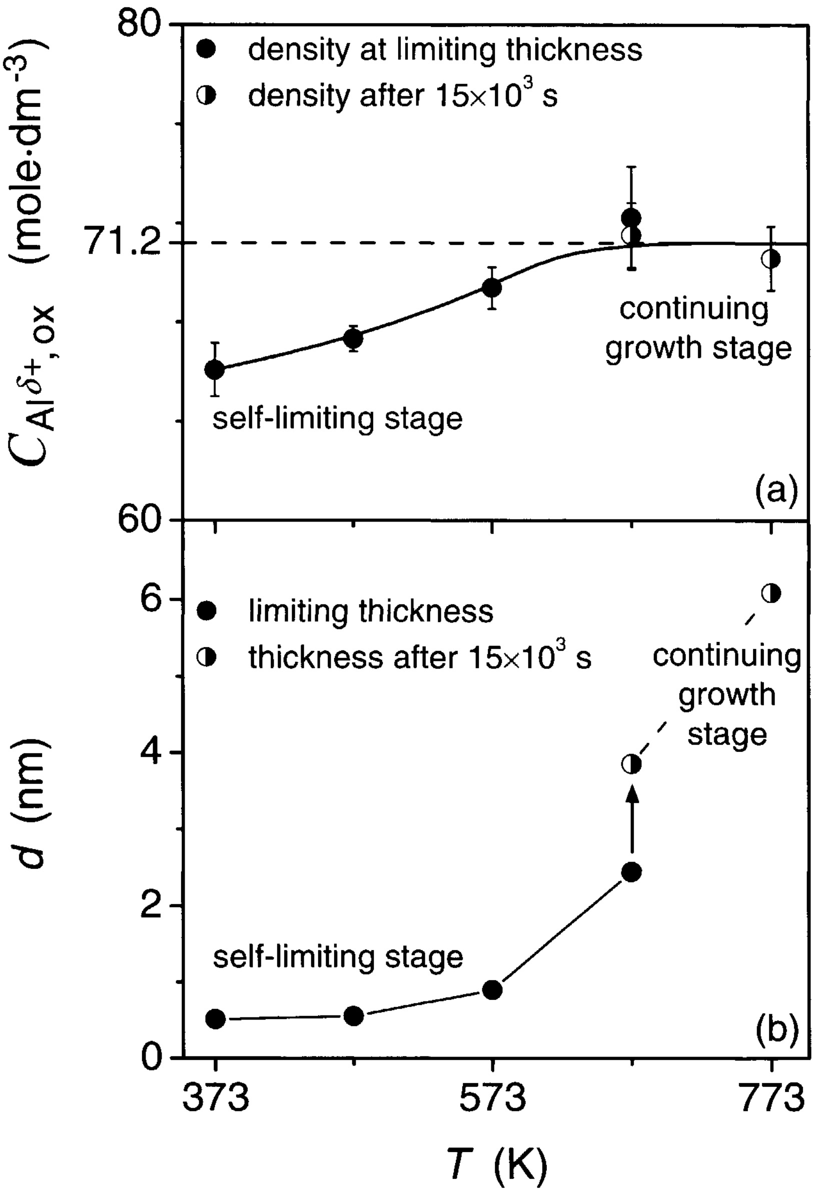

Figure 22. (**a**) Molar density of Al cations, $C_{\mathrm{Al}^{\delta+},\mathrm{ox}}$, in the oxide film at the limiting oxide-film thickness, and (**b**) the corresponding values of the limiting oxide-film thickness as a function of the oxidation temperature T, for the oxidation of the bare (431) Al substrate (at $p_{\mathrm{O}_2} = 1.33\times10^{-4}$ Pa). For T = 673 and 773 K, the thickness and (constant) Al molar density as reached in the second, slow (but *continuing*) oxidation stage after 15×10^3 s of oxidation (Sec. V) have been plotted too (*half open circles*). Note that for T = 773 K no limiting oxide-film thickness was identified. The Al molar density of γ-$\mathrm{Al_2O_3}$ equals 71.2 mole·dm^3 (*dashed horizontal line*).

As discussed in Sec. VII.B.1, the self-limiting oxide-film growth behaviour observed for oxidation temperatures $T \leq 573$ K, is typical for oxide-film growth under influence of the electric field set up by the negative oxygen ions chemisorbed onto the oxide surface (cf. Refs. [1-3, 45-50]). On this basis, from the observed deficiency of cations in these low temperature oxide films (cf. Fig. 22a), as well as the observed increase in Al cation concentration with both increasing oxidation temperature and oxidation time (for $T = 373$ K; see Fig. 21b), it is concluded that for $T \leq 573$ K the oxide-film growth rate during the initial, fast oxidation stage is governed by the electric-field enhanced, outward '*hopping*' (migration) of Al cations across the developing oxide-film (see Sec. VII.B.1). Similar to the oxide-film O/Al-ratio, the O/Al-ratio of the surface oxide may be expected to decrease with increasing oxidation temperature as well (due to the oxide film becoming relatively richer in Al at its surface for higher oxidation temperature), as indeed has been observed (see Fig. 23 in Sec. VI.B).

VI.A.2. High temperature oxide films

In contrast with the low temperature oxide films, the high temperature (i.e. $T \geq 673$ K) oxide films are relatively enriched with Al during the initial, fast oxidation regime (especially for the oxide films grown at 773 K; see Fig. 21b). Upon further oxidation the Al cation concentration decreases towards a constant value equal to that of γ-Al_2O_3, which is attained during the second, slow oxidation stage.[15] Note that during the initial fast oxidation stage at $T = 773$ K, there is also a small, but significant deficiency of O anions (as compared to γ-Al_2O_3), suggesting that the initial oxide film formed at 773 K contains a substantial amount of anion vacancies.

The presence of an excess of Al cations in thin Al-oxide films, as grown on an Al substrate by plasma or thermal oxidation, has been postulated earlier on work on the tunnelling behaviour of thin Al | Al-oxide | metal devices, to account for the low value of the measured electronic barrier height[16] as well as the increase of the barrier height upon both annealing and ageing (cf. Refs. [31-34]). The occurrence of an excess of Al cations and a deficiency of O anions in the developing oxide-films during the initial, fast oxidation stage at 773 K suggest that oxide-film growth during this stage may be rate limited by reactions at the oxide-gas interface such as oxygen desorption or oxide-film formation by surface reconstruction (see Sec. VII.B.2). The growth of the Al-enriched oxide-films during the initial, fast oxidation regime at 773 K is slower than the initial growth rate at 573 and 673 K (see Fig. 17 in Sec. V). This is attributed to the lower value of the O_2 sticking probability at 773 K (see Secs. V and VII.A).

---

[15] Since the corresponding oxide-film composition refers to a weighted averaged value due to the attenuation of the emitted photoelectrons (cf. footnote 2), it cannot be ruled out that an excess of Al cations in the oxide-film may be, to some extent, preserved in the near vicinity of the metal-oxide interface.

[16] The electronic barrier height, or metal-oxide work function is defined as the difference in energy between the Fermi level of the metal and the conduction band minimum of the oxide. An excess of Al cations in the oxide-film adjacent to the metal-oxide interface provides the means to lower the barrier height for electron tunnelling and/or thermal emission (cf. Refs. [31-34]).

For the thicker oxide-films grown at $T \geq 673$ K, i.e. with increasing oxidation time, the strong electric field across the developing oxide film due to the Mott potential has broken down (see Sec. VII.B.2 and e.g. Refs. [1-3, 45-50]). During this second, slow (continuing) oxidation stage (see Sec. V), the oxide film approaches its stoichiometric composition of Al_2O_3 (see Figs. 20-22 and footnote 15). As evidenced by the HREM analysis of oxide films grown after 20×10^3 s of oxidation at 673 and 773 K (see Sec. IV.A), the attainment of the oxide-films of their stoichiometric composition during the second, slow oxidation stage runs parallel with the transformation of the amorphous oxide into crystalline γ-Al_2O_3.

VI.B. Composition at the oxide surface

Since the surface oxide is very thin and located at the top of the developing oxide film in contact with UHV, a simple estimate for the O/Al-ratio of the surface oxide is obtained from

$$\frac{I_{O^{\xi-},ox}}{I_{Al^{\delta+},ox}} \cdot \frac{\sigma_{Al}}{\sigma_O} \tag{1}$$

where $I_{Al^{\delta+},ox}$ and $I_{O^{\xi-},ox}$ denote the PZL intensities of the resolved oxidic Al 2*p* and oxygen O 1*s* surface-oxide components (see Sec. III); and σ_{Al} and σ_O are the Al 2*p* and O 1*s* photoemission cross-sections, respectively (cf. Appendix A). Now, using the oxidic Al 2*p* and O 1*s* surface-oxide intensities given in Figs. 15a and c in Sec. IV.C, and taking the calculated Al 2*p* and O 1*s* photoemission cross-sections reported in Ref. [51], the thus obtained O/Al-ratio of the surface oxide has been plotted as a function of the oxidation temperature in Fig. 23.

Clearly, the O/Al-ratio of the surface oxide is much smaller than the value for stoichiometric Al_2O_3, i.e. O/Al-ratio $< \frac{3}{2}$. Its value decreases (approximately linearly) with increasing oxidation temperature from 0.7 (± 0.2) at 373 K to about 0.3 (± 0.1) at 673 K (see Fig. 23), indicating that the surface oxide becomes either more Al enriched or more O deficient with increasing oxidation temperature. An enrichment of Al at the Al-oxide surface is found both theoretically and experimentally for amorphous Al_2O_3 [52-54], γ-Al_2O_3 [55-57] as well as α-Al_2O_3 surfaces [58-60]. The relatively low O/Al-ratios between 0.3 and 0.7, as determined for the surface oxide in the present work, is compatible with similarly low values between 0.5 and 1.0 observed for the 'reduced' surface-oxide species present on an oxidised Al(111) surface [52], as well as for crystalline γ-Al_2O_3 surfaces [55]. As indicated by molecular dynamics (MD) simulations of unrelaxed and relaxed crystal surfaces of γ-Al_2O_3 in contact with vacuum at 300 K in Ref. [56], the occurrence of intrinsic cation vacancies in the defect spinel crystal structure of γ-Al_2O_3 (see also Sec. IV.A) has a large effect on the surface morphology. These MD simulations show that, Al atoms from below the surface region have migrated towards the surface during surface reconstruction, which resulted in an excess of Al atoms at the simulated surface as compared to the idealised (i.e. unrelaxed) γ-Al_2O_3 surface.

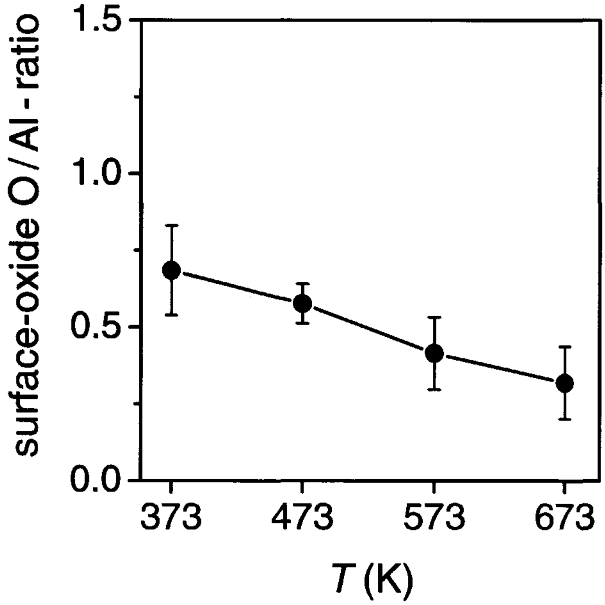

Figure 23. The average O/Al-ratio of the surface-oxide component as a function of the oxidation temperature T for the oxidation of the bare (431) Al substrate at $p_{O_2} = 1.33\times10^{-4}$ Pa. The error bars correspond to the standard deviations of the concerned O/Al-ratios for the different oxidation times (see Sec. II.B) at the temperature considered. Note that the surface-oxide component has not been observed for $T = 773$ K and has disappeared at $T = 673$ K for oxidation times $t > 2500$ s (see Sec. III).

VI.C. Chemical state of Al and O

The Al 2*p* BE, Al $KL_{23}L_{23}$ (^1D) KE and O 1*s* BE of both the surface-oxide and oxide-film component (cf. Sec. III) have been plotted as a function of the oxide-film thickness for the different oxidation temperatures considered in Figs. 24a - c, respectively. Literature values (ranges) for the oxide-film Al 2*p* BE for thin films of amorphous Al-oxide [61-64] and γ-Al_2O_3 [55, 63, 64] on an Al substrate have also been indicated in Fig. 24a.[17]

The estimated errors in the determined position of the peak maximum of the fitted Al 2*p*, Al $KL_{23}L_{23}$ (^1D) and O 1s (predominant) oxide-film components are 0.03, 0.07 and 0.03 eV, respectively. For the relatively much weaker surface-oxide components the corresponding estimated errors are 0.05, 0.1 and 0.05 eV, respectively. The average BE pertaining to the peak maximum of the metallic Al 2*p* main peak, as determined including all measured Al 2*p* XPS spectra recorded from the clean and oxidised Al(431) substrate, equals 72.80 (± 0.01) eV. The corresponding KE value of the subtracted metallic Al $KL_{23}L_{23}$ (^1D) and associated relative weak $KL_{23}L_{23}$ (^1S) main peak equal 1393.55 (± 0.01) and 1387.45 (± 0.01) eV, respectively. For each metallic peak, the position of the peak maximum in all spectra recorded is the same within the experimental error, indicating a high reproducibility of the XPS analysis (cf. Sec. III).

VI.C.1. The Al 2*p* oxide-film and surface-oxide components

The Al 2*p* BE of the *oxide-film* component increases with increasing oxidation temperature. For the oxide films grown at constant temperatures $T \leq 573$ K, the oxide-film Al 2*p* BE is practically independent of the oxide-film thickness (and oxidation time), whereas for the oxide-films grown at constant temperatures $T > 573$ K, the oxide-film Al 2*p* BE increases with increasing thickness. Note that, at $T > 573$ K, oxide films can be grown over a much wider thickness range than at lower temperatures (i.e. beyond the critical thickness up to which an amorphous oxide film is stable [5]; see Fig. 15 in Sec. V).

---

[17] The Al 2*p* BE values reported in the literature [55, 61-64] comprise the oxide-film Al 2*p* BE values of very thin (< 4 nm) Al-oxide films on all three low index single crystal faces of Al as well as on polycrystalline Al substrates. For assigning a value to the BE of the detected Al 2*p* photoelectrons of these thin oxide films, the same assumptions were made as in the present study (see Sec. III). If necessary the reported oxide-film Al 2*p* BE values were corrected (shifted) according to the difference in the value of the BE of the Al 2*p* metallic main peak as reported and as determined in this study (72.80 ± 0.01 eV).

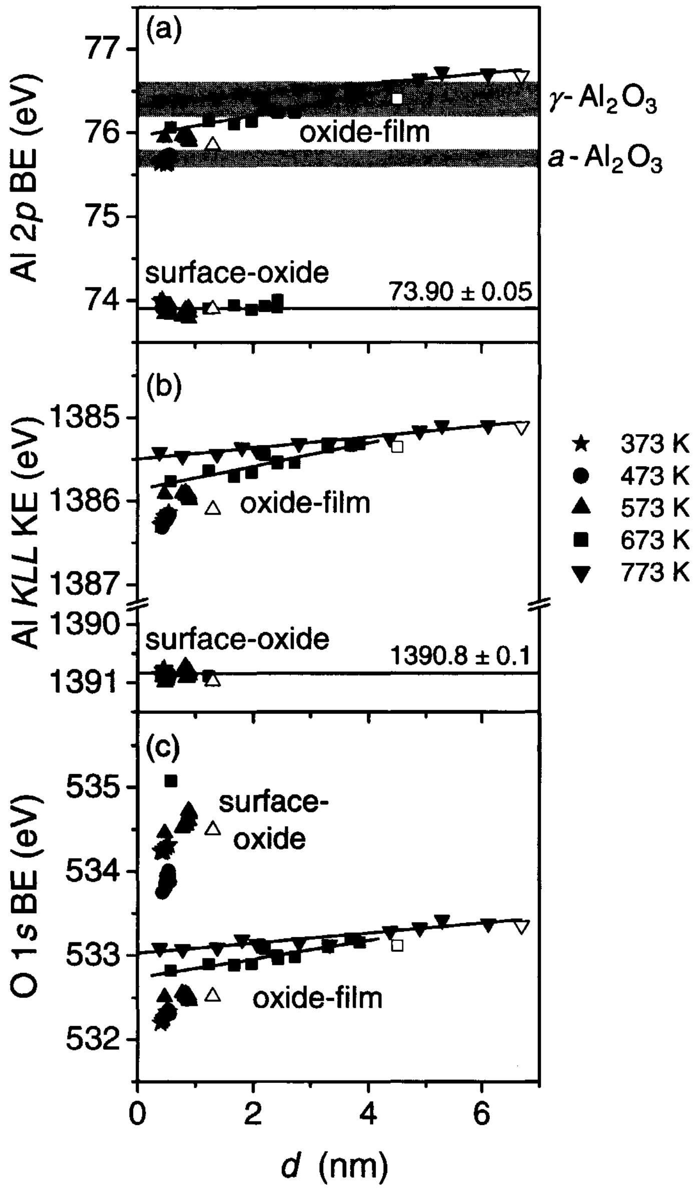

Figure 24. (**a**) Al 2*p* binding energy (BE), (**b**) Al $KL_{23}L_{23}$ (^1D) kinetic energy (KE) (note the opposite direction of the ordinate), and (**c**) O 1*s* BE of the surface-oxide and oxide-film components as resolved from the corresponding PZL spectra of the oxidised Al(431) substrate (see Sec. III) as a function of the oxide-film thickness *d* for the different oxidation temperatures considered. The open markers pertain to the oxide films also studied with HREM (see Sec. IV.A). In (**a**) the oxide-film Al 2*p* BE ranges for thin films of amorphous Al-oxide (i.e. *a*-Al_2O_3) [61-64] and γ-Al_2O_3 [55, 63, 64] on an Al substrate, as reported in the literature, have been indicated by the grey areas (cf. footnote 17). The solid lines given for $T = 673$ and 773 K represent linear fits through the data points concerned.

At 373, 473 and 573 K, the average value for the oxide-film Al 2*p* BE equals 75.65 (± 0.02), 75.71 (± 0.03) and 75.94 (± 0.03) eV, whereas at 673 and 773 K the oxide-film Al 2*p* BE increases with increasing thickness from 76.07 (± 0.03) to 76.45 (± 0.03) eV and from 76.38 (± 0.03) to 76.73 (± 0.03) eV, respectively.

Thus, it can be concluded that the *oxide-film* Al 2*p* BE increases with both increasing oxidation temperature and thickness (at 673 and 773 K). This is in contrast with the Al 2*p* BE of the *surface-oxide* component, which has a value of 73.90 (± 0.05) eV, independent of temperature and thickness (see Fig. 24a).

Comparison of the *oxide-film* Al 2*p* BE values, as determined in the present study, with the corresponding BE values reported in the literature for thin amorphous Al-oxide and (poly)crystalline γ-Al_2O_3 films on Al substrates (see Fig. 24a), confirms the present HREM analysis (see Sec. IV.A) showing that the oxide films grown at 373 and 473 K are amorphous, whereas at 773 K and during the second, slow oxidation stage at 673 K (cf. Sec. V) a crystalline γ-Al_2O_3 film is formed on the Al(431) surface. At 573 K and during the initial, fast oxidation stage at 673 K, the oxide-film Al 2*p* BE value lies in between those reported for amorphous and γ-Al_2O_3. Indeed, as evidenced by the HREM analysis of oxide films grown on an Al(431) substrate after 20×10^3 s of oxidation at 573, 673 and 773 K (see Sec. IV.A), the oxide film formed at 573 K is still entirely amorphous, whereas at 673 K and 773 K the grown oxide-film is predominantly constituted of crystalline γ-Al_2O_3. During the initial, fast oxidation stage at 673 K, the oxide-film Al 2*p* BE is about equal to the observed value of the oxide-film Al 2*p* BE of the amorphous oxide-films grown at 573 K, in agreement with the earlier interpretation (see Sec. IV.A) that oxide-film growth at 673 K starts with the formation of an amorphous oxide film, that gradually transforms into crystalline γ-Al_2O_3 during the second, slow oxidation regime.

The shift of the Al 2*p* surface-oxide components with respect to the Al 2*p* metallic main peak at 72.80 ± 0.01 eV (see above) of 1.1 (± 0.05) eV is about 0.2 eV lower than a reported XPS Al 2*p* BE shift of 1.3 - 1.4 (± 0.1) eV (cf. Refs. [54, 65, 66]), which was attributed to Al atoms of the Al substrate bound to chemisorbed oxygen at the surface. However, as will be discussed in Sec. VI.C.3, based on the O 1*s* BE of the surface-oxide component, it can be ruled out that the surface component is associated with a chemisorbed-oxygen species at the Al substrate or Al-oxide surface. Therefore, the Al 2*p* surface component found in the present work is attributed to a surface-oxide species (corresponding with an Al 2*p* BE of 73.90 ± 0.05 eV). Recognizing the low O/Al-ratio of the surface oxide component (as compared to the stoichiometric ratio of 1.5 for Al_2O_3; see Sec. VI.B), the Al-O bonds at the Al-enriched oxide surface will be less ionic than for γ-Al_2O_3 (cf. Refs. [54, 58-

60, 66]). The position of the Al $2p$ surface-oxide component at the lower BE side of the corresponding Al $2p$ oxide-film component is consistent with the Al-O bonds of the oxide-film being less ionic at its (Al-enriched) surface (cf. Refs. [54, 58-60, 66]).

VI.C.2. The Al $KL_{23}L_{23}$ oxide-film and surface-oxide components

The *oxide-film* Al $KL_{23}L_{23}$ (^1D) KE *decreases* (note the opposite direction of the ordinate in Fig. 24b) with both increasing temperature and thickness, and the *surface-oxide* $KL_{23}L_{23}$ (^1D) KE is (approximately) constant and located at the *higher* KE side of the oxide-film component, i.e. at 1390.8 ± 0.1 eV independent of temperature and thickness. At 373, 473 and 573 K, the average value for the oxide-film Al $KL_{23}L_{23}$ (^1D) KE equals 1386.22 (± 0.06), 1386.20 (± 0.06), 1385.93 (± 0.03), whereas at 673 and 773 K the oxide-film Al $KL_{23}L_{23}$ (^1D) KE decreases with increasing thickness from 1385.76 (± 0.07) to 1385.32 (± 0.07) eV and from 1385.46 (± 0.07) to 1385.09 (± 0.07) eV, respectively.

Because the oxide films grown at $T \leq 573$ K are relatively enriched with Al at the oxide surface (cf. Sec. VI.B), the chemical state of the Al ions will differ at the surface (cf. Sec. VI.C.1). Since the two-(core-electron)-hole state in the Auger process is more sensitive to the polarizability of the environment than the one-hole state in the photoemission process (cf. Ref. [35, 67-69]), it then follows that the chemical shift of the Al $KL_{23}L_{23}$ surface-oxide component with respect to the Al $KL_{23}L_{23}$ oxide-film component is expected to be *larger* than the corresponding chemical shift of the Al $2p$ surface-oxide component (with respect to the Al $2p$ oxide-film component). Indeed, the observed chemical shift of the Al $KL_{23}L_{23}$ surface-oxide component is about two to three times larger than the corresponding shift of the Al $2p$ surface-oxide component (compare Figs. 24a and b, respectively).

Likewise, if the shifts in oxide-film Al $2p$ BE and oxide-film Al $KL_{23}L_{23}$ KE with increasing temperature and thickness (for T = 673 and 773 K) would be related to a change in chemical state of the Al ions in the developing oxide film, then the concerned shift in oxide-film Al $KL_{23}L_{23}$ KE is expected to be relatively more pronounced. However, as follows from comparison of Figs. 24a and b, the absolute values of the shifts in oxide-film Al $2p$ BE and oxide-film Al $KL_{23}L_{23}$ (^1D) KE with both increasing temperature and thickness are of (practically) the *same magnitude*. Therefore, the concerned shifts in oxide-film Al $2p$ BE and oxide-film Al $KL_{23}L_{23}$ KE cannot be attributed (solely) to a change in chemical state of the Al ions in the developing oxide-film. The origin of these shifts will be further discussed in Sec. VI.C.5.

VI.C.3. The O 1*s* oxide-film and surface-oxide components

The *oxide-film* O 1*s* BE increases with both increasing temperature and thickness (at 673 and 773 K) with (practically) the same magnitude as the corresponding shifts in oxide-film Al 2*p* BE and oxide-film Al $KL_{23}L_{23}$ (^1D) KE (see Fig. 24). At 373, 473 and 573 K, the average value for the oxide-film O 1*s* BE equals 532.26 (± 0.05), 532.30 (± 0.03) and 532.52 (± 0.03) eV, whereas at 673 and 773 K the oxide-film O 1*s* BE increases with increasing thickness from 532.82 (± 0.03) to 533.20 (± 0.03) eV and from 533.08 (± 0.03) to 533.42 (± 0.03) eV, respectively.

The average value for the oxide-film O 1*s* BE of 532.36 (± 0.14) eV found for the oxide films grown at low temperatures (i.e. $T \leq 573$ K) agrees very well with the corresponding value of 532.3 (± 0.1) eV reported in Refs. [9, 10, 43]. The position of the O 1*s* surface-oxide component at the *higher* BE side of the O 1*s* oxide-film component (and the corresponding Al 2*p* surface-oxide component residing at the *lower* BE side of the Al 2*p* oxide-film component; see Sec. VI.C.1) is consistent with the Al-O bonds of the oxide-film being less ionic at the 'Al-enriched' oxide surface (cf. Refs. [54, 58-60, 66]).

In Refs. [9, 10, 43], an O 1*s* surface component at the *lower* BE side of the predominant O 1*s* oxide-film component has been reported (at 530.65 ± 0.5 eV), and attributed to an oxygen chemisorption species at the Al substrate and Al-oxide surface.[18] No such O 1*s* component has been observed in the present study.

In contrast with the surface-oxide Al 2*p* BE and surface-oxide Al $KL_{23}L_{23}$ (^1D) KE, which are independent of both temperature and thickness, the *surface-oxide* O 1*s* BE increases with increasing temperature for $T > 473$ K. At 373, 473, 573 and 673, the average surface-oxide O 1*s* BE equals 534.25 ± 0.05, 533.90 ± 0.09, 534.60 ± 0.08, and 535.08 ± 0.03 eV, respectively (note that the O 1*s* surface-oxide component has not been observed for $T = 773$ K and has disappeared at $T = 673$ K for oxidation times $t > 100$ s; see Sec. III). Recognizing the decrease in O/Al-ratio of the surface-oxide component with increasing temperature (see Fig. 23 in Sec. VI.B), then this might parallel with the increase of the surface-oxide O 1*s* BE with increasing temperature. However, it is not understood why such an effect is not observed for the surface-oxide Al 2*p* and Al $KL_{23}L_{23}$ (^1D) component.

---

[18] Besides the O 1*s* chemisorption component at the *lower BE side* of the predominant oxide-film O 1*s* peak, the O 1*s* XPS spectra in Figs. 4a and c of Ref. [10] also show a small, but distinct, shoulder at the *higher BE side* of the oxidic peak, which could be the surface-oxide component as discussed in the present study.

VI.C.4. Chemical and binding state plots

The changes in *chemical state* of the Al ions in the grown oxide films as a function of oxidation time and temperature can also be exhibited in a Chemical State (or Wagner [67, 68]) plot. This plot, as presented in Fig. 25a, is obtained by plotting the Al $KL_{23}L_{23}$ (^1D) KE values of both the surface-oxide and oxide-film component on the ordinate, and the corresponding Al $2p$ BE values on the abscissa (note the opposite direction of the abscissa). Then, the Modified Auger Parameter E_{Auger} = Al $KL_{23}L_{23}$ (^1D) KE + Al $2p$ BE, which is independent of the incident photon energy, reference level[19] and charging effects (cf. Refs. [35, 67-69]), is constant along straight lines with slope +1 in this plot (see Fig. 25a).

Since corresponding XPS spectra of the O $KL_{23}L_{23}$ Auger line before and after oxidation were not recorded, a chemical state plot for oxygen could not be constructed. Therefore, changes in the *binding state* of the Al-O bonds in the developing oxide film as a function of oxidation time and temperature are investigated by plotting the surface-oxide and oxide-film O $1s$ BE values versus the corresponding Al $2p$ BE values (in 'normal' direction along the ordinates) in Fig. 25b. Here, the 'Al-O binding state' parameter $E_{\text{Al-O}}$ = O $1s$ BE - Al $2p$ BE is constant along straight lines with slope +1 in this plot and, as holds for the modified Auger parameter E_{Auger} (see above), independent of the incident photon energy, reference level and charging effects.

The values of E_{Auger} for the surface-oxide and oxide-film component are practically independent of *both* the temperature and thickness and equal to 1464.7 (± 0.1) and 1461.85 (± 0.05) eV, respectively (Fig. 25a). The value of E_{Auger} = 1461.85 (± 0.05) eV for the oxide-film component pertains to the average value for the fully amorphous Al-oxide films grown at $T \leq 573$ K, as well as to the (predominantly) crystalline γ-Al_2O_3 oxide-films formed at $T >$ 573 K. The observed value of E_{Auger} lies in between the corresponding value of 1461.6 (± 0.1) eV reported for low-temperature oxidised (presumably amorphous) Al foils [62, 68-70] and γ-Al_2O_3 [35, 39, 68, 69, 71], and the average value of 1462.00 (± 0.05) eV reported for α-Al_2O_3 [35, 68-71].

---

[19] As also holds for the values of the Al $2p$, O $1s$ BE and Al $KL_{23}L_{23}$ (^1D) KE pertaining to Fig. 24 in Sec. VI.C, all BE or KE values measured with XPS are usually defined with respect to the Fermi level in the solid (here: oxide).

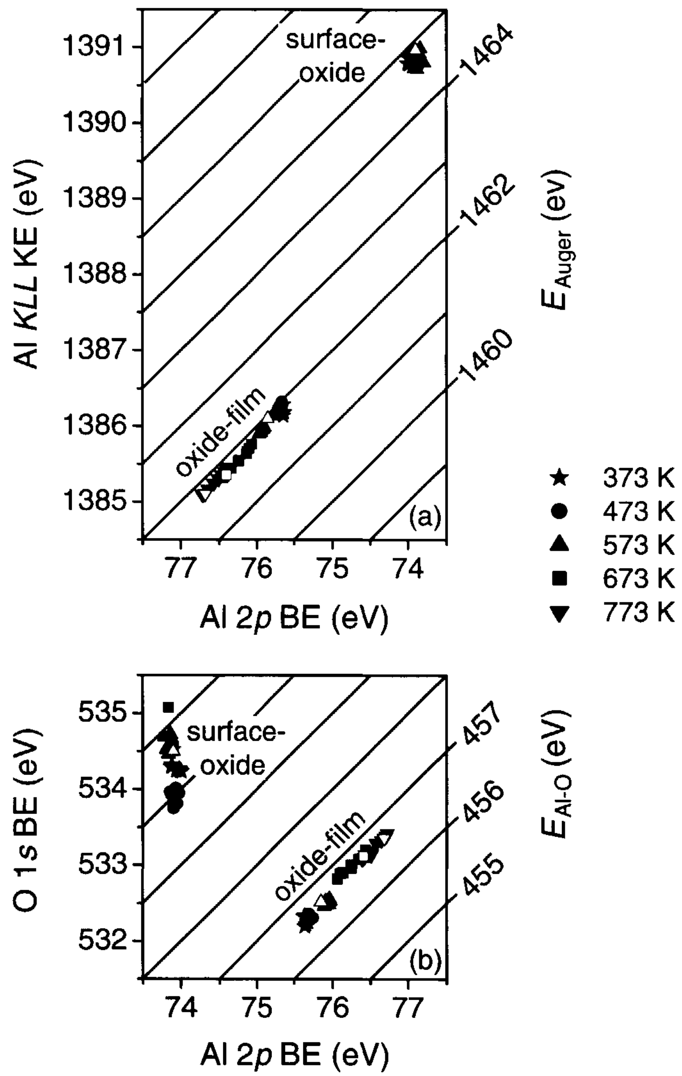

Figure 25. (**a**) Chemical state (or Wagner) plot obtained by plotting the surface-oxide and oxide-film Al $KL_{23}L_{23}$ (^1D) kinetic energies (KE) versus the corresponding Al 2*p* binding energies (BE) (note the opposite direction of the abscissa) for the oxidation of the Al(431) substrate (at $p_{O_2} = 1.33\times10^{-4}$ Pa) at the different oxidation times and temperatures concerned (see Sec. II.B). The Modified Auger Parameter E_{Auger} = Al $KL_{23}L_{23}$ (^1D) KE + Al 2*p* BE is constant along straight lines with slope +1. (**b**) Al-O binding state plot obtained by plotting the surface-oxide and oxide-film O 1*s* BE versus the corresponding Al 2*p* BE for the oxidation of the Al(431) substrate at the different oxidation times and temperatures concerned. The 'Al-O binding state' parameter $E_{\text{Al-O}}$ = O 1*s* BE - Al 2*p* BE is constant along straight lines with slope +1 in this plot. The open markers in (a) and (b) pertain to the oxide films also studied with HREM (see Sec. IV.A).

The values of $E_{\mathrm{Al-O}}$ for the surface-oxide and oxide-film component are also virtually independent of thickness. The value of $E_{\mathrm{Al-O}}$ of the *oxide-film* component, as determined for the fully amorphous oxide films grown at low temperatures (i.e. $T \leq 573$ K), i.e. $E_{\mathrm{Al-O}} = 456.59$ (± 0.04) eV, is only slightly (i.e. about 0.1 eV) smaller than the corresponding value of 456.71 (± 0.04) eV obtained for the (largely) crystalline γ-Al_2O_3 oxide films formed at higher temperatures (see Sec. IV.A). Both values of $E_{\mathrm{Al-O}}$ observed for the oxide-film component agree well with the corresponding (average) value of 456.6 (± 0.1) eV reported for low-temperature oxidised Al foils (presumably amorphous) [62, 70], and are about 0.5 (± 0.2) eV higher than the average value of 457.1 (± 0.2) eV reported for γ-Al_2O_3 [35, 69, 71]. The value of $E_{\mathrm{Al-O}}$ for the *surface-oxide* component increases distinctly with increasing temperature solely due to the increase of the surface-oxide O 1*s* BE with increasing temperature for $T > 473$ K (attributed to the decrease in ionicity of the Al-O bonds at the 'reduced' oxide surface with increasing temperature see Sec. VI.C.3). At 373, 473, 573 and 673 K, the average value of $E_{\mathrm{Al-O}}$ for the surface-oxide component equals 460.3 (± 0.1), 460.0 (± 0.1), 460.7 (± 0.1), and 461.1 (± 0.1) eV, respectively.

The values of E_{Auger} and $E_{\mathrm{Al-O}}$ for the *oxide-film* component are (practically) independent of both the temperature and thickness (see above), because the oxide-film Al 2*p* BE and O 1*s* BE increase, and the Al $KL_{23}L_{23}$ (^1D) KE decreases, with the ***same amount*** with both increasing temperature and increasing thickness (see Fig. 24; see also discussion in Sec. VI.C.2). Clearly, the major part of the shifts in BE (and KE) of the concerned oxide-film components can*not* be attributed to a change in chemical state of the Al ions and/or a change in Al-O binding state in the developing oxide-film due to the gradual transition from amorphous Al-oxide to crystalline γ-Al_2O_3 (see Sec. IV.A). This implies that the short range ordering of the amorphous Al-oxide films grown at relatively low temperatures in this study indeed (see Footnote 3 in Sec. III) closely resembles that of the crystalline γ-Al_2O_3 films grown at more elevated temperatures (cf. Sec. IV.A).

VI.C.5. Origin of binding (or kinetic) energy shifts of oxide-film components

As has already been shown in the previous section (Sec. VI.C.4), the chemical state of the Al ions as well as the Al-O binding state in the developing oxide film is practically independent of both temperature and thickness. Therefore, it will be argued in this section that the major part of the observed shift of the Al 2*p*, O 1*s* and Al $KL_{23}L_{23}$ KE *oxide-film* components, with both increasing temperature and increasing thickness, is due to a shift in the position of the Fermi level within the band gap of the developing oxide-film.

For an intrinsic insulator (at 0 K) - i.e. an insulator with a perfect crystal structure - the Fermi level is located at the centre of the energy gap between the valence and conduction band (i.e. the band gap) (cf. Ref. [72]). However, the oxide films grown in this study at $T \leq$ 573 K are amorphous (see Sec. IV.A), non-stoichiometric (see Sec. VI.A.1) and Al-enriched at the surface (see Sec. VI.B). It has already been recognised [57-59] that an enrichment of Al at the Al-oxide surface induces empty states within the band gap, at some 4 - 5 eV below the conduction band minimum for α-Al_2O_3 [58, 59] and γ-Al_2O_3 [57]. Consequently, the Fermi level occurs at a lower level within the band gap as compared to the intrinsic Fermi level (cf. Refs. [56-59, 72]). A lowering of the Fermi level results in a lower value of the oxide-film Al 2*p* BE and O 1*s* BE, and a higher value of the oxide-film Al $KL_{23}L_{23}$ KE, as measured with XPS, because these values are all defined with respect to the Fermi level in the oxide as a reference (as assumed to be coupled to that of the parent Al substrate and thus to the spectrometer; see Sec. III). The more Al-enriched the oxide surface, the more pronounced this lowering of the Fermi level (cf. Refs. [56-59, 72]), and consequently the lower the resulting value of the oxide-film Al 2*p* BE and O 1*s* BE, and the higher the value of the oxide-film Al $KL_{23}L_{23}$ KE. The amount of Al enrichment at the oxide surface is proportional to the intensity of the Al 2*p* *surface-oxide* component. Thus, if the shifts of the *oxide-film* Al 2*p*, O 1*s* and Al $KL_{23}L_{23}$ components *with increasing temperature* (see Fig. 24 in Sec. VI.C) are due to an Al-enrichment-at-the-oxide-surface induced shift of the Fermi level, then (*i*) these shifts as a function of the corresponding Al 2*p* *surface-oxide* intensities (see Fig. 15 in Sec. IV.C) should be identical, and (*ii*) the oxide-film Al 2*p* BE and O 1*s* BE should decrease, and the oxide-film Al $KL_{23}L_{23}$ KE increase, with increasing intensity of the Al 2*p* surface-oxide component (see above discussion). This is indeed in agreement with our observation (see Fig. 26).

Considering Fig. 24, it may be suggested that the shifts in BE (and KE) of the oxide-film component as a function of temperature are due to a gradual transition from amorphous Al-oxide to crystalline γ-Al_2O_3 (see Sec. IV.A). However, recognizing the constant chemical state of the Al ions as well as the constant Al-O binding state in the developing oxide film (cf. Fig. 25 in Sec. VI.C.4), the strong correlation of the oxide-film BE (and KE) shifts with the Al 2*p* surface-oxide intensity (see Fig. 26) makes it likely that the concerned shifts are mainly due to a decrease of the amount of surface oxide with increasing temperature (see Fig. 15 in Sec. IV.C), rather then structural changes of the oxide film.

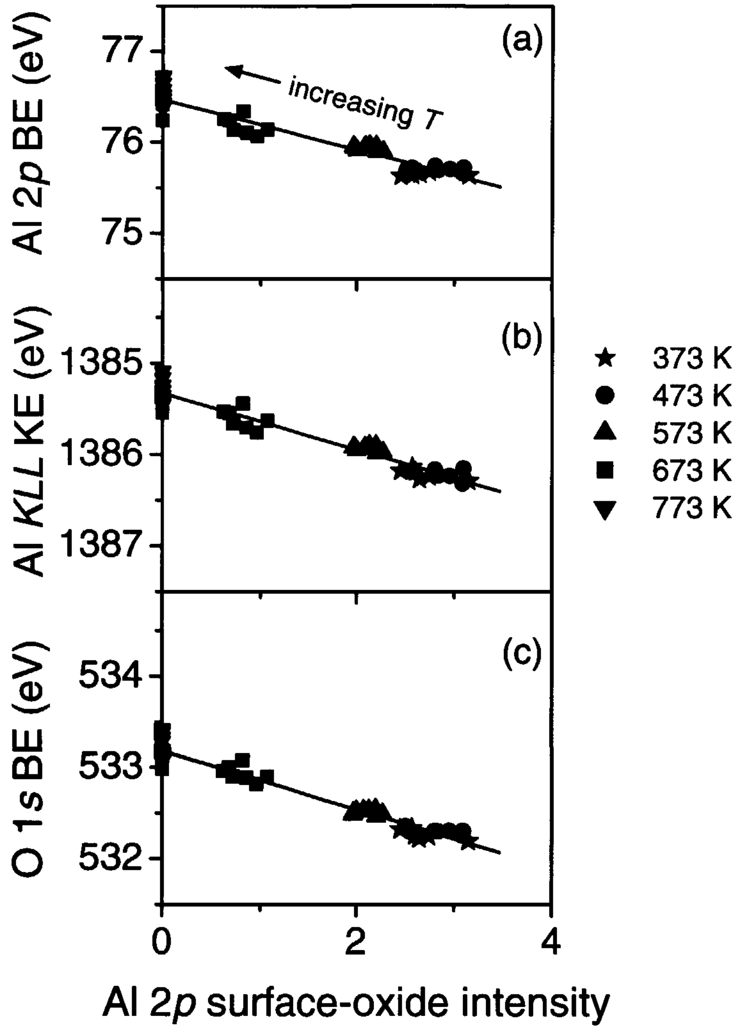

Figure 26. (**a**) Al 2*p* binding energy (BE), (**b**) Al $KL_{23}L_{23}$ (^1D) kinetic energy (KE) (note the opposite direction of the ordinate), and (**c**) O 1*s* BE of the *oxide-film* component (see Fig. 24 in Sec. VI.C) as a function of the average, normalised intensity of the Al 2*p* *surface-oxide* component (see Fig. 15 in Sec. IV.C) for the different oxidation temperatures considered.

For the crystalline oxide films grown at 773 K (and for the second stage of oxidation at 673 K), the Al 2*p*, Al $KL_{23}L_{23}$ and O 1*s* surface-oxide components have not been observed (see Sec. III). Therefore, the observed BE (and KE) shifts of the concerned oxide-film components *with increasing thickness* at constant temperature for T = 773 K (and for the second stage of oxidation at 673 K; see Fig. 24) cannot be attributed to a change in amount of surface oxide with increasing thickness at constant temperature. As explained below, these shifts are ascribed to the existence of a region of positive space charge in the oxide film near the metal/oxide interface (cf. Fig. 27). This space charge is induced by the remnant of the excess of Al cations near the metal/oxide interface present in the initially Al-enriched oxide film grown at high temperatures (see Fig. 21b and footnote 15 in Sec. VI.A; see also e.g. Refs. [31, 32, 34]). Consequently, a negative (counter) charge resides in the metal substrate at the metal/oxide interface. The corresponding resulting field in the oxide film will be such that the force on an electron in the oxide is directed away from the metal substrate (cf. Refs. [72-75]). As demonstrated in e.g. Refs. [72-75] and as schematically illustrated in Fig. 27, the potential energy of an electron in the space charge region of the oxide will be higher than in the absence of this space charge, and thus the BE (with respect to the Fermi level) increases with increasing distance to the metal/oxide interface. Since the measured oxide-film BE (and KE) values refer to weighted average values pertaining to the entire oxide film (cf. Sec. A.2 in Appendix A), it then follows that the measured XPS oxide-film Al $2p$ BE and O $1s$ BE increase (and the oxide-film Al $KL_{23}L_{23}$ KE decreases) with increasing oxide-film thickness for the initially Al-enriched, high temperature (i.e. $T \geq 673$ K) oxide films (see Fig. 24).

VII. General discussion

VII.A. Formation of a 'closed' oxide film

The rate of oxygen supply from the gas phase to the surface is controlled by the number of gas molecules I hitting a surface per unit time and area at constant p_{O_2} and constant T, which according to the kinetic gas theory obeys (cf. Refs. [1, 3]):

$$I = \frac{p_{O_2}}{\sqrt{2\pi mkT}} \qquad \textbf{(2)}$$

where m is the mass of the gas molecule and k (= 1.38×10^{-23} J·K^{-1}) is Boltzmann's constant. If oxygen supply from the gas phase to the oxide surface would limit the oxide-film growth rate, and because I does not depend on time [see Eq.(2)], a linear growth law would occur. Evidently, this is not the case here (at least not for oxidation times $t > 100$ s; cf. Fig. 17 in Sec. V).

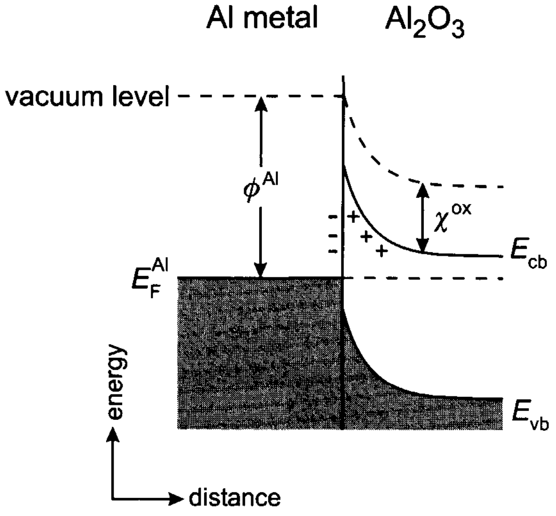

Figure 27. Simplified electron energy-level diagram of the contact region between the Al metal and an Al_2O_3 film containing excess Al cations near the metal/oxide interface (i.e. the Al_2O_3 film is conceived as a *n*-type semiconductor with a wide band gap; cf. Refs. [31-35]). The excess of Al cations induces a positive space charge region in the oxide near the metal/oxide interface (with a negative (counter) charge residing in the metal substrate at the metal/oxide interface). Consequently (cf. Refs. [72-75]), the potential energy of an electron in the space charge region of the oxide is higher near the metal/oxide interface than further away from this interface. For further details, see Sec. VI.C.5 and Refs. [31, 32, 34, 72-75]. The work function of the Al metal, the electron affinity of the oxide, the Fermi level of the Al metal (as assumed to be coupled to that of the oxide), as well as the valence band maximum and conduction band minimum of the oxide, have been indicated by ϕ^{Al}, χ^{ox}, E_F^{Al}, E_{vb} and E_{cb}, respectively. Note that the core-electron levels in both the metal and the oxide lie at much lower energies than the corresponding valence and conduction bands and therefore have not been indicated here.

Although the decrease of enthalpy upon dissociative chemisorption of $O_2(g)$ onto the Al surface is strong (i.e. the dissociation is strongly exothermic; cf. Ref. [76]), only a very small fraction of the impinging $O_2(g)$ molecules is expected to be chemisorbed onto the Al surface, because of the low value of 10^{-3} to 10^{-2} for the sticking probability[20] of $O_2(g)$ onto the bare (and oxidised) Al surface (cf. [9, 19, 45, 77, 78]). This low (i.e. very much less than unity) value for the $O_2(g)$ sticking probability may be attributed to a high activation energy for oxygen dissociation and/or the occurrence of a weakly bound oxygen, intermediate state of adsorption (cf. Refs. [9, 10, 19, 42, 43, 45, 77, 78]).

---

[20] The sticking probability has been defined as the ratio of the rate of oxygen (O_2) chemisorption to the rate of impingement of $O_2(g)$ molecules on the metal surface [cf. Eq. (2)].

The occurrence of island formation (see Sec. IV.B) suggest that the initial oxidation involves the lateral diffusion over the bare Al substrate surface of mobile oxygen species.[21] Apparently, at $T \leq 473$ K, the mobility of the oxygen species is very low, thus island formation is hindered, and consequently the bare Al substrate is already covered with a uniform 2 - 3 'oxide' MLs thick oxide film within 100 s of oxidation (see Secs. IV.A and V). With increasing temperature, both the lateral diffusion of the oxygen species and the rate of oxide formation increase: a decrease of the average oxide island density occurs.

3D oxide islands have already formed at $T > 473$ K within the shortest oxidation time (100 s) employed here (because both the *oxide-film* components and the SP plasmons peaks associated with the corresponding metallic main peak are observed in the XPS spectra of the oxidised metal; cf. Sec IV.B). The transformation of the chemisorbed oxygen into Al-oxide may have proceeded by one of the following mechanisms or a combination thereof (cf. Refs [1, 2, 42, 46, 47, 52, 78, 80-86]): (*i*) penetration (i.e. dissolution) of chemisorbed oxygen into the subsurface region of the parent metal substrate (cf. Refs. [52, 83-85]), (*ii*) a switching of places between the parent metal substrate atoms and the adsorbed oxygen atoms through a mechanism of place exchange (cf. Refs. [1, 80-82]), (*iii*) outward movement ('hopping') of Al substrate atoms or ions into the interstices of the closed-packing of chemisorbed oxygen atoms (cf. Refs. [1, 2, 45-47] and Sec. VII.B.1).

A 'closed' oxide film is formed after 200, 500 and 750 s of oxidation at 573, 673 K and 773 K, respectively (see Sec. IV.B). The local 'necks' in the oxide film, as observed in the studied HREM cross-sections (cf. Figs. 5 and 6 in Sec. IV.A), are interpreted as remnants of the island-by-layer oxide-film growth mechanism.

The sticking probability increases with increasing temperature within the temperature range of 243 – 600 K [9, 45] indicating that the dissociative chemisorption of O_2 is thermally activated [9, 10, 19, 42, 45]. At more elevated temperatures (i.e. $T > 600$ K) the sticking probability decreases with increasing temperature, due to a high oxygen desorption rate [9,

---

[21] Apparently, the oxide islands act as sinks, trapping the migrating oxygen species. As indicated by density-functional calculations for the clean and O-covered Al(111) substrate [79], the formation of oxygen islands on the Al(111) surface is driven by the strong nearest-neighbour attraction between oxygen atoms adsorbed on the Al(111) surface. This attraction for adsorbed oxygen atoms on the Al surface is in contrast with the strong repulsion that is usually found between adsorbed oxygen atoms on other metal surfaces (e.g. Cu and Ni) [79].

45]. This explains the slower initial growth rate observed here at 773 K as compared to the initial growth rates at 573 and 673 K (see Fig. 17 in Sec. V).

VII.B. Growth of a 3D oxide film

Oxide-film growth, after formation of a closed oxide film on the Al metal substrate, requires that Al substrate atoms and/or chemisorbed oxygen surface atoms move into and through the developing oxide film towards the oxide-gas and/or metal-oxide interface, respectively. The migrating species is generally assumed to be ionic (e.g. for Al, Fe, Cu and Ta substrates; cf. Refs. [1-3, 45-48, 87, 88]). For the realization of migration of an ionic species, electrons must move through the oxide as well to maintain overall charge neutrality. Energy barriers for both ion and electron movement into and through the oxide exist. The driving forces for overcoming these energy barriers form the basis for distinguishing low temperature from high temperature oxidation, as discussed below.

VII.B.1. Low temperature oxidation

Oxide-film growth on the bare Al metal substrate at $p_{O_2} = 1.33\times10^{-4}$ Pa for $T \leq 573$ K proceeds by an initial, very fast oxidation stage followed by an abrupt and drastic reduction of the oxide-film growth rate to virtually zero within less than about 250 s (see Sec. V). A model featuring this limiting-thickness behaviour of the oxide-film growth kinetics was first proposed by Mott and Cabrera (MC) [46, 47, 89] and further developed by Fromhold and Cook [2, 49, 50, 90, 91] and Fromm [3, 48].

Under the constraint that no net electric charge is transported through the oxide and no space charge builds up in the oxide film, the cation current, which is intrinsically the rate-determining step in this stage of the oxidation process, equals the small difference between the forward and the reverse tunneling flux of electrons (cf. Ref. [2, 3, 48-50, 90, 91]). As illustrated in Fig. 28, free electrons from the Fermi level of the parent metal substrate traverse the developing oxide film by either tunneling or thermionic emission and go into the acceptor levels of oxygen molecules or atoms adsorbed onto the oxide surface. An 'equilibrium' electric potential, designated as the Mott potential V_M, is established between the metal substrate and the resulting chemisorbed oxygen species (presumably O_2^- and/or O^-; cf. Refs. [1, 3, 48] and Fig. 28). The corresponding resulting uniform electric field $E_0 = - V_M / x(t)$ (where $x(t)$ denotes the oxide-film thickness at time t) provides the means to lower the energy barriers for the forward 'hopping' of cations from the parent metal substrate into and through the developing oxide film towards the reacting oxide/gas interface (see Fig. 28).

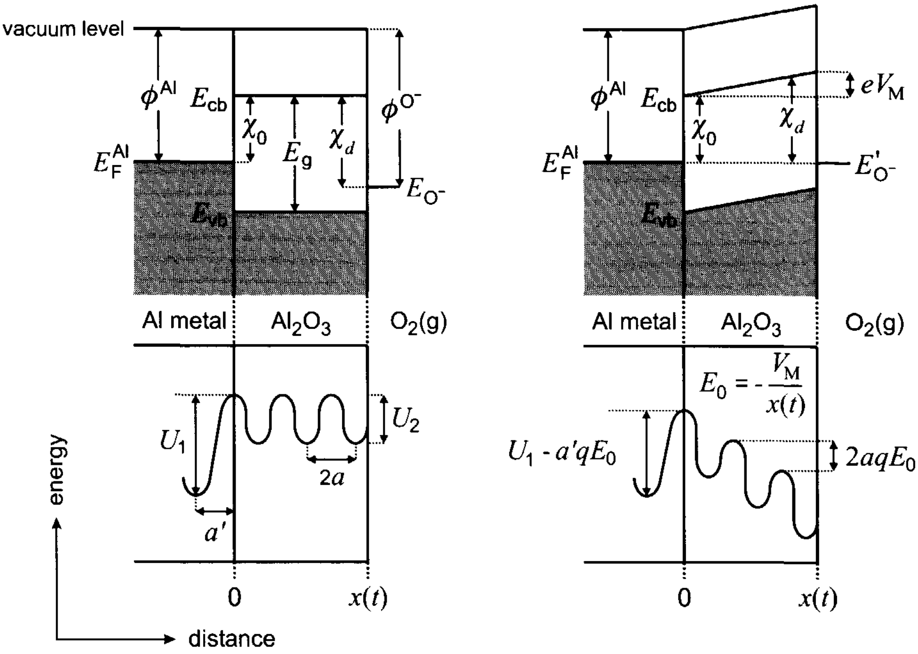

(*a*) before electron transfer
(i.e. without field)

(*b*) after electron transfer
(i.e. with field)

Figure 28. Schematic electron energy-level diagram of the model metal/oxide/oxygen system (*upper part*) and potential-energy diagram for Al cations near the metal/oxide interface and in a discrete lattice of the oxide (*lower part*): (**a**) before transport of free electrons from the Fermi level (E_F^{Al}) of the metal substrate towards acceptor levels (E_{O^-}) of oxygen molecules or atoms adsorbed onto the oxide surface, and (**b**) when coupled currents of Al cations and electrons occur, with Al cation transport as the intrinsically rate-limiting step for oxide-film growth. As a result an 'equilibrium' electric potential V_M = ($\chi_0 - \chi_d$) / e is established in (b), corresponding to a uniform electric field $E_0 = -V_M / x(t)$ across the oxide film of thickness $x(t)$ at time t. This electric field lowers the energy barriers U_1 and U_2 for the forward 'hopping' of cations between two adjacent potential minima across the metal/oxide interface (U_1) and within the oxide film (U_2) by an amount of $a'qE_0$ and of aqE_0, respectively (q is the charge of a cation, and a' and a are the distances from the potential minimum to the top of the barrier concerned). The metal-oxide and oxide-oxygen work functions χ_0 and χ_d are relative to the bottom of the conduction band (E_{cb}) in the oxide. The work functions ϕ^{Al} and ϕ^{O^-} are relative to the vacuum level. Further, the band gap and the valence band maximum in the oxide have been denoted by E_g and E_{vb}, respectively.

Thus, the forward current of cations is enhanced by the intrinsic electric field. This gives rise to the observed (very) fast initial oxidation rates (see Sec. V) as long as the Mott field is maintained (i.e. as long as electron transport by tunneling occurs intrinsically at a much faster rate than the intrinsic cation transport rate; at low temperatures, the concentration gradient driven diffusion of cations into and through the oxide film is usually negligibly small). The rate of electron transport across the developing oxide film by tunneling decreases exponentially with increasing oxide-film thickness (cf. Refs. [3, 48, 50]]). Consequently, at low temperatures, where the rate of electron transport by thermionic emission is effectively zero for metal-oxide systems with a metal-oxide work function χ_0 > 1 eV [89] (for Al/Al-oxide: χ_0 ~ 1.6 eV [32, 33]), the constraint of coupled currents of electrons and cations implies that a limiting oxide-film thickness occurs.

VII.B.1.a. Application of Mott-Cabrera model to low temperature oxidation of Al

The following equation has been derived for the initial oxide-film growth rate on the bare metal substrate at low temperatures, under the assumption that the growth rate is limited by the migration of cations under influence of the electric field $E_0 = -V_M / x(t)$ due to the Mott potential V_M (see Sec. VII.B.1 and e.g. Refs. [46, 47, 89])

$$\frac{dx}{dt} = \Omega n \nu \exp\left(\frac{-U + qaE_0}{kT}\right) \tag{3}$$

where Ω is the volume of oxide formed per cation; n the number of cations per unit area which may jump through the rate-limiting energy barrier U (where U can be U_1 or U_2; see Fig. 28 and footnote 22); ν the attempt frequency of the cation jump; q the charge of the migrating cation; $2a$ the distance from the potential minimum to the next potential minimum; k the Boltzmann constant; T denotes the temperature. Then, defining the effective 'limiting' oxide-film thickness x_{lim} as the value of the thickness reached when $dx / dt = 10^{-15}$ m/s (i.e. when the oxide-film growth rate has reduced to about one 'oxide' ML per 10^5 s; cf. Sec. V), it follows from Eq. (3), using $E_0 = -V_M / x_{\text{lim}}$, that

$$\frac{1}{x_{\text{lim}}} = -\frac{k\ln\left(10^{-15}/\Omega n \nu\right)}{qaV_M} \cdot T - \frac{U}{qaV_M} \tag{4}$$

---

[22] It is noted that Eq. (3) is equally valid whether the rate-limiting barrier is located at the metal-oxide interface or inside the oxide film (cf. Refs. [46, 47, 49]; see the potential-energy barrier diagrams shown in Fig. 28; U_1 vs. U_2).

Hence, a linear relation is predicted between the reciprocal of the 'limiting' thickness and the oxidation temperature. Indeed, considering the values for the limiting oxide-film thicknesses in the temperature range of 373 - 673 K, as observed in the present study on the dry, thermal oxidation of an Al(431) substrate at $p_{O_2} = 1.33 \times 10^{-4}$ Pa (see Sec. V), such a linear relation is observed; see Fig. 29.

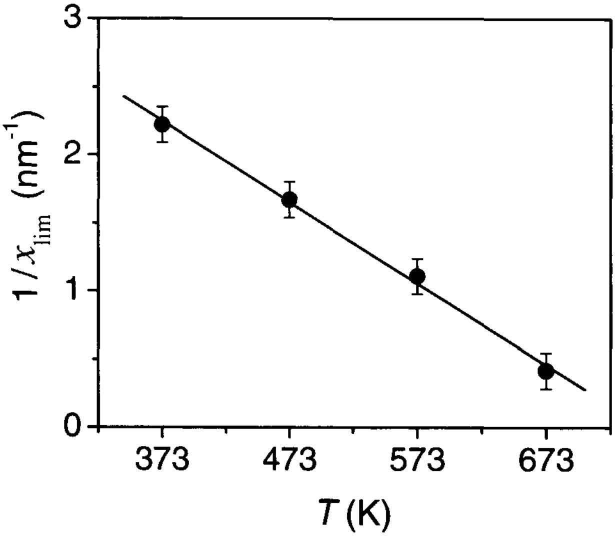

Figure 29. Reciprocal of the limiting oxide-film thickness in the temperature range of 373 - 673 K as a function of the oxidation temperature T, for the dry, thermal oxidation of an Al(431) substrate at $p_{O_2} = 1.33 \times 10^{-4}$ Pa (see Sec. V). The straight line represents a linear least squares fit through the data points.

The values of the Mott potential V_M and the rate-limiting energy barrier for cation motion U (where U can be U_1 or U_2; see Fig. 28), pertaining to the initial, fast oxide-film growth stage on the Al substrate (at $p_{O_2} = 1.33 \times 10^{-4}$ Pa) at low temperatures, can be determined straightforwardly from the tangent and the intercept of the straight line fitted through the data points of Fig. 29, provided that values for Ω, v, n, q and a are known. The volume of oxide formed per Al cation, the attempt frequency of the Al cation jump and the charge of the migrating Al cation are taken equal to $\Omega = 0.233$ nm^3 [5], $v = 10^{12}$ s^{-1} [45, 46] and $q = 3e$ C (the elementary charge $e = 1.6022 \times 10^{-19}$ C), respectively. The value for the number n of cations per unit area which may jump through the rate-liming energy barrier U, and the value for the distance $2a$ between the potential minimum and the next potential minimum depend on which cation jump is rate controlling: in simple, extreme cases the barrier is located either at the metal/oxide interface or within the oxide film (cf. Fig. 28; U_1 vs. U_2). If the rate-limiting energy barrier for cation motion is located at the metal/oxide interface, then U (= U_1) pertains to the hopping of an Al cation from the surface of the parent metal substrate into an octahedral or tetrahedral interstitial position in the oxide. On the other hand, if the rate-limiting energy barrier for cation motion occurs within the oxide, then U (= U_2) pertains to the hopping mechanism of Al cations between octahedral and/or tetrahedral interstices within the oxide. Estimates of n and $2a$ for the above hopping mechanisms considered, as well as the resulting values of the Mott potential V_M and the rate-limiting energy barrier for cation motion U have been gathered in Table II. It follows that the Mott potential is in the range of -1.3 to -1.9 V for the dry, thermal oxidation of the Al(431) substrate at $T \leq 673$ K (and $p_{O_2} = 1.33\times10^{-4}$ Pa). The corresponding value obtained for the height U of the rate-limiting energy barrier is about independent on the type of rate-limiting energy barrier considered: $U = 2.5 \pm 0.1$ eV (see Table II).

It may be assumed that diffusion in the amorphous oxide films (developing at the low oxidation temperatures considered here) is isotropic. Consequently, if the rate-liming energy barrier for cation motion would be located within the developing amorphous Al-oxide film, then the kinetics of oxide-film growth would be independent of the crystallographic orientation of the parent Al metal substrate. However, the oxide-film growth rate on single-crystalline Al substrates does vary with substrate orientation (cf. Ref. [7]). Hence, the rate-limiting energy barrier for cation motion must be located at the metal/oxide interface (and thus $V_M = -1.6$ V and $U = 2.6$ eV; cf. Table II).

Table II. Calculated values for the Mott potential V_M and the rate-limiting energy barrier for cation motion U, for the dry, thermal oxidation of the Al(431) substrate at $p_{O_2} = 1.33\times10^{-4}$ Pa, for three possible rate-limiting cation hopping mechanisms (as indicated in the first column). The values for V_M and U were determined from the tangent and the intercept of the straight line fitted through the data points of Fig. 29. The corresponding values used for the number of cations per unit area, n, which may jump through the rate-limiting barrier U, and the distance $2a$ between a potential minimum and the next potential minimum have been given too. The values of n and $2a$, pertaining to the amorphous oxide films grown at low temperatures in the present study, were taken to be equal to the corresponding values for γ-Al_2O_3 (cf. footnote 3 in Sec. III).

rate-limiting cation hopping mechanism	n (m^{-2})	$2a$ (nm)	V_M (V)	U (eV)
from metal substrate surface into octahedral or tetrahedral interstices within oxide	1×10^{19}	0.24	-1.6	2.6
between adjacent octahedral interstices within oxide	4×10^{18}	0.28	-1.3	2.5
between adjacent tetrahedral interstices within oxide	4×10^{18}	0.20	-1.9	2.5

VII.B.2. High temperature oxidation

Oxide-film growth on the bare Al metal substrate at p_{O_2} = 1.33×10^{-4} Pa at more elevated temperatures (i.e. $T \geq 673$ K) also proceeds by an initial, very fast oxidation stage followed by an abrupt and drastic reduction of the oxide-film growth rate after about 1500 s of oxidation (see Sec. V). However, for the oxidation at high temperatures, (*i*) the *initial*, fast growth regime is more prolonged (i.e. at low temperatures the growth rate already reduces to virtually zero within less than about 250 s; see Sec. V), and (*ii*) the oxide-film growth process is *not* self-limiting: the initial, very fast oxidation stage is succeeded by a *second* stage of much slower but continuing oxide-film growth.

The growth rate during the initial stage of fast oxidation at 773 K is lower than the initial growth rates at 573 and 673 K (see Fig. 17 in Sec. V). As discussed in Sec. VII.A, this is attributed to the decrease of the oxygen sticking probability (due to an increase of the oxygen desorption rate) with increasing temperature for $T > 600$ K. Then, the following two possibilities may be considered for the initial, fast oxidation stage at 773 K:

(*i*) Despite the lower sticking coefficient, the rate of supply of chemisorbed oxygen is still sufficiently high that it does not limit the oxide-film growth rate. However, the amount of oxygen chemisorbed on the oxide surface at 773 K will be lower than the amount present at $T < 773$ K. Consequently, the Mott potential will be lower at 773 K, resulting in a lower electric-field controlled transport rate of Al cations, and thus a lower oxide-film growth rate.

(*ii*) The rate of supply of chemisorbed oxygen is that low that the oxide-film growth rate is *directly* determined by the rate of supply of chemisorbed oxygen (thus, even though the Mott potential may be relatively low, the transport of Al cations is not determining the oxide-film growth rate).

The occurrence of an excess of Al cations and a deficiency of O anions in the developing oxide-films (as compared to γ-Al_2O_3) during the initial, fast oxidation stage at 773 K (cf. Fig. 21b in Sec. VI.A) suggests that oxide-film growth during this stage is not rate-limited by the electric-field controlled migration of Al cations into (or through) the developing oxide film. On the basis of these observations it is therefore suggested that the oxide-film growth rate during the initial, fast oxidation stage at 773 K is controlled by reactions at the oxide-gas interface (e.g. oxygen desorption or dissociation, or oxide-film formation by surface reconstruction).

For the oxidation of the Al substrate at high temperatures, the contribution of cation transport by the chemical diffusion of Al cations under influence of the concentration gradient cannot be neglected, and the contribution of electron transport by thermionic emission, a process that is *independent* on the oxide-film thickness, is strongly enhanced as compared to low temperature oxidation (see Sec. VII.B.1) (thus, at high temperatures, even beyond the thickness for which the contribution of electron transport by tunnelling is effectively zero, electron transport through the thickening film remains possible). Consequently, the constraint of coupled currents of cations and electrons implies that, for the high temperature oxidation, the initial oxidation regime of fast growth is succeeded by a *second stage* of much slower, but continuing oxide-film growth (cf. Fig. 16 in Sec. V). The transition from the first, fast growth regime to the second, slow oxidation stage is marked by a distinct drop in the oxide-film growth rate as a result of the rapid break down of the Mott potential due to the electron tunnel current becoming negligible small.[23] At 773 K, this transition occurs at an oxide-film thickness of about 3 nm (see Fig. 18 in Sec. V).

If, during the *second*, slow oxidation stage observed at high temperatures, electron transport through the oxide film by thermionic (and Schottky [92]) emission occurs intrinsically at a faster rate than the chemical diffusion of Al cations, the electric field (induced by negatively charged oxygen anions at the oxide surface) will retard further electron transport but enhance cation transport (cf. Ref. [45, 93).[24] Under the constraint that no net charge is transported through the oxide film, the magnitude of the established electric field will be such that the charge currents of the intrinsically less mobile species (i.e. cations) equals the charge current of the intrinsically more mobile species (i.e. electrons). Because the contribution of *fast* electron transport by tunneling has become negligible small for the second, oxidation stage (see footnote 23), the induced electric field (due to the so-called

---

[23] The region in film-thickness for which both electron transport by electron tunnelling and electron transport by thermionic emission needs to be considered is very limited, since the electron tunnel current is extremely large for very thin films (< 1 nm for Al/Al-oxide; see Sec. VII.B.1.a), but decreases sharply at a somewhat larger thickness [49]. For larger thicknesses, electron transport occurs by thermionic (and Schottky [92]) emission of electrons from the Fermi level of the metal into the conduction band of the oxide, a process which (even at high temperatures) is orders of magnitude slower than the initial tunnelling process (cf. Refs. [3, 48, 50]).

[24] It is noted that due to the existence of a positive space charge region (induced by an excess of Al cations) in the high-temperature oxide films near the metal/oxide interface (cf. Secs. VI.A.2 and VI.C.5), the barrier height for electron tunnelling and thermal emission (χ_0 in Fig. 28) may be considerably lower (cf. Refs. [31-34]) than the corresponding barrier height in the Al-deficient oxide films formed at lower temperatures (see Sec. VI.A.2).

'kinetic' potential V_K; see footnote 25 and e.g. Refs. [2, 49, 50, 93]) will be much weaker than the electric field set up during the initial, fast oxidation stage (due to the Mott potential V_M; see Sec. VII.B.1).

However, during the second, slow oxidation stage, the initial, presumably fully amorphous oxide film (gradually) transforms into *crystalline* γ-Al_2O_3 (cf. Secs. IV.A and VI.C.1) and attains its stoichiometric composition of Al_2O_3 (see Figs. 20-22 in Sec. VI.A). After prolonged oxidation, large γ-Al_2O_3 crystallites have grown into the parent metal substrate (cf. Fig. 10 in Sec. IV.A). This suggests that the growth of these γ-Al_2O_3 crystallites is *not* realized through outward cation transport as discussed in the preceding paragraph, but is due to the inward chemical diffusion of oxygen along the grain boundaries in the oxide film.

VIII. Conclusions

VIII.A. Oxide-film morphology

- The initial oxidation of the bare Al(431) substrate at $p_{O_2} = 1.33\times10^{-4}$ Pa proceeds by an island-by-layer growth mechanism, involving the lateral diffusion over the bare Al substrate surface of mobile oxygen species. At $T \leq 473$ K, the bare Al substrate is already covered with an *uniform*, 2 - 3 'oxide' monolayers thick oxide film within 100 s of oxidation due to the very low mobility of the oxygen species on the surface. With increasing temperature, the initial density of oxide islands decreases and the average island size increases, because both the lateral diffusion of the oxygen species and the rate of oxide formation increase with increasing temperature. A 'closed' oxide film is formed after 200, 500 and 750 s of oxidation at 573, 673 K and 773 K, respectively. The 'closed' oxide-film is of less uniform thickness for higher oxidation temperatures.
- The (average) oxide-film thicknesses of the grown oxide films as determined with XPS agree well with the corresponding average values obtained from the HREM analysis of metal/oxide cross-sections.

---

[25] Assuming that no net electric charge is transported through the oxide and no space charge builds up in the oxide film, the kinetic potential V_K is defined as the potential required to equalize the charge currents of electrons and cations (cf. Refs. [2, 49, 50]).

VIII.B. Oxide-film constitution and structure

- For all oxidation temperatures, the observed changes in the oxide-film composition (i.e. O/Al-ratio) with both increasing temperature and increasing oxidation time are mainly due to a change in the Al cation concentration (the O anion concentration is approximately constant). The amorphous, Al-oxide films formed at $T \leq 573$ K, as well as during the initial, fast oxidation stage at higher temperatures, are well described by a close packing of oxygen anions with the Al cations distributed over the octahedral and tetrahedral interstices.
- The initial (i.e. after 100 s of oxidation) Al cation concentration in the grown oxide-film increases with increasing temperature. At *low temperatures* ($T \leq 573$ K), an amorphous, Al-deficient (as compared to γ-Al_2O_3) oxide film of 'limiting' oxide-film thickness is formed. During the initial, fast oxidation stage at *higher temperatures* ($T \geq 673$ K), an Al-enriched, amorphous oxide film is formed, which gradually attains the stoichiometric composition of Al_2O_3 and becomes crystalline γ-Al_2O_3 during the second, slow oxidation stage.
- The 'critical' thickness up to which an amorphous oxide film is thermodynamically preferred on the parent Al(431) substrate (instead of a crystalline of γ-Al_2O_3 film) at a growth temperature of 673 K is about 4 nm.
- The orientation relationship between γ-Al_2O_3 and the parent Al(431) substrate is $(111)_{Al}\|(111)_{\gamma\text{-}Al_2O_3}$ and $[110]_{Al}\|[110]_{\gamma\text{-}Al_2O_3}$.
- The occurrence of an amorphous-to-γ-Al_2O_3 transition oxide phase was demonstrated for the oxide-films grown at 673 K. The spacings and the angles between the different lattice planes of this transition oxide deviate 2 – 4 % and 2 – 4 ° from those for γ-Al_2O_3, respectively. The nucleation of this transition oxide occurs preferentially at the substrate / oxide-film interface, where {111} lattice planes of the parent Al substrate are parallel to a lattice plane in the transition oxide.
- Employing angle-resolved XPS, it was demonstrated that the oxide-films of 'limiting' oxide-film thickness formed at oxidation temperatures $T \leq 673$ K, are relatively enriched in Al (as compared to Al_2O_3) at their surface. The strong decrease in quantity of Al-enriched surface oxide for $T > 573$ K coincides with the gradual transition from amorphous Al_2O_3 to crystalline γ-Al_2O_3, and thus also (see below) with the transition from the initial, fast oxidation stage to the second, slow oxidation stage.

- The oxide-film Al 2*p* BE and O 1*s* BE increase, and the Al $KL_{23}L_{23}$ (^1D) KE decreases, with the *same amount*, with both increasing temperature and increasing thickness. This implies that the chemical state of the Al ions and the Al-O binding state in the oxide are (practically) independent of both the temperature and thickness. Thus, the short range ordering of the amorphous Al-oxide films grown at relatively low temperatures in this study closely resembles that of the crystalline γ-Al_2O_3 films grown at more elevated temperatures.

- The increase in Al 2*p* and O 1*s* BE, and the decrease in Al $KL_{23}L_{23}$ (^1D) KE, of the oxide-film component with increasing oxidation *temperature* are due to an Al-enriched-oxide-surface induced shift of the Fermi level, which decreases with increasing temperature, because the concerned Al enrichment of the oxide surface decreases with increasing temperature.

- The increase in Al 2*p* and O 1*s* BE, and the decrease in Al $KL_{23}L_{23}$ (^1D) KE, of the oxide-film component with increasing oxide-film *thickness* (as only observed for the high-temperature oxide films) are attributed to the development of a positive space charge region in the oxide near the metal/oxide interface.

VIII.C. Oxide-film growth kinetics and mechanisms

- Two different oxide-film growth regimes have been recognised for the oxide-film growth on the Al substrate in the temperature range from 373 to 773 K and at p_{O_2} = 1.33×10^{-4} Pa: (*i*) an *initial* regime of (very) fast oxide-film growth, and (*ii*) a *second*, much slower oxidation stage, which is only observed at high oxidation temperatures ($T \geq$ 673 K).

- The *initial*, fast oxidation stage at *low temperatures* ($T \leq$ 573 K), culminates with an Al-deficient, amorphous oxide film of 'limiting' thickness. The 'limiting' thickness increases with increasing temperature. The fast oxide-film growth rate is realised by the *electric-field* controlled migration of Al cations across the developing oxide-film. A value of 2.6 eV was determined for the rate-limiting energy barrier for Al cation motion. This rate-liming energy barrier is located at the metal/oxide interface. The corresponding Mott potential V_M equals -1.6 V. At the end of the initial, fast oxidation stage, the electron tunnel current has become effectively zero. Then, under the constraint of coupled currents of electrons and cations, oxide-film growth stops at low temperatures, because the chemical diffusion of ions across the oxide film, as well as the contribution of electron transport by thermionic emission, are negligibly small.

- During the *initial*, fast oxidation stage at *high temperatures* ($T \geq 673$ K) an Al-enriched, amorphous oxide film is formed. The fast oxide-film growth rate is realised by the *electric-field* enhanced migration of Al cations through the developing oxide-film. However, the decrease of the oxygen sticking coefficient with increasing temperature for $T > 600$ K may either *indirectly* (due to a lower Mott potential; cation transport is rate-determining) or *directly* (supply rate of chemisorbed oxygen is rate-determining) lead to a lower oxide-film growth rate during the initial, fast oxidation stage as compared to the corresponding growth rate at lower temperatures.
- During the *second*, slow oxidation stage at *high temperatures* (i.e. $T \geq 673$ K), the initially Al-enriched, amorphous oxide film attains the stoichiometric composition of Al_2O_3 and becomes crystalline γ-Al_2O_3. As long as the oxide is amorphous, the oxide-film growth rate is realised by the interstitial, outward transport of Al cations under influence of the concentration gradient and the (small) electric field due to the 'kinetic potential' V_K. As soon as γ-Al_2O_3 crystallites develop, the inward (chemical) diffusion of oxygen along grain boundaries establishes the growth.

Acknowledgments

Financial support by the Foundation for Fundamental Research of Matter (FOM) is gratefully acknowledged. The authors are indebted to C.G. Borsboom for specimen preparation and experimental assistance, T.R. de Kruijff for the preparation of the HREM cross-sections, and J.F. van Lent for recording and analysis of the Laue photographs.

Appendix A: Calculation of oxide-film composition and thickness

A.1. Metallic, oxidic and oxygen PZL photoelectron intensities

The observed total *metallic* PZL photoelectron intensity $I^{\infty}_{\mathrm{Al}^0,\mathrm{met}}$ of photoelectrons emitted from the Al 2*p* core level of the Al atoms in the *bare* Al metal substrate is given by (cf. Eq. (B2) in Appendix B)

$$I^{\infty}_{\mathrm{Al^0,met}} = K\sigma_{\mathrm{Al}} C_{\mathrm{Al^0,met}} \lambda_{\mathrm{Al^0,met}} \sin\theta \qquad \textbf{(A1a)}$$

where K is an instrumental factor; σ_{Al} denotes the Al 2p photoemission cross-section (see footnote 26); $C_{\mathrm{Al^0,met}}$ represents the molar density of Al atoms in the metal substrate ; $\lambda_{\mathrm{Al^0,met}}$ is the IMFP of the photoelectrons emitted from and propagating through the Al substrate; and θ is the detection angle (here: $\theta = 45°$; see Sec. II.B). Likewise, the oxidic and oxygen PZL intensities $I^{\infty}_{\mathrm{Al^{3+},ref}}$ and $I^{\infty}_{\mathrm{O^{2-},ref}}$ of the photoelectrons emitted from the Al 2p and O 1s core levels of the $\mathrm{Al^{3+}}$ and $\mathrm{O^{2-}}$ ions in the α-$\mathrm{Al_2O_3}$ *reference* are expressed by

$$I^{\infty}_{\mathrm{Al^{3+},ref}} = K'\sigma_{\mathrm{Al}} C_{\mathrm{Al^{3+},ref}} \lambda_{\mathrm{Al^{3+},ox}} \sin\theta \qquad \textbf{(A1b)}$$

and

$$I^{\infty}_{\mathrm{O^{2-},ref}} = K'\sigma_{\mathrm{O}} C_{\mathrm{O^{2-},ref}} \lambda_{\mathrm{O^{2-},ox}} \sin\theta \qquad \textbf{(A1c)}$$

respectively. Here, $C_{\mathrm{Al^{3+},ref}}$ and $C_{\mathrm{O^{2-},ref}}$ represent the molar densities of Al and O ions in α-$\mathrm{Al_2O_3}$, respectively; $\lambda_{\mathrm{Al^{3+},ox}}$ and $\lambda_{\mathrm{O^{2-},ox}}$ denote the IMFPs of the photoelectrons emitted from the Al 2p and O 1s core levels in the oxide and propagating through the oxide, respectively; and σ_{O} is the O 1s photoemission cross-section.

The oxidic and oxygen PZL intensities $I_{\mathrm{Al^{\delta+},ox}}$ and $I_{\mathrm{O^{\xi-},ox}}$ of the photoelectrons emitted from the Al 2p and O 1s core levels of the $\mathrm{Al^{\delta+}}$ and $\mathrm{O^{\xi-}}$ ions in a homogenous Al-*oxide film* of uniform thickness d on the Al substrate are given by (see Eq. (B3) in Appendix B)

$$I_{\mathrm{Al^{\delta+},ox}} = K''\sigma_{\mathrm{Al}} C_{\mathrm{Al^{\delta+},ox}} \lambda_{\mathrm{Al^{3+},ox}} \sin\theta \left[1 - \exp\left(-\frac{d}{\lambda_{\mathrm{Al^{3+},ox}} \sin\theta}\right)\right] \qquad \textbf{(A2a)}$$

and

$$I_{\mathrm{O^{\xi-},ox}} = K''\sigma_{\mathrm{O}} C_{\mathrm{O^{\xi-},ox}} \lambda_{\mathrm{O^{2-},ox}} \sin\theta \left[1 - \exp\left(-\frac{d}{\lambda_{\mathrm{O^{2-},ox}} \sin\theta}\right)\right] \qquad \textbf{(A2b)}$$

---

[26] The photoemission cross section of the metal atom in the pure metal and the metal ion in the oxide can be taken the same as is justified by measured and calculated data in Refs. [51, 94].

respectively. Here, $C_{\mathrm{Al}^{\delta+},\mathrm{ox}}$ and $C_{\mathrm{O}^{\xi-},\mathrm{ox}}$ denote the molar densities of Al and O ions in the oxide film, respectively. The corresponding metallic PZL intensity $I_{\mathrm{Al}^0,\mathrm{met}}$ of the photoelectrons emitted from the Al 2*p* core level of the Al atoms in the Al substrate covered with an Al-oxide film of thickness *d* is expressed by (see Eq. (B4c) in Appendix B)

$$I_{\mathrm{Al}^0,\mathrm{met}} = K''\sigma_{\mathrm{Al}} C_{\mathrm{Al}^0,\mathrm{met}} \lambda_{\mathrm{Al}^0,\mathrm{met}} \sin\theta \exp\left(-\frac{d}{\lambda_{\mathrm{Al}^0,\mathrm{ox}} \sin\theta}\right) \tag{A3}$$

where $\lambda_{\mathrm{Al}^0,\mathrm{ox}}$ denotes the IMFP of the photoelectrons emitted from the Al substrate and propagating through the oxide film.

A.2. Calculation of oxide-film composition

Using Eqs. (A2a) and (A2b) in Sec. A.1 it follows that the *composition*, expressed as the O/Al atomic ratio, of a homogeneous Al-oxide film of uniform thickness *d* is related to the total *oxygen* O 1*s* and *oxidic* Al 2*p* PZL photoelectron intensities by

$$\frac{C_{\mathrm{O}^{\xi-},\mathrm{ox}}}{C_{\mathrm{Al}^{\delta+},\mathrm{ox}}} = \frac{I_{\mathrm{O}^{\xi-},\mathrm{ox}}}{I_{\mathrm{Al}^{\delta+},\mathrm{ox}}} \cdot \frac{\sigma_{\mathrm{Al}} \lambda_{\mathrm{Al}^{3+},\mathrm{ox}}}{\sigma_{\mathrm{O}} \lambda_{\mathrm{O}^{2-},\mathrm{ox}}} \cdot \frac{\left[1-\exp\left(-\dfrac{d}{\lambda_{\mathrm{Al}^{3+},\mathrm{ox}} \sin\theta}\right)\right]}{\left[1-\exp\left(-\dfrac{d}{\lambda_{\mathrm{O}^{2-},\mathrm{ox}} \sin\theta}\right)\right]} \tag{A4a}$$

Using Eqs. (A1b) and (A1c) pertaining to the oxidic and oxygen PZL intensities as observed from an infinitely thick (as compared to the IMFP) α-$\mathrm{Al_2O_3}$ reference (i.e. O/Al-ratio of $\frac{3}{2}$) it holds that

$$\frac{\sigma_{\mathrm{Al}} \lambda_{\mathrm{Al}^{3+},\mathrm{ox}}}{\sigma_{\mathrm{O}} \lambda_{\mathrm{O}^{2-},\mathrm{ox}}} = \frac{C_{\mathrm{O}^{2-},\mathrm{ref}}}{C_{\mathrm{Al}^{3+},\mathrm{ref}}} \cdot \frac{I^{\infty}_{\mathrm{Al}^{3+},\mathrm{ref}}}{I^{\infty}_{\mathrm{O}^{2-},\mathrm{ref}}} = \frac{3}{2} \cdot \frac{I^{\infty}_{\mathrm{Al}^{3+},\mathrm{ref}}}{I^{\infty}_{\mathrm{O}^{2-},\mathrm{ref}}} \tag{A4b}$$

By substitution of Eq. (A4b) into Eq. (A4a) it then follows that the composition of the oxide film of thickness *d* can be calculated from

$$\frac{C_{\mathrm{O}^{\xi-},\mathrm{ox}}}{C_{\mathrm{Al}^{\delta+},\mathrm{ox}}} = \frac{I_{\mathrm{O}^{\xi-},\mathrm{ox}}}{I_{\mathrm{Al}^{\delta+},\mathrm{ox}}} \cdot \frac{3}{2} \cdot \frac{I^{\infty}_{\mathrm{Al}^{3+},\mathrm{ref}}}{I^{\infty}_{\mathrm{O}^{2-},\mathrm{ref}}} \cdot \frac{\left[1-\exp\left(-\dfrac{d}{\lambda_{\mathrm{Al}^{3+},\mathrm{ox}} \sin\theta}\right)\right]}{\left[1-\exp\left(-\dfrac{d}{\lambda_{\mathrm{O}^{2-},\mathrm{ox}} \sin\theta}\right)\right]} \tag{A4c}$$

A.3. Calculation of oxide-film thickness

Since $\lambda_{\mathrm{Al}^0,\mathrm{ox}} \cong \lambda_{\mathrm{Al}^{3+},\mathrm{ox}}$ (see Sec. III), it follows using Eqs. (A2a) and (A3) in Sec. A.1 of Appendix A that the oxide-film thickness d (for the case of a homogeneous Al-oxide film of uniform thickness on the Al substrate) can be calculated from the ratio of the total *oxidic* to *metallic* Al $2p$ PZL photoelectron intensity according to

$$d = \lambda_{\mathrm{Al}^0,\mathrm{ox}} \sin\theta \ln\left(\frac{C_{\mathrm{Al}^0,\mathrm{met}} \lambda_{\mathrm{Al}^0,\mathrm{met}}}{C_{\mathrm{Al}^{\delta+},\mathrm{ox}} \lambda_{\mathrm{Al}^0,\mathrm{ox}}} \cdot \frac{I_{\mathrm{Al}^{\delta+},\mathrm{ox}}}{I_{\mathrm{Al}^0,\mathrm{met}}} + 1 \right) \qquad \textbf{(A5)}$$

The oxide-film thickness d is related to the total *oxygen* O $1s$ to *metallic* Al $2p$ PZL photoelectron intensity ratio by (see Eqs. (A2b) and (A3) in Sec. A.1 of Appendix A)

$$\frac{I_{\mathrm{O}^{\xi-},\mathrm{ox}}}{I_{\mathrm{Al}^0,\mathrm{met}}} = \frac{\sigma_{\mathrm{O}} C_{\mathrm{O}^{\xi-},\mathrm{ox}} \lambda_{\mathrm{O}^{2-},\mathrm{ox}}}{\sigma_{\mathrm{Al}} C_{\mathrm{Al}^0,\mathrm{met}} \lambda_{\mathrm{Al}^0,\mathrm{met}}} \cdot \frac{\left[1 - \exp\left(-\dfrac{d}{\lambda_{\mathrm{O}^{2-},\mathrm{ox}} \sin\theta} \right) \right]}{\exp\left(-\dfrac{d}{\lambda_{\mathrm{Al}^0,\mathrm{ox}} \sin\theta} \right)} \qquad \textbf{(A6a)}$$

which by substitution of Eq. (A4b) of Sec. A.2 becomes

$$\frac{I_{\mathrm{O}^{\xi-},\mathrm{ox}}}{I_{\mathrm{Al}^0,\mathrm{met}}} = \frac{I^{\infty}_{\mathrm{O}^{2-},\mathrm{ref}}}{I^{\infty}_{\mathrm{Al}^{3+},\mathrm{ref}}} \cdot \frac{2}{3} \cdot \frac{\lambda_{\mathrm{Al}^{3+},\mathrm{ox}} C_{\mathrm{O}^{\xi-},\mathrm{ox}}}{\lambda_{\mathrm{Al}^0,\mathrm{met}} C_{\mathrm{Al}^0,\mathrm{met}}} \cdot \frac{\left[1 - \exp\left(-\dfrac{d}{\lambda_{\mathrm{O}^{2-},\mathrm{ox}} \sin\theta} \right) \right]}{\exp\left(-\dfrac{d}{\lambda_{\mathrm{Al}^0,\mathrm{ox}} \sin\theta} \right)} \qquad \textbf{(A6b)}$$

Note that the oxide-film thickness in Eq. (A6b) can only be solved by iteration.

Appendix B: Derivation of PZL photoelectron intensity equations

The observed PZL photoelectron intensity I_A of photoelectrons ejected with kinetic energy E from the n^th core level of an atom (or ion) A situated in a solid at depth z below the solid's surface, can be written as (cf. Ref. [95])[27]

$$I_\mathrm{A} = K\sigma_\mathrm{A} \int_{z=0}^{\infty} C_\mathrm{A}(z)\exp\left(- \int_{z'=0}^{z} \frac{dz'}{\lambda_\mathrm{A}(z')\sin\theta} \right) dz \qquad \textbf{(B1)}$$

where K is an instrumental factor depending on the area analysed, the X-ray energy and intensity, etc.; σ_A is the photoemission cross-section, i.e. the probability for ejecting a photoelectron from the n^th core level of an A atom (or ion) in the solid per incident photon (see footnote 26 in Sec. A.1); the molar density $C_\mathrm{A}(z)$ is the number of A atoms per unit volume as a function of depth z below the surface; $\lambda_\mathrm{A}(z)$ is the inelastic mean free path (IMPF) of the photoelectrons with kinetic energy E in the solid as a function of z; and the detection angle θ is the defined as the angle between the specimen surface and the optical axes of the analyser input lens.

If the solid is thick as compared to the IMFP and the A atoms are homogeneously distributed in the solid, σ_Al, $C_\mathrm{A}(z)$ and $\lambda_\mathrm{A}(z)$ are constants, and Eq.(B1) may be integrated to give

$$I_\mathrm{A}^{\infty} = K\sigma_\mathrm{A} C_\mathrm{A} \lambda_\mathrm{A} \sin\theta \qquad \textbf{(B2)}$$

For a relatively thin solid film of uniform thickness d_A with a homogeneous distribution of A atoms, on the other hand, integration of Eq.(B1) leads to

$$I_\mathrm{A}^{d} = K\sigma_\mathrm{A} C_\mathrm{A} \lambda_\mathrm{A} \sin\theta \left[1 - \exp\left(-\frac{d_\mathrm{A}}{\lambda_\mathrm{A}\sin\theta} \right) \right] = I_\mathrm{A}^{\infty} \left[1 - \exp\left(-\frac{d_\mathrm{A}}{\lambda_\mathrm{A}\sin\theta} \right) \right] \qquad \textbf{(B3)}$$

Let us now consider the case of element A homogeneously distributed in a substrate A covered with a thin film of uniform thickness d_B of a solid B. (i.e. $C_\mathrm{A}(z) = 0$ within the overlayer B). In this case, the observed PZL intensity I_A of photoelectrons ejected with kinetic energy E from the n^{th} core level of element A in the substrate becomes

---

[27] In the derivation of Eq. (B1), the effect of elastic scattering of photoelectrons propagating through the solid has been neglected [61], but the depth dependence of the inelastic mean free path (IMFP) of the photoelectrons due to changes in composition (as experienced proceeding from the pure metal to the oxide) is accounted for [96].

$$I_{\text{A}} = K\sigma_{\text{A}}C_{\text{A}} \int_{d_{\text{B}}}^{\infty} \exp\left(-\left\{ \int_{z'=0}^{d_{\text{B}}} \frac{dz'}{\lambda_{\text{B}} \sin\theta} + \int_{z'=d_{\text{B}}}^{z} \frac{dz'}{\lambda_{\text{A}} \sin\theta} \right\} \right) dz \qquad \textbf{(B4a)}$$

where λ_B is the IMFP of the photoelectrons emitted from the substrate A but propagating through the film of solid B. Integration of the inner part of the exponent function in Eq. (B4a) gives

$$I_{\text{A}} = K\sigma_{\text{A}}C_{\text{A}} \exp\left(-\frac{d_{\text{B}}}{\lambda_{\text{B}} \sin\theta} \right) \exp\left(\frac{d_{\text{B}}}{\lambda_{\text{A}} \sin\theta} \right) \left\{ \int_{d_{\text{B}}}^{\infty} \exp\left(-\frac{z}{\lambda_{\text{A}} \sin\theta} \right) dz \right\} \qquad \textbf{(B4b)}$$

and further integration of Eq. (B4b) leads to

$$I_{\text{A}} = K\sigma_{\text{A}}C_{\text{A}}\lambda_{\text{A}} \sin\theta \exp\left(-\frac{d_{\text{B}}}{\lambda_{\text{B}} \sin\theta} \right) = I_{\text{A}}^{\infty} \exp\left(-\frac{d_{\text{B}}}{\lambda_{\text{B}} \sin\theta} \right) \qquad \textbf{(B4c)}$$

Appendix C: Gauss-Lorenz function

The Gauss-Lorenz function $f(x_i)$ describing the spectral intensity of the symmetrical peak component at energy position x_i in the Al 2*p* or Al $KL_{23}L_{23}$ PZL oxidic rest spectrum considered is given by

$$f(x_i) = g \cdot G(x_i) + (1-g) \cdot L(x_i) \qquad \textbf{(D1a)}$$

where $G(x_i)$ is the pure Gauss function

$$G(x_i) = A_0 \exp\left[-\ln(2) \cdot \left(\frac{x_i - x_0}{2W} \right)^2 \right] \qquad \textbf{(D1b)}$$

and $L(x_i)$ is the pure Lorenz function

$$L(x_i) = A_0 \left[1 + \left(\frac{x_i - x_0}{2W} \right)^2 \right]^{-1} \qquad \textbf{(D1c)}$$

Here, g denotes the fraction Gauss (i.e. $0 < g < 1$), x_0 and A_0 denote the energy and height of the peak at its peak maximum, and W represents the Half Width at Half Maximum (HWHM), respectively.

Appendix D: Estimation of molar densities of O and Al

Let us assume that the amorphous Al-oxide films grown in this study (cf. Sec. II.B) are well described by a homogeneous close packing of oxygen anion spheres with aluminium cation spheres in the interstices (see footnote 3 in Sec. III). Then, $V_{\mathrm{O}}^{\mathrm{spheres}} = N\frac{4}{3}\pi r_{\mathrm{O}}^3$ and $V_{\mathrm{Al}}^{\mathrm{spheres}} = N\frac{4}{3}\pi r_{\mathrm{Al}}^3$ are the volumes of one mole O and one mole Al spheres with ionic radii r_{O} and r_{Al}, respectively (where N is Avogadro's number). It follows that the total *sphere* volume and the total *free* volume in one mole amorphous (stoichiometric) $\mathrm{Al_2O_3}$ with molar volume $V_{\mathrm{Al_2O_3}}$ [$\mathrm{m^3 mole^{-1}}$ $\mathrm{Al_2O_3}$] are given by $V_{\mathrm{Al_2O_3}}^{\mathrm{spheres}} = 3V_{\mathrm{O}}^{\mathrm{spheres}} + 2V_{\mathrm{Al}}^{\mathrm{spheres}}$ and $V_{\mathrm{Al_2O_3}}^{\mathrm{free}} = V_{\mathrm{Al_2O_3}} - V_{\mathrm{Al_2O_3}}^{\mathrm{spheres}}$, respectively. Assigning a fraction of the total *free* volume $V_{\mathrm{Al_2O_3}}^{\mathrm{free}}$ in amorphous $\mathrm{Al_2O_3}$ to the O *ions*, equal to the fraction of the total *sphere* volume $V_{\mathrm{Al_2O_3}}^{\mathrm{spheres}}$ taken up by the O *spheres* in amorphous $\mathrm{Al_2O_3}$, i.e.

$$\frac{3V_{\mathrm{O}}^{\mathrm{free}}}{V_{\mathrm{Al_2O_3}}^{\mathrm{free}}} = \frac{3V_{\mathrm{O}}^{\mathrm{spheres}}}{V_{\mathrm{Al_2O_3}}^{\mathrm{spheres}}} \tag{D1}$$

then the molar volume $V_{\mathrm{O}^{\xi-},\mathrm{ox}}$ [$\mathrm{m^3 mole^{-1}}$ O] of the O ions in amorphous Al-oxide is estimated from

$$V_{\mathrm{O}^{\xi-},\mathrm{ox}} = V_{\mathrm{O}}^{\mathrm{spheres}} + V_{\mathrm{O}}^{\mathrm{free}} = V_{\mathrm{O}}^{\mathrm{spheres}} + \frac{V_{\mathrm{O}}^{\mathrm{spheres}}}{V_{\mathrm{Al_2O_3}}^{\mathrm{spheres}}} V_{\mathrm{Al_2O_3}}^{\mathrm{free}} \tag{D2a}$$

Note that this molar volume of the O ions in amorphous $\mathrm{Al_2O_3}$ includes a weighted part of the total free volume in the oxide. Likewise, an estimate for the corresponding molar volume $V_{\mathrm{Al}^{\xi+},\mathrm{ox}}$ of Al ions in amorphous $\mathrm{Al_2O_3}$ is obtained from

$$V_{\mathrm{Al}^{\xi+},\mathrm{ox}} = V_{\mathrm{Al}}^{\mathrm{spheres}} + V_{\mathrm{Al}}^{\mathrm{free}} = V_{\mathrm{Al}}^{\mathrm{spheres}} + \frac{V_{\mathrm{Al}}^{\mathrm{spheres}}}{V_{\mathrm{Al_2O_3}}^{\mathrm{spheres}}} \cdot V_{\mathrm{Al_2O_3}}^{\mathrm{free}} \tag{D2b}$$

Then, neglecting any possible changes in ionic radii and/or free volume of the developing amorphous oxide film (e.g. as a result of structural ordering), the *molar* densities $C_{\mathrm{Al}^{\delta+},\mathrm{ox}}$ and $C_{\mathrm{O}^{\xi-},\mathrm{ox}}$ [$\mathrm{mol \cdot m^{-3}}$] are related to the corresponding O/Al-ratio x of the oxide film by

$$C_{Al^{\xi+},ox} = \frac{1}{V_{Al^{\xi+},ox} + x \cdot V_{O^{\xi-},ox}} \qquad \textbf{(D3a)}$$

and

$$C_{O^{\xi-},ox} = \frac{1}{V_{O^{\xi-},ox} + 1/x \cdot V_{Al^{\xi+},ox}} \qquad \textbf{(D3b)}$$

respectively.

As can be demonstrated by substitution of Eq.(A5) in Eq. (A4c) (see Secs. A.3 and A.2 of Appendix A, respectively) the molar density of Al ions, $C_{Al^{\delta+},ox}$, can also be related to the O/Al-ratio, x, of the oxide film by the oxidic Al 2*p*, metallic Al 2*p* and the oxygen O 1*s* PZL intensities as resolved from a (single) measured XPS spectrum of the oxidised Al metal. Consequently, values for $C_{Al^{\delta+},ox}$ and x (and thus also for the corresponding thickness d and molar density of O ions $C_{O^{\xi-},ox}$) can be solved numerically from Eqs. (D3a), (A4c) and (A5) following the iteration procedure sketched in Fig. 30a. As shown in Fig. 30b, the values of d, x, $C_{Al^{\delta+},ox}$ and $C_{O^{\xi-},ox}$ can also be resolved from the oxygen O 1*s*, oxidic Al 2*p* and metallic Al 2*p* PZL intensities using the combination of Eqs. (D3b), (A4c) and (A6b). Of course, both iterations should result in (approximately) the same values of d, x, $C_{Al^{\xi+},ox}$ and $C_{O^{\xi-},ox}$. In the calculation, as an approximate for the molar volumes $V_{Al^{\xi+},ox}$ and $V_{O^{\xi-},ox}$ pertaining to Eqs. (D3a) and (D3b), the corresponding theoretical molar volumes of $V_{Al^{3+},ox} = 1.18\times10^{-6}$ and $V_{O^{2-},ox} = 8.58\times10^{-6}$ m^{3}mole^{-1} in γ-Al$_2$O$_3$ were taken.[28] Consequently, the difference in free volume between the amorphous Al-oxide and γ-Al$_2$O$_3$ is neglected.

It is noted that (*i*) in the calculation the oxidic Al 2*p* and O 1*s* PZL intensities of *only* the oxide-film component must be considered (i.e. excluding the corresponding PZL intensities of the surface-oxide component; cf. Sec. III), (*ii*) both iterations pertaining to Fig. 30 indeed resulted in the same values for the oxide-film thickness, composition and molar densities, and (*iii*) any difference between the actual molar volumes of Al and O in the grown oxide films and those in γ-Al_2O_3 as chosen for the calculation (see above), only affects the absolute (an not the relative) values of the calculated molar densities $C_{Al^{\delta+},ox}$ and $C_{O^{\delta-},ox}$.

---

[28] The ionic radii of the Al and O ions in γ-Al$_2$O$_3$ are generally considered as a good approximate of the corresponding ionic radii in amorphous Al$_2$O$_3$ (cf. Refs [28, 29]). As obtained from molecular dynamic simulations of γ-Al$_2$O$_3$ in Ref [97]: $r_{Al^{3+}} = 0.62$ Å and $r_{O^{2-}} = 1.20$ Å. Using the theoretical molar volume of γ-Al$_2$O$_3$ of 2.81×10^{-5} m^{3}mole^{-1} (see Sec. III), it then follows (see Appendix D) that the molar volumes of aluminium cations and oxygen anions in γ-Al$_2$O$_3$ are equal to $V_{Al^{\xi+},ox} = 1.18\times10^{-6}$ and $V_{O^{\xi-},ox} = 8.58\times10^{-6}$ m^{3}mole^{-1}, respectively.

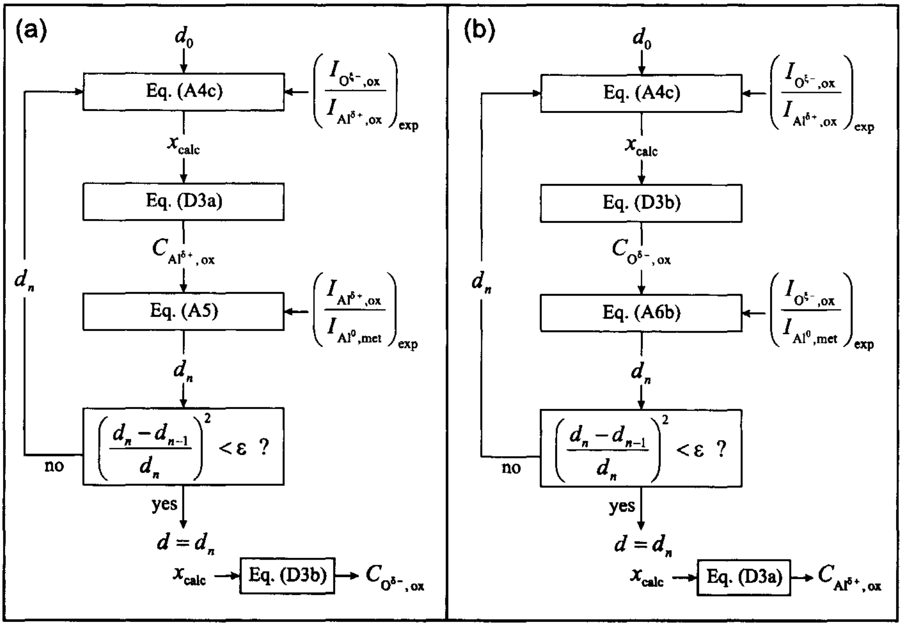
(a)
d_0
Eq. (A4c)
$\left(\frac{I_{O^{\delta-},ox}}{I_{Al^{\delta+},ox}}\right)_{exp}$
x_{calc}
Eq. (D3a)
$C_{Al^{\delta+},ox}$
d_n
Eq. (A5)
$\left(\frac{I_{Al^{\delta+},ox}}{I_{Al^0,met}}\right)_{exp}$
d_n
$\left(\frac{d_n-d_{n-1}}{d_n}\right)^2 < \varepsilon$?
no
yes
$d = d_n$
x_{calc}
Eq. (D3b)
$C_{O^{\delta-},ox}$
(b)
d_0
Eq. (A4c)
$\left(\frac{I_{O^{\delta-},ox}}{I_{Al^{\delta+},ox}}\right)_{exp}$
x_{calc}
Eq. (D3b)
$C_{O^{\delta-},ox}$
d_n
Eq. (A6b)
$\left(\frac{I_{O^{\delta-},ox}}{I_{Al^0,met}}\right)_{exp}$
d_n
$\left(\frac{d_n-d_{n-1}}{d_n}\right)^2 < \varepsilon$?
no
yes
$d = d_n$
x_{calc}
Eq. (D3a)
$C_{Al^{\delta+},ox}$

Figure 30. Schematic representation of the two possible iteration procedures followed to numerically solve the oxide-film thickness (*d*), the O/Al-ratio (*x*) and the aluminium cation ($C_{Al^{\delta+},ox}$) and oxygen anion ($C_{O^{\delta-},ox}$) molar density, from the metallic Al 2*p* ($I_{Al^0,met}$), oxidic Al 2*p* ($I_{Al^{\delta+},ox}$) and O 1*s* ($I_{O^{\delta-},ox}$) PZL intensities of the oxide-film component as resolved from a single XPS spectrum of the oxidised Al metal (see Sec. III). In the iteration of (**a**) the thickness is determined from the resolved Al cation density using Eq. (A5), whereas in (**b**) the thickness is calculated from the resolved O anion density using Eq. (A6b). The iteration was repeated as long as $\left[(d_n - d_{n-1})/d_n\right]^2 > 10^{-10}$. See text for details.

References

[1] F.P. Fehler, Low-temperature oxidation: the role of vitreous oxides (Wiley-Interscience, New York, 1981).

[2] A.T. Fromhold and R.G. Fromhold, in *Comprehensive chemical kinetics*, Vol. 21: Reactions of solids with gases, edited by C.H. Bamford, C.F.H. Tipper and R.G. Compton (Elsevier, Amsterdam, 1984), Chap. 1.

[3] E. Fromm, *Kinetics of Met-Gas Interactions at Low Temperatures: Hydriding, Oxidation, Poisoning* (Springer, Berlin, 1998), Chap. 5.

[4] K.R. Lawless, Rep. Prog. Phys. **37**, 231 (1973).

[5] L.P.H. Jeurgens, W.G. Sloof, F.D. Tichelaar and E.J. Mittemeijer, Phys. Rev. B **62** (2000), 4707.

[6] P. E. Doherty and R. S. Davis, J. Appl. Phys. **34**, 619 (1963).

[7] J. I. Eldridge, R. J. Hussey, D. F. Mitchell and M. J. Graham, Oxid. Met. **30**, 301 (1988).

[8] A.F. Beck, M.A. Heine, E.J. Caule and M.J. Pryor, Corrosion Sci. **7** (1967), 1.

[9] Z. Zhukov, I. Popova, and J.T. Yates, J. Vac. Sci. Technol. A **17** (1999), 1727.

[10] I. Popova, Z. Zhukov and J.T. Yates, J. Appl. Phys. **87** (2000), 8143.

[11] D.R. Jennison, C. Verdozzi, P.A. Schultz and M.P. Sears, Phys. Rev. B **59** (1999), R15605.

[12] A. Bogicevic and D.R. Jennison, Phys. Rev. Lett. **82** (1999), 4050.

[13] J.M. De Teresa , A. Barthélémy, A. Fert, J.P. Contour, F. Montaigne and P. Seneor, Science **286** (1999), 507.

[14] M. Sharma, S.X. Wang and J.H. Nickel, Phys. Rev. Lett. **82** (1999), 616.

[15] T.W. Hickmott, J. Appl. Phys. **88** (2000), 2805.

[16] E.S. Snow, P.M. Campbell, R.W. Rendell, F.A. Buaot, D. Park, C.R.K. Marrian and R. Magno, Semicond. Sci. Technol. **13** (1998), A75.

[17] A.T.M. van Gogh, S.J. van der Molen, J.W.J. Kerssemakers, N.J. Koeman and R. Griessen, Appl. Phys. Lett. **77** (2000), 815.

[18] S.W. Gaarenstroom, J. Vac. Sci. Techn.A **15** (1997), 470.

[19] H. Brune, J. Wintterlin, J. Trost and G. Ertl, J. Wiechers and R.J. Behm, J. Chem. Phys. **99** (1993), 2128.

[20] F. Jona, J. Phys. Chem. Solids **28** (1967), 2155.

[21] B.D. Cullity, *Elements of X-ray diffraction*, (Second Edition, Addison-Wesley Publishing Company, Don Mills, Ontario, 1978), p. 492.

[22] J.E. Castle and R.H. West, J. Electr. Spectros. Rel. Phenom. **16** (1979), 195.

[23] American Society for Testing and Materials, Surf. Interface Anal. **17** (1991), 889.

[24] L.P.H. Jeurgens, W.G. Sloof, F.D. Tichelaar, C.G. Borsboom and E.J. Mittemeijer, Appl. Surf. Sci. **144-145** (1999), 11.

[25] L.P.H. Jeurgens, W.G. Sloof, C.G. Borsboom, F.D. Tichelaar and E.J. Mittemeijer, Appl. Surf. Sci. **161** (2000), 139.

[26] C. Jansson, S. Tougaard, G. Beamson, D. Briggs, S.F. Davies, A. Rossi, R. Hauert, G. Hobi, N.M.D. Brown, B.J. Meenan, C.A. Anderson, M. Repoux, C. Malitesta and L. Sabbatini, Surf. Interf. Anal. **23** (1998), 484.

[27] S. Tanuma, C.J. Powell and D.R. Penn, Surf. Int. Anal. **17** (1991), 911 & 927.

[28] L.A. Aleshina, E.A. Nikitina, and A.D. Fofanov, Crystallography Reports **42** (1997), 836.

[29] R. Manaila, A. Dévényi and E. Candet, Thin Solid films **116** (1984), 289.

[30] Powder Diffraction file, 29-0063 from International Center for Diffraction Data (ICDD).

[31] J.C. Fisher and I. Glaever, J. Appl. Phys. **32** (1961), 172.

[32] S.R. Pollack and C.E. Morris, J. Appl. Phys. **35** (1964), 1503.

[33] K.H. Gundlach and J. Hölzl, Surf. Sci. **27** (1971), 125.

[34] J. Schäfer and C.J. Adkins, J. Phys.: Condens. Matter **3** (1991), 2907.

[35] Chi-Chang Kao, *Characterization of the electronic and geometric structures of aluminas using XPS, Auger, EELS, and LEED*, Ph. D. Thesis, Cornell University (1984).

[36] K. Shinohara, T. Seo and H. Kyogoku, Z. Metallkd. **73**, 774 (1982).

[37] K. Thomas and M. W. Roberts, J. Appl. Phys. **32**, 70 (1961).

[38] R. K. Hart and J. K. Maurin, Surf. Sci. **20**, 285 (1970).

[39] H.J. van Beek and E.J. Mittemeijer, Thin Solid Films **122** (1984), 131.

[40] F.H. Streitz and J.W. Mintmire, Phys. Rev. B **60** (1999), 773.

[41] B.C. Lippens and J.H. de Boer, Acta Crystallogr. **17** (1964), 1312.

[42] J. Trost, H. Brune, J. Wintterlin, R.J. Behm and G. Ertl, J. Chem. Phys. **108** (1998), 1740.

[43] I. Popova, V. Zhukov and J.T. Yates, Appl. Phys. Lett. **75** (1999), 3108.

[44] P.C.J. Graat, M.A.J. Somers, A.M. Vredenberg and E.J. Mittemeijer, J. Appl. Phys. **82** (1997), 1416.

[45] V. Zhukov, I. Popova and J.T. Yates, Surf. Sci. **441** (1999), 251.

[46] N. Cabrera and N.F. Mott, Rep. Progr. Phys. **12** (1949), 163.

[47] F.P. Fehlner and N.F. Mott, Ox. Metals **2** (1970), 59.

[48] V. Grajewski and E. Fromm, in *Science of Ceramic Interfaces*, edited by J. Nowotny (Elsevier, Amsterdam, 1991), p. 487-506.

[49] A.T. Fromhold and E.L. Cook, Phys. Rev. **158** (1967), 600.

[50] A.T. Fromhold and E.L. Cook, Phys. Rev. **163** (1967), 650.

[51] J.H. Scofield, J. Electr. Spectr. Rel. Phenom. **8** (1976), 129.

[52] C. Ocal, B. Basurco and S. Ferrer, Surf. Sci. **157** (1985), 233.

[53] K. G. Lynn, Phys. Rev. Lett. **44** (1980), 1330.

[54] C.F. McConville, D.L. Seymour, D.P. Woodruff and S. Bao, Surf. Sci. **188** (1987), 1.

[55] A. Jimenéz-Gonzaléz and D. Schmeisser, Surf. Sci. **250** (1991), 59.

[56] S. Blonski and S.H. Garofalini, Surf. Sci. **295** (1993), 263.

[57] B. Ealet, M. H. Elyakhoufi, E. Gillet and M. Ricci, Thin Solid Films **250** (1994), 92.

[58] S. Ciraci and I. P. Batra, Phys. Rev. B **28** (1983), 982.

[59] W. J. Gignac, R. S. Williams and S. P. Kowalezyk, Phys. Rev. B **32** (1985), 1237.

[60] M. Gautier, J. P. Duraud, L. Pham Van and M. J. Guittet, Surf. Sci. **250** (1991), 71.

[61] W. Eberhardt and C. Kunz, Surf. Sci. **75** (1978), 709.

[62] A. Barrie, Chem. Phys. Lett. **19** (1973), 109.

[63] A. Bianconi, R.Z. Bachrach, S.B.M. Hagstrom and S.A. Flodstrom, Phys. Rev. B **19** (1979), 2837.

[64] R.M. Henry, B.W. Walker and P.C. Stair, Solid State Comm. **42** (1982), 23.

[65] S.A. Flodstrom, R.Z. Bachrach, R.S. Bauer, S.B. Hagström, Phys. Rev. Lett. **37** (1976), 1282.

[66] D. Norman, S. Brennan, R. Jaeger, J. Stöhr, Surf. Sci. **105** (1981), L297.

[67] C.D. Wagner and A. Joshi, J. Electr. Spectr. Rel. Phenom. **47** (1988), 283.

[68] C.D. Wagner, H.A. Six, W.T. Jansen and J.A. Taylor, Applications of Surf. Sci. **9** (1981), 203.

[69] C.D. Wagner, D.E. Passoja, H.F. Hillery, T.G. Kinisky, H.A. Six, W.T. Jansen and J.A. Taylor, J. Vac. Sci. Techn. **21** (1982), 933.

[70] J.A. Taylor, J. Vac. Sci. Techn. **20** (1982), 751.

[71] O. Böse, E. Kemnitz, A. Lippitz, W.E.S. Unger, J. Anal. Chem. **358** (1997), 175.

[72] A.M. Ferendeci, *Physical foundations of solid state and electron devices* (McGraw-Hill, New York, 1991).

[73] R.H. Williams, Comtemp. Phys. **23** (1982), 329.

[74] A.P. Sutton and R.W. Ballufi, *Interfaces in crystalline Materials* (Clarendon, Oxford, 1995), Chap. 11.

[75] N.F. Mott and R.W. Gurney, *Electronic processes in ionic crystals*, 2nd Ed. (Clarendon, Oxford, 1948), Chap. 5.

[76] I.P. Batra and L. Kleinman, J. Electr. Spectr. Rel. Phenom. **33** (1984), 175.

[77] L. Österlund, I. Zorić and B. Kasemo, Phys. Rev. B **55** (1997), 15452.

[78] P.O. Gartland, Surf. Sci. **62** (1977), 183.

[79] J. Jacobsen, B. Hammer, K.W. Jacobsen and J.K. Nørskov, Phys. Rev. **B** (1995), 14954.

[80] D. D. Eley and P.R. Wilkinson, Proc. Roy. Soc. (London) **A227** (1955), 387.

[81] D. D. Eley and P.R. Wilkinson, Proc. Roy. Soc. (London) **A254** (1960), 327.

[82] A.T. Fromhold, J. Electrochem. Soc. **127** (1980), 411.

[83] M.W. Roberts and B.R. Wells, Surf. Sci. **8** (1967), 453.

[84] M.W. Roberts and B.R. Wells, Surf. Sci. **15** (1969), 325.

[85] H.L. Yu, M.C. Muñoz, F. Soria, Surf. Sci. **94** (1980), L184.

[86] C. Benndorf, H. Seidel, F. Thieme, Surf. Sci. **67** (1977), 469.

[87] T.N. Rhodin, J. Am. Chem. Soc. **72** (1950), 5102.

[88] T.N. Rhodin, J. Am. Chem. Soc. **73** (1951), 3143.

[89] N.F. Mott, Trans. Faraday Soc. **43** (1947), 429.

[90] A.T. Fromhold, J. Phys. chem. Solids **24** (1963), 1309.

[91] A.T. Fromhold and E.L. cook, Phys. Rev. Lett. **17** (1966), 1212.

[92] P.R. Emtage and W. Tantraporn, Phys. Rev. Lett. **8** (1962), 267.

[93] B.J. Kooi, M.A.J. Somers and E.J. Mittemeijer, Thin Solid Films **281-282** (1996), 488.

[94] C.D. Wagner, L.E. Davis, M.V. Zeller, J.A. Taylor, R.H. Raymond and L.H. Gale, Surf. Interf. Anal. **3** (1981), 211.

[95] S. Hofman, in: *Practical Surface Analysis*, Vol. 1, 2nd edn., Eds. D. Briggs and M.P. Seah (Wiley, Chichester, 1990), p. 143; M.P. Seah, p. 201.

[96] P.C. Graat, M.A.J. Somers and A. Böttger, Surf. Interf. Anal. **23** (1995), 44.

[97] L.J. Álvarez, L.E. León, J.F. Sanz, M.J.Capitán, J.A. Odriozola., J. Phys. Chem. **99** (1995), 17872.

On the Initial Oxidation of Aluminium in Oxygen Gas

Summary

Thin aluminium-oxide films (< 10 nm) are of great technological importance, because of their specific physical and chemical properties; i.e. large dielectric constant, large barrier height for electron tunnelling, high corrosion resistance, good thermal and mechanical stability and good adhesion. In order to control the thickness, chemical composition, morphology and (micro)structure, and thus the physical and chemical properties, of these thin aluminium-oxide films as produced by e.g. thermal or plasma oxidation of bare aluminium surfaces, a comprehensive and fundamental understanding of the oxidation process is required. The oxide-film growth, chemical composition, morphology and (micro)structure of very thin aluminium-oxide films (< 10 nm) produced by dry, thermal oxidation of bare aluminium surfaces has been studied. These oxide films are, for example, used in various types of microelectronic devices as a dielectric, diffusion and/or tunnelling barrier.

To investigate the stability of amorphous versus crystalline aluminium-oxide films on single-crystalline Al substrates as a function of growth temperature, oxide-film thickness and crystallographic orientation of the substrate, a thermodynamic model has been developed (Chapter 2). To this end, expressions have been derived for the estimation of the energies of the metal-substrate / amorphous-oxide film interface and the metal-substrate / crystalline-oxide film interface as a function of growth temperature, and crystallographic orientation of the substrate (including the effect of the strain due to the lattice mismatch at the interface between the metal substrate and the crystalline oxide film). It follows that, up to a certain critical thickness of the amorphous oxide film, the higher bulk Gibbs free energy of the amorphous oxide film, as compared to the corresponding crystalline oxide film, can be compensated for by its lower sum of the surface and interfacial energies. The model was applied to aluminium-oxide films on aluminium substrates. The predicted stabilities for an amorphous Al_2O_3 film on an Al substrate agree well with previous transmission electron microscopy observations: amorphous Al_2O_3 develops on {100} Al and {110} Al and crystalline γ-Al_2O_3 develops on {111} Al.

To establish the relations between the growth kinetics, chemical composition, morphology and microstructure of the developing oxide-film as a function of the oxidation conditions, bare single-crystalline Al substrates were exposed to oxygen at a low partial oxygen pressures ($\leq 1.33\times10^{-4}$ Pa) in the temperature range from 373 to 773 K. The oxidised samples were investigated with in-situ X-ray photoelectron spectroscopy (XPS) and high-resolution transmission electron microscopy (HREM). To explain the various relations as determined in this study, models were adopted for the mechanisms that govern the oxide-film growth during the different stages of oxidation at different temperatures.

XPS was applied to determine the oxide-film thickness, chemical composition, morphology, as well as the changes in chemical and binding state of the concerned ions in the grown oxide films. A novel method has been developed to accurately determine the thickness and the composition of oxide films on metal substrates from the measured XPS spectra of the bare and the oxidized metal (Chapter 3). The method comprises the determination of both the *total* metallic and the total oxidic *primary zero loss* (PZL) intensity for each core-electron level in the measured XPS spectra of the bare and the oxidised metal. The contribution of the intrinsic plasmon structure to the total metallic PZL intensity is taken into account using the intrinsic bulk (BP) and surface (SP) plasmon excitation probabilities for the concerned core-level electron emission process in the free-electron like metal. As demonstrated for the Al 2*p* photoemission process in the Al metal, values for these intrinsic BP and SP excitation probabilities can be determined separately from a series of intensities of the metallic and oxidic main peaks. This series of intensities is obtained from a measured photoelectron spectra recorded from the bare metal substrate and the metal substrate covered with a thin oxide overlayer of which the thickness is varied. The total *oxidic* PZL intensity is obtained from the measured spectrum of the oxidised metal after subtraction of a reconstructed metallic main peak. The method was successfully applied to determine the thicknesses and composition of the thin aluminium-oxide films grown on aluminium substrates by thermal oxidation (Chapter 4).

HREM was applied to determine the development of the microstructure and morphology of the oxide film as a function of oxidation temperature, as well as the crystallographic orientation relation(s) between the observed crystalline oxide phases and the parent Al metal substrate.

Application of the above techniques, and employing the method for the determination of the oxide-film thickness and its composition, led to the following results for the initial oxidation of a bare Al(431) substrate at a partial oxygen pressure of 1.33×10^{-4} Pa in the temperature range of 373 - 773 K.

The initial oxidation of the bare Al substrate proceeds by an island-by-layer growth mechanism, involving the lateral diffusion over the bare Al substrate surface of mobile oxygen species. At $T \leq 473$ K, the bare Al substrate is already covered with 2 - 3 oxide monolayers within 100 s of oxidation due to the very low mobility of the oxygen species on the surface. With increasing temperature both the lateral diffusion of the oxygen species and the rate of oxide formation increase: a decrease of the initial oxide island density and an increase of the oxide island size occur. An oxide film covering the entire Al substrate surface is formed after 200, 500 and 750 s of oxidation at 573, 673 K and 773 K, respectively. The 'closed' oxide-film is of less uniform thickness for higher oxidation temperatures.

Two different oxide-film growth regimes have been recognised for the oxide-film growth on the Al substrate in the temperature range from 373 to 773 K and at $p_{O_2} = 1.33\times10^{-4}$ Pa: (*i*) an initial regime of (very) fast oxide-film growth, and (*ii*) a second, much slower oxidation stage, which is only observed at high oxidation temperatures ($T \geq 673$ K).

The *initial*, fast oxidation stage at *low temperatures* ($T \leq 573$ K) culminates with an Al-deficient, amorphous oxide film of 'limiting' thickness. This 'limiting' thickness increases with increasing oxidation temperature. It was shown that the oxygen content of the amorphous oxide films is practically constant, whereas their Al content increases with temperature and time. The fast oxide-film growth rate is realised by the outward, *electric-field* controlled migration of Al cations across the developing oxide-film. The corresponding Mott potential V_M equals -1.6 V. A value of 2.6 eV was determined for the rate-limiting energy barrier for Al cation motion, which is located at the metal/oxide interface. At the end of the initial, fast oxidation stage, the electron tunnel current has become effectively zero. Then, under the constraint of coupled currents of electrons and cations, oxide-film growth stops at low temperatures, because both the chemical diffusion of ions across the oxide film and the contribution of electron transport by thermionic emission are negligibly small.

During the *initial*, fast oxidation stage at *high temperatures* ($T \geq 673$ K) an Al-enriched, amorphous oxide film is formed. The fast oxide-film growth rate is realised by the *electric-field* enhanced migration of Al cations through the developing oxide-film. However, the decrease of the oxygen sticking coefficient with increasing temperature for $T > 600$ K may either indirectly (the electric-field-enhanced migration of Al cations is rate-determining) or directly (supply rate of chemisorbed oxygen is rate-determining) lead to a lower oxide-film growth rate during the initial, fast oxidation stage as compared to the corresponding growth rate at lower temperatures.

During the *second*, slow oxidation stage at *high temperatures* ($T \geq 673$ K), the amorphous oxide film attains the stoichiometric composition of Al_2O_3 and becomes crystalline γ-Al_2O_3. As long as the oxide is amorphous, the oxide-film growth rate is realised by the interstitial, outward transport of Al cations under influence of the concentration gradient and a (small) electric field. As soon as γ-Al_2O_3 crystallites develop, the inward (chemical) diffusion of oxygen along grain boundaries establishes the growth.

The 'critical' thickness up to which an amorphous oxide film is thermodynamically preferred on the parent Al(431) substrate (instead of a crystalline of γ-Al_2O_3 film) at a growth temperature of 673 K is about 4 nm. The co-existence of both crystalline γ-Al_2O_3 and an amorphous-to-γ-Al_2O_3 transition oxide phase in the oxide-films grown at 673 K indicates that the initially fully amorphous oxide film gradually transforms into crystalline γ-Al_2O_3 during the second, slow oxidation regime at high temperatures. The orientation relationship between γ-Al_2O_3 and the parent Al(431) substrate is: $(111)_{Al} \| (111)_{\gamma\text{-}Al_2O_3}$ and $[110]_{Al} \| [110]_{\gamma\text{-}Al_2O_3}$.

Employing angle-resolved XPS, it was demonstrated that the oxide-films of 'limiting' oxide-film thickness formed at oxidation temperatures $T \leq 673$ K, are relatively enriched in Al (as compared to stoichiometric Al_2O_3) at their very surface. The disappearance of the Al-enriched oxide surface for higher oxidation temperatures (773 K), as well as during the second, slow oxidation stage (at 673 K), coincides with the transition from amorphous Al_2O_3 to crystalline γ-Al_2O_3. As indicated by both the constant chemical state of the Al cations, as well as by the nearly constant Al-O binding state, in the grown oxide films (independent of temperature and thickness), the short range ordering of the low-temperature, amorphous Al-oxide films closely resembles that of the crystalline γ-Al_2O_3 films grown at more elevated temperatures. The major part of the observed shifts in *oxide-film* O 1*s* en Al 2*p* binding energies and Al $KL_{23}L_{23}$ kinetic energy with both increasing temperature and thickness can be related to shifts of the Fermi level within the band gap of the oxide. These shifts of the Fermi level are induced by defect states within the band gap of the developing oxide-film due to the Al-enrichment of the oxide surface (at low temperatures) and/or the presence of an excess of Al in the oxide film near the metal/oxide interface (at high temperatures).

De Initiële Oxidatie van Aluminium in Zuurstof Gas

Samenvatting

Dunne aluminiumoxide films (< 10 nm) zijn van groot technologisch belang om hun specifieke fysische en chemische eigenschappen zoals: grote diëlektrische constante en barrièrehoogte voor elektronen tunneling, en grote weerstand tegen corrosie, alsmede goede thermische en mechanische stabiliteit en hechting. Dunne aluminiumoxide films kunnen worden gemaakt door bijvoorbeeld thermische of plasmaoxidatie van een schoon aluminium metaaloppervlak. Om de dikte, chemische samenstelling, morfologie en (micro)structuur, en dus de fysische en chemische eigenschappen, van dergelijke oxidefilms te beheersen (c.q. te manipuleren) is een gedegen en fundamenteel inzicht in het oxidatieproces noodzakelijk. Daarom is in dit proefschrift de groeikinetiek, de chemische samenstelling, de morfologie en de (micro)structuur bestudeerd van zeer dunne aluminiumoxide films (< 10 nm), zoals gevormd door droge, thermische oxidatie van schone aluminiumoppervlakken. Dergelijke oxidefilms worden bijvoorbeeld gebruikt als dielectrische-, diffusie- en/of tunnelbarrière in verschillende typen micro-elektronische schakelingen.

Om de stabiliteit van amorfe versus kristallijne aluminiumoxide films op eenkristallijne aluminiumsubstraten te bestuderen als functie van de groeitemperatuur, de dikte van de oxidelaag en de kristallografische oriëntatie van het substraat, is een thermodynamisch model ontwikkeld (Hoofdstuk 2). Hiertoe zijn uitdrukkingen afgeleid voor het afschatten van de energieën van het metaalsubstraat / amorfe oxidefilm grensvlak en het metaalsubstraat / kristallijne oxidefilm grensvlak als functie van de groeitemperatuur en de kristallografische oriëntatie van het substraat. Hierbij is rekening gehouden met het effect van de rek ten gevolge van de roostermispassing aan het grensvlak tussen het substraat en de kristallijne oxidefilm. Het blijkt dat, tot een zekere kritische dikte van de oxidefilm, de hogere bulkenergie van de amorfe oxidefilm ten opzichte van de corresponderende kristallijne oxidefilm, gecompenseerd kan worden door zijn lagere som van de oppervlakte- en de grensvlakenergieën. Het model is toegepast voor aluminiumoxide films op aluminium substraten. De voorspelde stabiliteiten voor een amorfe Al_2O_3 film op een Al substraat komen goed overeen met eerdere elektronenmicroscopische waarnemingen: amorf Al_2O_3 vormt zich op {100} en {110} Al en kristallijn γ-Al_2O_3 vormt zich op {111} Al.

Om de relaties te bepalen tussen de groeikinetiek, de chemische samenstelling, de morfologie en de microstructuur van de oxidefilm als functie van de oxidatiecondities zijn schone, eenkristallijne Al substraten blootgesteld aan zuiver zuurstofgas bij lage zuurstofpartiaaldrukken ($p_{O_2} \leq 1.33\times10^{-4}$ Pa) in het temperatuurbereik van 373 tot 773 K. De geoxideerde preparaten werden vervolgens onderzocht met behulp van in-situ röntgenfotoelektronenspectroscopie (XPS) en hoge-resolutie transmissie-elektronenmicroscopie (HREM). Om de verschillende relaties zoals verkregen in deze studie te verklaren, zijn modellen toegepast die de verschillende mechanismen van oxidelaaggroei beschrijven tijdens de opeenvolgende stadia van oxidatie bij verschillende temperaturen.

XPS is toegepast om de dikte van de oxidefilm, de chemische samenstelling, de morfologie en de chemische- en bindingstoestand van de desbetreffende ionen in de gevormde oxidefilms, te bepalen. Een nieuwe methode is ontwikkeld om nauwkeurig de dikte en de chemische samenstelling van oxidefilms op metaalsubstraten te bepalen uit gemeten XPS spectra van het schone en het geoxideerde metaal (Hoofdstuk 3). De methode omvat de bepaling van de *totale* metallische en de totale oxidische *primaire 'zero loss'* (PZL) intensiteit voor ieder elektron-energieniveau in de gemeten XPS spectra van het schone en het geoxideerde metaal. Hierbij is rekening gehouden met de bijdrage van de intrinsieke plasmonintensiteit aan de totale metallische PZL intensiteit door gebruik te maken van de waarschijnlijkheden van excitatie van intrinsieke bulk (BP) en oppervlakte (SP) plasmonen tijdens het desbetreffende elektronenemissieproces in het metaal. Voor het Al 2*p* foto-emissie proces in aluminium is gedemonstreerd dat waarden voor deze intrinsieke BP en SP excitatiewaarschijnlijkheden afzonderlijk kunnen worden bepaald uit een serie van intensiteiten van de metallische en oxidische hoofdpieken. Deze serie intensiteiten zijn verkregen uit gemeten fotoelectronenspectra van het schone metaal en het metaal bedekt met een dunne oxidefilm waarvan de dikte is gevarieerd. De totale oxidische PZL intensiteit is verkregen uit het gemeten spectrum van het geoxideerde metaal na aftrekken van een gereconstrueerde metallische hoofdpiek. De methode is met succes toegepast om de dikte en de chemische samenstelling te bepalen van dunne aluminiumoxide films op aluminium substraten gevormd door thermische oxidatie (Hoofdstuk 4).

HREM is toegepast om de ontwikkeling van de microstructuur en de morfologie van de aluminiumoxide film te bepalen als functie van de oxidatietemperatuur en de kristallografische voorkeursoriëntatie(s) tussen de kristallijne oxidefasen en het onderliggende Al substraat.

Met bovengenoemde technieken en door gebruik te maken van de methode voor de bepaling van de dikte en de chemische samenstelling van de oxidefilms, zijn de volgende resultaten verkregen voor de initiële oxidatie van een schoon Al(431) substraat bij een zuurstofpartiaaldruk van $p_{O_2} = 1.33\times10^{-4}$ Pa in het temperatuurbereik van 373 tot 773 K.

De initiële oxidatie van het schone Al substraat verloopt via de vorming van oxide-eilanden op het schone metaaloppervlak gevolgd door oxidelaaggroei. Dit gaat gepaard met de laterale diffusie van mobiel zuurstof over het schone metaaloppervlak. Bij oxidatietemperaturen $T \leq 473$ K is het oppervlak van het Al substraat al binnen 100 s oxideren bedekt met 2 - 3 oxide monolagen, omdat de mobiliteit van zuurstof op het Al substraatoppervlak erg laag is. Met toenemende temperatuur nemen zowel de laterale diffusie van zuurstof over het Al substraatoppervlak als de snelheid van oxidevorming toe. Dit resulteert in een afname van de initiële dichtheid van oxide-eilanden en een toename van de grootte van de oxide-eilanden. Bij oxidatietemperaturen van 573, 673 en 773 K is het hele Al substraatoppervlak bedekt met oxide na respectievelijk 200, 500 en 750 s oxidatie. De 'gesloten' oxidefilm is minder uniform in dikte voor hogere oxidatietemperaturen.

Er zijn twee verschillende regimes van oxidelaaggroei te onderscheiden voor de oxidatie van het Al substraat in het temperatuurbereik van 373 tot 773 K (bij $p_{O_2} = 1.33\times10^{-4}$ Pa): (*i*) een initieel regime van zeer snelle laaggroei, en (*ii*) een tweede stadium van langzame groei, dat alleen is waargenomen bij hoge oxidatietemperaturen ($T \geq 673$ K).

Het *initiële* regime van snelle groei bij *lage temperaturen* ($T \leq 573$ K) resulteert in de vorming van een Al-deficiënte, amorfe oxidefilm van begrensde ('limiting') dikte. De begrensde dikte van de oxidefilm neemt toe met toenemende oxidatietemperatuur. De zuurstofconcentratie in deze oxidefilms is praktisch constant, terwijl de aluminiumconcentratie toeneemt met toenemende temperatuur en oxidatietijd. De hoge groeisnelheid tijdens dit regime wordt gerealiseerd door de migratie van Al kationen door de oxidefilm naar het oppervlak onder invloed van een sterk elektrisch veld. De hiermee corresponderende Mott potentiaal bedraagt –1.6 eV. Een waarde van 2.6 eV is bepaald voor de energiebarrière aan het metaal/oxide grensvlak voor Al kationmigratie. Deze energiebarrière is bepalend voor de snelheid van oxidelaaggroei tijdens het initiële regime.

Aan het einde van het initiële regime van snelle groei is de tunnelstroom van elektronen door de oxidefilm effectief nul geworden. Bovendien zijn bij lage temperaturen zowel de diffusie van kationen onder invloed van de concentratiegradiënt als de bijdrage van elektronentransport door thermische emissie verwaarloosbaar klein. Omdat er geen netto lading door de oxidefilm wordt getransporteerd tijdens oxidatie (dus de simultane stromen van kationen en elektronen zijn aan elkaar gekoppeld) stopt de oxidelaaggroei aan het einde van het initiële regime bij lage temperaturen.

Tijdens het *initiële* regime van snelle groei bij *hoge temperaturen* ($T \geq 673$ K) vormt zich een amorfe oxidefilm met overmaat aan Al. De hoge groeisnelheid wordt gerealiseerd door de migratie van Al kationen door de oxidefilm naar het oppervlak onder invloed van een sterk elektrisch veld. Echter, de afname van de stickingscoëfficiënt van zuurstof met toenemende temperatuur voor $T > 600$ K kan indirect (kationentransport onder invloed van het elektrische veld is snelheidsbepalend) dan wel direct (de aanvoer van gechemisorbeerd zuurstof is snelheidsbepalend) resulteren in een lagere groeisnelheid tijdens het initiële, snelle groeiregime (in vergelijking met de initiële groeisnelheid bij lagere temperaturen).

Tijdens het *tweede* stadium van langzame groei bij *hoge temperaturen* ($T \geq 673$ K) bereikt de amorfe oxidefilm de stoiciometrische samenstelling van Al_2O_3 en wordt kristallijn γ-Al_2O_3. Zolang de film amorf is, wordt de groei van de oxidefilm gerealiseerd door transport van Al kationen door interstitiële holtes in de dichte pakking van zuurstofionen van het oxide naar het oppervlak onder invloed van de concentratiegradiënt en een gering elektrisch veld. Zodra er zich γ-Al_2O_3 kristallieten vormen, wordt de laaggroei gerealiseerd door de (chemische) diffusie van zuurstof langs korrelgrenzen door de oxidefilm naar het metaal/oxide grensvlak.

Een amorfe oxidefilm op het Al(431) substraat is bij een oxidatietemperatuur van 673 K thermodynamisch stabieler dan de corresponderende kristallijne γ-Al_2O_3 film op het substraat tot een 'kritische' filmdikte van ongeveer 4 nm. De oxidefilms gevormd bij 673 K bestaan uit zowel kristallijn γ-Al_2O_3 als een overgangsoxide tussen amorf Al_2O_3 en kristallijn γ-Al_2O_3. Dit wijst erop dat de initieel volledig amorfe oxidefilm geleidelijk kristallijn γ-Al_2O_3 wordt tijdens het tweede stadium van langzame groei. De oriëntatierelatie tussen γ-Al_2O_3 en het onderliggende Al(431) substraat is: $(111)_{Al} \| (111)_{\gamma\text{-}Al_2O_3}$ and $[110]_{Al} \| [110]_{\gamma\text{-}Al_2O_3}$.

Met behulp van hoekafhankelijke XPS metingen is aangetoond dat de oxidefilms met begrensde dikte, gevormd bij oxidatietemperaturen $T \leq 673$ K, aan het oppervlak relatief rijk zijn aan Al (ten opzichte van stoichiometrisch Al_2O_3). Het verdwijnen van deze overmaat aan Al aan het oxideoppervlak bij hogere oxidatietemperaturen (773 K) én tijdens het tweede stadium van langzame groei (bij 673 K) valt samen met de overgang in de structuur van de oxidefilm van amorf Al_2O_3 naar kristallijn γ-Al_2O_3. Zowel de chemische toestand van de Al kationen als de Al-O bindingstoestand in de gevormde oxidefilms zijn nagenoeg constant, onafhankelijk van de oxidatietemperatuur en dikte. Dit betekent dat de korte afstandsordening in de amorfe oxide films gevormd bij lage temperaturen overeenkomt met die in de kristallijne γ-Al_2O_3 films gevormd bij hogere temperaturen. Het grootste deel van de waargenomen verschuivingen in de O 1*s* en Al 2*p* bindingsenergieën en de Al $KL_{23}L_{23}$ kinetische energie van de oxidefilm zijn het gevolg van verschuivingen van het Fermi-niveau in het oxide. Deze verschuivingen van het Fermi-niveau worden veroorzaakt door defecttoestanden in de 'bandgap' van het oxide door een overmaat aan Al aan het oxideoppervlak (bij lage temperaturen) en/of de aanwezigheid van een overmaat aan Al in de oxidefilm aan het metaal/oxide grensvlak (bij hoge temperaturen).

Curriculum Vitae

Lars Petrus Henricus Jeurgens

geboren op 29 juni 1971 te Aarle-Rixtel

1983 – 1989	Atheneum, Carolus Borromeus College te Helmond.
1989 – 1995	Studie Geologie aan de Universiteit Utrecht. Afgestudeerd in de groep Petrochemie & Kristallografie op het onderwerp '*Synthese en contrasterend adsorptiegedrag van amorf ijzeroxyhydroxide*'. Scriptie gehonoreerd met de AMOCO-prijs.
1995 – 1996	Onderzoeksmedewerker bij de afdeling Petrofysica in het Koninklijke Shell Exploratie en Produktie Laboratorium te Rijswijk. Onderwerp: ‘*Ontwikkelen van nieuwe methodes om de fysische en chemische eigenschappen van gesteentes te bepalen met behulp van Nucleaire Magnetische Resonantie (NMR).*
1996 – 2000	Onderzoeker in Opleiding in de sectie Fysische Chemie van de Vaste Stof, Laboratorium voor Materiaalkunde, Technische Universiteit Delft. Promotieonderzoek op het onderwerp '*De initiële oxidatie van aluminium in zuurstof gas*'.
2000 -	Post-doctoraal onderzoeker in de sectie Fysische Chemie van de Vaste Stof, Laboratorium voor Materiaalkunde, Technische Universiteit Delft. Onderwerp: '*Ontwikkelen van preoxidatiebehandelingen van hoge-temperatuur metallurgische coatings ter verbetering van zowel de weerstand tegen corrosie alsmede de hechting met de bovenliggende thermische-barrière laag.*'